UNIVERSITY OF CAPE TOWN

IYUNIVESITHI YASEKAPA • UNIVERSITEIT VAN KAAPSTAD

The influence of cylindrical charge geometry on the velocity of blast-driven projectiles in one dimension

Ruixuan Qi

Supervisor:

Prof. Genevieve Langdon

Co-Supervisors:

A/Prof. Steeve Chung Kim Yuen

Mr Trevor Cloete

March 2020

Blast Impact and Survivability Research Unit

Department of Mechanical Engineering

Faculty of Engineering and the Built Environment

University of Cape Town

This work is submitted in partial fulfilment of the requirements of the degree of Master of Science in Engineering specialising in Mechanical Engineering

Abstract

The impact of improvised explosive devices (IEDs) on the safety of civilians can be devastating, especially when solid objects are inserted into the explosives. These inserts are propelled at high speed and increase the lethality of an IED detonation. Due to the wide range of possible IED configurations, a fundamental understanding of momentum transfer from explosives to the solid inserts is required.

This project investigated the influence of charge geometry on the velocity of a 5 mm diameter stainless steel ball bearing. The ball bearing was half-buried and centrally placed on the flat face of a cylindrical charge which was detonated centrally on the opposite face. The geometric parameters of interest were the charge diameter and the charge aspect ratio (length/diameter).

Investigations were carried out in the project through blast and impact experiments as well as numerical simulations.

The impact velocity of the explosively driven ball bearing was inferred using the impact crater depth on a witness plate. The correlation between crater depth and the impact velocity was determined using impact experiments which was performed using a gas gun. The average velocity (between detonation and impact) was captured by tracking the time of detonation and impact. The time of impact was recorded through a Hopkinson Pressure Bar (HPB) behind the witness plate. Additionally, the total axial impulse and the localised impulse, over the face of the HPB, were recorded by a ballistic pendulum and the HPB.

Numerical simulations were conducted using a commercial software, Ansys Autodyn 18.0. The blast arrangement was simulated using a two-dimensional, axisymmetric model. The maximum velocity, average velocity, impact velocity, total axial impulse and localised impulse were 'extracted' from the simulations. The simulated velocities agreed well with experimental measurements, showing less than 2% variation. The deformed shape of the blasted ball bearings displayed similar characteristics to the model predictions. There were differences in the simulated impulse, with the numerical model predicting higher magnitudes but a less localised distribution.

For a constant charge diameter, the bearing velocity increased in a nearly logarithmic manner with the increase in aspect ratio until a critical aspect ratio of $\sqrt{3}/2$ was reached. At a constant charge mass, the bearing velocity decreased with the increase in charge diameter. The numerical model suggested that the influence of charge geometry on the bearing velocity was likely caused by the shape of the detonation pressure waves. The detonation pressure profile is sensitive to the charge aspect ratio and the diameter.

Plagiarism declaration

I know the meaning of plagiarism and declare that all the work in the document, save for that which is properly acknowledged, is my own. This thesis/dissertation has been submitted to the Turnitin module (or equivalent similarity and originality checking software) and I confirm that my supervisor has seen my report and any concerns revealed by such have been resolved with my supervisor.

Signed: Signed by candidate 29 March 2020.

Ruixuan Qi

Acknowledgement

Firstly, I would like to express gratitude to my primary supervisor, Prof. Genevieve S Langdon, for her patience and guidance throughout this project and with my Master's degree. I am very grateful for the time and effort she invested in this project despite her busy schedule. It has been a great pleasure working with you.

To my co-supervisor, A/Prof Steeve Chung Kim Yuen, your input in the project was greatly appreciated, in particular with initialising the project concept and experimental methods.

Many of the components and techniques used in the experimental arrangements, particularly in the work related to Hopkinson Pressure Bar and the gas gun would not have succeeded if were not for the guidance from my co-supervisor, Mr Trevor Cloete.

I would like to acknowledge the staff members of the mechanical workshop for machining many of the experimental parts, especially to Pierre Smith, Heinrich Christians, Grant Springle and Gavin Doolings.

The help from George Du Plessis with gauging the Hopkinson Pressure Bar is greatly appreciated.

The polystyrene bridges were manufactured in the UCT School of Architecture's workshop. The help from the workshop officers, John Coetzee and Shafiek Matthews are invaluable.

I would also like to thank Dr Richard Curry for his assistant with installing Autodyn and setting up the data acquisition system for the Hopkinson bar.

Tensile test of the aluminium was conducted under the help of Penny Louw. She along with Soraya Von Willingh also provided with assistant with using the stereomicroscope.

The inputs from Prof Gerald Nurick and Dr Reuben Governder were greatly appreciated.

Lastly, I would like to thank my parents for supporting me not only through my Master's degree but also the life long education background they built for me without which would not lead to my current achievement.

Table of Contents

List of Figures

List of Tables

Chapter 1

Introduction

1.1 Background and motivation of research

Between 2011 and 2016, over 130 000 people [1] were injured or died from the use of improvised explosive devices (IED), 81% of which were civilians. Catastrophic events such as the Manchester attack, still remind the world that threats from IEDs are lethal and are of great concern to the health and safety of the general public. As the name 'IED' suggests, this type of explosive weapon is improvised, often home-made and can therefore take on many forms or shapes. Furthermore, the devices have typically been adapted or modified using non-standard parts (such as nails or ball bearings) to enhance their lethality. One of the great difficulties in IED research is the wide variety of possible configurations. Hence, a fundamental understanding of the mechanisms of momentum transfer to these solid particles from the explosive is needed. This will allow model validation at the fundamental level so that more complex models representing real IEDs can be developed with confidence.

This work focuses on the analysis of an IED in one of its simplest forms. As shown in Figure 1.1, this simple representation comprised of an unconfined, rear detonated cylindrical charge with a single ball bearing which was half-barred on the opposite face. From this, the influence of charge geometric parameters, such as the aspect ratio ($Length/Diameter$, i.e. L/D) and the charge diameter on the one-dimensional velocity of the ball bearing was investigated. The investigation was carried out numerically and experimentally. Given the limited time of the project, the explosive experiments were designed to maximize the range of diameters and aspect ratios tested. No repeat experiments were designed, instead, extensive experimental design and numerical validations were used to ensure the accuracy of the findings.

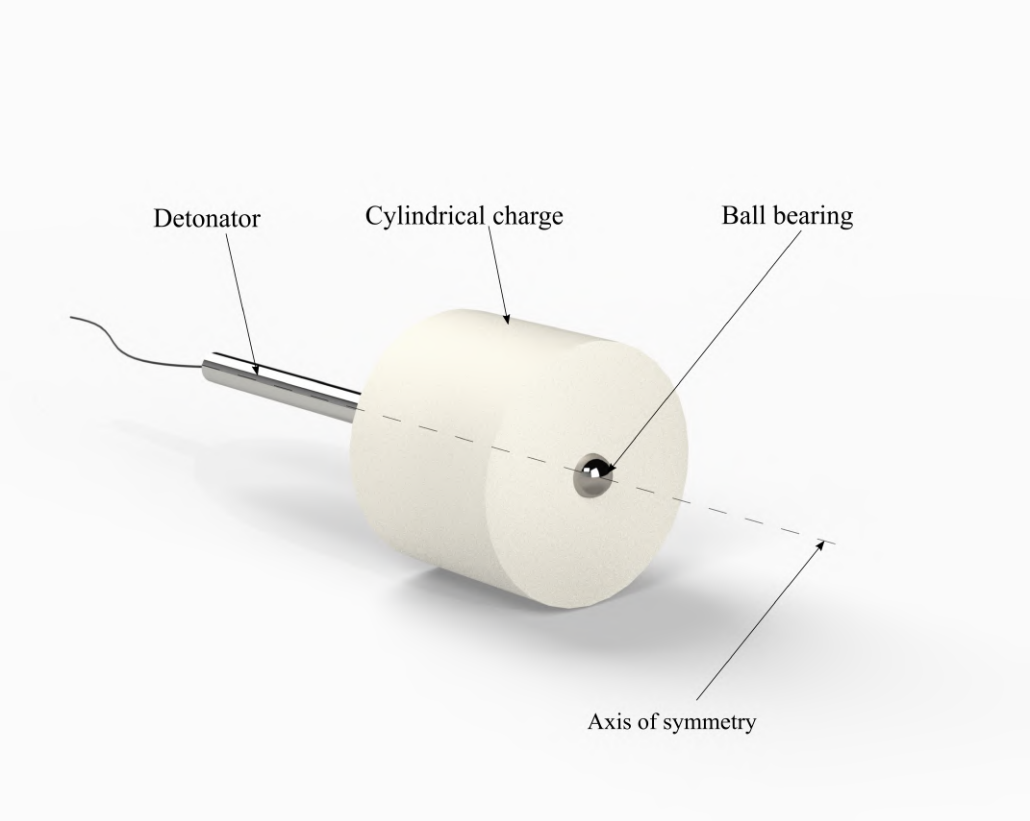

Figure 1.1: Schematic showing the basic arrangement of the problem to be solved in this dissertation.

Part of the reason for the simplicity in the geometry was to reduce the complexity introduced into the numerical models. It also allows the isolation of key variables, such as aspect ratio or charge diameter, and determine their subsequent effects. Thus, the chosen geometry facilitated the validation of numerical predictions of detonation shock wave propagation and shock-solid interactions. These test fundamental multiphysics abilities which are prerequisites in providing predictions on the aforementioned IED performances with confidence. This is a particularly important capability for commercially available software as they will be more accessible when designing protection against IEDs.

1.2 Aim and Objectives

The main aim was to investigate the characteristics of momentum transfer from the detonation of a cylindrical charge to a ball bearing in the axial direction. The detailed objectives were as follows:

- To investigate the influence of charge aspect ratio on the velocity of the ball bearing in one dimension experimentally.
- To investigate the influence of charge diameter on the velocity of the ball bearing in one dimension experimentally.
- To simulate, using commercially available software, blast propagation and solid-shock interactions by employing the dimensions used in the experimental arrangement.
- To validate the model using experimental data.

- Use the simulation results to gain additional insights beyond what could be measured experimentally.

1.3 Outline of the dissertation

A review of relevant literature is presented in Chapter 2. The experimental arrangements used to achieve the first two objectives are reported in detail and presented in Chapter 3. This is followed by the reporting of characterisation of materials in Chapter 4. The characterised data was used in the numerical simulations. A detailed description of the numerical model and the supporting reasoning made for some choices in the model is presented in Chapter 5. In Chapter 6, the experimental results and the observations are presented. In Chapter 7, the numerical results are presented and compared with the experimental results. Thereafter, the results are discussed. Finally, conclusions and recommendations are given in Chapter 8.

Chapter 2

Literature Review

The chapter presents the background related to explosives and some common blast properties. The current methods available to study impulse transfer from explosives at near-field are also reported. This is followed by a summary of the existing research in blast driven projectile, including their limitations and results. Finally, some empirical equations to relate projectile velocity to crater depth are presented.

2.1 Background review of explosives and blast research

2.1.1 Classifications of explosives

Explosions are violent, sudden, noisy and startling [2]. Despite their nature, explosives have been used for centuries since the discovery of black powder in the 7th century. Today, explosives are categorised by their sources into three groups [2, 3]: physical explosions (such as the rupture of pressurised vessels), chemical explosions and nuclear explosions. Chemical explosives can be identified as primary explosives, secondary explosives or propellants. Primary explosives are highly sensitive to shock, friction, electric spark or high temperatures. They are therefore, mostly used as detonators to initiate secondary explosives. Secondary explosives do not detonate easily but can achieve much higher detonation velocities of up to 9000 m/s. The detonation velocity for the secondary explosive PE-4, a variation of RDX based plastic explosive is estimated at 8190 m/s [2].

2.1.2 Ideal Pressure history

Explosives can release an intense burst of energy in a few microseconds [3]. During the detonation process, rapid expanding hot gases produce a sudden jump in pressure. This discontinuous jump in pressure is known as the shock front. A shock front can travel faster than the speed of sound. As the shock front propagates, gasses behind the shock front are expanded, causing an exponential decrease in pressure. The idealised far-field blast pressure profile observed from a stand-off distance (SOD) from an unconfined blast can be described by the Friedlander waveform [4] as shown in Equation 2.1. It relates the change of pressure to time observed from the detonation of a high explosive under no confinement. This is given as:

$$P(t) = P_s e^{-\frac{t}{t^*}}(1 - \frac{t}{t^*}) \tag{2.1}$$

where P_s is the peak overpressure, t^* is the time at which the pressure first decays below the atmospheric or ambient pressure (P_a) before detonation.

It is observed from Figure 2.1 that the pressure history graph is divided into two zones: above and below the atmospheric pressure which are the positive and negative phases, respectively. Impulse generated from the blast can be calculated from integrating pressure with respect to time. In an unconfined environment, the total impulse from the positive and negative phase over a large time is zero. This is expected as all pressure from the blast in an unconfined space would dissipate completely. Mathematically, the impulse can be expressed as:

$$I_{total} = \int_{t_0}^{t_N} P(t)dt = 0 \tag{2.2}$$

Where t_0 is the time at which peak pressure occurs, and t_N is the time at which pressure equalises to the atmospheric pressure. The positions for t_0 and t_N are illustrated on Figure 2.2.

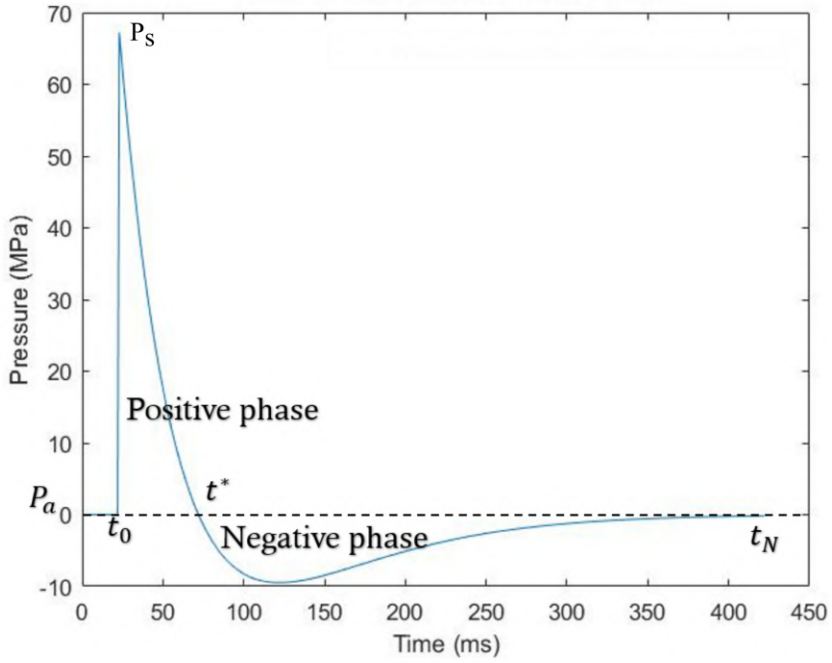

Figure 2.1: Idealised pressure-time graph from Friedlander waveform [4].

2.1.3 Blast scaling

Blast overpressure is dependent on both its charge mass and the stand-off distance (SOD). It is therefore convenient to express distance in terms of the charge mass as a 'scaled distance'. The scaled distance is usually calculated using the Hopkinson-Cranz Scaling Law [5, 6] which is given in Equation 2.3 as:

$$Z = \frac{R}{W^{\frac{1}{3}}} \tag{2.3}$$

Where Z is the scaled distance, R is the stand-off distance in meters and W is the mass of a spherical explosive in kilograms of TNT.

2.1.4 Basic effect of geometry

Cylindrical charges have unique blasting properties when compared to spherical charges. A typical shock wave profile from spherical charges is shown in Figure 2.2. Circular shock waves were observed to propagate outward from the point of detonation. In comparison, cylindrical charges produce distinctively different pressure profile where pressure generated from the detonation is divided into the axial and the radial direction of the cylinder connected by a weaker 'bridge wave'. This is illustrated in Figure 2.3.

Knock et al. [7, 8] studied the blast profile of cylindrical charges in both axial and radial direction under no confinement. The blast profile of a cylindrical charge was captured using high-speed photography shown in Figure 2.4. The positions of the side and axial wave (end wave) as well as the bridge wave are indicated clearly.

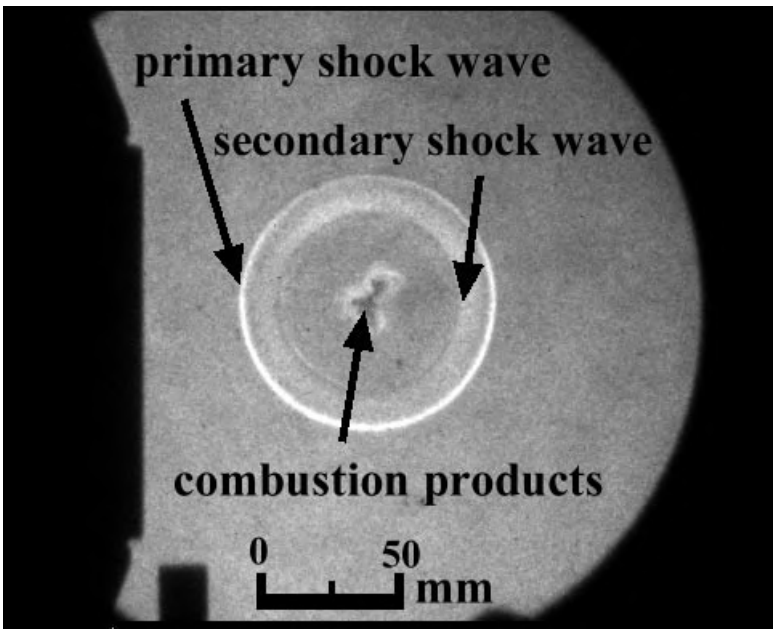

Figure 2.2: Photograph showing the pressure profile of a spherical charge [9].

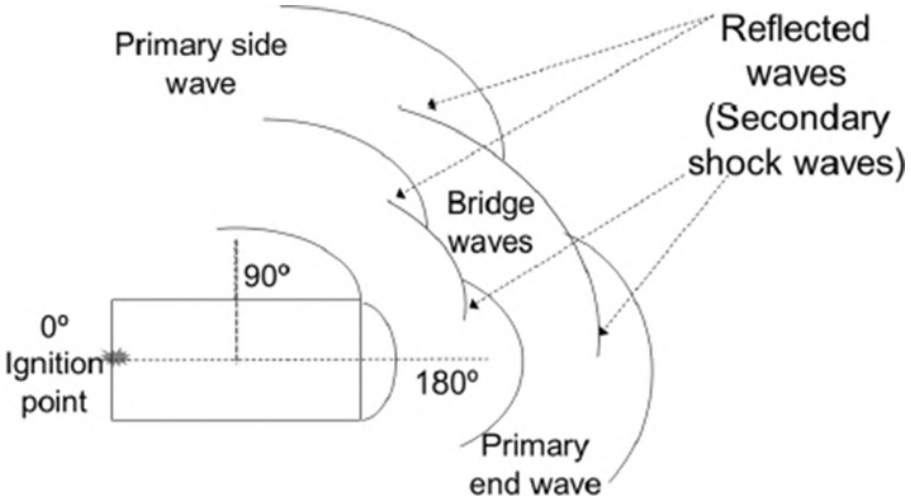

Figure 2.3: Pressure profile from a cylindrical charge [8].

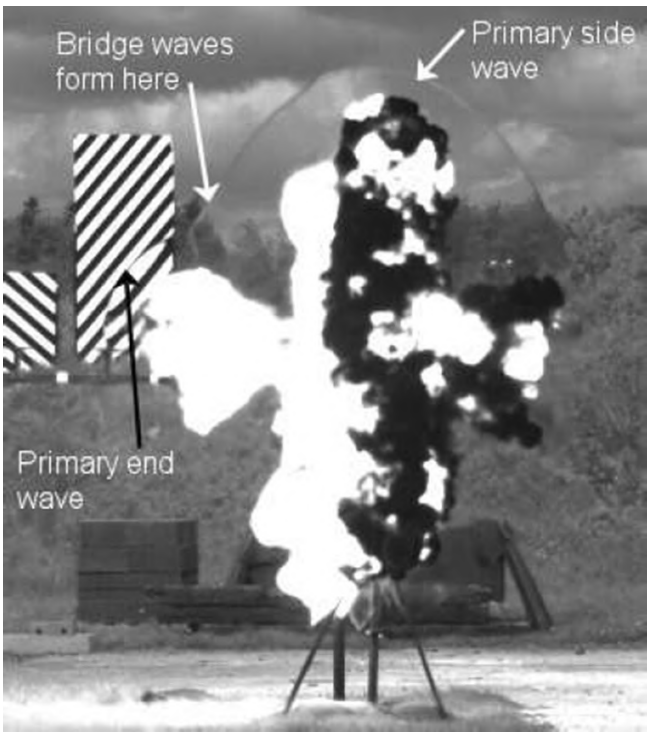

Figure 2.4: High-speed image of a cylindrical shock profile [8].

Effective charge mass

Kennedy [10] reported that the axial properties of cylindrical charges are affected by 'side losses'. It was suggested, based on the effect of lateral rarefaction waves, that explosives within 30°of the normal of an edge on the side of the cylindrical charge cannot contribute to axial impulse. Figure 2.5 illustrates the two scenarios in which effective charge mass for axial impulse can be calculated.

Note that the axis of symmetry is illustrated in grey dotted lines in Figure 2.5. The black box at the bottom of the illustration represents a solid object for the charge to accelerate. The cylindrical charge has height l. The green region is the effective charge mass that will contribute to the acceleration of the plate. This region is a circular cone with a height h note that two scenarios can occur. The two scenarios are when $l \leq h$ and $l > h$. The left schematic in Figure 2.5 depict $l \leq h$. In this case:

$$h = l \tag{2.4}$$

and that the effective mass becomes the mass of a truncated cone.

$$m_{effective} = \rho \frac{\pi}{12}(d_1^2 + d_1 d_2 + d_2^2)h \tag{2.5}$$

For $l > h$ the effective mass is the mass of a right circular cone.

$$m_{effective} = \pi d_1^2 \frac{h}{12} \tag{2.6}$$

The magnitude of the aspect ratio for maximum axial impulse can then be calculated as:

$$AR_{max} = \frac{h}{d_1} \tag{2.7}$$

This means that as the aspect ratio increases above the maximum effective ratio, the axial impulse reaches the asymptote.

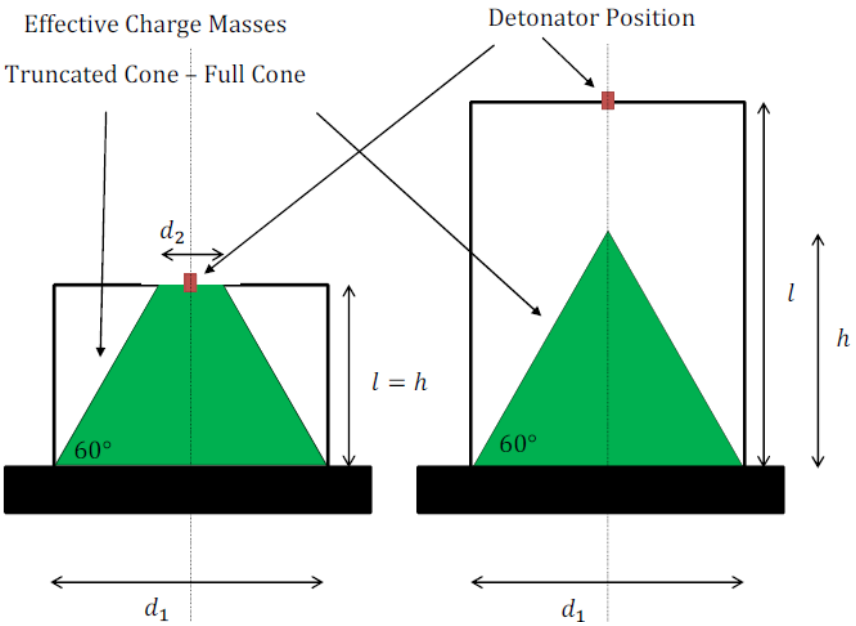

Figure 2.5: Schematic showing the region of effective charge mass for axial impulse[11].

2.1.5 Loading condition

Blast loads generated from explosives can be impulsive, dynamic or a combination[12]. The load type is determined by the duration of load and the response which is affected by stiffness and mass of the structure. Baker et al. [13] defined the classification of impulse, dynamic and quasi-static loading to be:

$$\text{Impulsive Loading} \rightarrow \omega t_d < 0.4$$

$$\text{Dynamic Loading} \rightarrow 0.4 \leq \omega t_d \leq 40$$

$$\text{Quasi-static Loading} \rightarrow \omega t_d > 40$$

where ω is the natural frequency of the structure.

The NORSAK standard [14]classified the three load types as:

$$\text{Impulsive Loading} \rightarrow t_d/T < 0.3$$

$$\text{Dynamic Loading} \rightarrow 0.3 \leq t_d/T \leq 3$$

$$\text{Quasi-static Loading} \rightarrow t_d/T > 3$$

where T is the fundamental period of the structure. For both cases, t_d is the load duration.

2.2 Methods to predict response of structures to blast loading

It is impractical to model real detonation processes as they are highly complex. Consequently, various simplified approaches have been used. These were summarised by Nurick et al. [15].

The first approach is to use ideal detonation theories such as the Chapman-Jouguet (CJ) model [16, 17] and the Zel' dovich-Von Neumann-Doring (ZND) model [18, 19, 20]. These models can be used to estimate the blast profile and provide an estimate for blast parameters in one-dimension. The second approach uses empirical methods to estimate blast properties. For example, far-field blast pressure can be predicted using the Kingery and Bulmash empirical methods [12] which are experimentally based. This can be improved further by using TNT equivalence methods and Hopkinson-Cranz scaling methods to provide predictions in ranges exceeding the experimental data. It is limited to far-field applications and will therefore not be discussed further. The third method is to assume idealised impulse loading conditions as introduced by Taylor [21] to model material response. This can be further refined by incorporating finite element numerical methods to estimate structural responses [22]. This is not a reasonable assumption in this application.

The fourth approach is to use non-ideal detonation theories based on the gas dynamic principles to estimate blast properties. This includes Detonation Shock Dynamics (DSD) theory developed by Bdzil [23] and Stewart [24, 25]. This method incorporates equation of states, such as the Jones-Wilkins-Lee (JWL) equation of states (EOS) [26] with numerical methods to provide a relatively accurate estimate of the pressure development. The detonation pressures and the attenuation of shock waves through different mediums over a wide range of complex geometries in two dimensions can be simulated. The method can be further incorporated with commercial multi-physics solvers such as Ansys Autodyn or LS Dyna to accurately model structural response from blast loading.

The last method described in [15] is to use experimental measurements of blast properties, such as overpressure or impulse transfer. This approach often uses pressure transducers in the far-field [7] or Hopkinson Pressure Bars (HPB) [27, 28, 29] and ballistic pendula [30, 31, 32] in the near-field. Pressure transducers provide an averaged global estimation of the pressure history at far-field. At near-field, the Hopkinson bar records an average force history over of the surface area of the bar. Two-dimensional maps of the force history can be obtained using a HPB array [29]. While in the case of ballistic pendula, the total impulse over the blast duration is captured. Other experimental techniques include tracking the displacement of blasted aluminium cans as used by Held [33] or studying the plastic blast response of characterised monolithic material; using digital image correlation to investigate the transient blast response of monolithic materials by Curry et al. [34] or using energy equivalent impulse methods to predict plate response by Rigby et al. [35]. Despite the differences in the experimental methods, impulse distribution and material responses recorded by different methods can produce highly consistent results with one and other as shown by Rigby et al. [36].

The last two approaches (two-dimensional numerical methods and HPB) were employed in this project.

2.2.1 Ideal detonation models

Ideal detonation theories are one-dimensional. The Chapman and Jouguet (CJ) model [16, 17] and the Zel' dovich-Von Neumann-Doring (ZND) models [18, 19, 20] are two popular models used to describe the ideal detonation process. Some of the key differences between ideal and non-ideal detonation theories are highlighted in Table2.1.

Table 2.1: Table highlighting the differences between ideal and non-ideal detonation models.

	Ideal Detonation	Non-ideal Detonation
Reaction rate	Instantaneous	Reaction takes time
Velocity of detonation	Equal to CJ velocity at reaction zone	Less than CJ velocity
Lateral expansion	No	Yes
Shock wave front	Planar, one-dimensional	Curved, 2D or 3D
Energy release	Instantaneously released in the reaction zone.	Released within and out of the detonation driving zone
Detonation models	CJ model, ZND model	Wood and Kirkwood [37], Detonation Shock Dynamics, Direct Numerical Solution

Chapman-Jouguet detonation model

The Chapman-Jouguet (CJ) model was introduced independently by Chapman [16] and Jouget [17] over a century ago. The pressure versus displacement graph of an unconfined detonation resulted from the CJ model is presented in Figure 2.6, where P_0 is the atmospheric pressure and P_{CJ} is the CJ pressure of the given explosive. This is one of the simplest detonation theories and it assumes the following conditions:

- The detonation and flow of detonation products are in one dimension
- The detonation front is a plane where the chemical reaction of the explosive products reacts instantaneously. The reaction zone has a negligible thickness and causes a discontinuous jump in pressure.
- The reaction is in equilibrium i.e. the shock front is moving at a constant speed, the CJ velocity of the explosive.
- The flow immediately following the shock front is subsonic and the expanding rarefaction waves do not disturb the shock front.

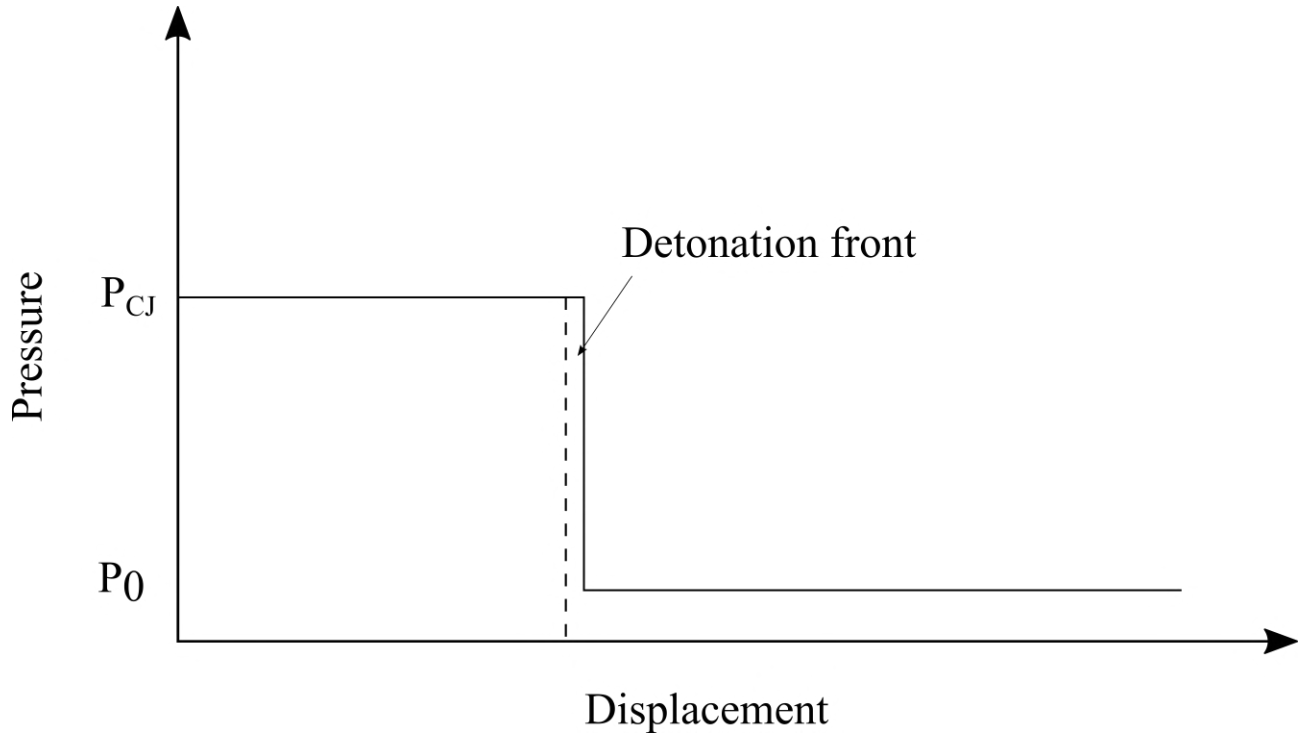

Figure 2.6: Schematic showing the pressure-displacement from an ideal CJ detonation model, modified from [38].

Zel'dovich-Neumann-Dring model

The Zel'dovich-Neumann-Dring (ZND) model, also known as the Simple Model, was proposal during World War II independently by Zel'dovich [18], Neumann [19] and Dring [20]. It is based on the CJ model, but the reaction zone is no longer infinitely small. In the ZND model, the shock front has zero thickness. It purely acts as an interface between the reacted and unreacted explosives, creating a discontinuous jump in pressure. The reaction zone follows immediately after the shock front, generating a higher pressure jump to what is known as the Von Neumann spike. The gas flow after the reaction zone follows the same assumption as the CJ model. The resultant pressure-displacement graph is shown in Figure 2.7. This is a slightly more realistic approach than the CJ model.

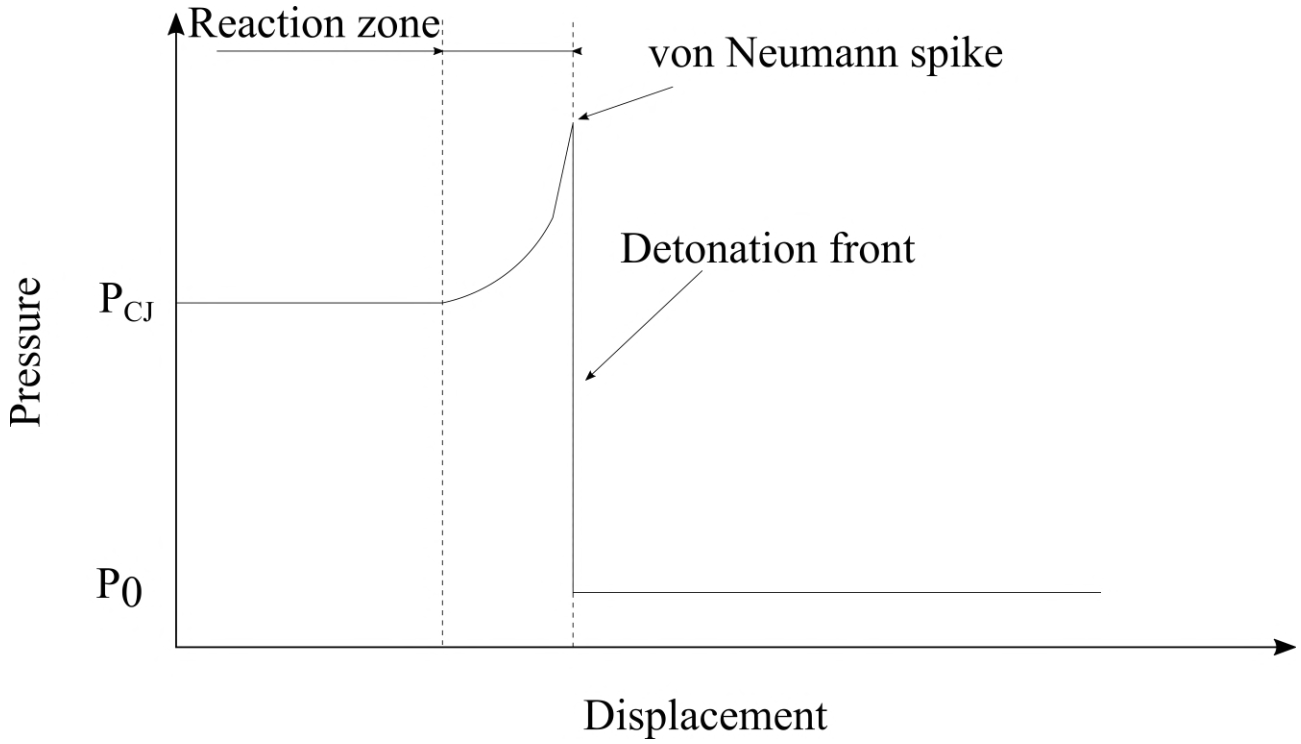

Figure 2.7: Schematic showing the pressure-displacement from the ZND model, modified from [38].

This one dimensional model, along with the theory of effective charge mass, was used by Nurick et al. [15] to describe the pressure profile of explosives with different geometries immediately after detonation as shown in Figure2.8. The charge shapes used in the study were cylindrical (CY), inverted truncated cone (ITC) and truncated cone (TC). Additionally, the influence of aspect ratio of these shapes was investigated. The pressure contour from 'thick' (high L/D) and 'thin' (low L/D) of the three shapes were also presented. Nurick et al. [15] described the 'length' of the shock waves between the three shapes as:

$$L_{CY} = \frac{M_{CY}}{M_{TC}} L_{TC} \tag{2.8}$$

$$L_{ITC} = \frac{M_{ITC}}{M_{TC}} L_{TC} \tag{2.9}$$

Where $M_{CY}M_{TC}$ and M_{ITC} are the effective charge masses.

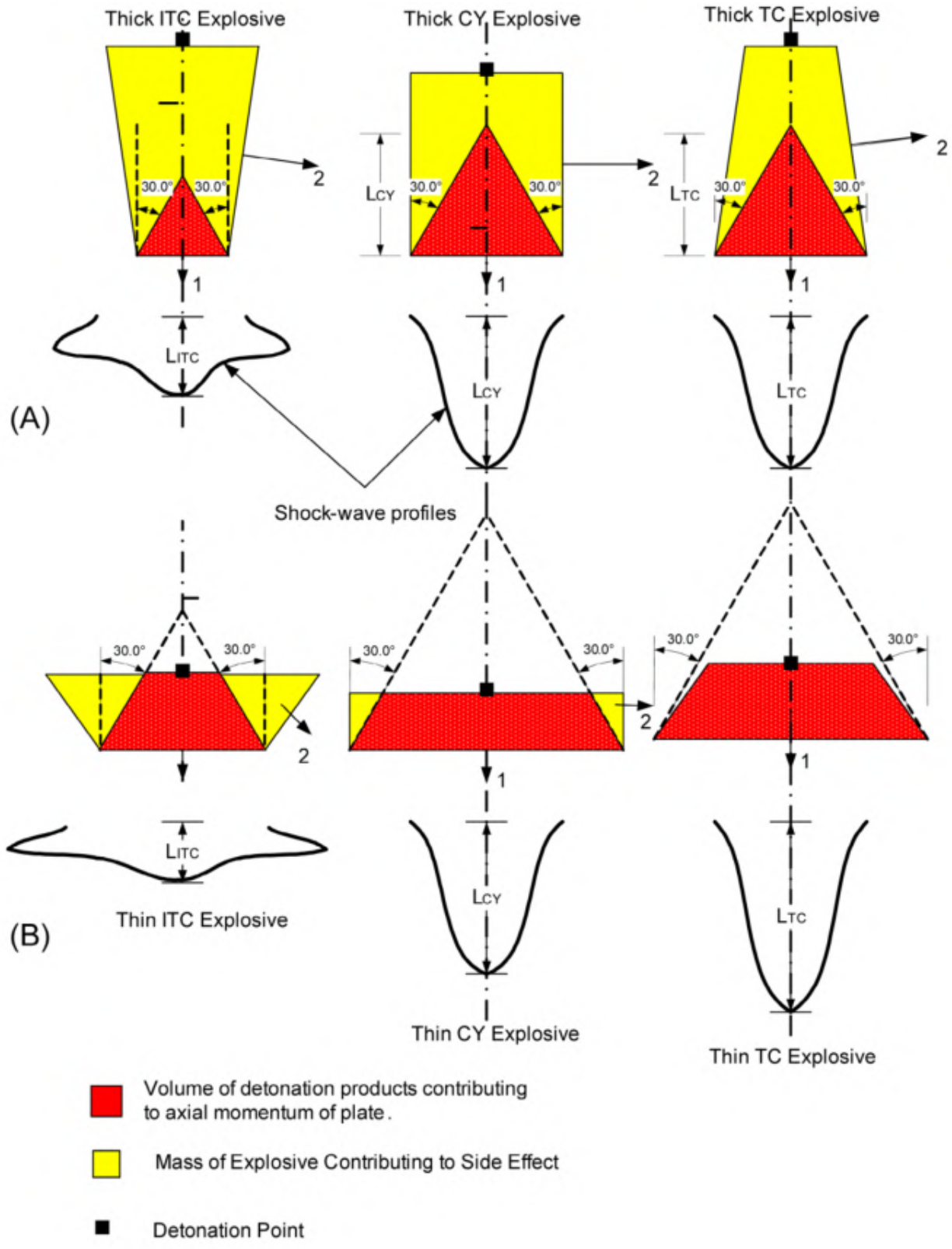

Figure 2.8: Schematic of the shock wave profiles developed using the ZND model and the concept of effective charge mass for (A) 'thick' and (B) 'thin' charge shapes, taken from [15].

2.2.2 Two-dimensional non-ideal detonation models

Detonation shock dynamics

Hill et al. [39] showed that, unlike the assumptions made in the ideal detonation models, real detonation usually have a curved shock front. Additionally, depending on the shape of the explosive, the curvature can have a strong influence on the detonation properties. It has been shown that the detonation velocity of explosives can change up to 40% from multi-dimensional effects [40]. Therefore there was a need to develop 2-D and 3-D detonation models.

The DSD theory developed by Bdzil and Stewart [24, 25] is an asymptotic theory which employed intrinsic partial differential equations (PDEs) that captured the dynamics of the detonation shock front instead of solving the reactive Euler equations directly which are computationally demanding. Appropriate boundary (interface problems) and initial conditions were used to further improve the accuracy of DSD. Furthermore, the solution is coupled with an EOS which calculates the explosive-specific values such as shock pressure, density or other pertinent properties. DSD has been found to produce accurate shock front propagation results when compared against direct numerical solutions [41] without the heavy computational costs.

Figure 2.9 illustrates the geometry of the shock propagation described in the DSD model [24, 25]. This model is based on the following assumptions:

- The detonation front is curved as a result of lateral expansion. The radius of the curvature is much larger than the thickness of the reaction zone.
- The shape change of the reaction zone takes much longer than the time it takes for a particle to pass through the reaction zone.
- The flow that follows the reaction zone does not affect the reaction zone. i.e there is no upwinding between the flow zone and reaction zone.
- Within the reaction zone, the particle velocity u travels at $u + c \approx D_n$, where D_n is the local shock speed. This yields $(u - D_n)/c \approx -1$. That is, the relevant Mach number squared is approximately equal to 1. Therefore, behind each shock front, there exists a sonic locus.

The local shock speed D_n for an uncased charge is given as:

$$D_n = Dcos\theta_M \tag{2.10}$$

Where θ_M is the angle between normal of the shock to the direction of the shock propagation.

Note that the DSD model [24, 25] was calculated using the intrinsic coordinates along the diverging streamlines to produce a more realistic result.

Interface interactions can affect the detonation process[24, 25]. The interaction between the oblique detonation wave with an inert boundary differs based on the type of interface material. In general, interaction at the oblique detonation wave depends on the impedance experienced at the interface as

shown in Figure 2.10. At a low impedance interface, such as air, a rarefaction wave is reflected into the explosive as a Prandtl-Meyer fan [42, 43]. At an interface with high impedance, the detonation is reflected, creating interference with the reaction zone. In addition, the angle of attack also changes the interaction. The angle of attack, denoted as ω, is the angle between the normal of the incident shock D_1 and the angle of the normal of the un-shocked inert material D_{nin}. For a small ω, as observed in low impedance materials, the disturbances as a result of the interaction do not affect the reaction of the detonation.

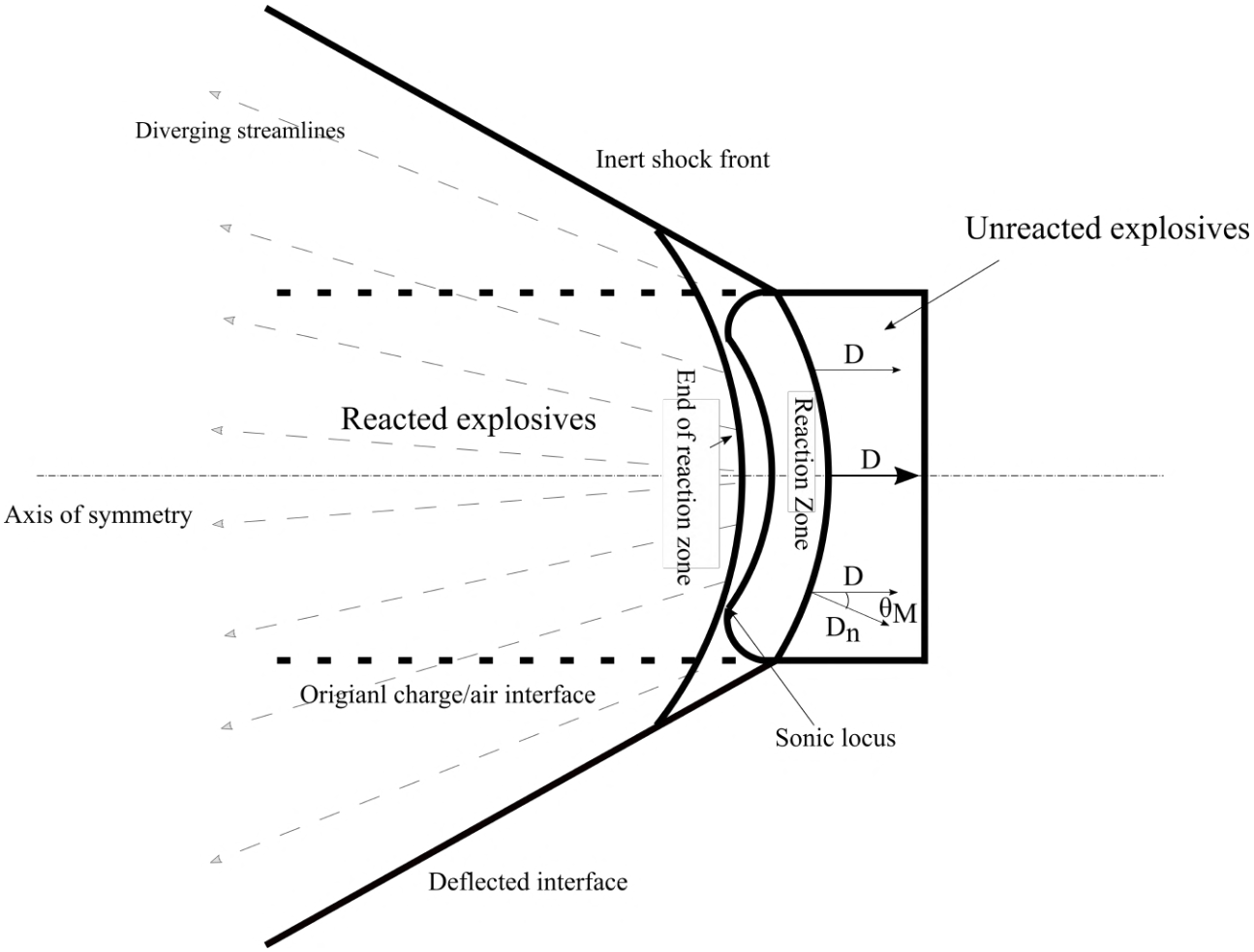

Figure 2.9: Schematic showing the two-dimensional steady non-ideal detonation based on the DSD model, modified from [40]

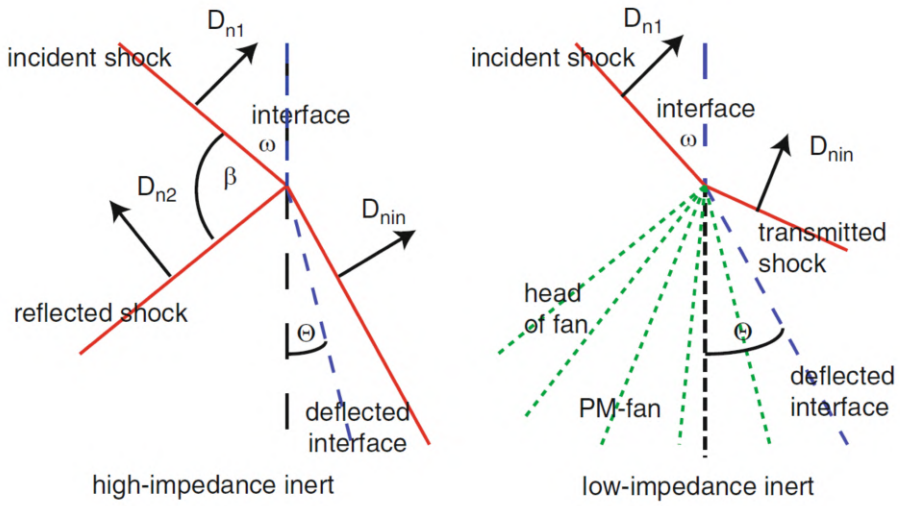

Figure 2.10: Schematic showing two classes of interfaces, high-impedance inert and low-impedance inert boundaries and their respective reactions [40].

Jones-Wilkins-Lee equation of state

Equation of states for explosives can be classified by their inclusion or exclusion of chemistry. The Jones-Wilkins-Lee (JWL EOS) [26] is one of the most widely used EOS without explicit chemistry. It is an EOS that describes the adiabatic expansion of detonation products based on experimental data on metal cylinder experiments. The EOS was first proposed by Jones and Miller [44], later improved by Wilkins [45] and lastly improved by Lee [26] who introduced the final EOS as JWL. This is given in Equation 2.11 as:

$$P = A\Big(1 - \frac{\omega}{R_1 V}\Big)e^{-R_1 V} + B\Big(1 - \frac{\omega}{R_2 V}\Big)\omega^{-R_2 V} + \frac{\omega E}{V} \tag{2.11}$$

Where V is the relative volume V/V_0, the initial volume V_0 is calculated using the initial density of the explosive as $V_0 = 1/\rho_0$, ω is the Grüneisen coefficient[46]. Lastly, A, B, R_1, R_2 are explosive specific parameters.

2.2.3 Experimental methods to determine impulse transfer at near-field

The term 'near-field' in blast loading is typically used for scaled distance $Z < 1\ m/kg^{1/3}$, where Z is the Hopkinson-Cranz scaled distance [29, 47]. In this region, the blast loading is characterised by extreme magnitude in temperature and pressure, and very often highly non-uniform loading conditions, both spatially and temporally. At $Z < 0.4\ m/kg^{1/3}$, very few direct measurements exist, particularly for cylindrical charges. Experimental techniques such as the use of ballistic pendula and Hopkinson bar have shown high reliability and repeatability in the past for near-field blasts [30, 32, 48]. This section presents some of these methods and their findings that might contribute to the investigation of this project.

Unconfined impulse data from the ballistic pendulum

The ballistic pendulum is a simple yet robust technique that is able to estimate the axial impulse imparted to a blast loaded structure. It has been used extensively in the study of plate deformation from explosive loading in the near-field [30, 32, 48, 49, 50].

Jacob et al., Langdon et al. and Nurick et al. [15, 49, 50] investigated various metal plate responses from cylindrical charges using similar experimental arrangements as shown in Figure 2.11. In these three works, disk-shaped PE-4 cylindrical charges from ⌀18 mm to ⌀70 mm were used with aspect ratios ranging from 0.0262 to 0.477 [15, 49, 50]. These aspect ratios were all well below the maximum effective aspect ratio discussed in Section 2.1.4. The charge mass ranged from 3 g to 20.5 g. The scaled distances ranged between 0.0438 to 0.083 $m/kg^{1/3}$.

The axial impulse versus charge mass from the experimental results in [15, 49, 50] are presented in Figure 2.12. It was observed that the experimental results were consistent and that the axial impulse increased linearly with increased charge mass. It is possible to fit a linear trend line through all the test data with a strong correlation coefficient of 0.9698. A more extensive review of other experimental studies from Yuen et al. [51] produced similar findings when results were translated into non-dimensionalised forms.

The effect of charge diameter on axial impulse can be observed from the results captured by [15] and [49], since [50] only used one charge diameter. For the clarity of demonstration, the results from [15] (Figure 2.13) and [49] (Figure 2.14) are presented separately.

The data labels shown in Figure 2.13 are the charge masses measured in grams. Explosive charges with the same mass produced higher impulses when the discs had a larger diameter. For example, the 3.6 g charge with ⌀25 mm produced higher impulse than the 3.7g charge with ⌀18 mm.

In the data presented by [49], the axial impulse from similar charge diameters increased with the increase in aspect ratio. However, for the charge diameters between 24 to 32 mm, where a larger range of aspect ratio was tested, axial impulse did not increase entirely linearly with the increase in charge length. This was likely due to the effect of effective charge mass. Furthermore, the increase in impulse as a result of charge diameter appeared to be limited by a minimum aspect ratio, below which point the axial impulse would decrease with the increase in charge diameter. The impulse from 8 and 9 g charges are colour coded in blue and red. It can be noted that for 9 g detonations, the axial impulse did not increase with the diameter at ⌀38 mm and decreased at ⌀48 mm. For 8 g charges, the increase in axial impulse started to asymptote at ⌀38 mm.

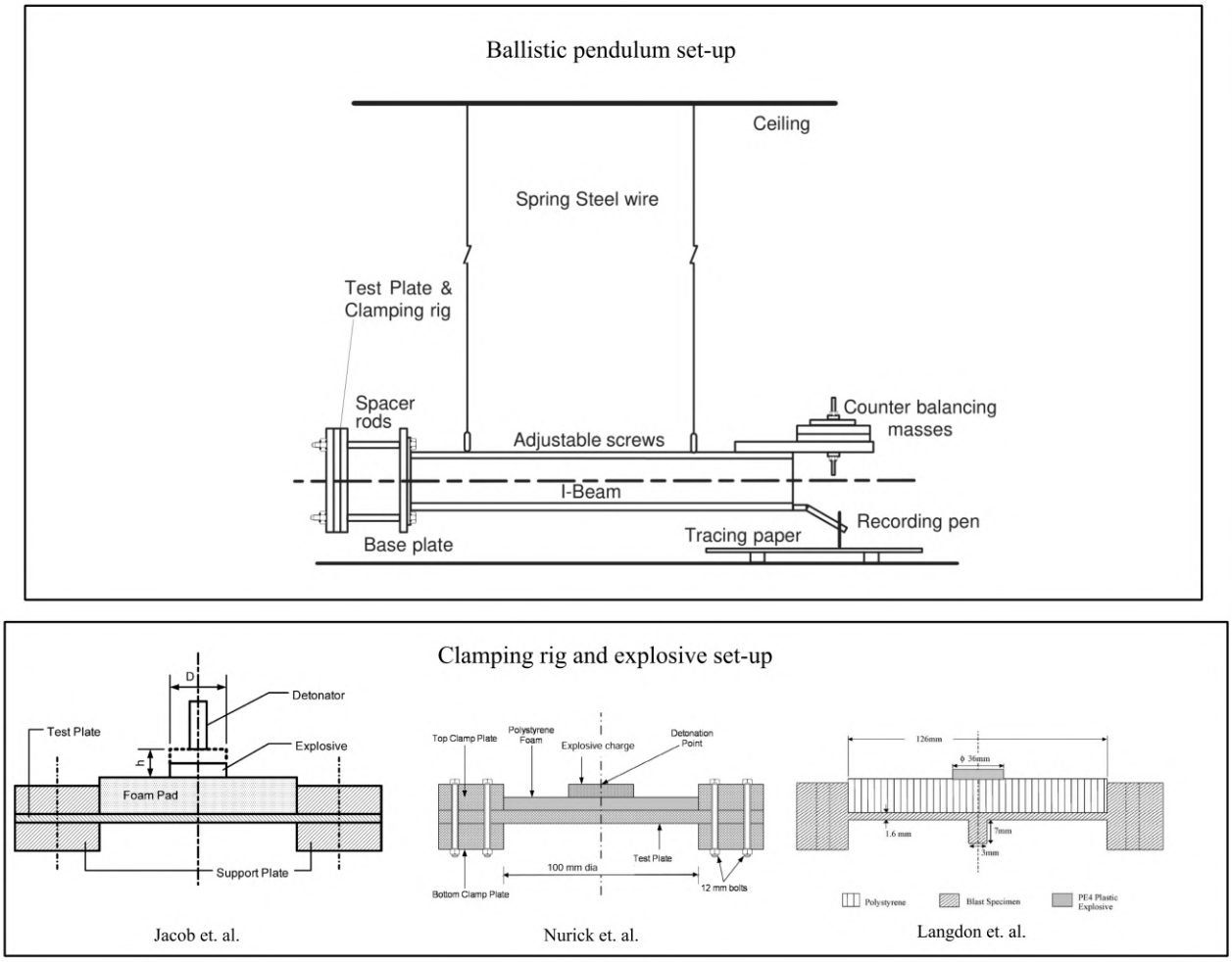

Figure 2.11: Schematic of the ballistic pendulum and different clamping arrangements used by Jacob et al. [49], Langdon et al. [50] and Nurick et al. [15]

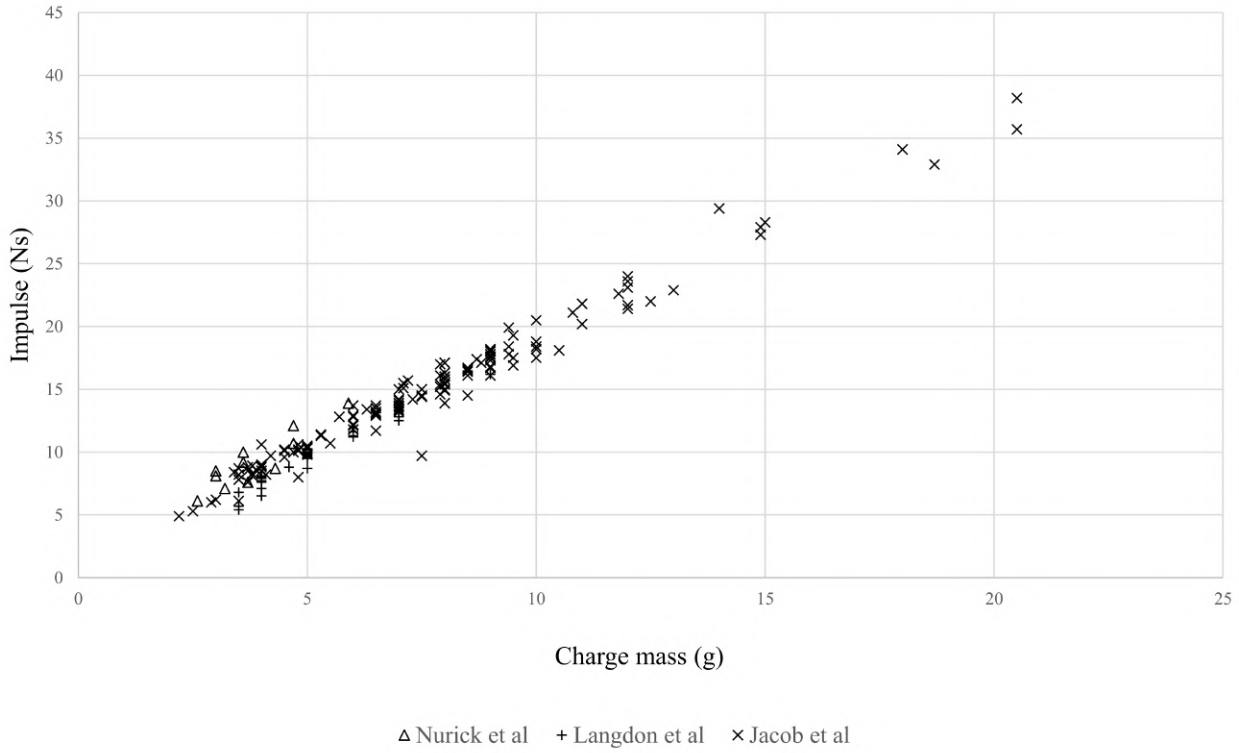

Figure 2.12: Graph of axial impulse versus charge mass from the experimental results captured by Jacob et al. [49], Langdon et al. [50] and Nurick et al. [15]

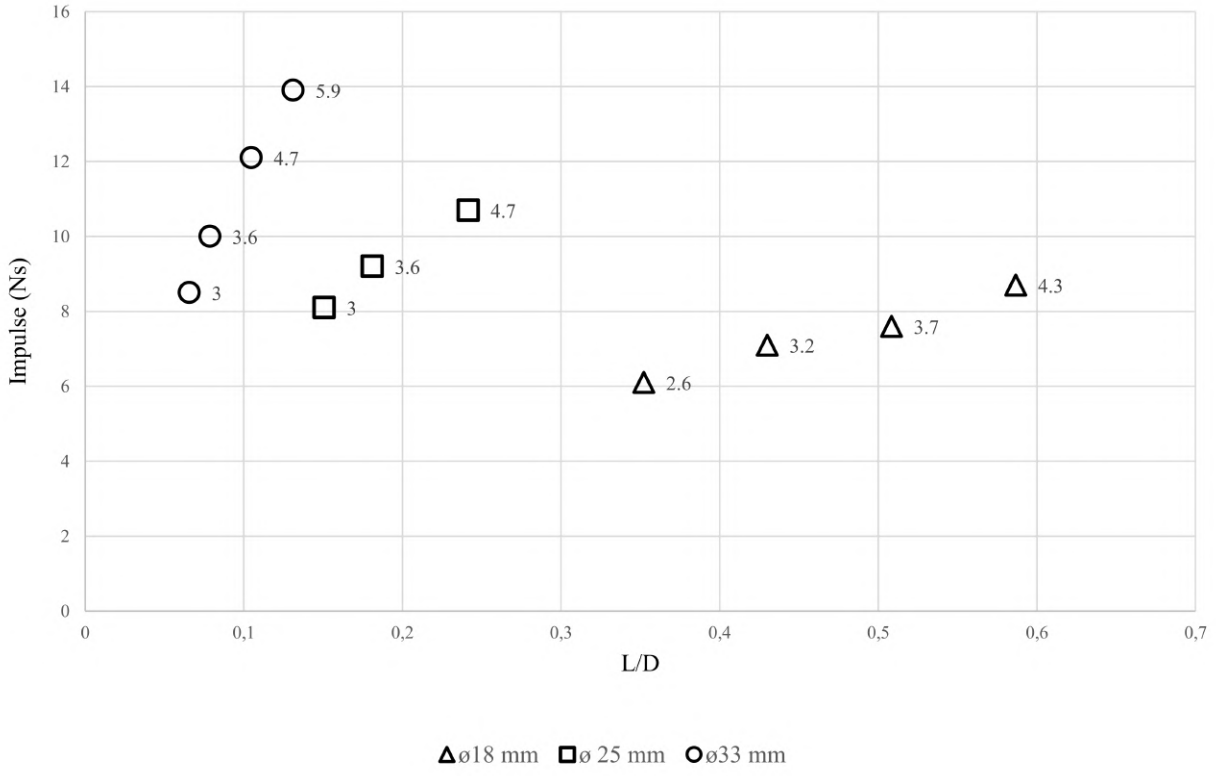

Figure 2.13: Graph showing the impulse versus charge aspect ratio using results reported by Nurick et al. [15], grouped by charge diameters. Data labels indicate the mass of the detonation in grams.

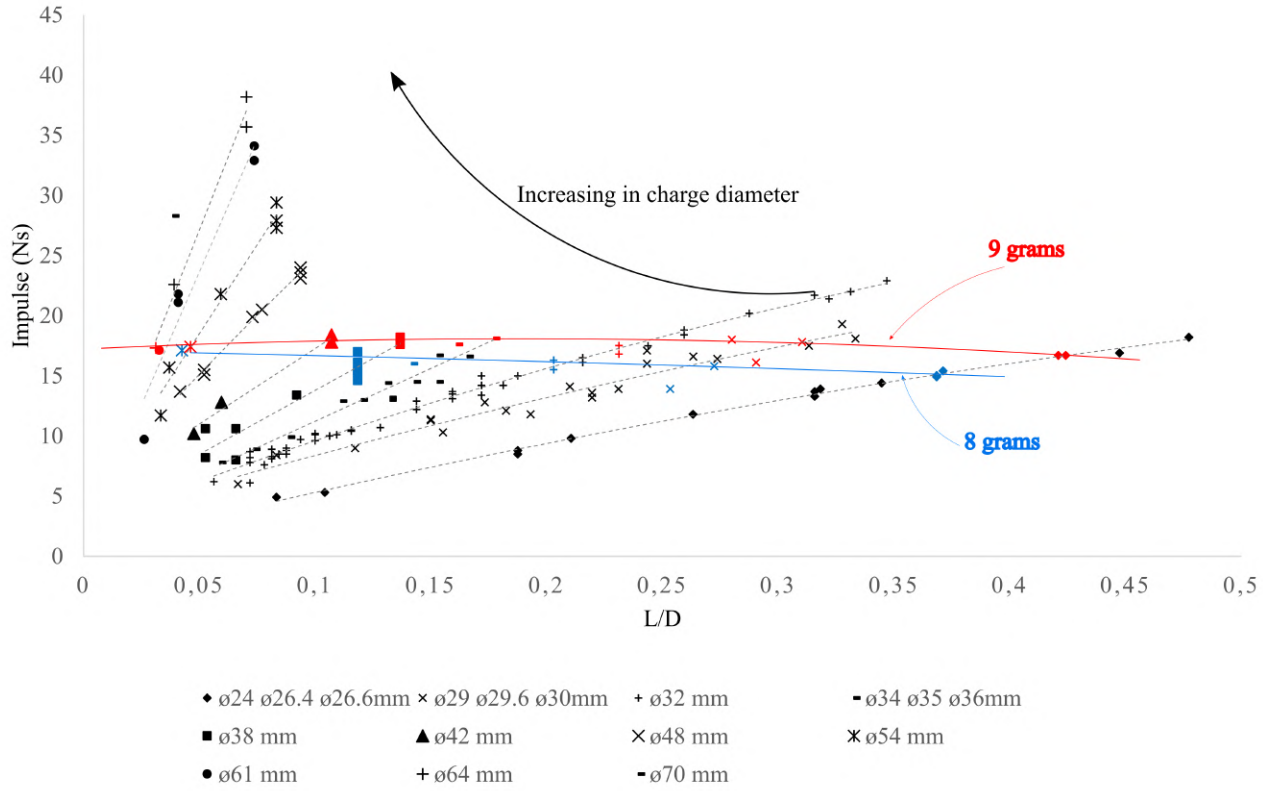

Figure 2.14: Graph showing the impulse versus charge aspect ratio using results reported by Jacob et al. [49], grouped by charge diameters.

Semi-confined impulse data from the ballistic pendulum

Internally blast loaded, laboratory scaled tests were investigated by Davids et al. [11] using the same ballistic pendulum arrangement as [15, 49, 50]. The geometry and dimensions of the arrangement are shown in Figure 2.15. The charges were placed at 150 mm to the closed end of the tube. Results of the axial impulse versus charge mass were compared against the unconfined experiments as shown in Figure 2.16. A similar linear-gradient could be observed from the semi-confined results when compared against unconfined results. Additionally, there is a near-constant increase in impulse as a result of confinement.

A graph of axial impulse versus charge aspect ratio is shown in Figure 2.17, using results from Davids et al. [11]. Impulse that resulted from constant charge mass are colour-coded and their masses are shown in grams. A similar increase in impulse as a result of charge diameter can be observed in the semi-confined environment. A nearly 'perfect' linear increase in axial impulse with the increase in aspect ratio was observed. Furthermore, this linear relationship extended passing the effective charge mass limit at $\sqrt{3}/2$ to 2.5. This is likely due to the additional contribution to axial motion of the pendulum from the reflected shock waves emitted by the curved side of the cylindrical charges. Davids et al. [11] A decrease in impulse occurred when the blast tube was ruptured, which would have reduced the reflection. The axial impulse from numerical simulation yielded very close results to the experimental findings.

Davids et al. [11] simulated the experimental arrangement inside the blast tube. The model was

axisymmetric and was performed in Ansys Autodyn. In the model, air was simulated using the ideal gas model and the C-4 parameters in the JWL EOS [26] was used to simulated PE-4 explosives used in the experiment. The pressure contours from the simulation were presented by Davids et al. [11]. Figure 2.18 illustrates the simulation set-up and the pressure contours of two 43 g charges with aspect ratios of 0.8 and 2.2 at different times after detonation. At 20 μs after detonation, the shock front emitted from the curved side of the charge reached the inner tube wall while the shock front emitted from the front face of the charge propagated to the right. The confinement caused by the wall forced the pressure to propagate longitudinally along the tube. Thus, part of the pressure emitted from the side of the charge was propagating in the same direction as the pressure emitted from the flat face. This is more evident when observing the differences of the pressure profiles between $t = 20\mu s$ and $t = 30\mu s$. At $t = 30\mu s$, the pressure from the flat face has reached the tube wall while a significant portion of the side pressure is propagation towards the end of the tube. Both of which will contribute to the axial impulse captured by the ballistic pendulum.

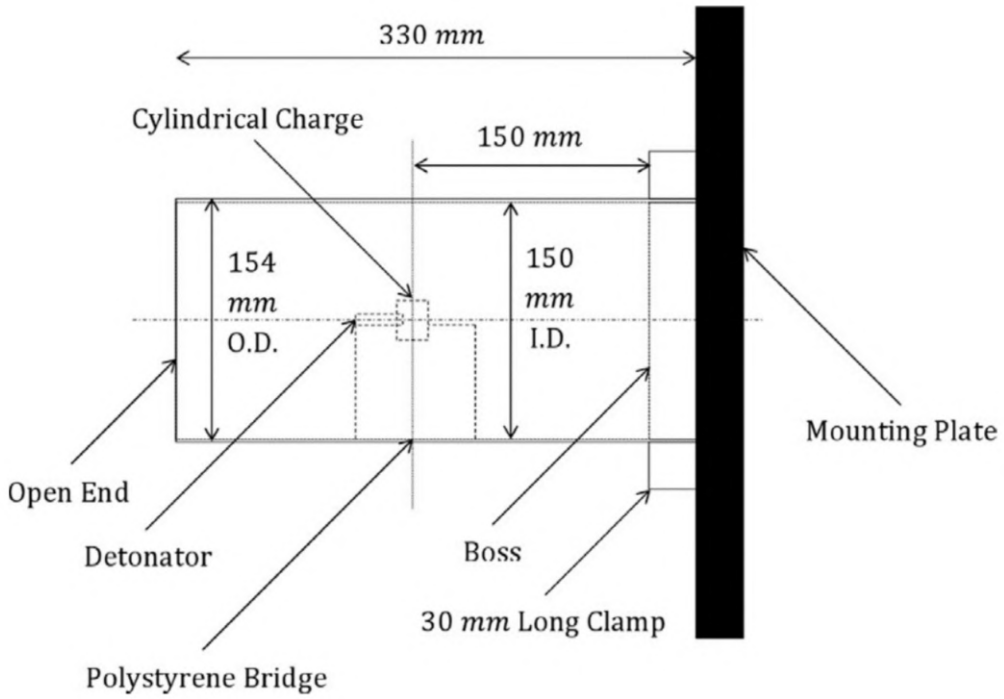

Figure 2.15: Schematic showing the blast tube arrangement used by Davids et al. [11].

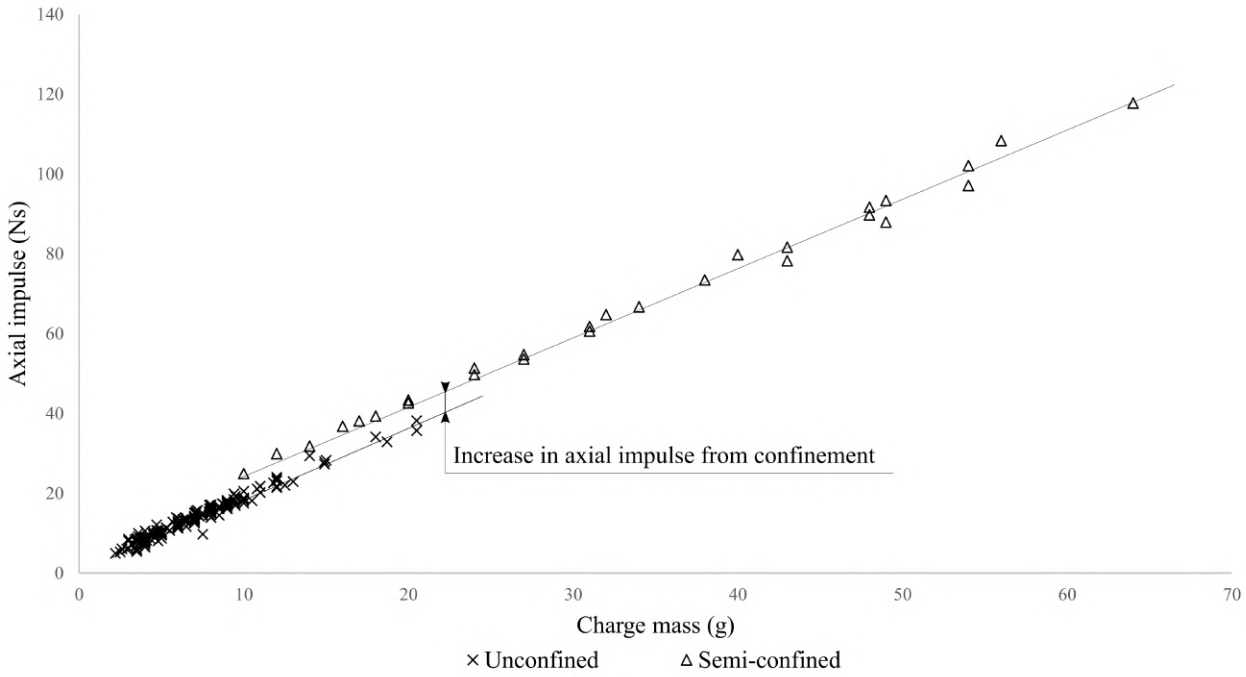

Figure 2.16: Graph showing the comparison of axial impulse versus charge mass reported by David et al. [11] and the unconfined studies reported by Jacob et al. [49].

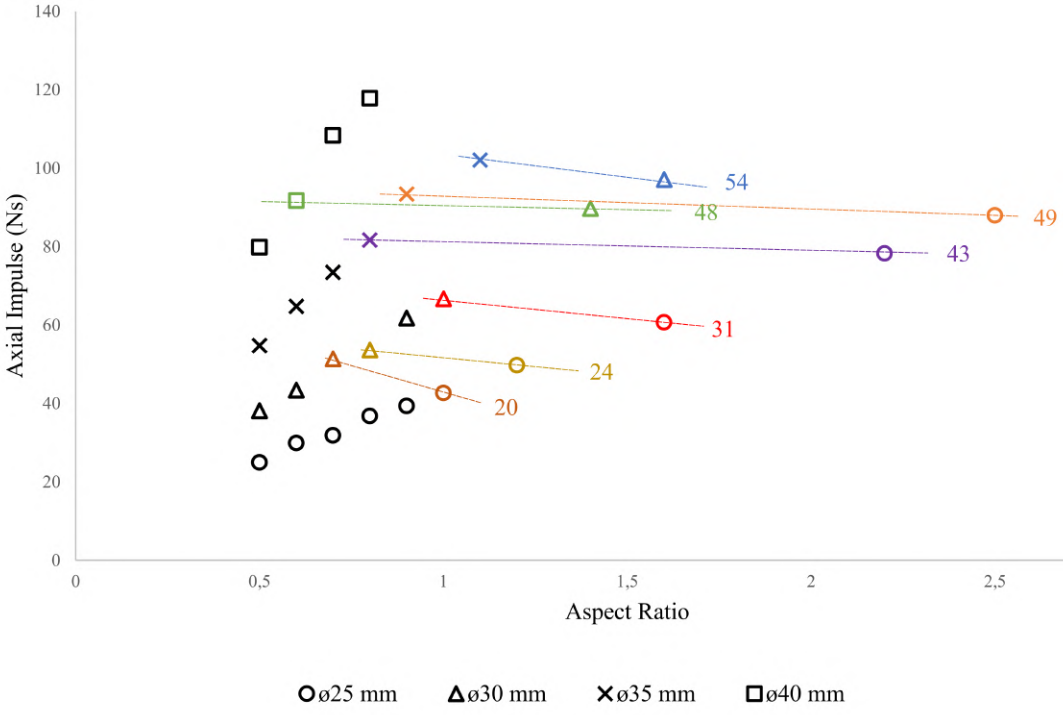

Figure 2.17: Graph showing the result of axial impulse versus charge aspect ratio reported by Davids et al. [11] under the semi-confined environment.

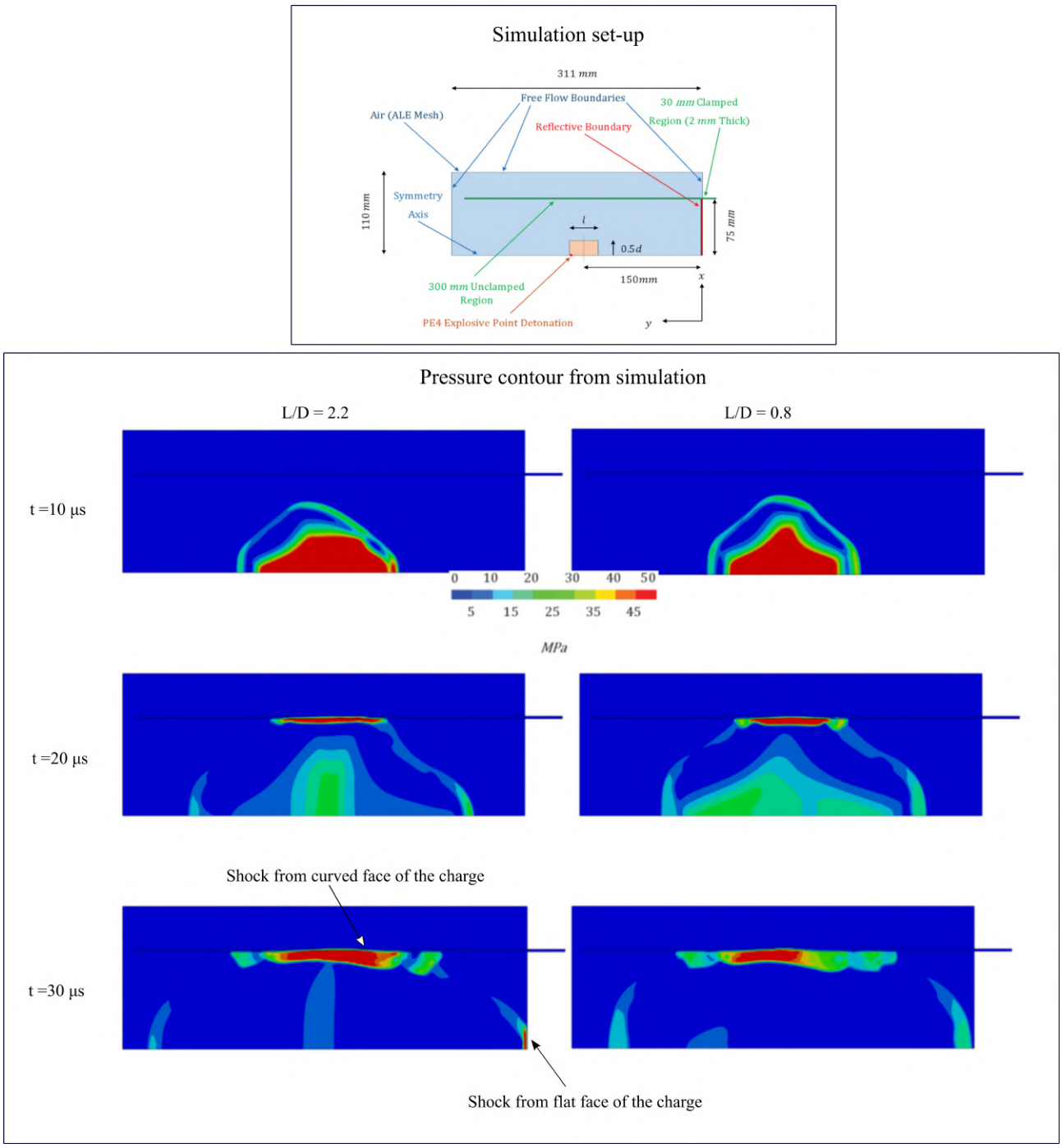

Figure 2.18: Figure showing the geometry and boundary conditions used in the simulation set-up and the pressure contours from two 43g charges with different aspect ratios at different times after detonation by Davids et al. [11].

Blast characterisation using HPB

Hopkinson pressure bars were introduced by Hopkinson [52] to capture near-field blast loading (detonation of gun-cotton) as well as impact loading. It has the unique advantage of affixing the fragile sensors in a more protected environment rather than being subjected to the often hundreds of megapascals of blast pressure and high heat from the fireballs. Prior to the invention, pioneering high strain-rate testing was introduced by the father of Bertram Hopkinson, John Hopkinson [53, 54] who measured impulse using an iron wire. Other early works include the longitudinal vibrational theories

in cylindrical bars from Pochhammer [55] and Chree [56]. The original HPB worked similarly to that of a ballistic pendulum and could not capture detailed pressure history. Improvements have since been made over the century. Two recent uses of the HPB from [27, 29] are presented. Both of these methods are able to capture pressure history from blasting as well as the axial impulse.

An instrumented ballistic pendulum was developed by Cloete et al. [27, 28] which consisted of a ballistic pendulum with a centrally mounted HPB. Part of the work was to determine the necessary length required for a blast tube to produce an idealised impulse load. Blast tubes with inner diameter of ⌀100 mm that varied in length were used in the experiments as shown in Figure 2.19. Disk charge with ⌀34 mm were used. At 100 mm tube length, high degree of localisation was observed.

The instrumented ballistic pendulum used by Cloete et al. [27, 28] was modified and adapted for this work so similar impulse observations are expected here.

An instrument consisting of arrays of HPBs were developed and used to map two-dimensional pressure histories from blast loading [29]. The schematic of the experimental set-up is presented in Figure 2.20. Arrays of HPBs were mounted using a rigid frame. The blast loaded face of the HPBs were placed flush with the surface of a rigid plate. The rigid plate was used to capture the axial impulse. An interpolation routine was used to plot a 2D blast pressure contour. This arrangement is able to capture any asymmetry that may arise from the blast loading. However, the load cells used to calculate impulse need to be calibrated to eliminate the effect of strain rate, vibrations and gravity.

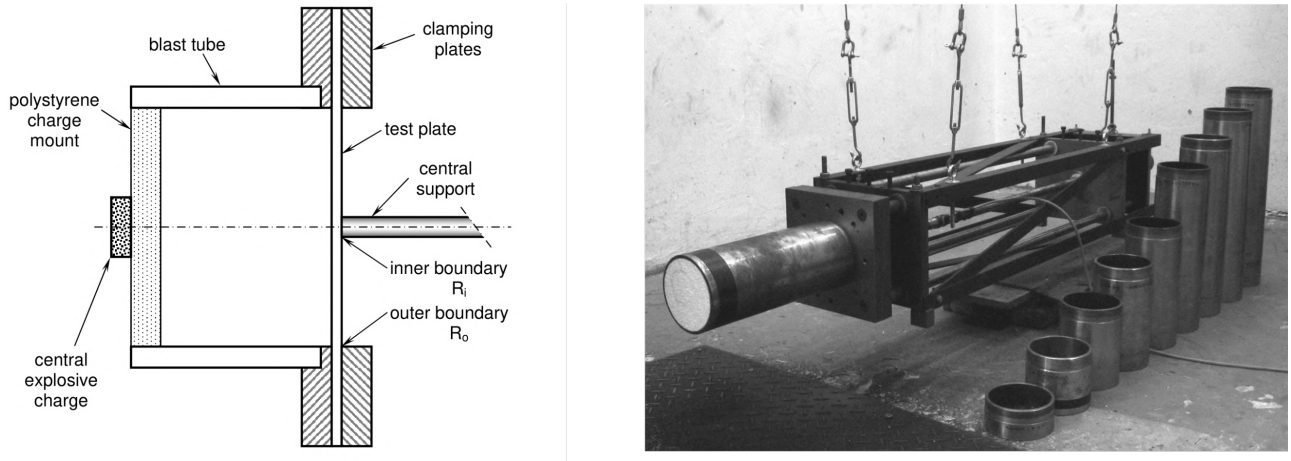

Figure 2.19: Figure showing a photo of the instrumented ballistic pendulum arrangement(right) and a schematic of the blast tube and clamping assembly (left) [27].

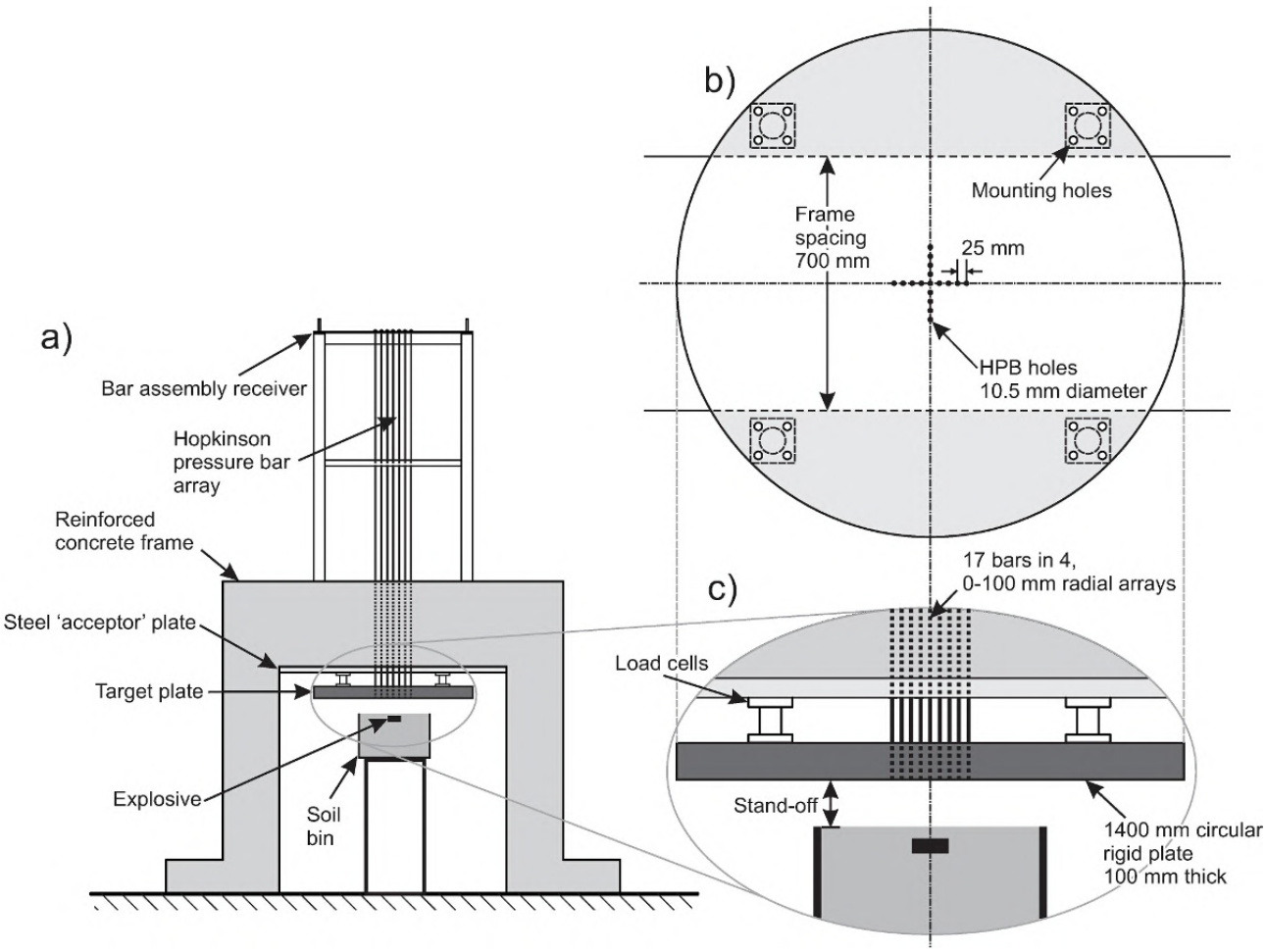

Figure 2.20: A schematic showing the HPB array from [29], a) overall arrangement, b) bottom view and c) side view of the array closer to the blast loaded face.

2.3 Blast induced projectile work

Research conducted on the topic of blast induced projectiles have focused on fragmentation [22, 57, 58, 59, 60, 61], or blast driven metal [62, 63, 64]. No work was found on the immediate transfer of momentum from the charge to a single unrestricted projectile in an unconfined environment.

2.3.1 The Gurney Model for theoretical velocity estimates

The Gurney model [65] is a one-dimensional method to estimate the velocity of blast driven metal based on the conservations of energy and momentum. Additionally, the Gurney model assumes a linear gas velocity and density distribution as shown in Figure 2.21. From which, the gas distribution across the explosive can be expressed as:

$$v_{gas}(y) = (v_0 + v)\frac{y}{y_0} - v \tag{2.12}$$

Where $v_{gas}(y)$ is the gas distribution, v_0 is the maximum gas velocity, v is the velocity of the plate and y is a function of position of the explosive. Additional assumptions are made to calculate the velocity

of the driven metal plate. The velocity of the plate is assumed to be constant across its thickness and the plate is assumed to not deform. This allows the total energy (CE) and momentum balance of the one-dimensional plate (per unit area) to be written as:

$$CE = \frac{1}{2}Mv^2 + \frac{1}{2}\rho_e \int_0^{y_0} [(v_0 + v)\frac{y}{y_0} - v]^2 dy \tag{2.13}$$

$$0 = -Mv + \rho_e \int_0^{y_0} [(v_0 + v)\frac{y}{y_0} - v] dy \tag{2.14}$$

Where ρ_e is the density of the explosive before detonation and M is the mass of the plate.

It is then convenient to substitute $\frac{M}{\rho_e y_0}$ as M/C where C is the mass of the explosive, which gives Equation 2.15.

$$V = \sqrt{2E}\left[\frac{1 + (1 + 2\frac{M}{C})^3}{6(1 + \frac{M}{C})} + \frac{M}{C}\right]^{-1/2} \tag{2.15}$$

This is the Gurney's velocity for metal under the Open-Face configuration. The explosive-specific constant $\sqrt{2E}$, known as the Gurney velocity, is determined experimentally using standardised cylinder tests [65, 66].

Similar equations are derived for the other common configurations including the flat sandwich, cylindrical and spherical as shown in Figure 2.22. An additional improvement can be made to model by substituting, the charge mass C, with the effective charge mass for a cylindrical explosive as suggested by Kennedy [62].

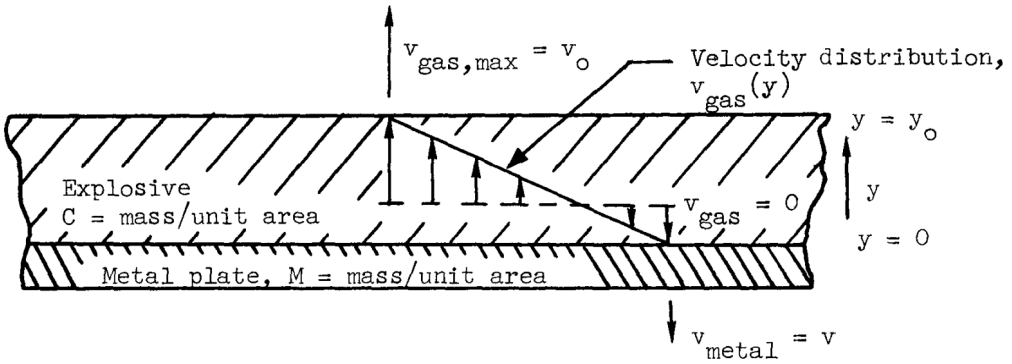

Figure 2.21: Schematic showing the gas velocity distribution assumption of the Gurney model using the Open-Faced Sandwich configuration by Kennedy[62].

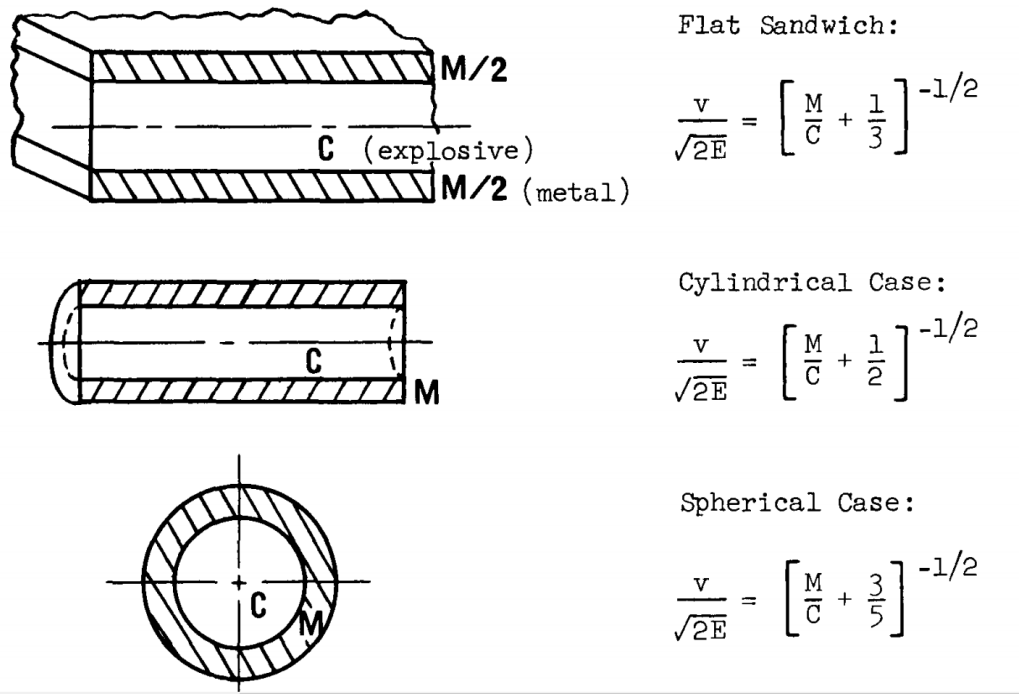

Figure 2.22: Figure showing the schematic of the common Gurney configurations and their corresponding velocity formula presented by Kennedy [62].

Gurney's model [65] provides a simple and relatively accurate prediction to metal velocity under explosive loading in one dimension. It has been used extensively in warhead fragmentation designs [57, 60] and explosive welding [3]. However, it is not suitable as a model to predict projectile velocity from improvised explosive devices. The IED configuration used herein one of the simplest, yet, the problem requires at least a two-dimensional solution to predict projectile velocity since the contact between the explosive and the projectile is curved. Additionally, there exist other limitations of the Gurney model which have been summarised by Kennedy [62].

There is a limiting M/C range for which the model is accurate. Kenney and Norwood [63] compared the one-dimensional results using the Open-Face Sandwich configuration against the CTH wave-propagation code [67] over a large range of M/C values. They reported three driving mechanisms for the metal plates which can be classified based on the M/C and metal velocity values v. At $M/C < 0.3$ and $v > 2900$ gas dynamics effects, such as the two-dimensional non-ideal detonation theory described in Section2.2.2, dominates. At $0.3 < M/C < 7$ and $2900 > v > 350$, the energy transfer mechanism which was used to derive Gurney's model, dominates. At $M/C > 7$ and $v < 350$ momentum transfer mechanism dominates. Although conservation of energy and momentum were used to derive the Gurney model, the experiments performed to determine the Gurney velocity $\sqrt{2E}$ was only captured at $0.3 < M/C < 7$. Prior work from Henry [64] recommended the limiting range of the Gurney model to be $0.2 < M/C < 10$. Note that the experimental set-up used for this thesis are all at $M/C < 0.2$ which is the gas-dynamic driven range.

Some of the additional limiting factors are listed below:

- Gurney model does not predict the velocity history of the metal, as its derivation method requires the gas velocity and metal velocity to reach equilibrium. Furthermore, the direction of the driven metal is assumed to be co-linear with the detonation. Under this assumption, any shearing effect

will not be captured and the metal will not experience rotation.

- As discussed previously in Section 2.2.1 and Section 2.2.2, even the simplest detonation does not assume a linear gas distribution behind the denotation front. A linear gas velocity distribution is a gross oversimplification of the real gas behaviour. Although, Henry [64] reported that ignoring the high detonation pressure and the rarefaction pressure appears to have the effect of cancelling errors.
- The driven metal is treated as a rigid body. The energy absorbed during the deformation of metal is not included. Additionally, the spallation of metal is not included in the model.
- The metal is assumed to not fail under blast loading.

2.3.2 Fragment velocity measurements during blast tests

The response of the monolithic metal plates under blast loading has been an on-going research topic. The failure of plates have been classified into three modes: mode I (large ductile deformation), mode II (tensile-tearing and deformation), and mode III (transverse shear failure) as defined by Menkes and Opat [68]. Three additional sub-modes were observed in failure mode II [30]. These are classified as mode II* (partial tearing), mode IIa (complete tearing with increasing mid-point deformation) and mode IIb (complete tearing with decreasing mid-point deformation). Failure modes IIa, IIb and III result in completely torn plate from blast loading. The velocities of the torn plates were reported by Nurick and Shave [30] as well as by Teeling-smith and Nurick [32]. Experiments performed by Nurick and Shave [30] studied the failure of 2 mm thick square steel plates with a clamped length of 175 mm while Teeling-Smith and Nurick [32] performed experiments on circular steel plates at 1.6 mm thickness with a clamped diameter of 100 mm. In both experiments, thin metal plates were clamped peripherally and was blast loaded by a strip of explosive. The axial impulse was recorded via the motion of a pendulum with known mass as shown in Figure 2.23. The velocities of the fragments are recorded by the wire curtain trigger set-up shown in Figure 2.24.

The velocity of the torn disks from failure mode IIa&b and III from [30, 32] were compiled and is presented in Figure 2.25. Teeling-smith [32] did not report the failure mode of any individual experiment. However, since a velocity data was reported, the plate must produced a fragment. The graph in Figure 2.25 has a linear velocity scale versus a logarithmic impulse scale. Within each failure mode, the velocity of the disk increases linearly on the log-scale. At low impulses, there is a considerable scatter in the disk velocity but as the impulse increased to approximately 35 Ns, data from the two sources overlap more consistently. Unsurprisingly, the trend line would not intersect at the origin since a non-zero impulse is required to initiate tearing.

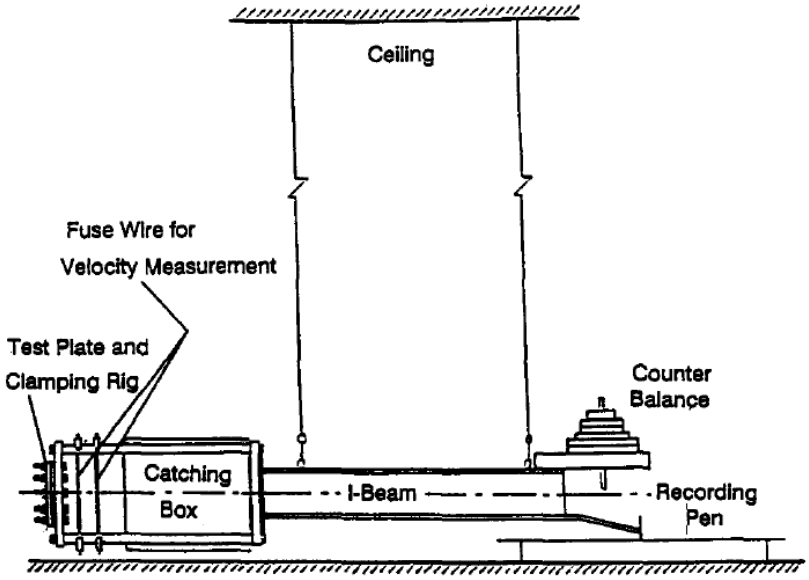

Figure 2.23: Schematic showing the ballistic pendulum arrangement, clamping assembly and the catch-box in [30, 32].

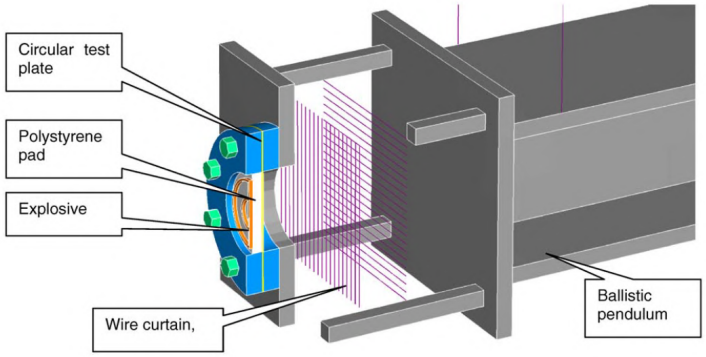

Figure 2.24: Schematic showing the clamping and wire curtain set-up used in [30, 32].

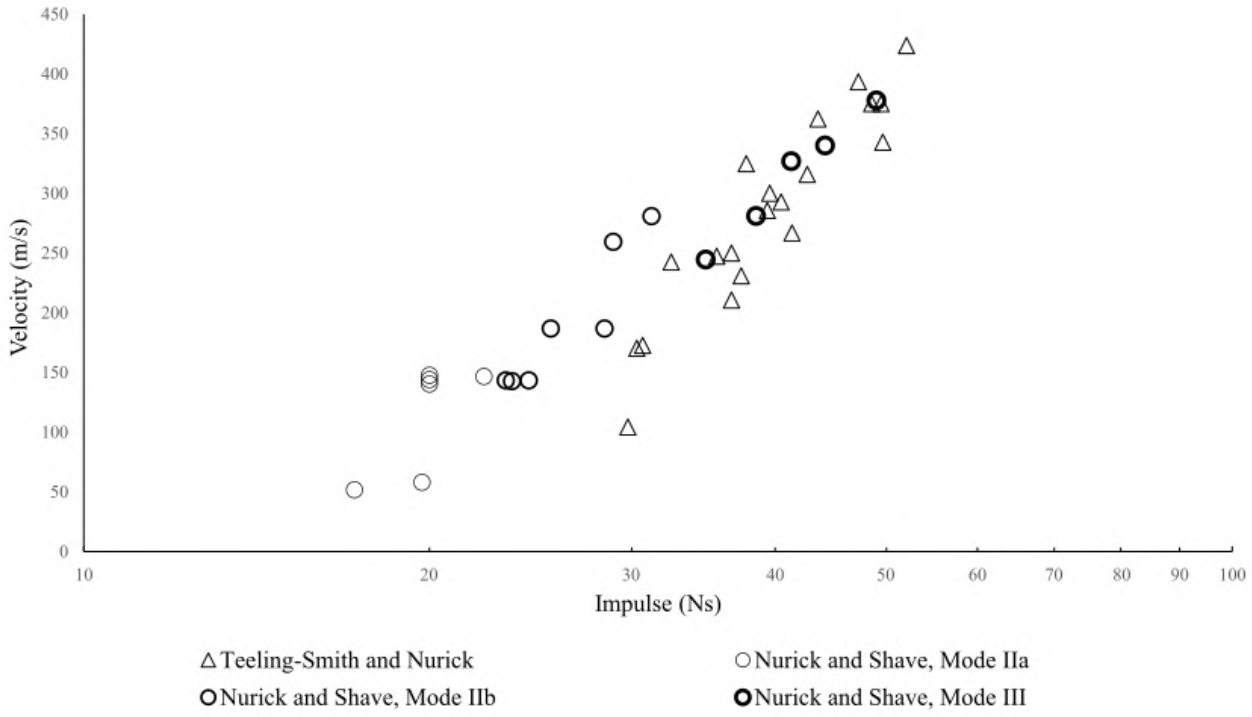

Figure 2.25: Graph of velocity of the torn disks versus logarithmic axial impulse reported by in [30, 32].

2.4 Experimental techniques to determine projectile velocity

Traditional optical techniques used for projectile velocity measurements such as light traps and high-speed photography are difficult to implement for blast-induced projectiles. The fireball created from detonation as well as the dust generated from intense pressure bursts from blast waves all create obstacles for direct optical methods.

A popular experimental technique used determine the velocity of blast formed projectile dating back to the Manhattan Project is flash x-radiography [69]. This technique uses x ray pulses to "photograph" high velocity objects. The object of interest is placed between the x-ray generator and the detector. This method is not practical in some arrangements. For example, in this project the projectile's trajectory will be completely enclosed within stainless steel right circular cylinders as a safety precaution.

2.4.1 Impact velocity and Crater Depth measurement techniques

An indirect way to measure the velocity of projectiles is through the geometry of the impact crater. Extensive research on the correlation between projectile velocity on crater geometry has been conducted by The National Aeronautics and Space Administration (NASA) [70, 71, 72, 73, 74]. The goals of the research were to provide design guidelines for the outer plate thickness of space vessels such as SkyLab before and during the Apollo mission to protect these vessels from space debris. These equations were empirically correlated in certain velocity ranges. The simplest is the Fish-Summers Equation

[71] shown in Equation 2.16 where all target material characteristics are reduced to a constant, k_{1t}.

$$t = k_{1t} m_p^{0.352} V^{0.875} \rho_p^{\frac{1}{6}} \tag{2.16}$$

Where t is the target thickness in cm, k_{1t} is a material constant, m is the projectile mass in g, ρ_p is the projectile density in g/cm^3 and V is the impact velocity measured in km/s.

Equation 2.16 was developed using projectiles with speeds from 0.5 to 8.5 km/s using materials with a higher hardness as targets and softer materials such as aluminium alloy, as the projectiles.

The Schmidt-Holsapple Equation [72] used the ultimate tensile strength and density of the target in its formulation. It is given as:

$$d = 2.06(\frac{\rho_p}{\rho_t})^{-0.159}(\frac{2.68 U_{ts}}{\rho_p V_n^2})^{0.236} \tag{2.17}$$

Where d is the projectile diameter in in, t is the target thickness in in, ρ_p is the projectile density and ρ_t is the target density, both measured in$(lb/in^3$, U_{ts} is the ultimate tensile strength of target in $(lb/in^2$ and V_n is the normal component of the projectile velocity measured in ft/s.

A large range of materials were tested as projectiles. This included tungsten, carbide and stainless steel. Stainless steel and aluminium were used as target material.

Equations 2.18-2.20 were developed by NASA to characterise materials properties by their hardness and density. The Rockwell Equation [70] in Equation 2.18 and JSC (Cour-Palais) [73] in Equation 2.19 were independently developed during the Apollo project. JSC(Cour-Palais) Equation [74] was later modified to Equation 2.20.

$$p = 1.38 d^{1.1} BH^{-0.25} \rho_p^{0.5} \rho_t^{-0.169} V^{0.67} \tag{2.18}$$

$$p = 5.24 d^{1.056} BH^{-0.25} \rho_p^{0.5} \rho_t^{-0.169} E^{-0.33} V^{0.67} \tag{2.19}$$

$$p = 5.24 d^{\frac{19}{18}} BH^{-0.25} \frac{\rho_p}{\rho_t}^{0.5} \frac{V}{C} \tag{2.20}$$

Where p is the crater depth of target in cm, d is the projectile diameter in cm, ρ_p is the projectile density in g/cm^3, is the target density in g/cm^3, BH is the Brinnell hardness for target, E is the Young's modulus for the target in GPa, V is the normal component for projectile velocity in km/s and C is the speed of sound for the target which is given as

$$\sqrt{\frac{E}{\rho_t}}$$

and is measured in km/s.

2.5 Outcome of literature review

In this chapter, some of the existing methods to investigate impulse transfer from blast were reported. It was also found the axial impulse from cylindrical charges increases with the increase in effective charge mass in an unconfined environment. When confinement such as a blast tube was used, the

reflected pressure caused the axial impulse to increase with charge mass. In both unconfined and confinement environment, the axial impulse increased with the increase in charge diameter, possibly in an asymptotic manner. For blast driven projectile, some results from literature showed that the projectiles' velocities increased linearly with the logarithmic increase in impulse.

Based on the findings of the literature review, simple ideal detonation theories, such as the Gurney model, are not suitable methods to be used for this project. Non-ideal detonation theories such as DSD incorporating JWL EOS could be employed to investigate the objectives numerically. The HPB and ballistic pendulum are suitable experimental instruments to use for this investigation

Chapter 3

Experimentation

The experimental investigation conducted on the influence of charge aspect ratio, diameter on the velocity of the ball bearing is presented in this chapter. A series of blast tests and separate validating impact experiments were performed and are reported in detail.

The methods used to infer the mean in-flight velocity and the impact velocity of the blast driven ball bearing are reported. The theoretical and experimental methods used to infer the average velocity of the ball bearing are presented. Correlation impact experiments, which were performed using a two-stage light gas gun and various other methods and used to infer the impact velocity of the ball bearing, are reported.

The results of the blast experiments, including the testing matrix, the number of tests and the variables tested are presented in Chapter 6.

3.1 General overview

An experimental arrangement was designed to record the velocity of the ball bearing after detonation. Optical techniques are not suitable due to the presence of fireballs and shock pressure fronts which will obscure the ball bearing in flight. Additionally, the small size of the ball bearing makes it difficult for optical equipment to track and focus. Therefore, two alternative methods were used to infer velocities of the blast-driven projectile. These methods includes:

- recording of flight duration of the projectile over a known distance (average velocity)
- correlating projectile impact velocity with the impact crater depth (impact velocity)

This was performed using the experimental arrangement shown in Figure 3.1. The key components in the arrangement are depicted in colour with corresponding labels. These components form four sub-arrangements which are colour coded. The sub-arrangements are presented in detail in this chapter. The detailed engineering drawings are included in Appendix B. A photograph of the pendulum is shown in Figure 3.2.

The axial alignment sub-arrangement included the detonator, charge, polystyrene bridge and ball bearing. As the name suggests, the precise axial alignments of these components were designed and implemented.

The witness plates were designed to optimize the capturing of the crater and to transmit impact signals to the HPB. This is presented in detail in Section 3.3 as the witness plates sub-arrangement. The correlation method between the crater depth and the impact velocity which included a separate impact experiment is presented separately in Section 3.6.

The method to capture axial impulse from the motion of the pendulum is presented as the pendulum subsection which is in Section 3.4.

The average velocity of the ball bearing was calculated using the time difference between the detonation and the impact over the flight distance. Both times were recorded using the HPB arrangement. The detailed method to determine the detonation time, impact time and other relevant methods used to determine the average velocity is presented in Section 3.5.

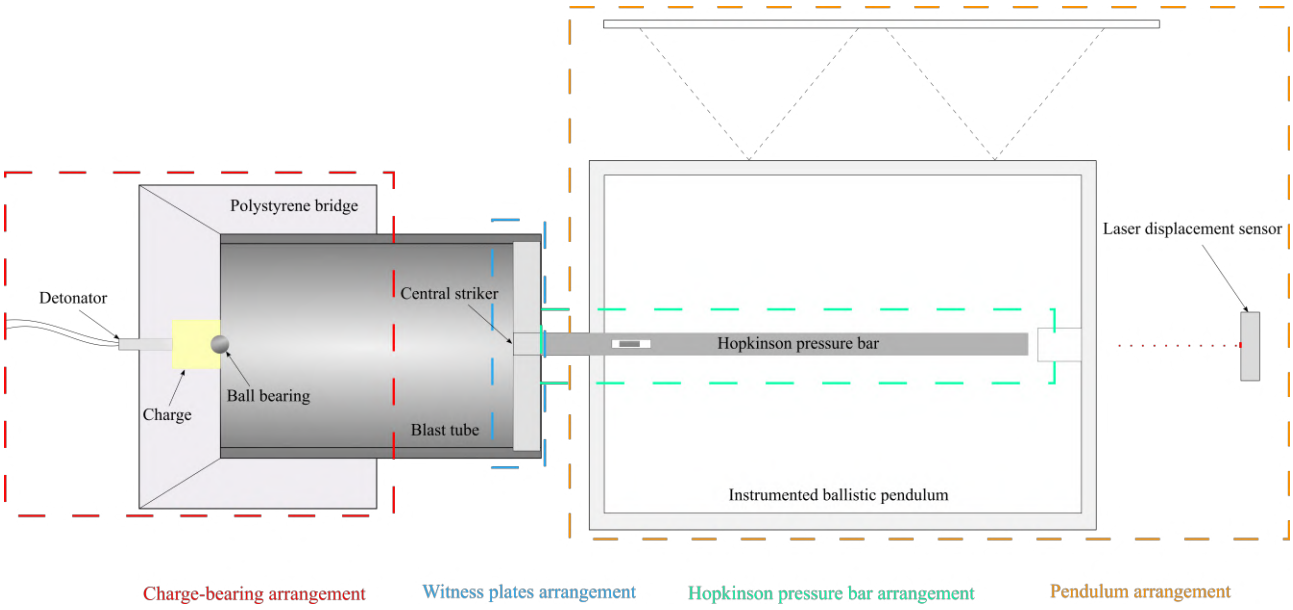

Figure 3.1: A not-to-scale schematic depicting an overview of the experimental arrangement.

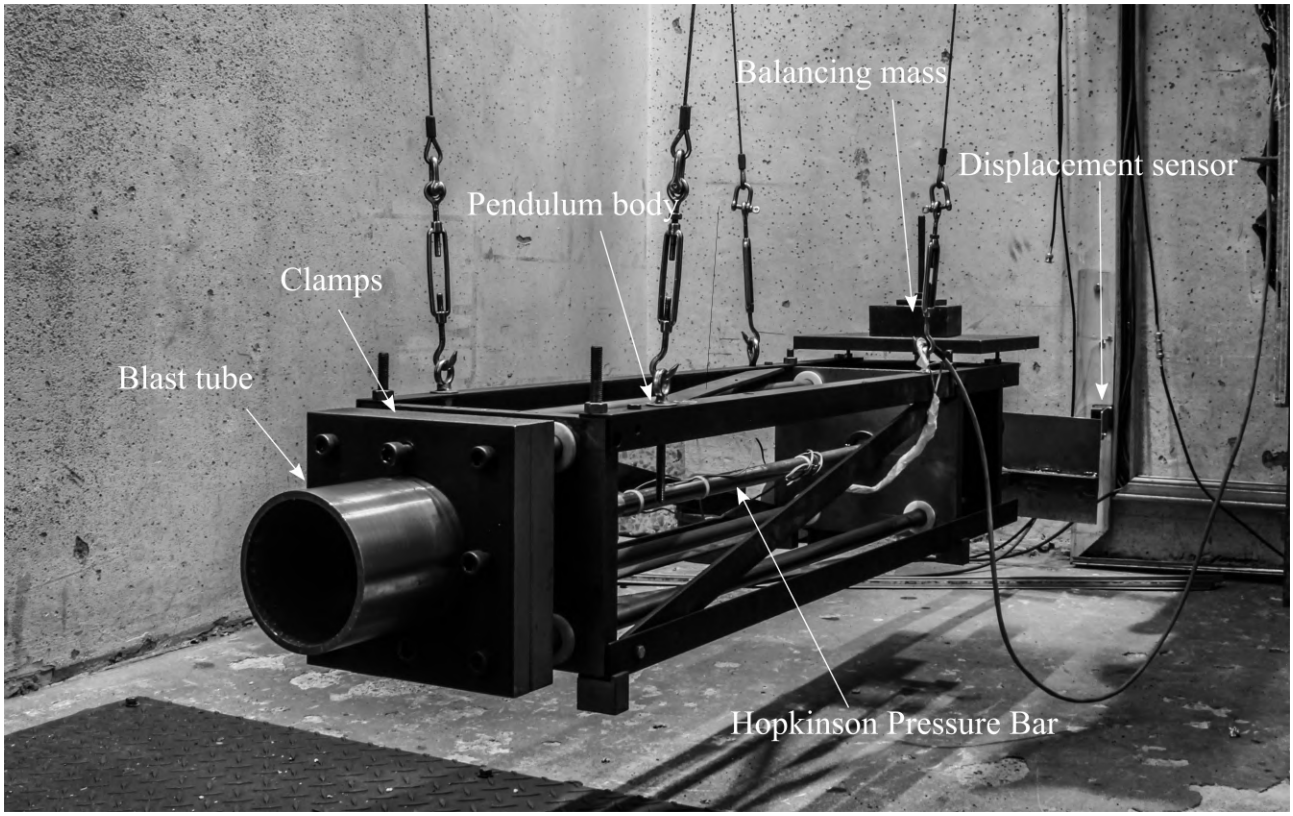

Figure 3.2: Photograph showing the experimental arrangement used in the blast tests.

3.2 Axial alignment arrangement

Achieving the correct alignment to ensure that the ball bearing impacted on the central striker was particularly challenging. Unconfined charges are extremely sensitive to their shapes and the positions of detonation [75], especially when used to accelerate a small, lightweight projectile. A novel polystyrene bridge design and an improved split mould design were used to align the ball bearing,

charge and witness plate as shown in Figure 3.3 and Figure 3.4.

3.2.1 Polystyrene bridge

Expanded polystyrene (EPS) pads have been used by [15, 49, 50] to position the explosive and the detonator before detonation. EPS pads were expendable and were assumed to have a negligible effect on the impulse transfer as only thin polystyrene sheets were used. Jacob [76] showed that the effect of EPS decreased with increase in SOD. Improvements were there therefore made for near-field blast arrangements. The pad was replaced by using a EPS bridge by Davids [77] who also placed the EPS behind the charge rather than in between the charge and the target. In this work, the influence of EPS was further reduced by designing a EPS bridge which directed blast pressure away from the charge.

This investigation was particularly sensitive to the influence of EPS bridge since the impulse transfer from the charge to the ball bearing occurs during the detonation (SOD = 0). Furthermore, the small metal mass to charge mass ratio also increased the sensitivity of metal displacement to reflected detonation waves. This would not only produce inaccurate experimental results but also would cause the ball bearing to travel skew if the reflection was asymmetrical. Therefore a polystyrene arrangement was developed to minimise interference with the detonation pressure waves while providing locational accuracy for the positioning of the charges and the detonator. This arrangement consisted of three 'V' shaped beams which deflected axial and radial blast waves away from the ball bearing as shown in Figure 3.3. Two side bridges fit into the main bridge which hosts the charge and the detonator. All three bridges were hot-wire cut to ensure surface smoothness.

The distance between the two side bridge was made to be slightly smaller than the outer diameter of the blast tube. This was to create tension to hold the bridge in place when it was pressed against the tube. A hole for the detonator was melted/drilled by using a heated undersized drill-bit. A slot was cut in the centre of the main bridge so that the front face of the charge is flush against the blast tube as shown in Figure 3.3. The distance between the front face of the charge and the witness plate was kept at 100 $\pm$ 3 mm. The bridge assembly was aligned with the central striker post cutting by adjusting the height of side-bridges carefully to account for any imperfections during manufacturing.

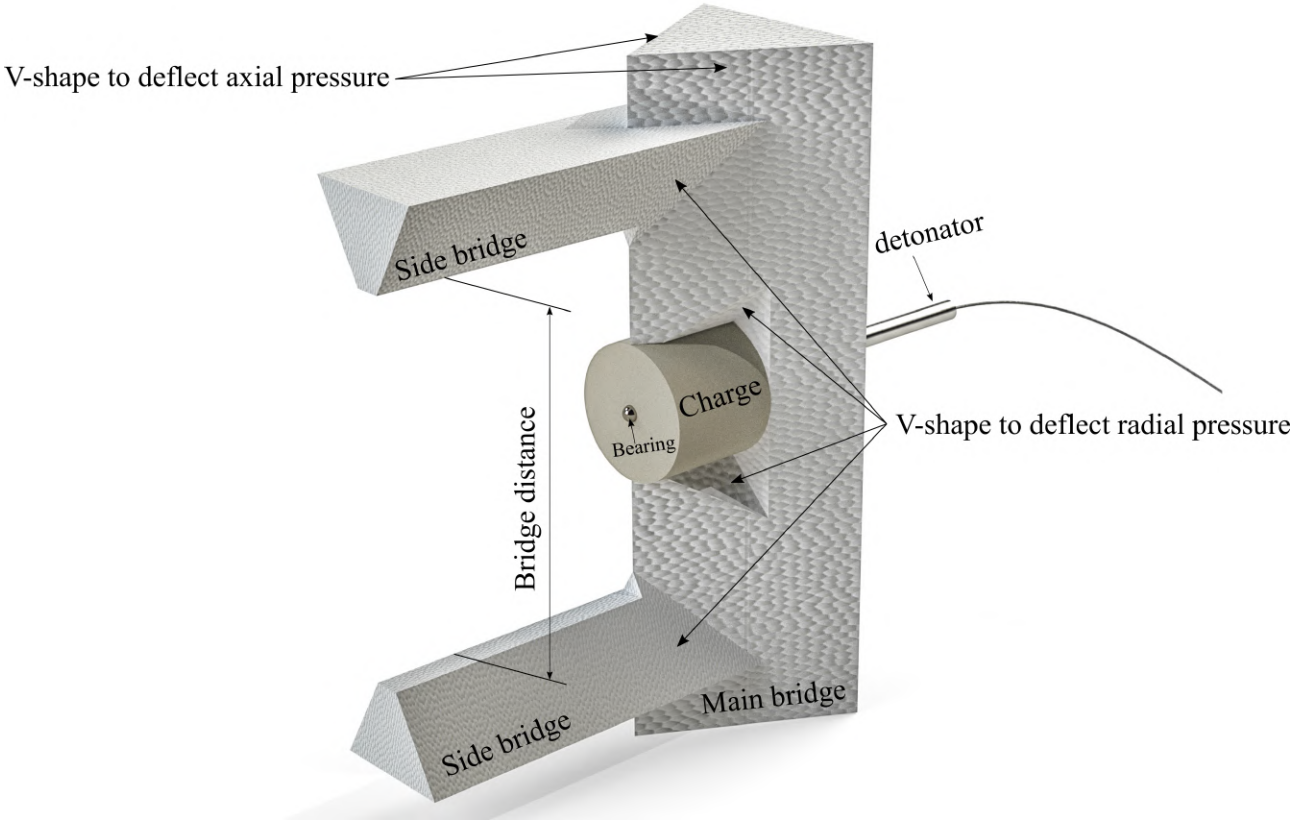

Figure 3.3: Schematic showing the use of polystyrene in the blast experiments.

3.2.2 Charge mould

The split mould was machined from polytetrafluoroethylene (PTFE) to minimise the sticking of explosive with the mould. As shown in Figure 3.4, the mould consisted of two, half cylinders and two plungers. A cylindrical slot was made in the centre of the bottom press to allow half the ball bearing to be buried. Four dowel pins were used to align the left with the right mould body. After the mould body was closed, it was tightened by using the nut and bolts on either side of the mould. The charge was then be formed using the two plungers. Two release sockets were machined for two screwdrivers to clip open the mould. Five moulds were made for the different diameters used for the blast arrangement.

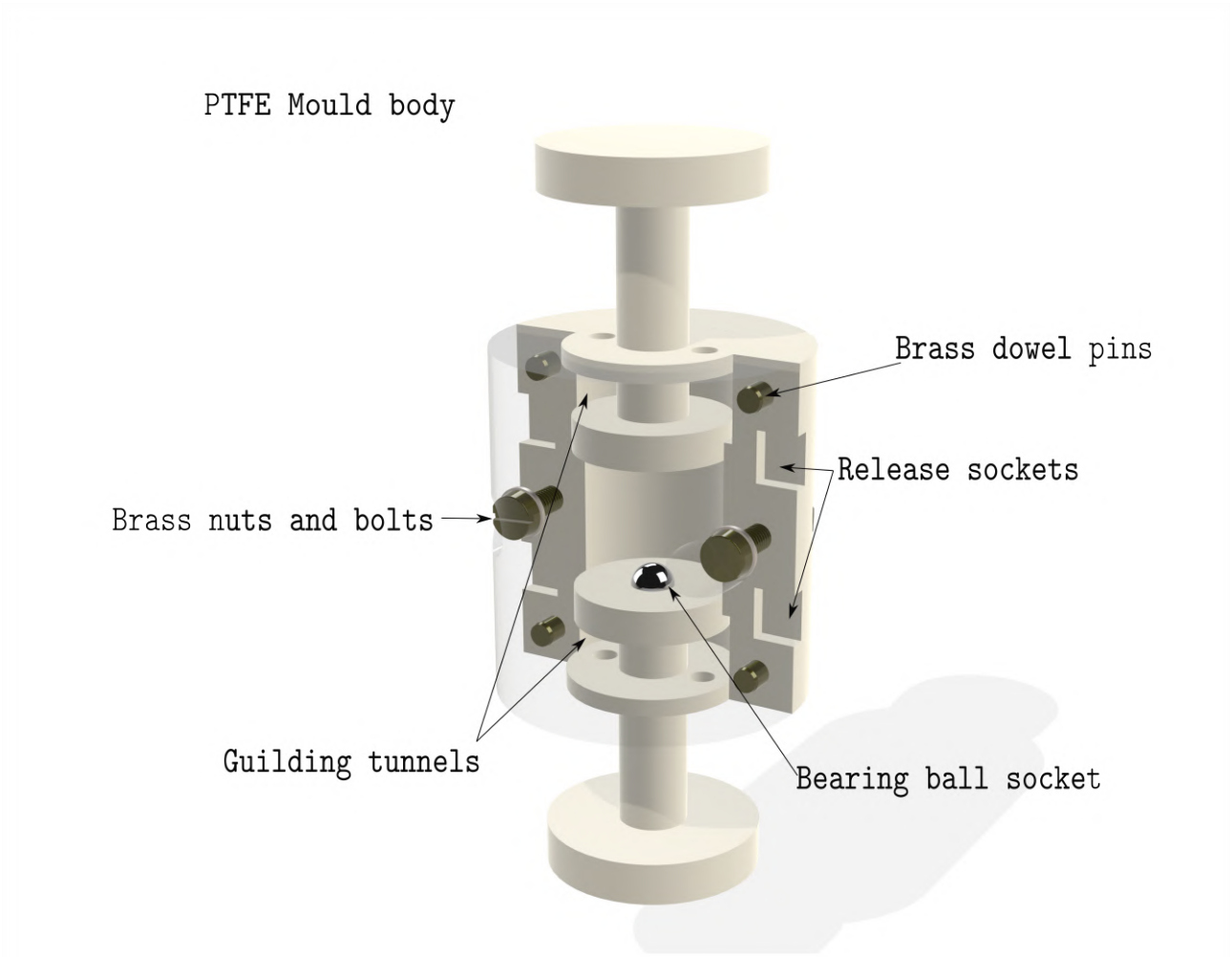

Figure 3.4: Schematic of the split mould which was used to shape cylindrical charges with a 5 mm stainless-steel ball bearing insert.

3.3 Witness plate arrangement

An Al 6082-T6 witness plate was placed in front of the HPB to serve three goals: allow cratering from each impact, allow stress waves to be transmitted to the HPB and to protect the HPB from the impact and blast load.

The witness plate covered the diameter of the blast tube, as shown in Figure 3.5, but was divided into two parts: the outer witness plate and the central striker. The central striker had the same diameter as the HPB and was allowed to move axially with minimum friction. This arrangement allowed stress waves to be transmitted to the strain gauges on the HPB without additional interference from shear deformation of the witness plate.

The diameter of the central striker was 0.5 mm smaller than the hole diameter in the outer witness plate. This was to allow the impacted face of the central striker to expand radially freely during and after impact. The expansion was assumed to be limited by the depth of the crater in the design.

A steel ring machined to a close tolerance was placed at the back face of the striker to allow axial alignment where no radial expansion was expected.

The back face of the striker had a small extrusion to prevent the front face of the striker passing beyond the outer witness place when the HPB is pushed against it. The outer plate was clamped peripherally between the clamps on the pendulum and a slot machined into the blast tube. The slot was deeper than the thickness of the witness plates to allow for different future experimental arrangements. In this arrangement, a steel plate was placed behind the witness plates to occupy the extra depth. A thin polymer sheet (1 mm) was clamped in between the witness and the steel plate to minimise spallation of the witness plate.

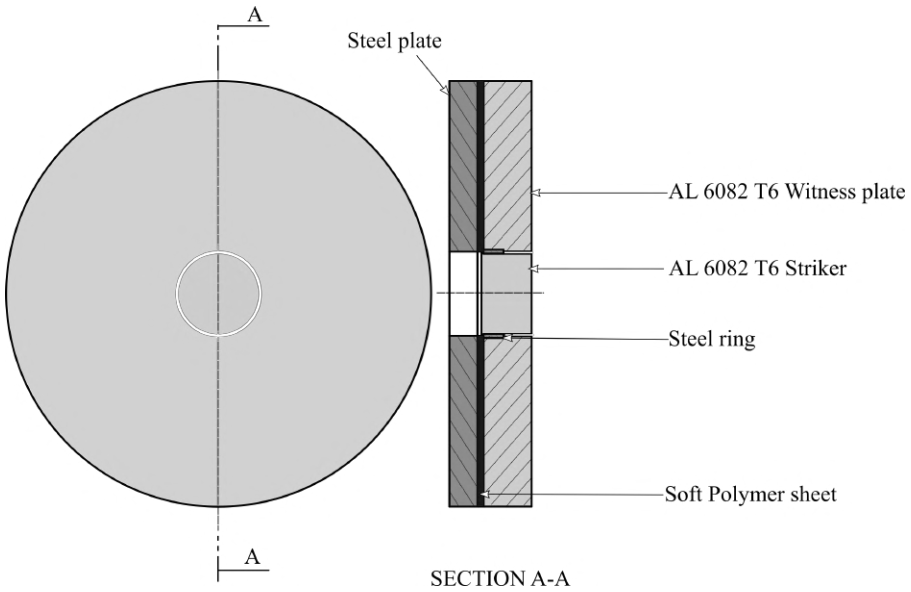

Figure 3.5: A schematic showing the witness plates arrangement used in the blast tests.

3.4 Pendulum arrangement

The axial impulse was recorded by tracking the movement of the ballistic pendulum with a laser displacement sensor. The motion of the pendulum was assumed to be purely one dimensional. The displacement of the pendulum could then be expressed using the equation of motion for a single degree of freedom (SDF) system as:

$$m\ddot{x} + c\dot{x} + kx = 0 \tag{3.1}$$

Where m, c, k are the mass, linear damping coefficient and the linear elastic stiffness coefficient of the pendulum.

The general solution of Equation 3.1 in terms of time (t) is given as:

$$x(t) = x_0 + \frac{e^{-\beta t}\dot{x}_0 sin(\omega_d t + \theta)}{\omega_d} \tag{3.2}$$

Where x_0 is the initial distance between the back of the pendulum and the sensor, $\dot{x}_0$ is the initial velocity of the pendulum, ω_d is the damped frequency, θ is the phase of the motion and β is a ratio expressed as $\beta = \frac{c}{2m}$.

And that the axial impulse transferred to the pendulum is:

$$I = m\dot{x}_0 \tag{3.3}$$

The displacement history of the pendulum was assumed to behave as described in Equation 3.2. Therefore the unknown variables, x_0, $\dot{x}_0$, β, ω_d and θ could be found by fitting Equation 3.2 with the raw displacement history using a non-linear least square method as shown in Figure 3.6. The sum of the least squares, S, is given as:

$$S = \sum_{i=1}^{m} r_i^2 \tag{3.4}$$

And is minimised through iterations, $i = 1, 2, ..., m$. And that the residuals, r_i is given as:

$$r_i = X_i - x(t_i, \alpha) \tag{3.5}$$

Where X_i is the fitted function, and α is the vector of fitting parameters given as:

$$\alpha = (x_0, \dot{x}_0, \beta, \omega_d, \theta) \tag{3.6}$$

The iteration was terminated when the difference in the sum of least squares between iterations was less than 1×10^{-8}.

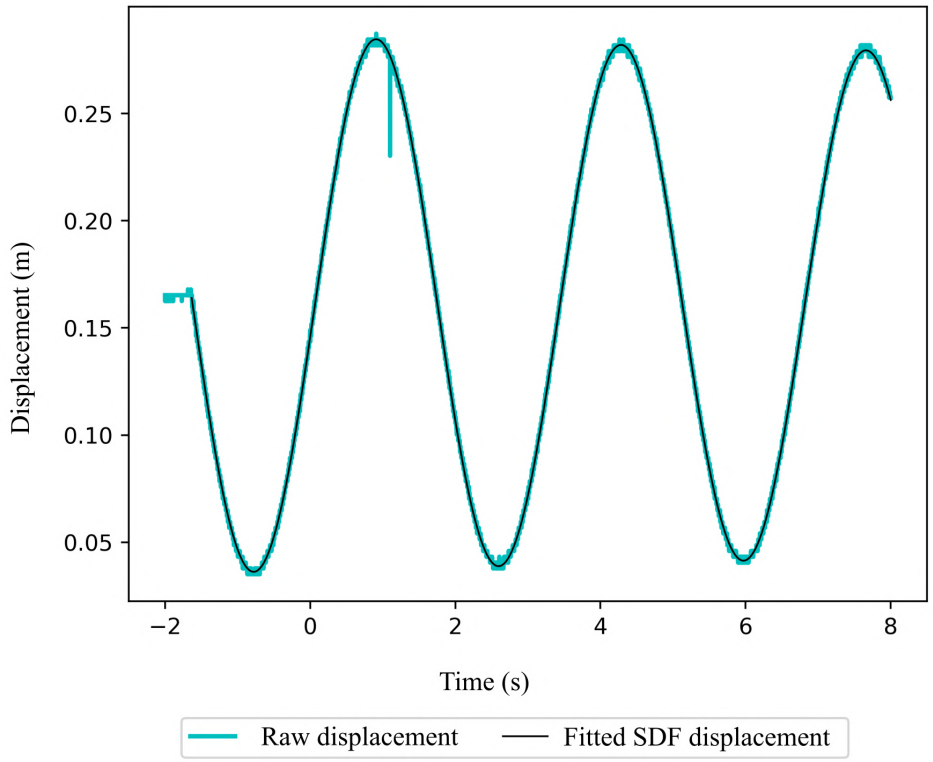

Figure 3.6: Graph showing the raw signal from the laser displacement sensor and the fitted SDF motion.

Additional balancing masses were added to the pendulum to prevent the motion of the pendulum swinging beyond the sensor's detectable region. They were added in a such a way to bring the centre of gravity of the pendulum as close to the centroid as possible and to minimise lateral moment.

3.4.1 Calibration of laser displacement sensor

The calibration coefficient $K_{laser} = \frac{Displacement}{Voltage}$ was determined experimentally by observing the voltage at the closest and furthest distance from the sensor. The sensor produced signals from -5 V to 5 V. At 5V, the pendulum was 50 mm from the sensor while at -5 V, it was at 350 mm from the sensor. The calibration coefficient is therefore:

$$K_{laser} = \frac{350 - 50}{5 - (-5)} = 30\frac{mm}{V} \tag{3.7}$$

3.5 Experimental methods to infer average velocity

The measurement of impact time was achieved using a Hopkinson Pressure Bar (HPB) that was mounted centrally on a ballistic pendulum as shown in Figure 3.7, similar to the instrumented ballistic pendulum used by Cloete et al. [27].

A 1 m long silver steel round bar with ⌀20 mm (20 mm in diameter) was used as the HPB for these experiments. Silver steel was selected for its dimensional accuracy attributed to its manufacturing technique, thus eliminating the need for additional machining. The length of the bar allowed the stress waves from the pressure and impact event to be recorded by the HPB without having interference caused by the reflected signal.

Four EN 8 support bars were used to connect the blast tube and clamps with the pendulum. This allowed stress waves to propagate through the length of the pendulum before creating interference with the HPB, by which time, the events of interests have already been recorded by the strain gauges.

Two pairs of double-eccentric bushings were used to align the HPB with the clamps and the central striker in the witness plates. Each pair of double-eccentric bushings consisted of two eccentric bushings. The outer bushing was made of brass while the inner bushing was made of PTFE. Both of which had an eccentricity of e. By rotating the double-eccentric bushings, the HPB could translate between $e_1 - e_2$ to $e_1 + e_2$, i.e from 0 to $2e$. This arrangement was a simple and effective method to make both minute and large adjustments. Adjustments were needed to compensate for any inaccuracies which may occur during manufacturing.

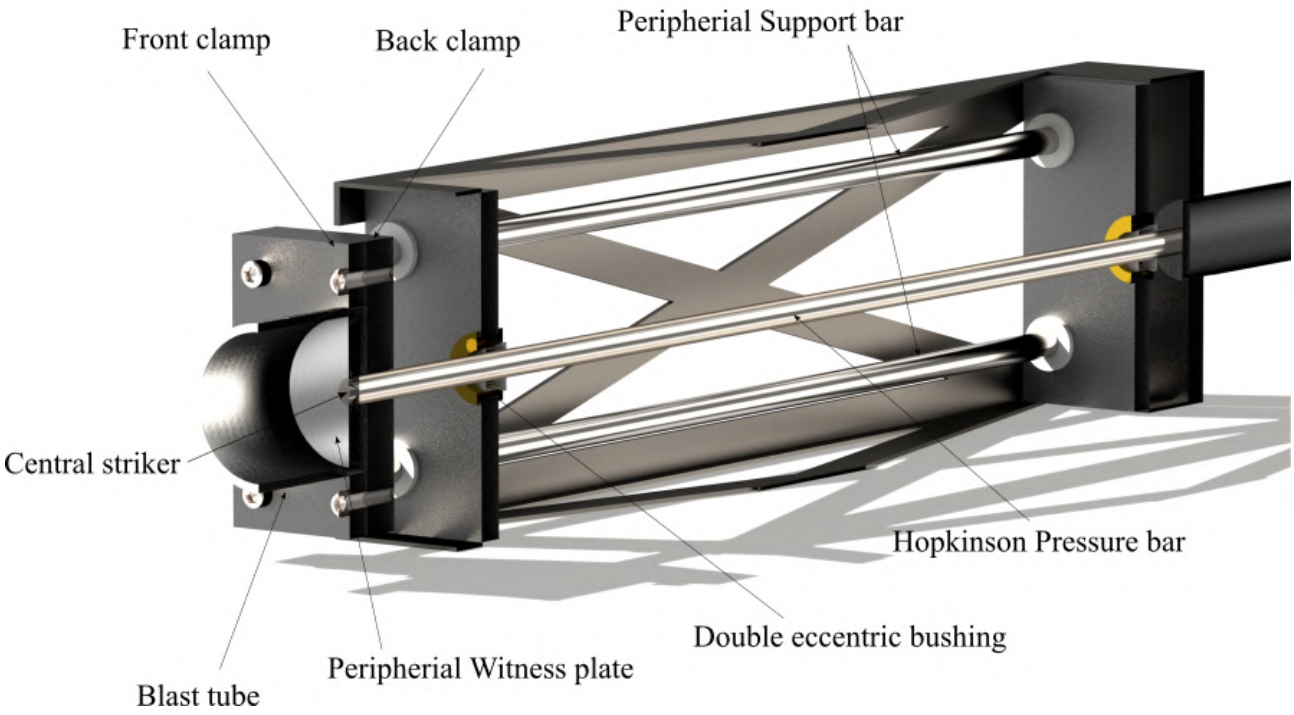

Figure 3.7: A schematic of the blast experimental arrangement showing the cross section of the HPB and the ballistic pendulum.

3.5.1 Strain gauge calibration

A pair of strain gauges were mounted diametrically in a half bridge configuration on the silver-steel round bar at 210 mm away from the blast loaded face. This conformed to the "rule of thumb" of "greater than 10 diameters" used in HPB to minimise the effect of small non-uniformity in blast load across the face [78, 79]. The gauges were connected to a 1MHz bandwidth amplifier and a data logging device which recorded at 10MHz with a 12-bit resolution. The gauge factor K was obtained experimentally by recording the voltage response of the HPB from known stress. This stress was generated by accelerating a steel striker using a single-stage gas gun. The theory of 1-D stress wave propagation was used to obtain the calibration factor from the experiment.

The change of momentum of a uniform bar with cross-sectional area A over a given time period t from impact load is equal to the transferred impulse.

$$\rho A c v t = \sigma A t \tag{3.8}$$

Where v is the particle velocity as a result of the impact load,and therefore:

$$\sigma = \rho c v \tag{3.9}$$

The equilibrium of forces at the impact interface of two uniform bars of the same material can be expressed as:

$$\sigma_1 A_s = \sigma_2 A_b \tag{3.10}$$

The vector sum of the striking/incident (v_0) and particle velocities (v_s and v_b) can be expressed as:

$$v_0 = v_s + v_b \tag{3.11}$$

Substituting into Equation 3.10, yields:

$$v_b = \frac{\rho c v_0 \frac{A_s}{A_b}}{1 + \frac{A_s}{A_b}} \tag{3.12}$$

Substituting into Equation 3.9 yields:

$$\sigma_b = \frac{\rho c v_0 \frac{A_s}{A_b}}{1 + \frac{A_s}{A_b}} \tag{3.13}$$

The calibration factor can now be calculated as:

$$K = \frac{\sigma_b}{V_{max}} \tag{3.14}$$

where V_{max} is the maximum voltage registered on the strain gauge from the impact of the striker.

The calibration factor was 59.064 MPa/V and the speed of sound in the HPB was 5060.8 m/s.

3.5.2 Basic signal processing

In general, signals captured from HPB contains high-frequency oscillations. They do not represent a physical oscillation in pressure but is rather a result of dispersion. Therefore, the effects of dispersion should be removed. The effect of stand-off distance to the dispersive phenomenon in HPB was studied by Cloete et al.[27] using the same ballistic pendulum with very similar blast tube diameters. In this study, the ID was 102.3mm compared to 100mm used by Cloete et al.[27]. It was found that at 100 mm stand-off, stringent correction for dispersion was not necessary but smoothing of the signal should still be applied.

Two additional processing techniques were applied before the smoothing. First, the signal was zeroed according to the initial 10 μs signal. The signal was then shifted to account for the time taken for the stress wave to arrive at the strain gauge. After which, the signal was smoothed using a three-step procedure similar to that used by Cloete et al.[27]. The first step was to compute the moving-time average of 1.2 μs and 3.6 μs. In the second step, the weighting factor was calculated by using the normalised and rectified first derivative of the averaged signal over 3.6 μs. Lastly, the weighted sum between the averaged signal of 1.2μs and 3.6 μs was calculated. This procedure allowed longer duration signal peaks as a result of physical phenomena to be preserved while reducing the effects of electrical interference. Figure 3.8 shows the raw signal and the processed signal.

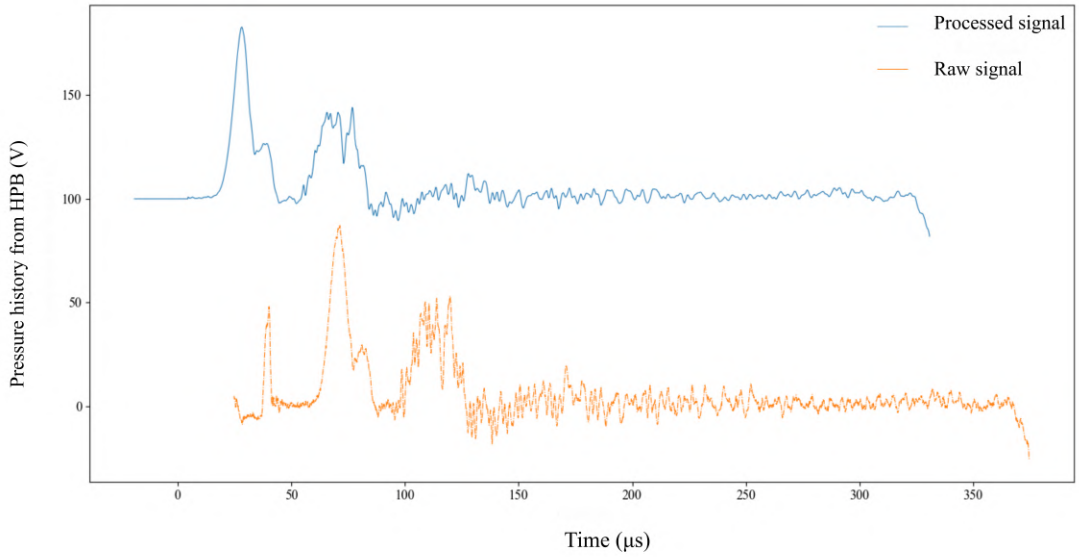

Figure 3.8: A graph showing the difference between a raw signal and a post-processed signal (the processed signal is shifted upward by 100 MPa for clarity of illustration).

3.5.3 Impact signal identification

The HPB records the pressure history from both the blast event and the impact event. The overall gas pressure and pressure peaks captured by the HPB were expected to decay exponentially as the blast arrangement is semi-confined. Therefore any large positive deviation from the exponential decay indicated an impact event from the fragments of the ball bearing, detonator and the intact ball bearing. This is demonstrated in Figure 3.9 where the pressure history from the detonation of a charge with no ball bearing is compared to a test where the ball bearing impacted the HPB. Despite the difference in charge diameter (⌀18 mm for a and 24 mm in b) and charge mass (8.07 g in a and 10.42 g in b), their pressure histories followed roughly the same pattern. Both histories had two larger initial pressure peaks followed by a much smaller third peak. However, in Figure 3.9 b, the third pressure peak was followed by an additional large peak. This must therefore be as a result of the differences in their experimental set-up, that in test b, a ball bearing was used. The pressure signal as a result of ball bearing impact could then be clearly and easily identified.

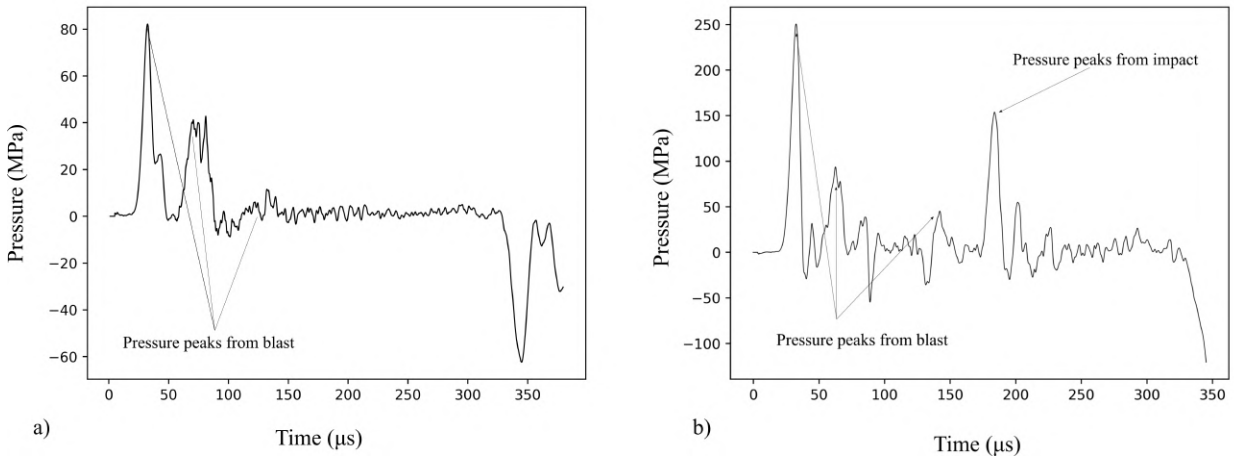

Figure 3.9: Graph showing the characterising differences between from a) HPB pressure history from a detonation with no ball bearing, b) detonation with ball bearing.

3.5.4 HPB impulse calculation

The axial impulse captured by the HPB, I_{HPB}, was calculated as using Equation 3.15.

$$I_{HPB} = \int_{t_5}^{t_5+1.58/c} P(t)dt - I_{impact} \tag{3.15}$$

Where 1.58 m is the length that the stress wave needed to travel before passing the strain gauges again, c is the speed of sound in the bar and I_{impact} is the impulse recorded by the HPB from the impact of the ball bearing. The I_{impact} was calculated in a similar method as Equation 3.15 but only for the duration of the impact signal. This method assumed that the impulse as a result of gas pressure through the impact duration is negligible.

3.5.5 Identification of detonation time

The time of detonation is required to determine the time of flight of the ball bearing. This was obtained initially by using a physical trigger. A 30 mm wide, 0.08 mm thick strip of light aluminium foil was placed on the back face of the main polystyrene bridge. The foil was connected to a single-board micro-controller. The controller generated a trip signal of 5 V when the circuit was broken and was received by the same data-logging device used by the strain gauges. It was discovered that the blast arrival time calculated using the trip signal of similarly-sized charges were not consistent. A more sensitive set-up was then used by placing a narrower, 5mm-wide aluminium foil on the rear face of the charge. However, the inconsistency persisted. Hence, the detonation time had to be determined by identifying the specific characteristics of the detonation electromagnetic (EM) signal captured by the HPB.

Expected properties of detonation signal

Electric detonators (M2A3) with aluminium shells were used in the blast tests. Although the exact configuration of the detonator is classified, the basic configuration of any electric detonator is largely the same as shown in Figure 3.10. During detonation, EM signals can only be expected from electronic components which are the capacitor and the delay circuit. The shape of the EM signal and its duration should correlate with the physical properties of the emitting components. However, the magnitude and the polarity of the signal may change at any time since the emitter and the receiver of the signals were not physically connected in the same circuit.

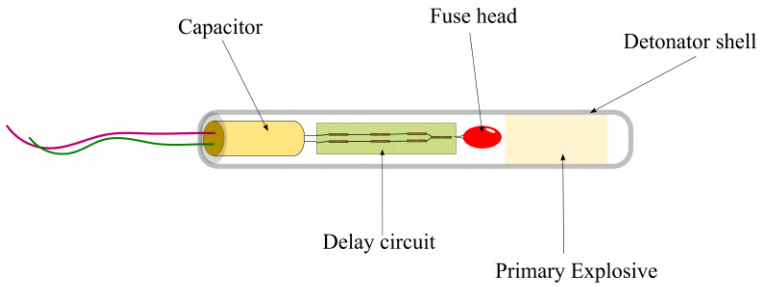

Figure 3.10: A schematic showing the composition of a typical electric detonator, adapted from [80].

The hypothesised sequence of events is illustrated in Figure 3.11. A series of EM noises emitting from the detonation processes are expected in the following order. First, at time t_1, the capacitor would discharge through a typical exponential decay. Since the specifications of the capacitors in the same batch of detonators are expected to be the same, the duration of the discharge should also be relatively constant.

Then the current flows into the delay circuit at time t_2, which consists of a series of resistors. EM signals are expected as the current passes through them. No 'delay detonators' were used in the experiments. Therefore, the exact duration of delay is expected to vary as the manufacturer was not obligated to be consistent with the delay time.

The temperature of the resistor in the delay circuit increases until a critical temperature which causes the fuse head to explode (t_3). This subsequently causes the booster or a primary explosive to detonate. This rapid increase in pressure would rupture the aluminium shell of the detonator and cause the detonation of the PE4. The explosion of the fuse head is thus the time of detonation for the detonator.

This explosion then breaks the circuit in the detonator which would likely cause a strong release of EM pulse. However, the capacitor often survives the explosive event and therefore would still have some remaining electrical energy stored in the circuit. Therefore, the destruction of the capacitor would emit another EM pulse (t_4). After this point, no electrical component is left in the detonator and therefore, EM noises are not expected to be emitted from the now, a fully detonated detonator.

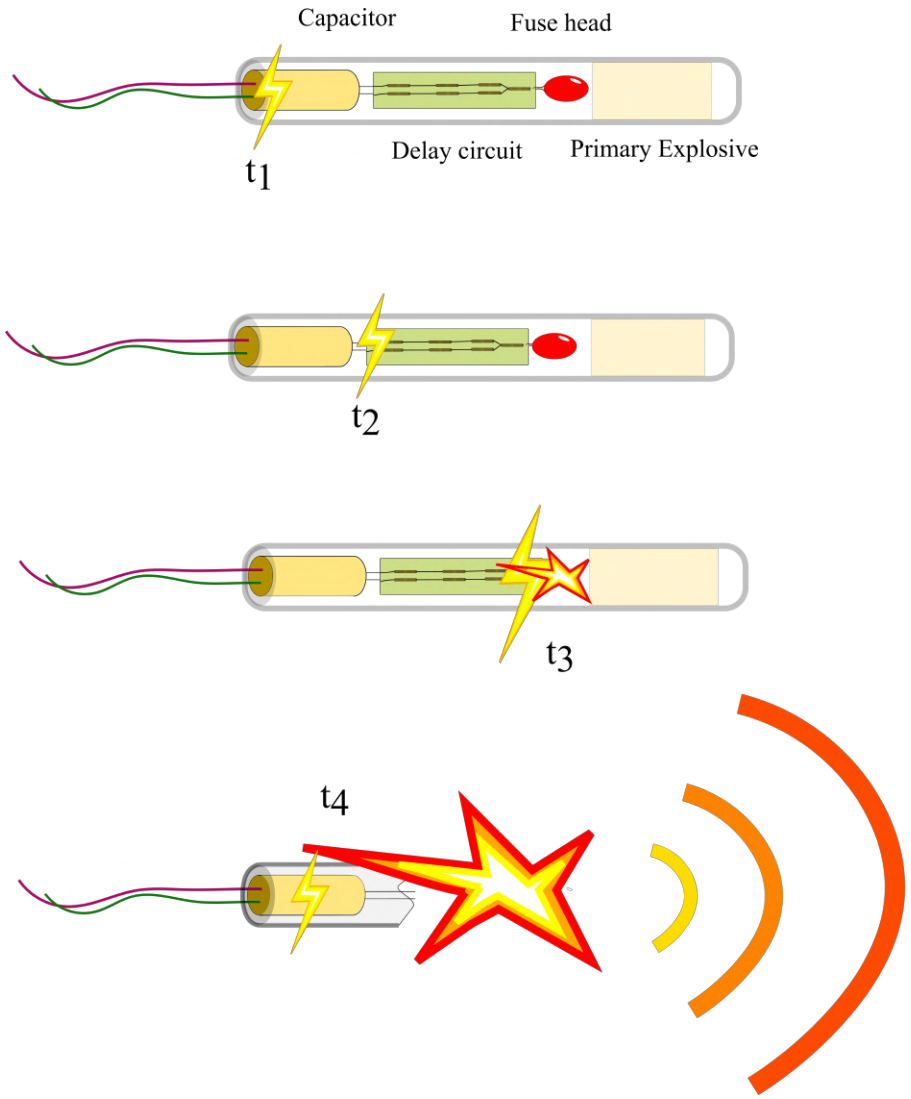

Figure 3.11: A schematic showing the hypothesised detonation sequence from a typical electric detonator.

This hypothesis is then combined with the EM signal recorded by the data logger to generate a model signal sequence as shown in Figure 3.12. Time t_1 is the time at which the capacitor began to discharge, t_2 is the time at which the current entered the delay circuit, t_3 followed immediately after the fuse head exploded, while t_4 is when the capacitor releases its residual energy and t_5 is the arrival time of the blast wave.

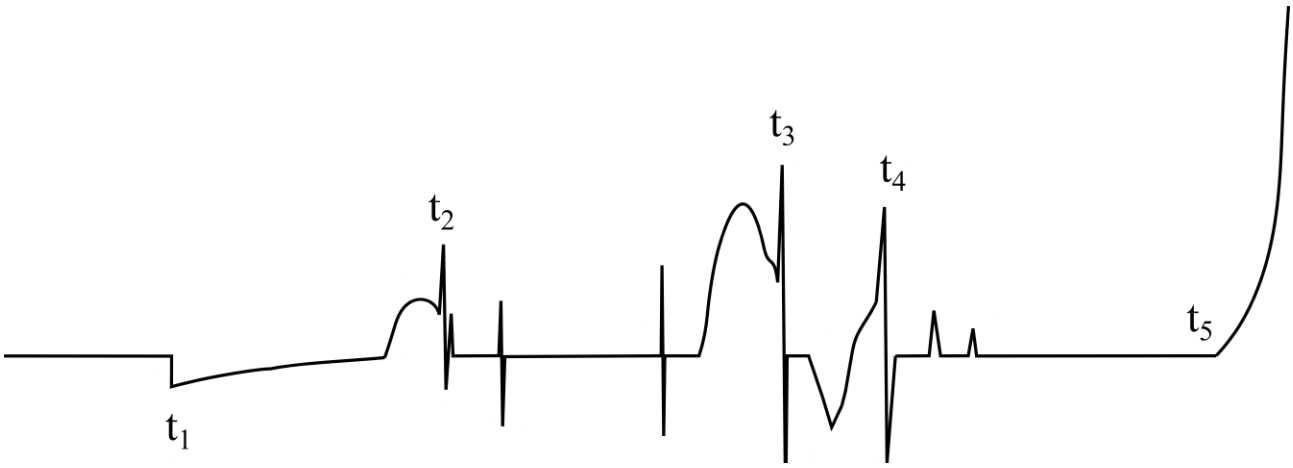

Figure 3.12: Illustrative (fictional) voltage trace indicating the signal produced during the detonation of a typical electric detonator.

Identification procedure

The model EM signal can now be applied to all experimentally obtained HPB EM signals to identify time events t_1 to t_5. Two examples are demonstrated in this chapter, shown in Figures 3.13 and 3.14. Times t_1, t_2 ,t_5 can easily be identified in the two examples using the features drawn in the model signal. The shape of t_3 and t_4 are however not as obvious. Three rules were then developed and were used to identify them in order to maintain consistency. The rules were defined as the following:

- t_3 and t_4 are EM signals that occur after t_2 and before t_5
- t_3 and t_4 can be positive or negative voltage peaks however the signal cannot oscillate with high frequency as shown in Figure 3.15.
- t_4 is the last EM signal emitted and t_3 is the second last signal emitted by the detonator .

As the characterising times are caused by the release of electrical energy, the EM signal should be characterised by lower frequency and higher magnitude since the release of such energy is likely to not be instantaneous. Whereas EM signals that are lower in magnitude but extremely high in frequency are more likely to EM noise which can come from static electricity.

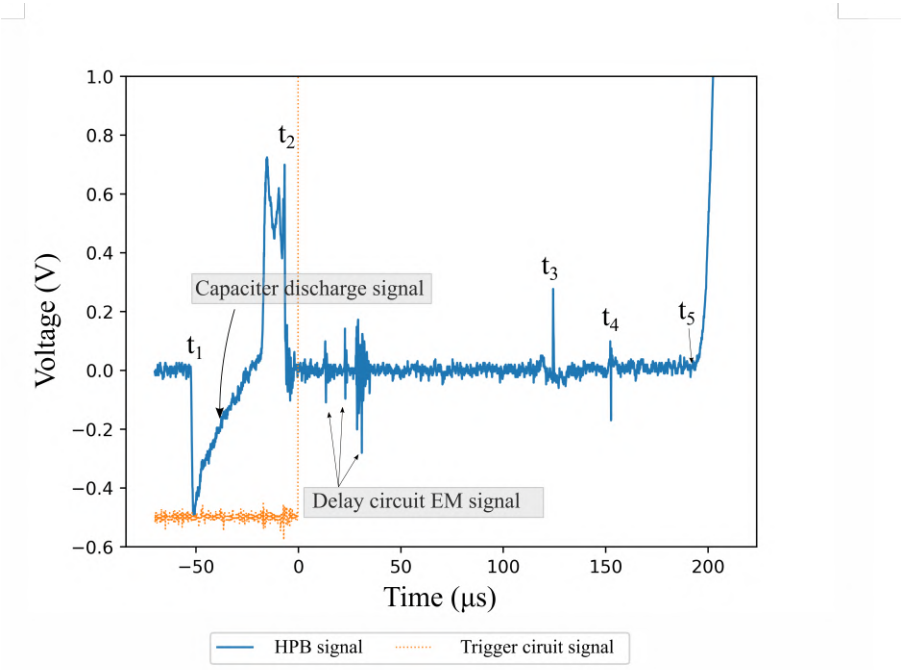

Figure 3.13: Graph illustrating the positions of signals t_1 to t_5 for 7.33 g, ⌀18 mm charge. Note that the triggering signal was shifted down by 0.5 volts for the clarity of illustration.

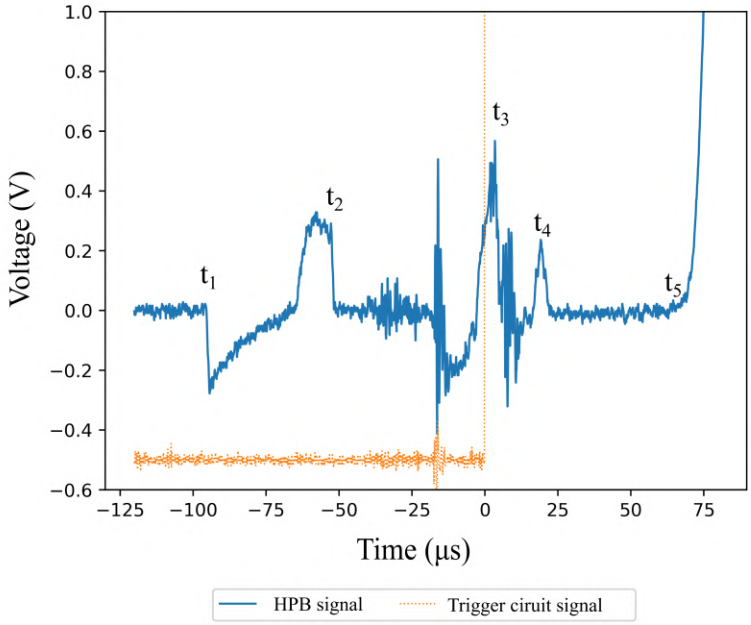

Figure 3.14: Graph illustrating the positions of signals t_1 to t_5 for 5.21 g, ⌀24 mm charge. Note that the triggering signal was shifted down by 0.5 volts for the clarity of illustration.

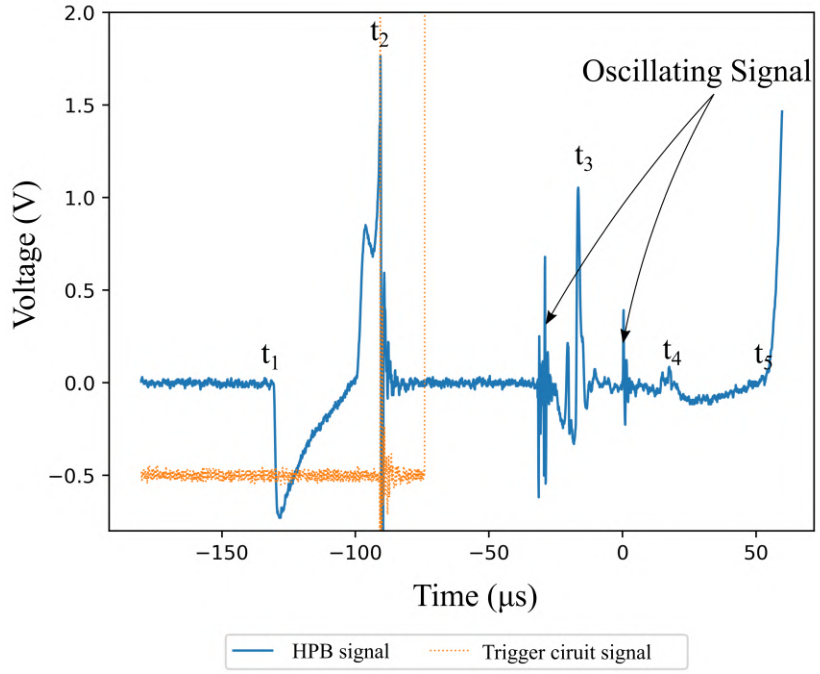

Figure 3.15: Graph illustration the rules used to identify t_3 and t_4.

3.5.6 Ball bearing velocity calculations

The average velocity of the ball bearing was calculated from the voltage history using Equation 3.16.

$$v_{average} = \frac{x}{\Delta t} \tag{3.16}$$

and that:

$$x = \sqrt{x_{normal}^2 + x_{hori}^2} \tag{3.17}$$

$$\Delta t = (t_{impact} - \frac{x_{gauge}}{c}) - t_3 + \Delta t_{detonation} \tag{3.18}$$

Where x_{normal} is the normal distance between ball bearing and the witness plate; x_{hori} is deviation from the centre of the witness bar to the centre of the impact crater; x_{gauge} is the distance from the front face of the HPB to the centre of the strain gauge and c is the speed of sound in the HPB and $\Delta t_{detonation}$ is the time it takes for the detonation wave to propagate the specific explosive. $\Delta t_{detonation}$ was estimated using the ideal detonation velocity of PE4 at 8190m/s [2].

Although the detonation velocity follows an estimated asymptotic relationship with charge diameter in cylindrical charges [3], the increase in detonation velocity after 18 mm, the smallest diameter used in this project, becomes negligible. The time taken for the detonator shell to rupture was also treated as negligible. A small piece of aluminium shell of the detonator was found after the blast test, the thickness of the shell was measured at 0.115 mm.

3.6 Experimental method to infer impact velocity

3.6.1 Correlation of crater depth and impact velocity

An empirical relationship between impact crater depth and the impact velocity was determined from the impact experiments using a two-stage light inert gas gun [81]. The standard arrangement was modified to accommodate a 5 mm ball bearing as the projectile. The geometry of the two-stage gas gun is presented in Figure 3.16. Part 5, 6 and 7 forms the piston assembly which moves forwards (right) as one unit when the gas gun is fired.

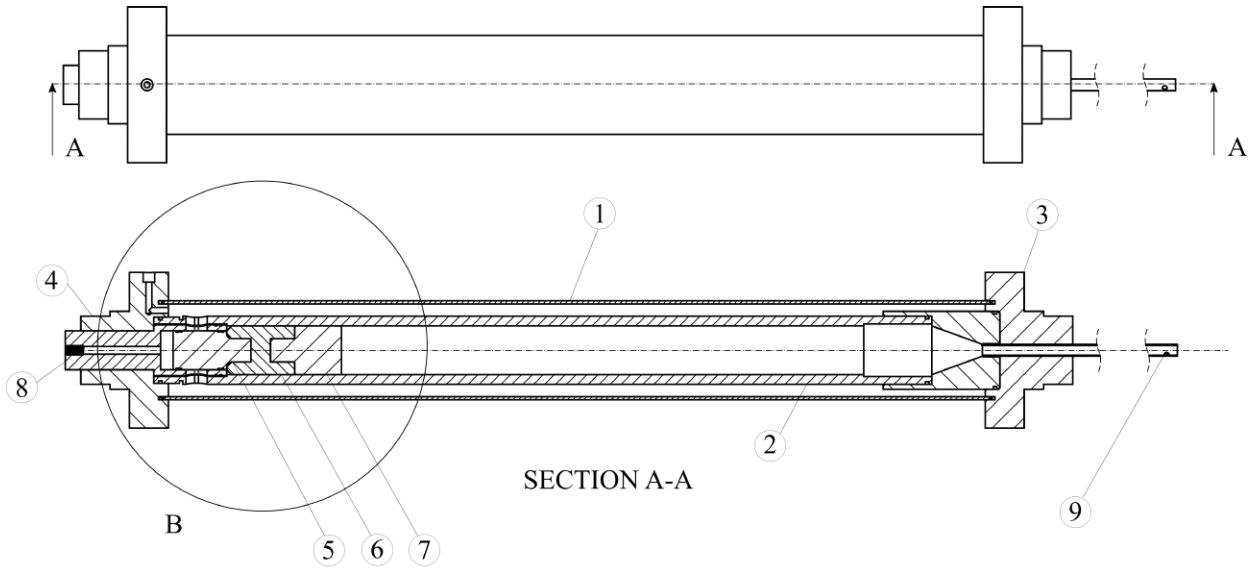

Figure 3.16: Schematic showing the front view and section view of the two-stage gas gun used in the impact experiments, designed by Cloete et al.[81].

Table 3.1: Table showing the Bill of Material for Figure 3.16.

Part number	1	2	3	4	5	6	7	8	9
Part name	Reservoir	Pump tube	Rear flange	Front flange	Piston driver	Piston	Piston cap	Initiator	Barrel
Material	Aluminium	Mild steel	Aluminium	Aluminium	HDPE	Al7075-T6	Polyethylene	Mild steel	Aluminium

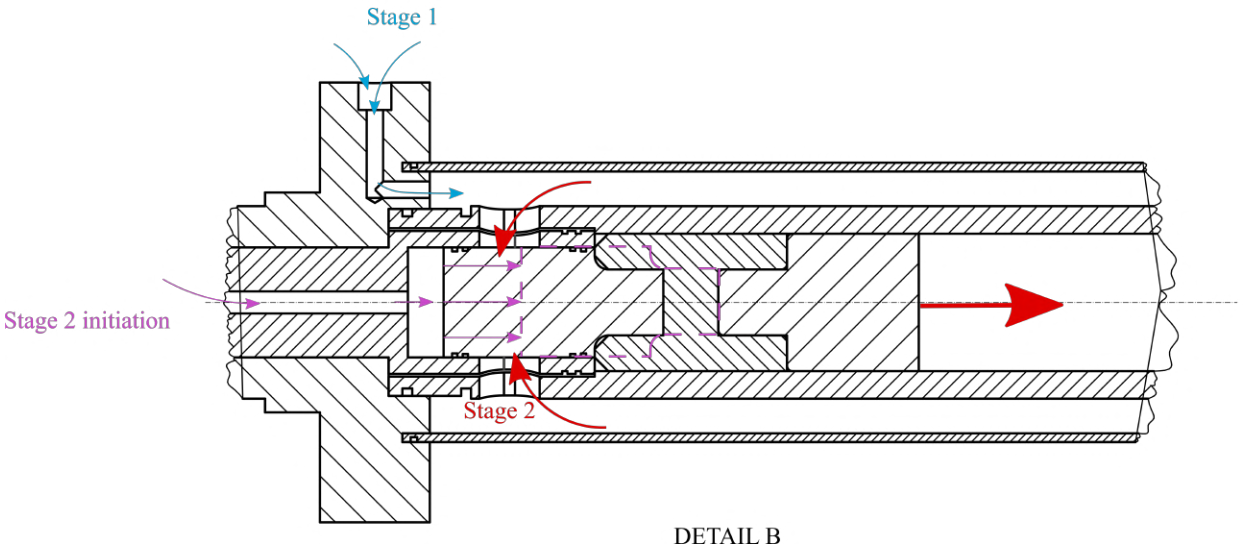

Figure 3.17: Schematic showing the detailed view of area B and the firing sequence of the two stage gas gun, designed by [81].

A detailed view of area B is shown in Figure 3.17 to illustrate the firing sequence of the two stage gas gun. In the first stage, air from a gas tank was used to fill the reservoir until the desired pressure was reached. The gas tank was disconnected before proceeding. Pressures up to 10 bars were used for this stage. Then, a very small amount of gas, leftover in the pneumatic piping, was used to move the piston assembly forward until the rear face of the piston driver is in front of the filling holes (stage 2 initiation). At this instant, gas from the reservoir flowed into the pump tube (stage 2) and drive the piston assembly forward. The piston assembly then compressed gas in front of it and fired the projectile.

The projectile and witness plates were consistent with what was used during the blast experiments. Initially a 3D printed polylactic acid (PLA) sabot with standard sized O-rings were used but the original design could not achieve an impact velocity above Mach 1. The sabot design was improved here by using a paraffin wax sabot which allowed the ball bearing to reach 580 m/s. The wax sabot provided excellent sealing abilities while created sufficient lubrication from the molten contact surface with the barrel. A photograph of the wax sabot with the ball bearing is shown in Figure 3.18. The wax was dyed black to make it more visible to the speed sensor which was manufactured by melting wax in a custom machined brass mould.

Other minor adjustments to the gus gun were made, such as re-lubricating the inner tube and using better fitted O-rings.

Figure 3.18: Photograph showing the wax sabot manufactured for the impact experiment with the ball bearing inserted.

The impact experiments were performed using a 2860 mm barrel with ⌀9.8 mm which consisted of a flute section of 270 mm in length. The flute section allowed gas to escape before passing through the speed sensor which could potentially damage the photo-transistors in the sensor. The effective acceleration length was thus 2590 mm thereafter, the sabot-bearing assembly reduced in velocity. This barrel length was used as it was sufficient for the ball bearing to self-detach from the sabot as a result of the differences in the rate of deceleration. The detached sabot and ball bearing were observed through high-speed video footage and through the signal from the velocity sensor as shown in Figures 3.19 and 3.20. The first, smaller set of voltage peaks were generated by the ball bearing passing and the second set of voltage peaks, which were much bigger, were generated by the wax sabot passing through the sensor. The interpretation method of the voltage history is presented in Section 3.6.3.

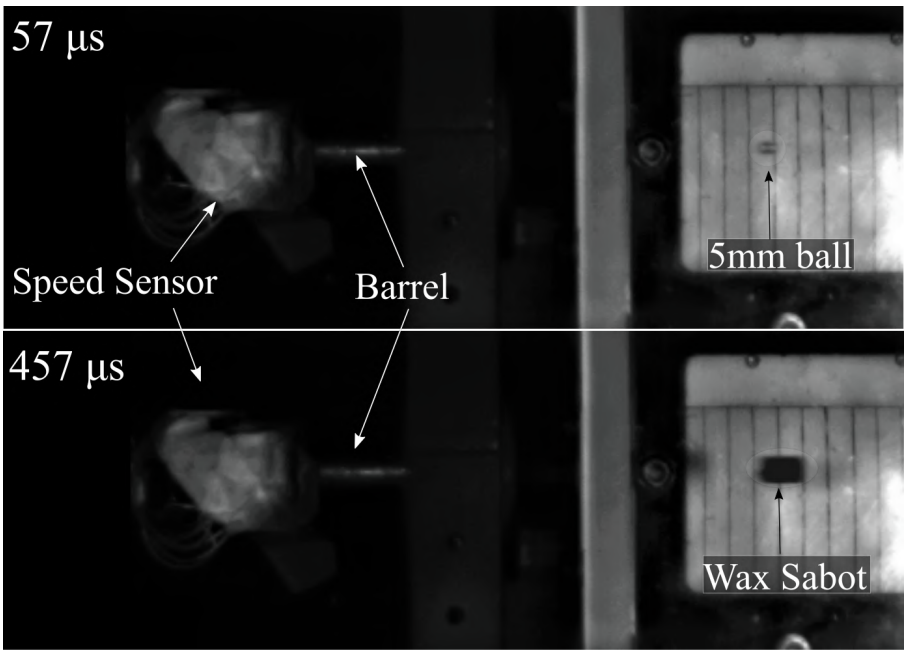

Figure 3.19: High-speed footage showing the end of the barrel and the exit sequence of the ball bearing and the sabot.

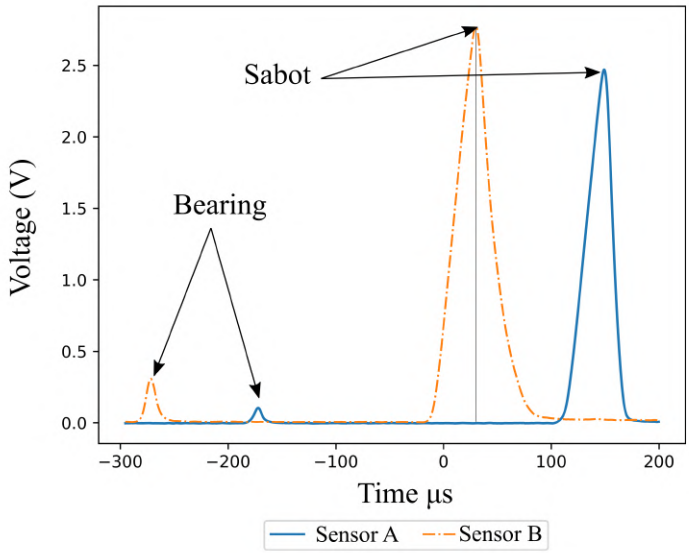

Figure 3.20: Graph showing the voltage history recorded by the velocity sensor.

3.6.2 Sabot deflector

An empty wax sabot containing no ball bearing was fired at 7 bar at the aluminium target to determine whether the sabot would affect the cratering process. Figure 3.21 presents a photograph of the witness plate after the impact from the empty wax sabot. A small dent with a maximum depth of 0.04 mm was visible. Thus, it was clear that the effects of the sabot were not negligible. While sabot catchers used in the literature [82, 83] are often designed to separate the sabot from the projectile, in this experimental arrangement, the ball bearing was able to self-release. So, a device was designed to deflect the sabot instead of catching and slowing it.

The schematic illustrating the sabot deflector is presented in Figure 3.22. It was made of mild steel and had a central hole diameter that allowed the ball bearing to pass while deflecting the wax sabot. The deflector was fitted at the end of the barrel and was used as a bushing for the barrel. To test its effectiveness, an empty sabot was fired once again, but this time a piece of standard printing paper was clamped as the target. No dent was found on the paper, thus the wax sabot was deflected.

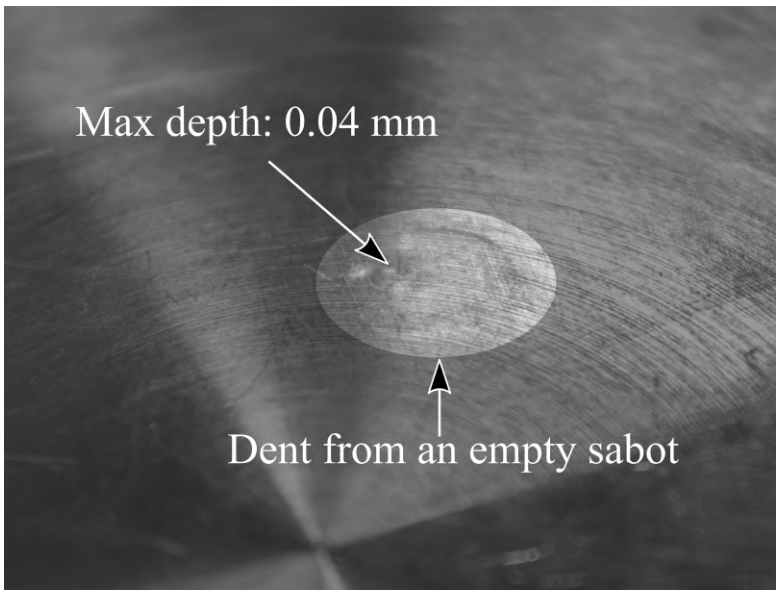

Figure 3.21: Photograph of a dent on the aluminium witness plate from the impact of an empty sabot accelerated at 7 bar.

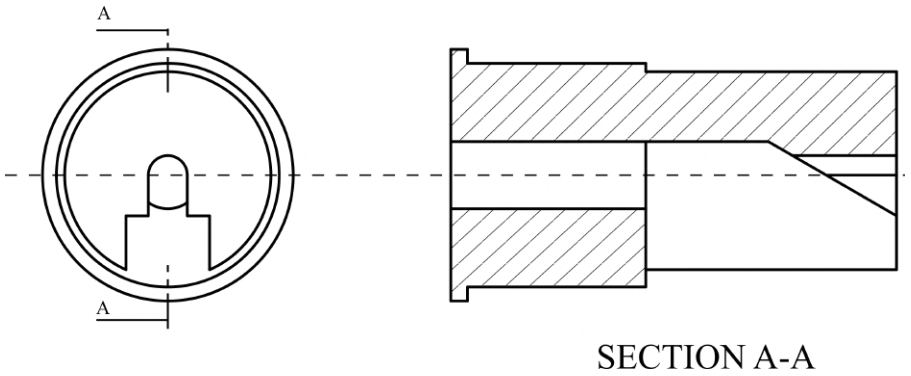

Figure 3.22: A schematic drawing showing the front and side view of the sabot deflector.

3.6.3 Interpreting velocity from velocity sensor output

The velocity sensor was made from two light traps mounted in a polyvinyl chloride cylinder. The light traps were normal to the barrel, with a centre to centre distance of 40mm. The distance verified by slowly lowering the measuring rod of a depth micrometer while observing the voltage output from the sensors. During the experiments, the sensor was mounted at the end of the barrel. A catch box of length 100 mm was placed between the sensor and the witness plate for safety reasons.

As shown in Figure 3.20 as the ball bearing and sabot passes the two sensors, the sensors would register two voltage peaks. Since the ball bearing was much smaller than the total observing region of the sensor, its passing produced a voltage peak that was much smaller in magnitude. It can also be noted that sensor A and B do not produce the same magnitude or duration when the same object passes through them as their sensitivities are slightly different. Therefore, to calculate the time difference for an object to pass the sensors, the rise-to-rise time cannot be used. Instead, the voltage history must be interpreted physically. As an object moved closer to the sensor, it is obstructed more of the sensing surface and caused an increase in voltage. The opposite is true as the object moved past the

mid-point of the sensor and moved away. Therefore, the point of inflexion in the voltage history must be the midpoint of the sensor. Therefore, the velocity of the ball bearing and the sabot was calculated using the centre-to-centre distance between the sensor divided by the peak-to-peak time.

3.6.4 Crater depth measurement

Figure 3.23 illustrates the arrangement used to measure the depth of the crater. Ball bearing with diameters ranging from 1.2 mm to 12 mm were placed in and allowed to slide to the lowest point of the crater. A depth micrometer was rested on two dowel pins with its measurement rod extending to touch the ball bearing. The depth of the crater was measured by using the smallest ball bearing. Ball bearing of other diameters were used to trace the profile of the crater.

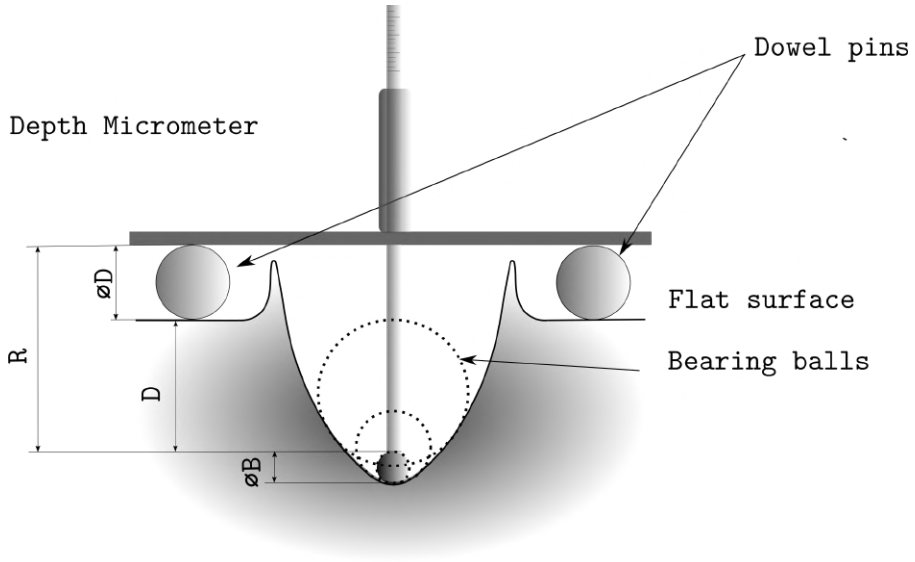

Figure 3.23: Schematic showing the impact crater depth measurement arrangement.

The depth of a crater is therefore:

$$Depth = R - \varnothing D + \varnothing B \tag{3.19}$$

Where $\varnothing D$ and $\varnothing B$ are the diameters of the dowel pins and ball bearings, and R is the reading from the depth micrometer.

3.6.5 Impact velocity and crater depth

During the impact experiment, barrel exit velocities ranging from 200 m/s to 309 m/s were achieved using a 3D printed sabot. The exit velocities were increased by using the wax sabot to 570 m/s. The highest pressure used in the first stage of the two-stage gas gun was 9 bar. This was as a result of the increase in barrel vibrations with the increase in gas pressure which would obscure the velocity sensor at pressures beyond 9 bar. The vibration in the barrel is caused by the high pressure that immediately followed the sabot. This did not cause disturbance to the capturing of the velocity when the ball bearing separated from the sabot. The separation was consistently observable at pressures up

to 7 bar. For experiments between 7 bar and 9 bar, a frozen sabot was used which promoted the ball bearing-sabot separation. This method did not work consistently at pressures beyond 9 bar.

The graph of exit velocity versus crater depth is shown in Figure 3.24. Despite the different sabots used in the experiments, the results appear to show consistent increase in crated depth with the increase in impact velocity. There was a low level of correction between the JSC (Equation 2.19) and the experimental results. The modified JSC (Equation 2.20) results have a similar gradient as the experimental result but over-predicted the crater depths.

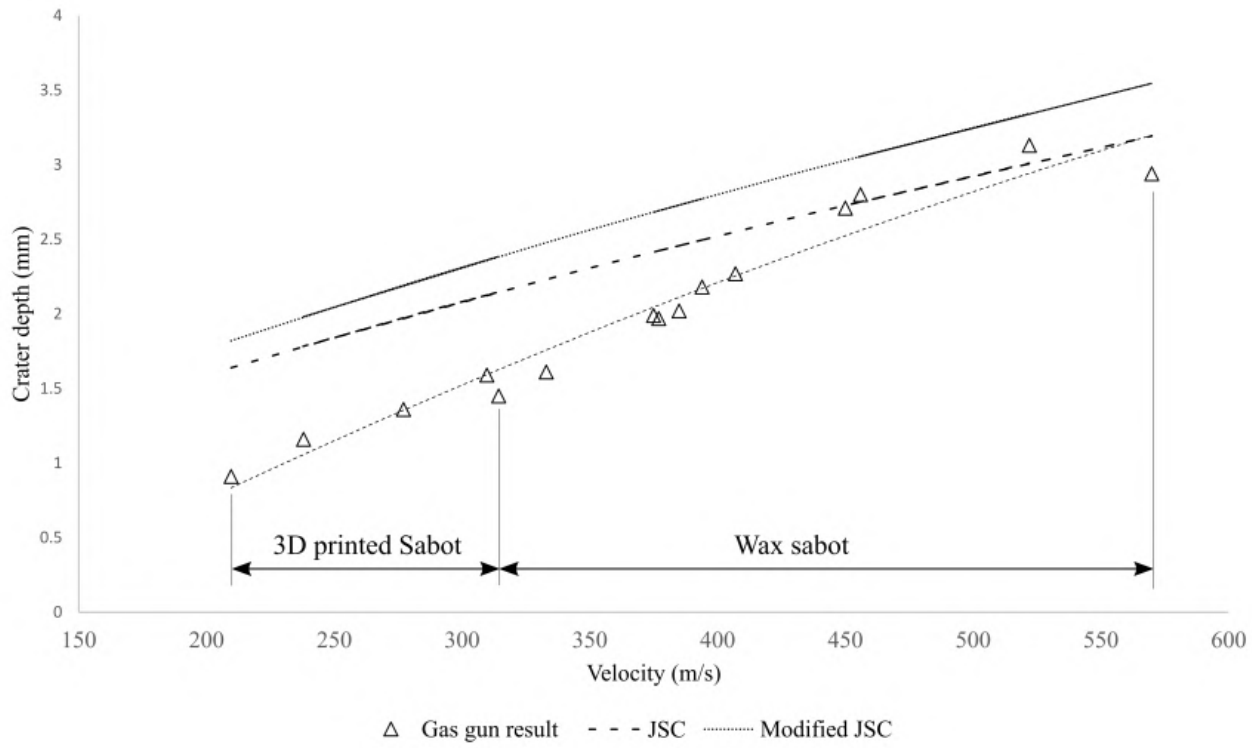

Figure 3.24: Graph of crater depth versus velocity showing the experimental results using the gas gun as well as empirical solutions from the JSC and modified-JSC equation.

A quadratic polynomial was fitted over the experimental results and was manipulated to express velocity in terms of crater depth as shown in Equation 3.20. This equation was used to infer impact velocity using the measured crated depth.

$$v(t) = -4.833t^2 + 164t + 66.798 \tag{3.20}$$

Chapter 4

Material Characterisation

In this section, the method and the results of material testing conducted during the course of the investigation are reported. The quasi-static tensile test of Al6082-T6 was conducted alongside an undergraduate student, K Kekana, who used the same material for her undergraduate dissertation. This was to obtain material properties for the witness plate impacted by the ball bearing in the blast tests. The sphericity and the mass of the ball bearings were also measured.

4.1 Testing of Al6082-T6

Four quasi-static tensile tests were conducted for Al6082-T6 at10^{-3} s^{-1} strain rate on round bar tensile specimens using the Zwick 1484 Universal Tensile/Compression Testing Machine following the DIN EN 1002-1 standard. The unprocessed force versus displacement history graph for the four specimens is presented in Figure 4.1. Before computing the engineering stress-strain curve, the force-displacement data must be calibrated and the effect of machine compliance must be removed.

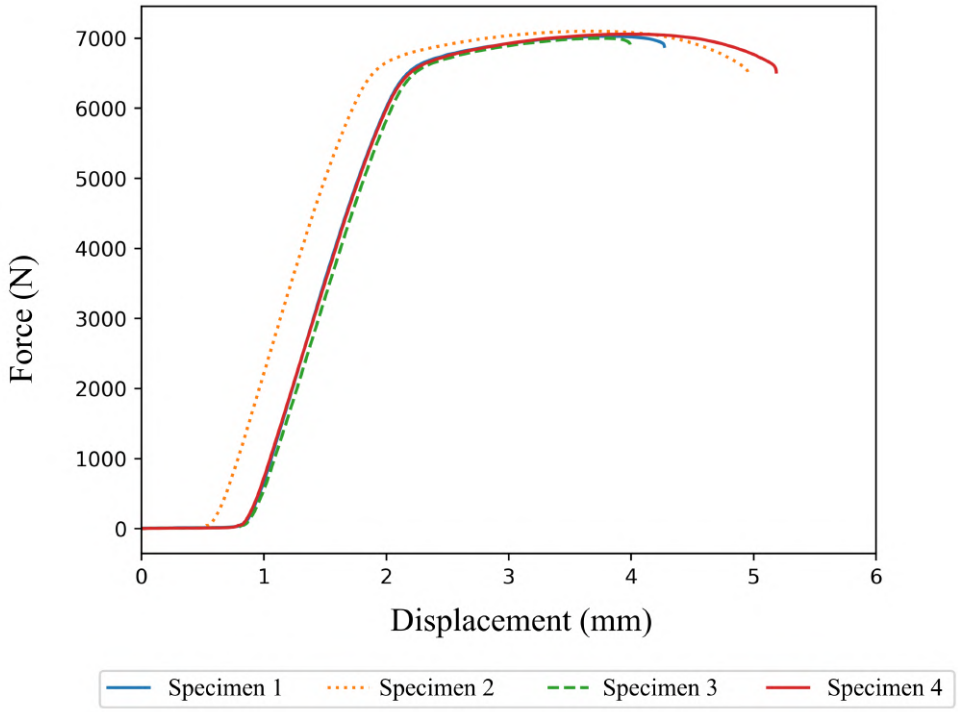

Figure 4.1: Graph of force versus displacement (strain) as recorded from the Zwick Universal Tensile Machine for the four specimens.

The machine and the test specimens were assumed to be in parallel springs. Therefore, the stiffness of the machine k_m can be expressed as:

$$\frac{1}{k_m} = \frac{1}{\frac{1}{k_t} - \frac{1}{k_s}} \tag{4.1}$$

where k_t is the combined stiffness recorded by the machine and k_s is the stiffness of the test specimens. The stiffness of the test specimens can be obtained using:

$$k_s = \frac{E_s A}{L_0} \tag{4.2}$$

where E_s is the Young's Modulus, A is the cross sectional area and L_0 is the original gauge length of the specimen which is given as:

$$L_0 = 5.65\sqrt{A} \tag{4.3}$$

The combined stiffness of the machine and the specimen was found by fitting a linear curve over

the linear elastic region of the force-displacement graph. The gradient of this curve is taken as the combined stiffness. The force-displacement history is then shifted so that the fitted curves of the four specimens would intercept at the origin as expressed in Equation 4.4. This removes the effect of the first non-linear region of the data where the specimen was 'slacking'.

$$d_i^1 = d_i^0 - (-\frac{c}{k_t}) \tag{4.4}$$

Where d_1 is the new displacement history, d_0 is the original displacement history and c is the y intercept for the fitted linear curve.

This effect of machine compliance can now be removed as shown in equation

$$d_i = d_i^1 - \frac{F_i}{k_m} \tag{4.5}$$

The engineering stress σ and strain ϵ can then be evaluated as:

$$\epsilon_i = \frac{d_i}{L_0} \tag{4.6}$$

$$\sigma_i = \frac{F_i}{A} \tag{4.7}$$

The engineering stress versus strain calculated using this method is shown in Figure 4.2. A linear curve passing through 0.002 strain at zero stress with the gradient of E was plotted. The intercepts of this line with the four stress-strain graphs were used as the yield stress of the material.

The dimensions of the specimens and their corresponding mechanical properties are presented in Table 4.1. The Young's Modulus E was also provided by the manufacturer as 70 GPa [84].

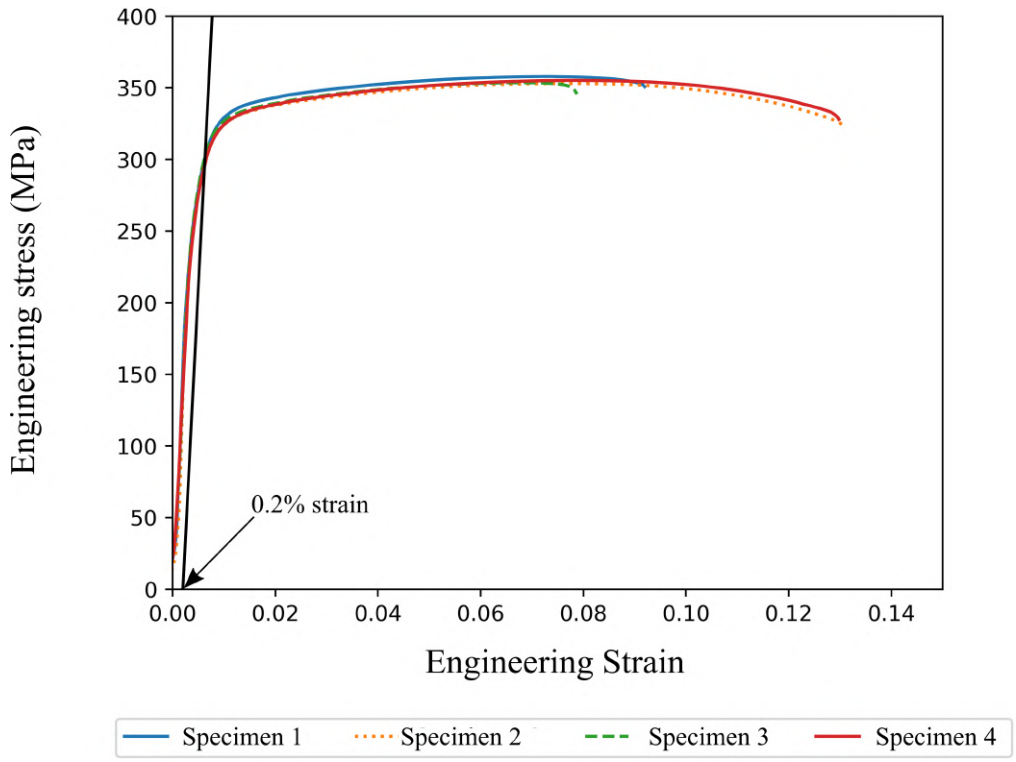

Figure 4.2: A graph of engineering stress versus strain obtained from tensile tests.

Table 4.1: Table with the dimensions of the machined test specimens.

Specimen number #	Diameter mm	Yield Strength MPa	Ultimate tensile strength MPa	Fracture Strain
1	5.00	300.6	358.0	0.092
2	5.06	297.2	354.1	0.131
3	5.02	302.1	353.6	0.079
4	5.03	295.8	355.2	0.130
Mean	5.03	298.9	355.2	0.108
Standard deviation	0.025	2.9	1.9	0.027
Specified by the manufacturer		255 to 315	295 to 330	0.07 to 0.1

It can be noted that the results from the four tensile tests are consistent with each other with the exception of the fracture strain. The mean yield strength of the materials is 298.9 $\pm$2.9 MPa and was within the manufacturer's specification. The ultimate tensile strength and the fracture strain of the material exceeded the specifications and were found to be 355.2 $\pm$1.9 MPa and 0.108 $\pm$0.027 respectively. The standard deviation of yield strength and ultimate tensile strength are relatively small at 1.0 % and 0.55 % of the mean. While large standard deviation was observed for the fracture strain which was at 25% of the mean.

4.2 Testing of ball bearing

4.2.1 Testing of sphericity

The sphericity of the 420 stainless steel bearings was measured using the arrangement shown in Figure 4.3.

The ball bearing was clamped between a machined metal rod (left) with a conical cavity and the tailstock on the lathe (right). The conical cavity was machined first after which the ball was clamped without the removal of the steel rod. This ensured the concentricity alignment between the conical cavity and the ball bearing. A dial gauge with resolution up to 1 μm was then placed on a stable stand with the head of the dial gauge pressing gently on the ball bearing. No movement was observed from the dial gauge as the lathe was rotated. This process was repeated for 5 ball bearings and no variation in diameter could be observed. For the purpose of this project, the ball bearing were treated as spherical.

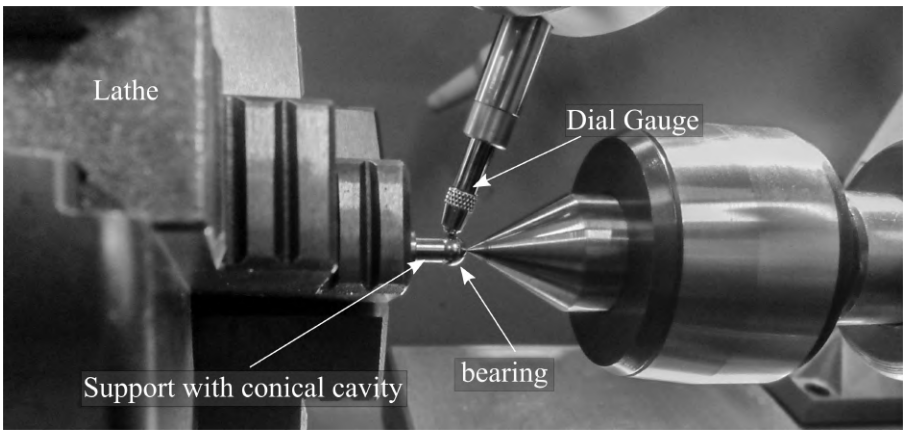

Figure 4.3: Ball bearing sphericity set-up.

4.2.2 Testing of mass variation

The mass of fifty 420-stainless ball bearings were weighed on an electronic balance. The mean mass was recorded as 0.50548g with a standard deviation of 0.00061g which is 0.12% of the mean mass. The least and most massive ball bearings were measured at 0.50246g and 0.5067 g which were 0.241% and 0.242% of the mean mass.

The mass variation of the ball bearings were small, as expected. Therefore, the velocity percentage error as a result of the mass variation of the ball bearings under the same momentum would be -0.241% to +0.242%.

Chapter 5

Numerical formulation

In this chapter, the methods used for formulating the geometry, mesh sizes and the choices made to select different numerical techniques are reported.

5.1 General formulation

The blast arrangements presented in Chapter 3 were modelled in numerical simulations. The simulations were performed using the commercial hydrocode ANSYS Autodyn. A two-dimensional axisymmetric model was constructed using the geometries from the experimental arrangement.

The simulation included experimental arrangements used inside the blast tube. The front clamp, back clamp and HPB were modelled as fixed boundaries that were applied on the witness plates. The blast tube wall was modelled as a reflective boundary. The rest of the pendulum, along with the polystyrene bridge, and aluminium foil were not included in the simulation.

The impact and average flight velocity of the ball bearings for the corresponding charge configuration were used to validate the numerical model. These validations are presented and discussed in detail in Chapter 7.

A schematic of the simulation space is shown in Figure 5.1. The dimensions of the air mesh were 162 mm by 51.15 mm. In its left section, an 'outflow' boundary condition was applied to simulate the blast chamber environment where the charge was detonated. On its right section, reflective boundaries were used to simulate the blast tube as the transient behaviour has the tube wall was not included as the scope of this project. The witness plates were modelled using two rectangular parts, which were separated by 0.25 mm. The rear faces of witness plates were fixed in the x-direction.

A 3.2 mm line detonation was used to simulate the ⌀6.4 mm detonator used in the blast tests. The detonation initiated simultaneously across its line in the simulation.

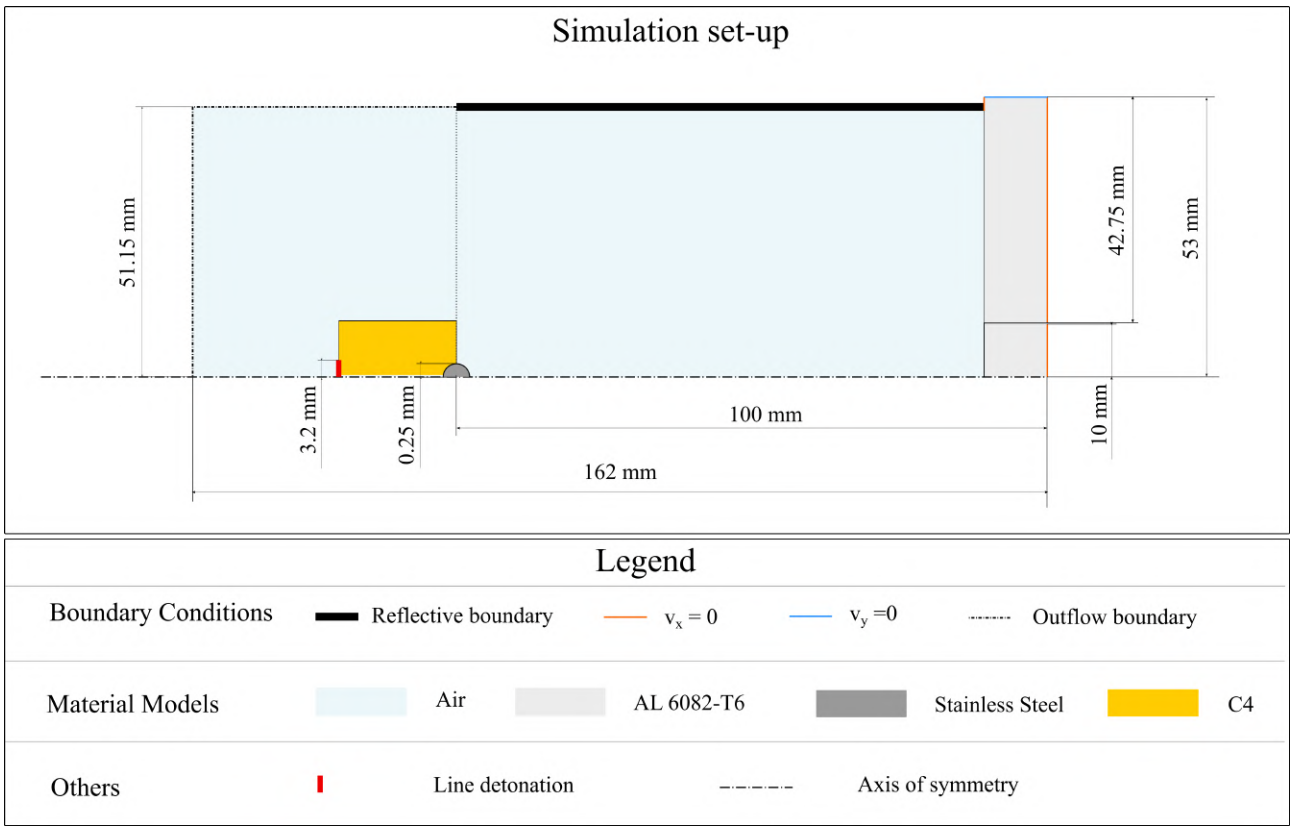

Figure 5.1: Schematic showing the geometry and boundary conditions used in the numerical simulations.

5.2 Air and PE4 formulation

The responses of materials to loading was computed using its equation of state (EOS) and its strength model. EOS provides a general relationship between the thermodynamic 'states' of material, mostly commonly in the form of internal energy, volume, temperature, pressure and phase. Strength models in Autodyn are the constitutive model that describes the mechanical stress-strain relationship.

5.2.1 Equation of States used for Air and PE4

An ideal-gas EOS was selected for air, with the initial conditions specified as $25°C$ at 1 bar. The adiabatic expansion of air from the detonation of PE4 was modelled using JWL EOS using parameters for C4. PE4 and C4 have the same active ingredient with 88% RDX. The differences in their explosive properties was negligible for the purpose of this project. Additionally, many numerical work in the literature used C4 materiel properties to model PE4[11, 85]. The parameters for these equations of states were provided by the Autoydn library [86] and is presented in Table 5.1.

Table 5.1: Material properties[86] used to simulate the air and PE4 in Autodyn.

Material	Material model/ Equation of state	Property	Value
Air	Ideal Gas	Density (g/cm^3)	0.001225
		Gamma	1.4
		Specific Heat (J/kgK)	717.6
C4	JWL	Density (g/cm^3)	1.601
		Parameter A (kPa)	6.10×10^8
		Parameter B (kPa)	1.30×10^7
		Parameter R1	4.5
		Parameter R2	1.4
		Parameter W	0.25
		C-J Detonation velocity (m/s)	8190
		C-J Energy / Unit Volume	9.00×10^6
		C-J Pressure	2.80×10^7

5.2.2 Mesh sensitivity analysis for air mesh

A two-dimensional, structured axisymmetric mesh sensitivity analysis was conducted for the air mesh using the same dimensions as the final simulation. A 6.71 g C-4 spherical charge was modelled using the JWL EOS. The ideal gas was used for air with the same initial conditions as the final model. Flow-out boundary conditions were used for all boundaries. The peak overpressure versus the number of elements was recorded for mesh size ranging from 4 mm to 0.1 mm at 42.43 mm SOD as shown in Figure 5.2. A typical exponential convergence can be observed from this result. The 0.2 mm mesh size was selected as it was not as computationally demanding as the 0.1 mm but provided very similar results. The peak incident pressure was at 4 % difference from that estimated from using the Kingery-Bulmash [87] method.

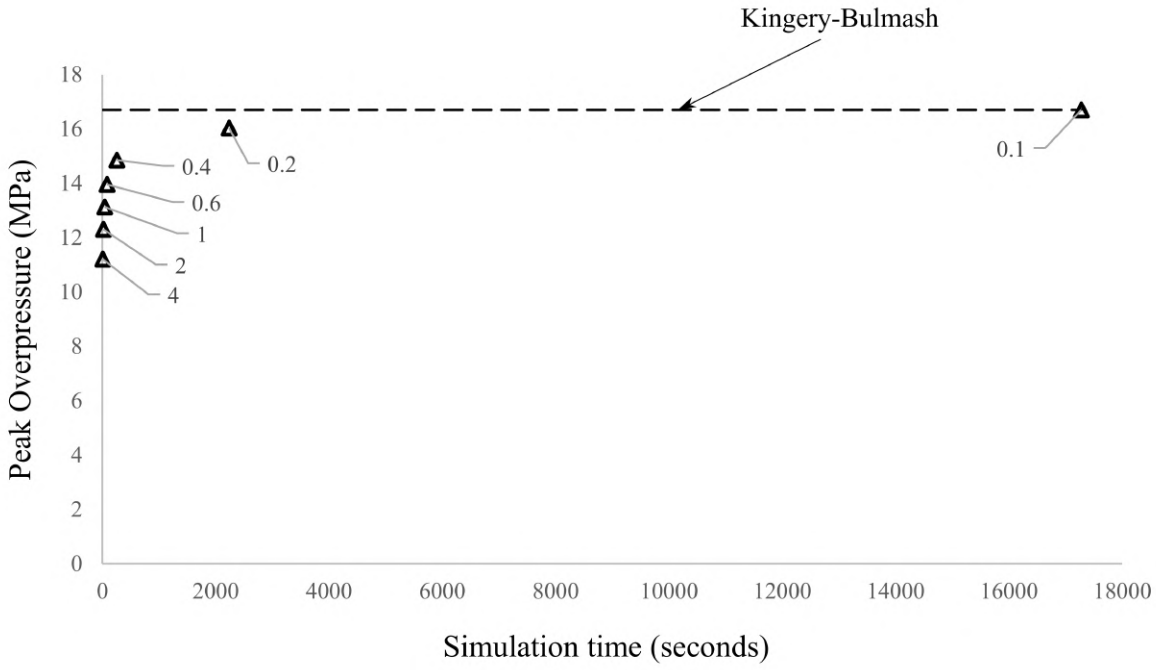

Figure 5.2: Graph showing the peak overpressure versus number of element captured in the mesh sensitivity analyses

5.3 Formulation of witness plates

5.3.1 Equation of States used for Al6082-T6

The 'Shock EOS' was used to relate particle velocity in the material to density, pressure and shock velocity using the Rankine-Hugoniot [88, 89]equations. This assumes that a linear relationship exists between the particle velocities in the shocked material (u_p) and the shock front velocity U. This can be expressed as:

$$U = c_0 + su_p$$

Where c_0 is the bulk velocity of the material and s is a material parameter. The pressure-volume relationship under shock can be expressed using the Mie-Gruneisen equation and the Hugoniot conservation equations as:

$$p = p_H + \Gamma\rho(e - e_H)$$

Where p_H is the Hugoniot pressure, Γ is the Gruneisen parameter [46] which represent the vibration of atoms from thermal energy and e_H is the Hugoniot internal energy per unit mass.

The Hugoniot pressure and energy and then be calculated using the Hugoniot conservation of momentum and energy in Equation 5.1.

$$p_H = \frac{\rho_0 c_0^2 u(1+\mu)}{[1-(s-1)\nu]^2} \tag{5.1}$$

where

$$\mu = \frac{1-\rho}{\rho}$$

$$e_H = \frac{p_H}{2\rho_0}\frac{\mu}{1+\mu}$$

Al6082-T6 is a strain rate-sensitive material, thus the Johnson-Cook strength model [90] was selected. The parameters were characterised by Yibo et al.[91]. The quasi-static uni-axial tensile test results presented in Chapter 5 matched closely with results obtained by Yibo et al[91]. At 0.001 s^{-1} strain rate, the yield and ultimate tensile strength are within 2.4 and 3.2 %, respectively.

The Johnson-Cook [90] strength model is sensitive to strain, strain-rate and temperature. This model relates the aforementioned variables to stress Y as:

$$Y = (A + B\epsilon_p^n)(1 + Cln_{\epsilon_p^*})(1 - T_H^m) \tag{5.2}$$

Where A, B, n, C, m and T_m are material parameters that are commonly refined as the yield stress, hardening constant, hardening exponent, strain rate constant, thermal softening exponent and melting temperature of the material.

Failure models provide more realistic simulations once the tensile limit of materials have been reached. Spallation is known to be one of the driving failure mechanisms in high-speed impact. Thus, Grady's spall failure model [92] was used which relates a critical strain ϵ_c, density (ρ) and speed of sound (C) for the material to a critical stress (S) for spallation to initiate.

$$S = \sqrt{2\rho c^2 Y}\epsilon_c \tag{5.3}$$

Where $\epsilon_c = 0.15$ is typically used for aluminium.

The highly distorted finite elements used in high-speed impact simulations required an automatic element deletion mechanism before the elements become inverted. This is known as erosion in Autodyn[86] . This was used in the aluminium model. The material parameters used in the EOS and strength model are presented in Table 5.2.

Table 5.2: Parameters used in the Shock EOS [86] and Johnson-Cook Strength model for Al6082-T6[91].

Material	Material model/ Equation of state	Property	Value
Al6082-T6	Shock	Density (g/cm^3)	2.70
		Gruneisen coefficient	1.97
		Parameter C1 (m/s)	5240
		Parameter S1	1.3
		Specific heat (J/kgK)	885
	Johnson Cook	Shear Modulus (kPa)	2.76×10^7
		Yield Stress (kPa)	3.06×10^5
		Hardening Constant (kPa)	3.049×10^5
		Hardening Exponent	0.68
		Strain Rate Constant	4.37×10^{-3}
		Thermal Softening Exponent	1.00
		Melting Temperature (K)	877
		Ref. Strain Rate /s	1.00
	Grady Spall Failure model	Critical strain value	1.5
	Geometric Erosion	Erosion strain	1.5
		Type	Instantaneous

5.3.2 Mesh sensitivity analysis for Al6082-T6

The analysis on the mesh size on the central witness plate was conducted by modelling the impact experienced during the blast impact as shown in Figure 5.3. A constant fine mesh (15 by 30) was selected for the bearing. It was observed from the impact experiments (using the gas gun) that the bearing did not experience plastic deformation when viewed with the naked eye from impacting the witness plate even when performed at velocities exceeding 500 m/s. Therefore, the bearing is not expected to experience large deformation as a result of the impact alone. Consequently, the meshing of the bearing should be insignificant during the impact compared to the meshing of the witness plate.

An asymmetrical Lagrangian mesh was implemented for the witness plate with a constant geometric ratio of 1.125 in the x direction with the finer mesh being placed on the impact surface. A uniform, structured Lagrangian mesh was used in the y-direction.

The resultant crater from impact at 200 m/s from the mesh sensitivity test is presented in Figure 5.4, in which, n_x and n_y are the number of elements used in the x and y direction.

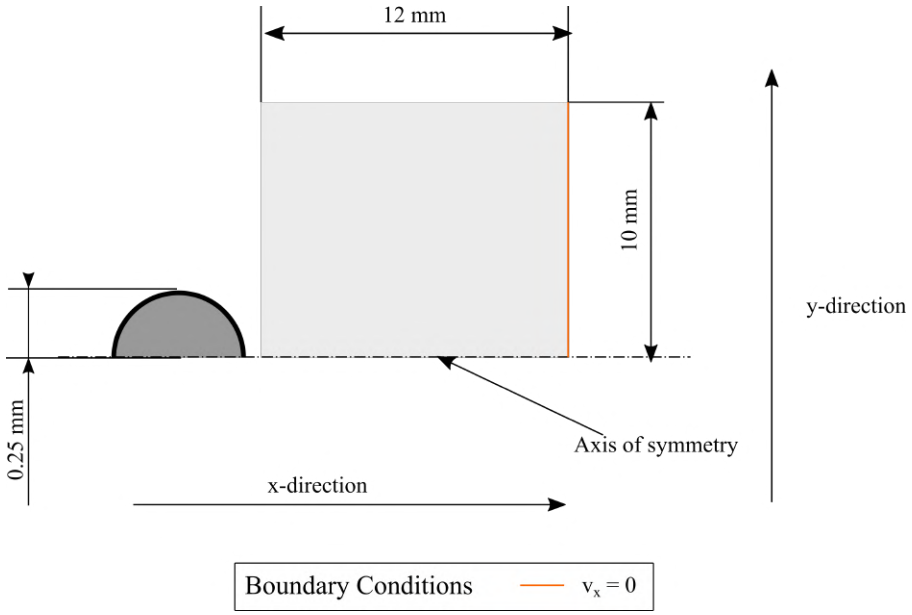

Figure 5.3: Schematic showing the geometry of the mesh-sensitivity set-up.

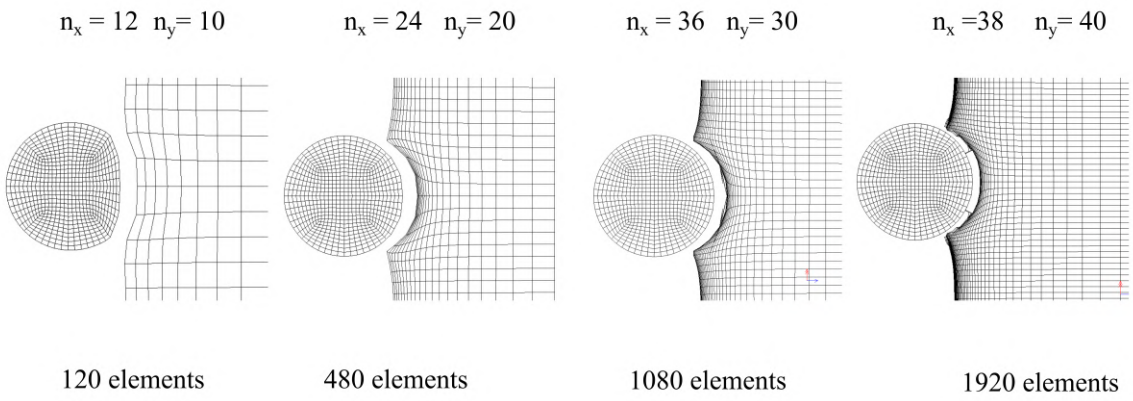

Figure 5.4: Simulated result showing the craters from a 200 m/s impact of different meshing sizes.

The ball bearing was damaged in the mesh containing 120 elements. This was unrealistic and was caused by numerical discretisation error as a result of the coarse mesh. Unlike results from the gas-gun experiment, the result from 480 element experiment produced a rugged crater surface which was also an indication for the mesh being too coarse. There were no obvious visual differences between the results from 1080 elements and 1920 elements. The crater surfaces were smooth and fragmentation were present in both cases. The difference between the meshes can be compared quantitatively by comparing the maximum crater depth as shown in Figure 5.5

In all but the mesh with 1920 elements, crater depth increased consistently with the increase in velocity. The suggests that the 1920 element became inaccurate with the increase in velocity. The crater depths from the 1920 elements (except at 500 m/s) were very close to the mesh containing 1090 elements. Therefore $n_x = 36$ and $n_y = 30$ (1080 elements) were used in the final simulation.

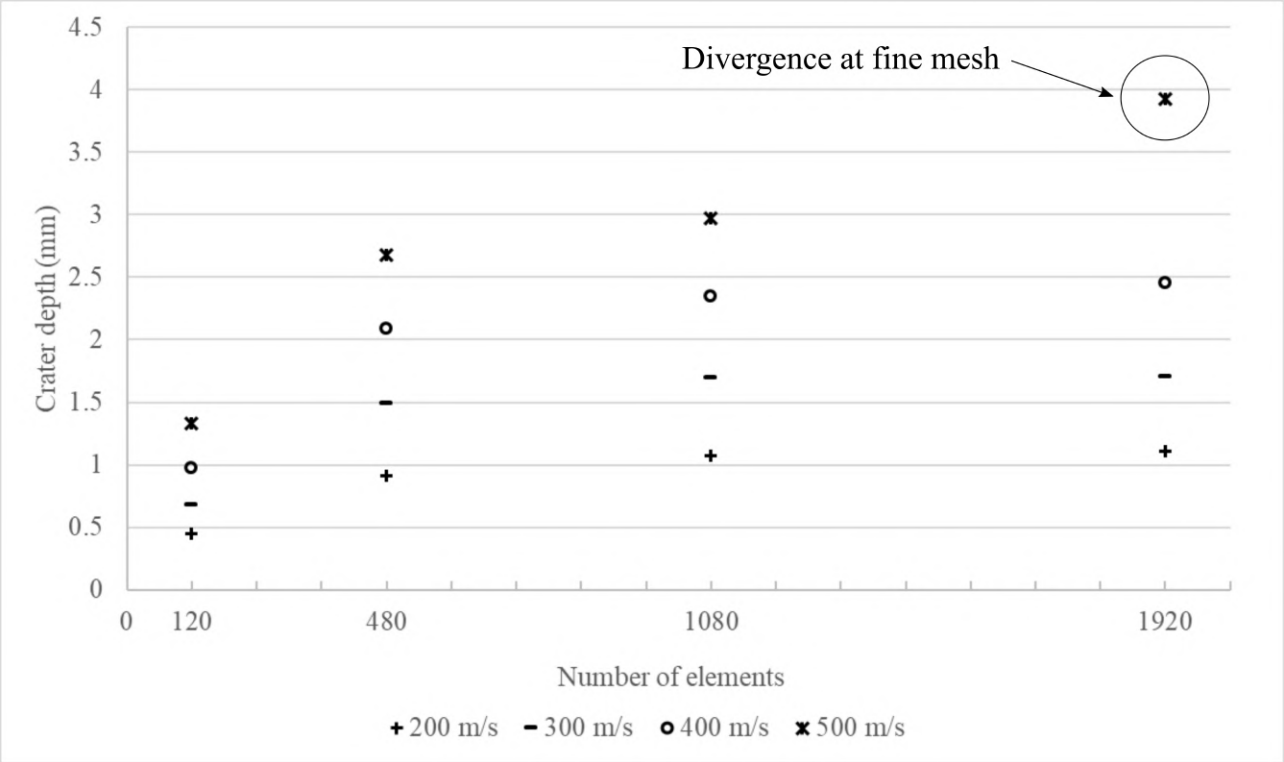

Figure 5.5: Graph showing the simulated results of maximum crater depth versus number of elements for 4 meshes at different impact velocities.

5.4 Formulation of ball bearing

5.4.1 Material model

The ball bearings were made of martensitic stainless steel AISI 420C (X46Cr13). Due to its small size and the strict material tolerance that were already in place for the manufacturing of ball bearings, the ball bearings were not tested. Designing the appropriate apparatus for dynamic testing of a 5 mm sphere was considered to be beyond the scope of this project. Thus, the closest material model available in the Autodyn library was used. Once, again, Johnson-Cook strength model, Shock EOS, Grady's spall failure and erosion control were used. The yield stress at 0.2% strain and ultimate tensile strength of AISI 420C reported by Brnic et al. [93] at room temperature was 657.5 MPa and 781.7 MPa, respectively. The yield stress was 689 MPa in Autodyn material library for STNL.STEEL[86]. The material parameters used for stainless steel is presented in Table 5.3.

Table 5.3: Parameters used in the Shock EOS and Johnson-Cook Strength model for AISI 420C[86].

Material	Material model/ Equation of state	Property	Value
STNL.STEEL	Shock	Density (g/cm^3)	7.86
		Gruneisen coefficient	1.67
		Parameter C1 (m/s)	4610
		Parameter S1	1.73
	Piecewise Johnson Cook	Shear Modulus (kPa)	7.3×10^7
		Yield Stress (kPa)	6.89×10^5
		Eff. Plastic Strain # 1	0.3
		Yield Strength #1 (kPa)	1×10^6
		Strain Rate Constant	4.37×10^{-3}
		Thermal Softening Exponent	1.00
	Grady Spall Failure model	Critical strain value	1.3
	Geometric Erosion	Erosion strain	2
		Type	Instantaneous

5.4.2 Mesh sensitivity of the ball bearing model

A mesh sensitivity test was conducted by modelling the deformation of ball bearing under blast pressure as it would in the final simulation. The peak velocity of the ball bearings with different meshes were compared. The schematic of the mesh sensitivity model used is shown in Figure 5.6.

The simulation proceeded for 0.1 ms and the results of the blast-deformed ball bearings are compared as shown in Figure 5.7, where the positions of detonation are indicated in red.

It can be observed that the shape of the ball bearing does not influence its velocity significantly, even with an extremely coarse mesh. In fact, the difference in velocity between the coarsest and the finest mesh is only 3.2%. However, the coarsest mesh did not result in a smooth geometric shape. Therefore, the 10 by 5 mesh was selected for the final simulation.

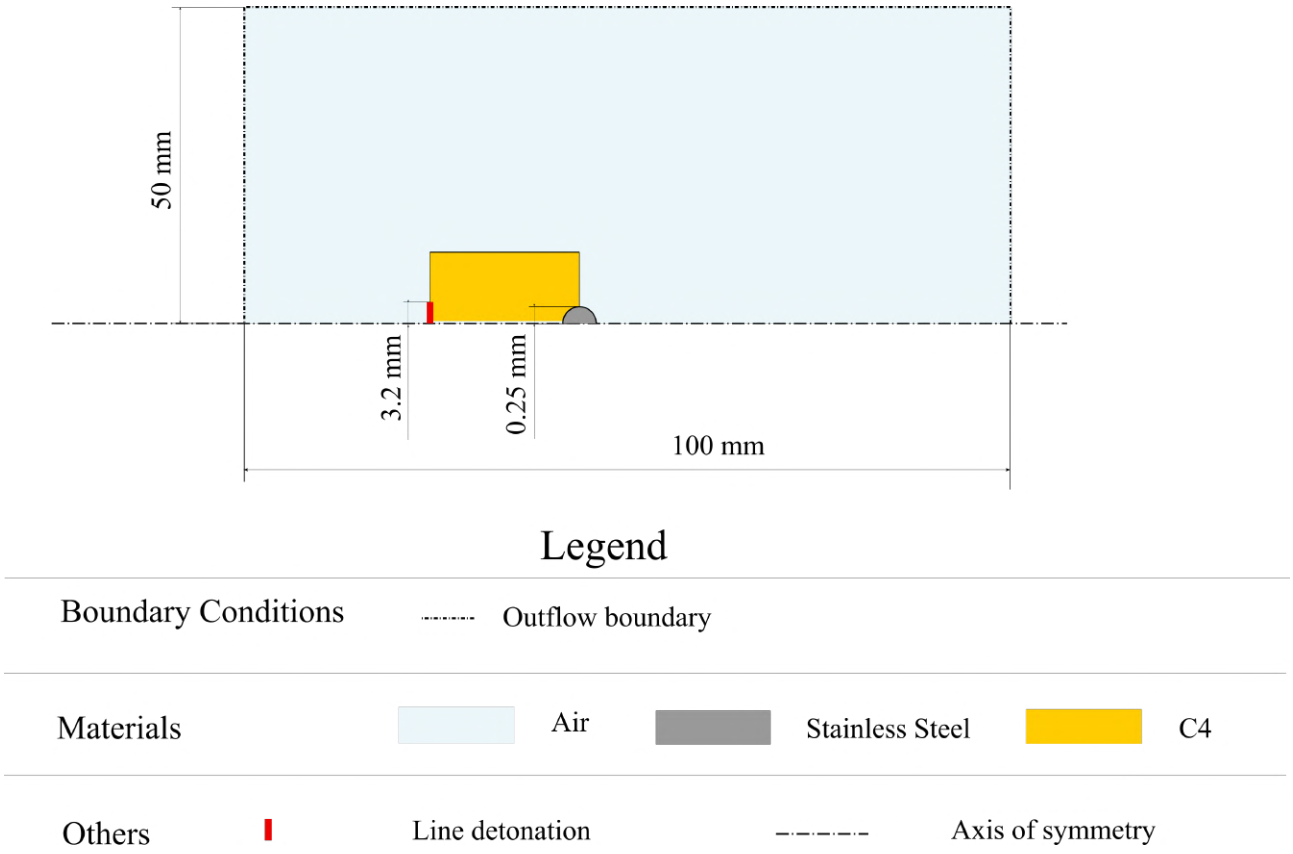

Figure 5.6: Schematic of the simulation set-up used to test the mesh sensitivity of the ball bearing, showing its geometry, boundary conditions and material models used.

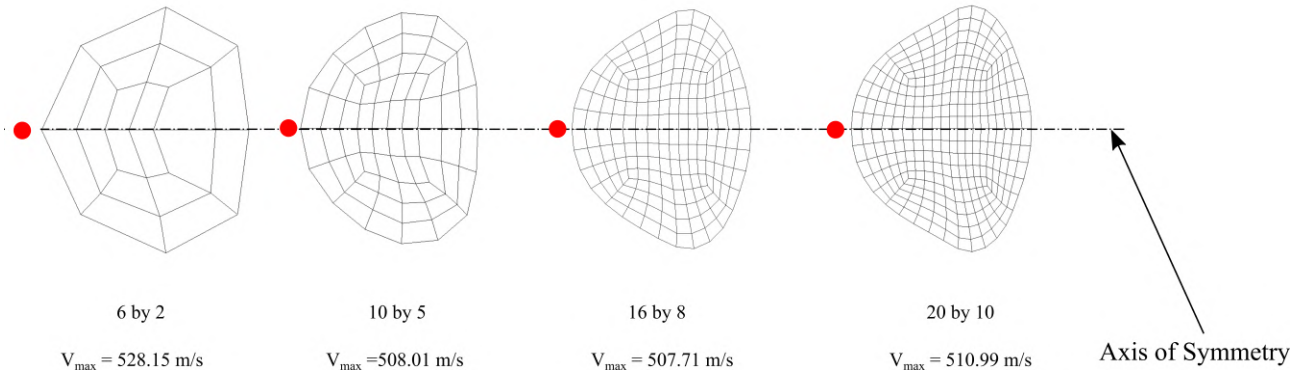

Figure 5.7: Simulation results showing the deformed geometries of the ball bearings as well as the peak velocities achieved for each mesh.

5.5 Impulse calculations

Numerical pressure gauges were placed at every 0.4 mm across the rear face of the blast tube. Let r_i be an array of the increasing position across the axisymmetric model ranging from $r_0 = 0$ to $r_n = R$ where R is the radius of the inner diameter of the blast tube. The total axial impulse I_{total} experienced at the rear face of the blast tube can then be calculated using the trapezoidal rule as:

$$I_{total} = \sum_{r_i=0.4}^{r_i=R} \frac{p(r_i) + p(r_{i-1})}{2} \pi (r_i^2 - r_{i-1}^2)(\Delta t) \tag{5.4}$$

Chapter 6

Experimental results

Experiments were performed following the procedures detailed in Chapter 3. This chapter presents the experimental data captured during the blast experiments. Brief discussions based on the experimental results are provided.

6.1 General observations

In total, 21 blast tests were performed with the inclusion of a ball bearing. A summary of the measured data is presented in Table 6.1. The 'result type' column is an indication on the location of the impact crater on the witness plates. As shown in Figure 6.1, a type 'A' result is where the impact crater was circumscribed by the inner witness plate's diameter; a type 'B' result is where a part of the crater was formed within the inner plate's diameter; a type 'P' result is where the crater was only found on the outer witness plate and a type 'N' result is when the ball bearing did not strike the plate. HPB was able to record the stress waves produced during the crater formation in all type 'A' and 'B' experiments with the exception of experiment 5.87-36-0.1 where the recording did not trigger. From the 21 tests containing ball bearings, 17 tests produced type 'A' (7) or 'B' (10) results, 5 produced a type 'P' result and 1 result was type 'N'.

During a 27g detonation (experiment 27.16-30-0.8) the tube wall and the ball bearing were damaged significantly. A photograph of the deformed tube wall is shown in Figure 6.3. The ball bearing was fragmented, half of which was embedded in the witness plate as shown in Figure 6.2. Therefore, blast experiments were only performed up to 27 g.

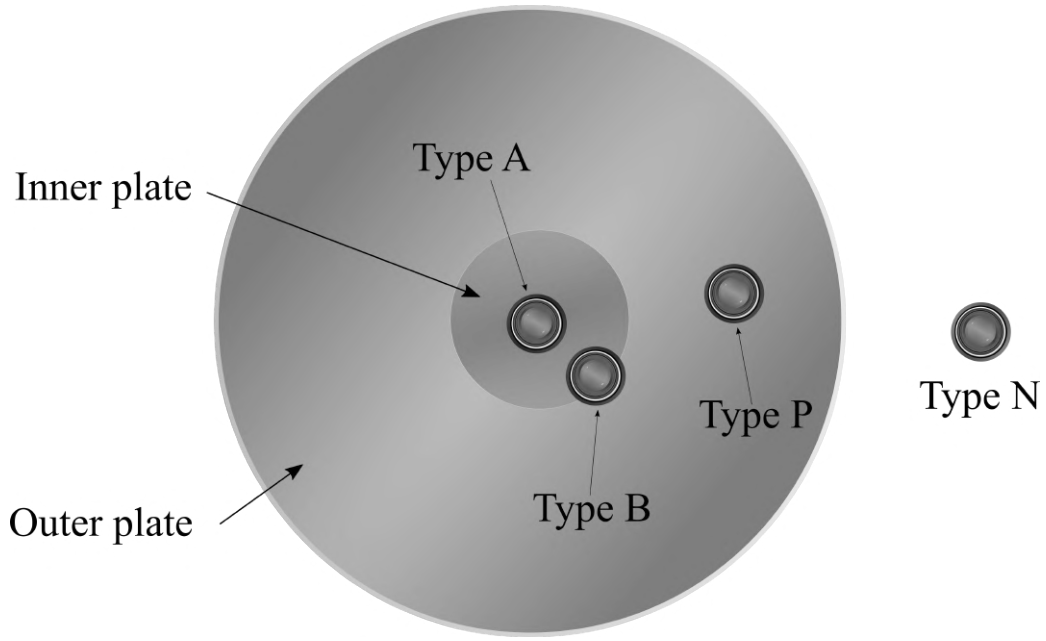

Figure 6.1: Schematic showing the different result types observed from the experiments.

Table 6.1: Summary of results measured from the blast tests.

Test ID	Charge mass (g)	Charge diameter (mm)	Aspect ratio	Charge length (mm)	Result type	Impulse (Ns)	Crater depth (mm)	Deviation[1] (mm)
2.20-0.3-18	2.2	18	0.3	5.4	B	5.5	1.54	10
3.67-0.5-18	3.67	18	0.5	9	A	7.3	2.24	3
4.40-0.6-18	4.4	18	0.6	10.8	P	7.8	2.11	22.5
5.13-0.7-18	5.13	18	0.7	12.6	B	8.7	2.26	10
5.87-0.8-18	5.87	18	0.8	14.4	B	9.4	3.18	9
7.33-1.0-18	7.33	18	1	18	B	10.9	3.47	12
8.07-1.1-18	8.07	18	1.1	19.8	N/A	10.9	n/a	
9.53-1.3-18	9.51	18	1.3	23.4	B	10.7	3.75	9
11.00-1.5-18	11	18	1.5	27	P	14.0	2.5	16
5.21-03-24	5.21	24	0.3	7.2	A	9.8	1.9	4
6.953-04-24	6.95	24	0.4	9.6	B	11.3	2.75	8
10.43-06-24	10.42	24	0.6	14.4	A	16.6	2.94	3
13.91-08-24	13.91	24	0.8	19.2	A	19.2	3.55	7
17.38-1.0-24	17.38	24	1	24	N	24.7		
6.79-02-30	6.79	30	0.2	6	P	13.7	1.68	19
13.58-04-30	13.58	30	0.4	12	B	22.3	2.8	10
20.37-06-30	20.37	30	0.6	18	B	26.4	3.96	10
27.16-0.8-30	27.16	30	0.8	24	A	36.4		7
5.87-0.1-36	5.87	36	0.1	3	P	12.5	1.12	15
11.73-0.2-36	11.73	36	0.2	6	B	22.0	2.13	10
17.60-0.3-36	17.38	36	0.3	9	B	32.2	3.31	11
9.32-01-42	9.32	42	0.1	4.2	A	19.2	1.36	6
18.63-02-42	18.63	42	0.2	8.4	A	34.1	2.28	7

[1]Distance from the centre of the crater to the centre of the witness plates assembly.

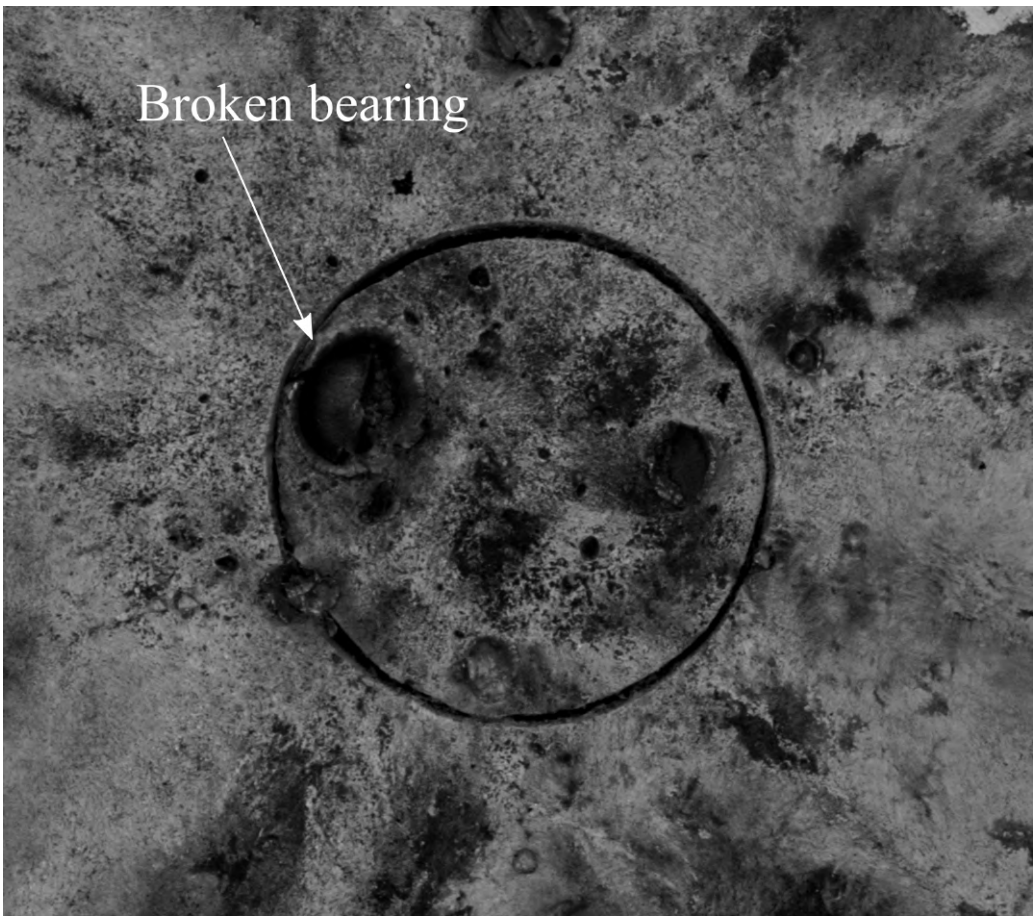

Figure 6.2: Photograph showing the 27g experiment where the fragmented ball bearing is clearly indicated.

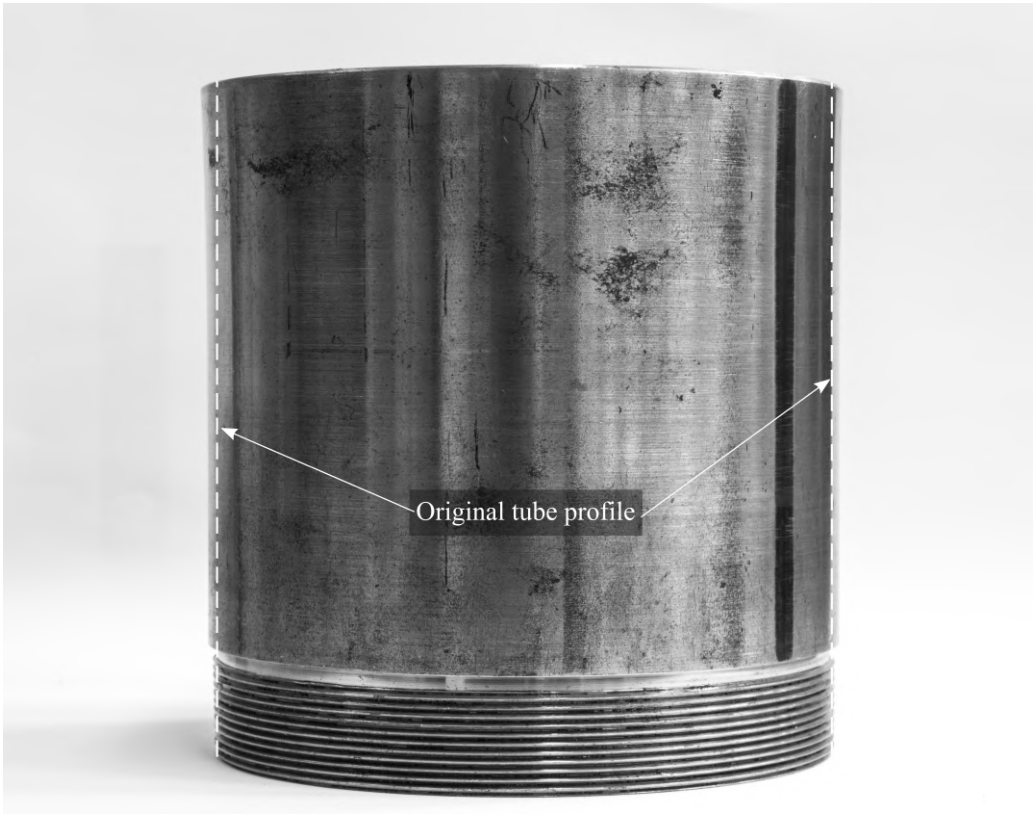

Figure 6.3: A photograph of the blast tube after experiment a 27g detonator (experiment 27.16-30-0.8).

6.1.1 Visual observations

Photographs of the blasted witness plates are presented in Figure 6.4 and 6.5, arranged by the charge mass used (in (f) and (m) only the inner witness plates are shown). Figure 6.4 (a) shows a witness plate subjected to a detonator without additional explosive. In this experiment, the broken shell of the detonator created visible craters scattered across the witness plates. In experiments with the inclusion of ball bearings, the smaller craters could be a combined effect of the detonator shells and the ball bearings. One simple way to differentiate the difference between the source was to study the scattering area. Evenly distributed fragmentation over the entire surface of the witness plate, shown in Figures 6.4 (a) and 6.4 (k), are more likely to be caused by the detonator. Whereas fragmentation that only scattered around impact crater was more likely to be as a result of the ball bearing. Generally, there was a reduction in the evidence of fragmentation on the witness plate as the charge mass increased. This was likely as a result of pressure waves emitted on the rear face of the charge increased in magnitude with charge mass which accelerated the detonator shrapnel away from the witness plates. Thus, only the fragmentation from the ball bearing was visible.

Additionally, the area with burn marks found on the witness plates increased with the increase in charge mass, possibly owning to the increase in the size of the fireball.

Unfortunately, it was not always possible to recover the ball bearings. The photographs of the recovered ball bearings are shown in Figure 6.6 where m_0 and m_a are the ball bearing mass before and after blasting. It can be clearly observed that ball bearings are no longer spherical after the blast experiments. Most of the ball bearings have been damaged but did not experience significant mass loss. Maximum mass loss was observed at 6.8% and the arithmetic mean mass loss 2.8% (using the mean mass of the ball bearing before blasting). The ball bearings are clearly separated across the hemisphere. One half of the ball bearing had surfaces that were shiny while the other half were darkened with visible streamlines. Most of the fragmentation of the ball bearing occurred in the shiny hemisphere immediately above the line of separation. This was possibly due to the different stress conditions at different regions of the ball bearing generated from the blast load.

From the visual observation alone, the shinier hemisphere was more likely to be the blast loaded side. The spalling and deformation were likely to be as a result of the direct contact with the charge as no deformation was observed during the impact experiments. However, simulation results and more in-depth analyses are needed to draw conclusions.

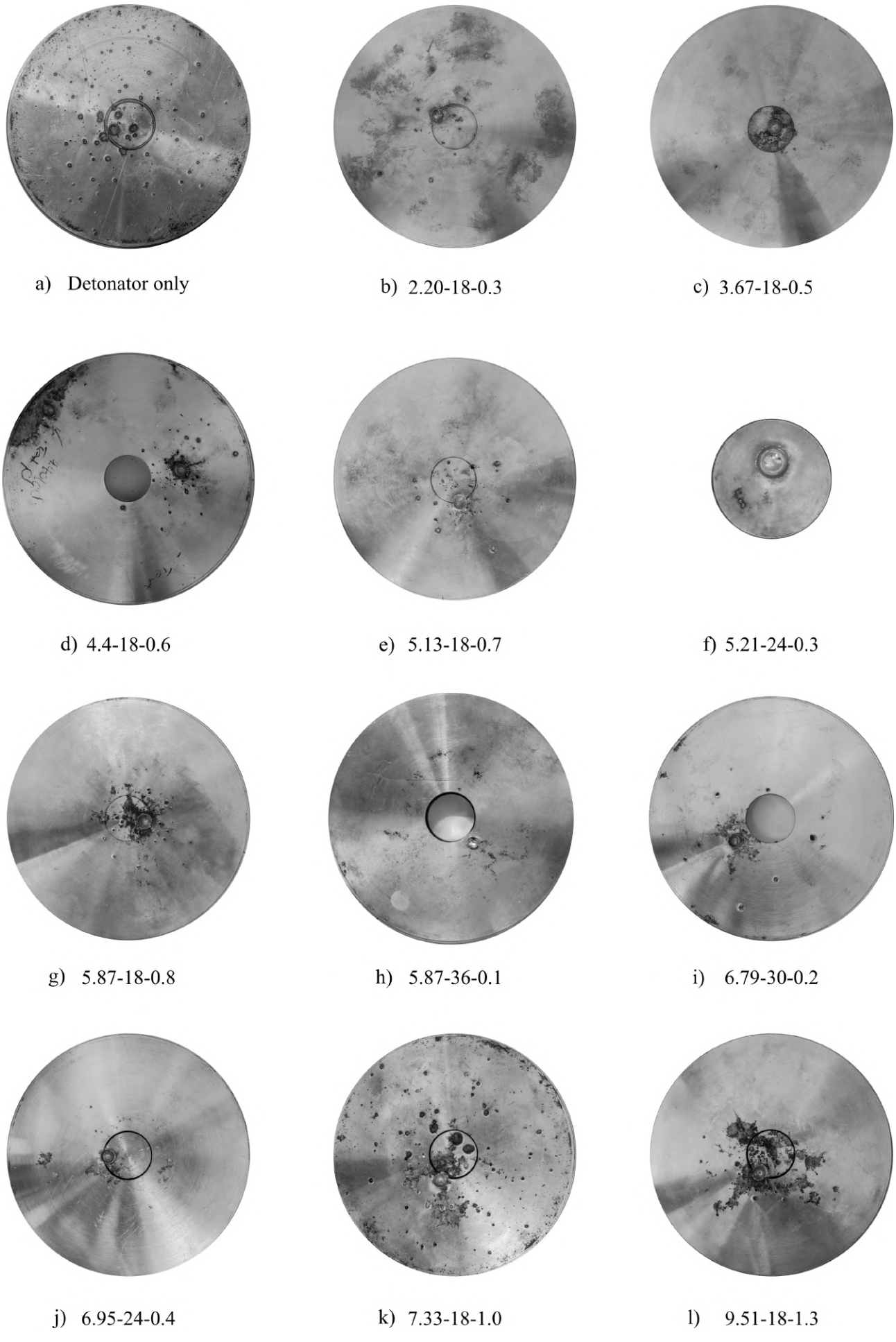

Figure 6.4: A collection of the witness plates used in the experiments, photographed normal to the blast loaded face, arranged according to the charge mass used ($< 10g$).

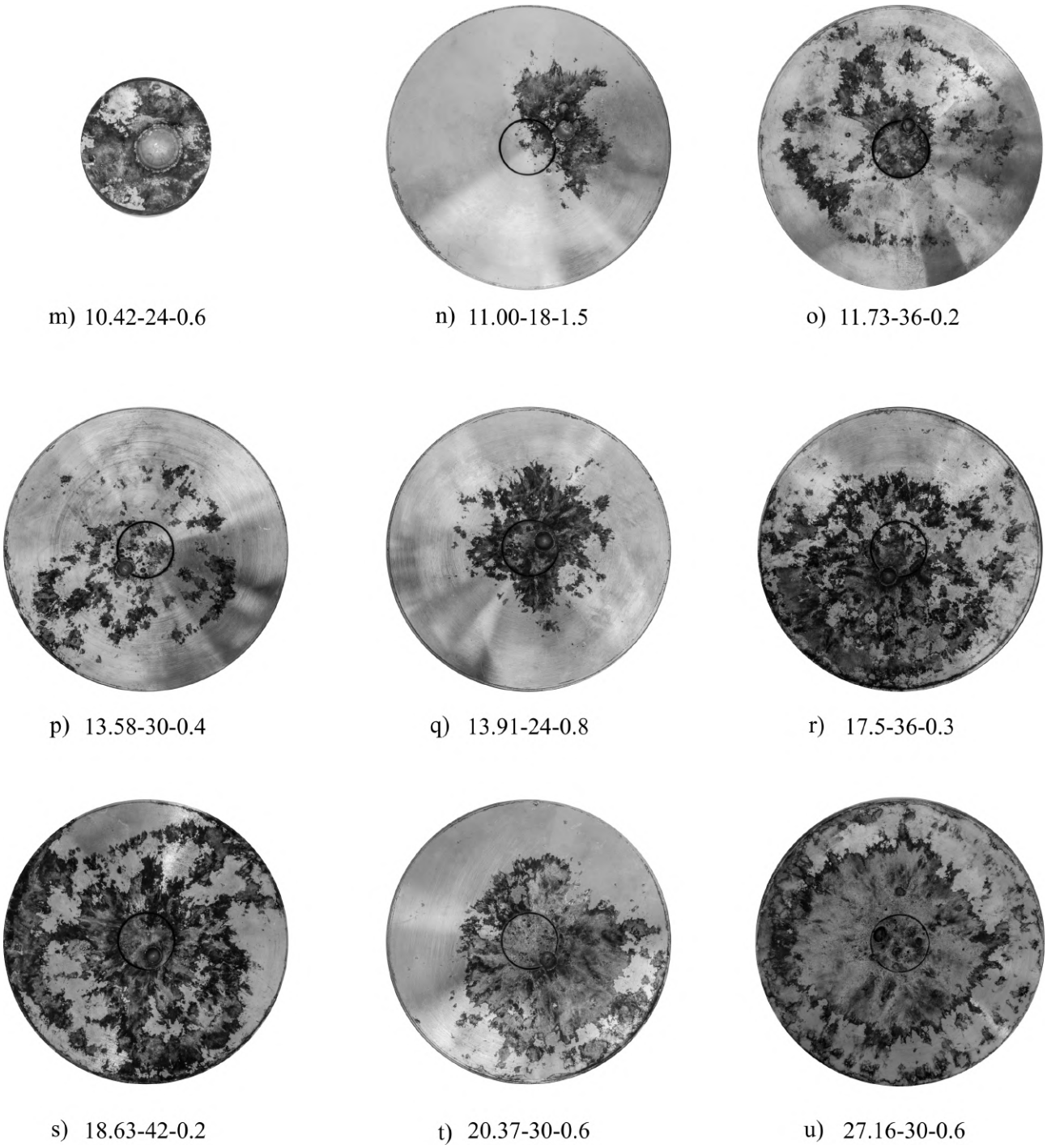

Figure 6.5: A collection of the witness plates used in the experiments, photographed normal to the blast loaded face, arranged according to the charge mass used ($> 10g$).

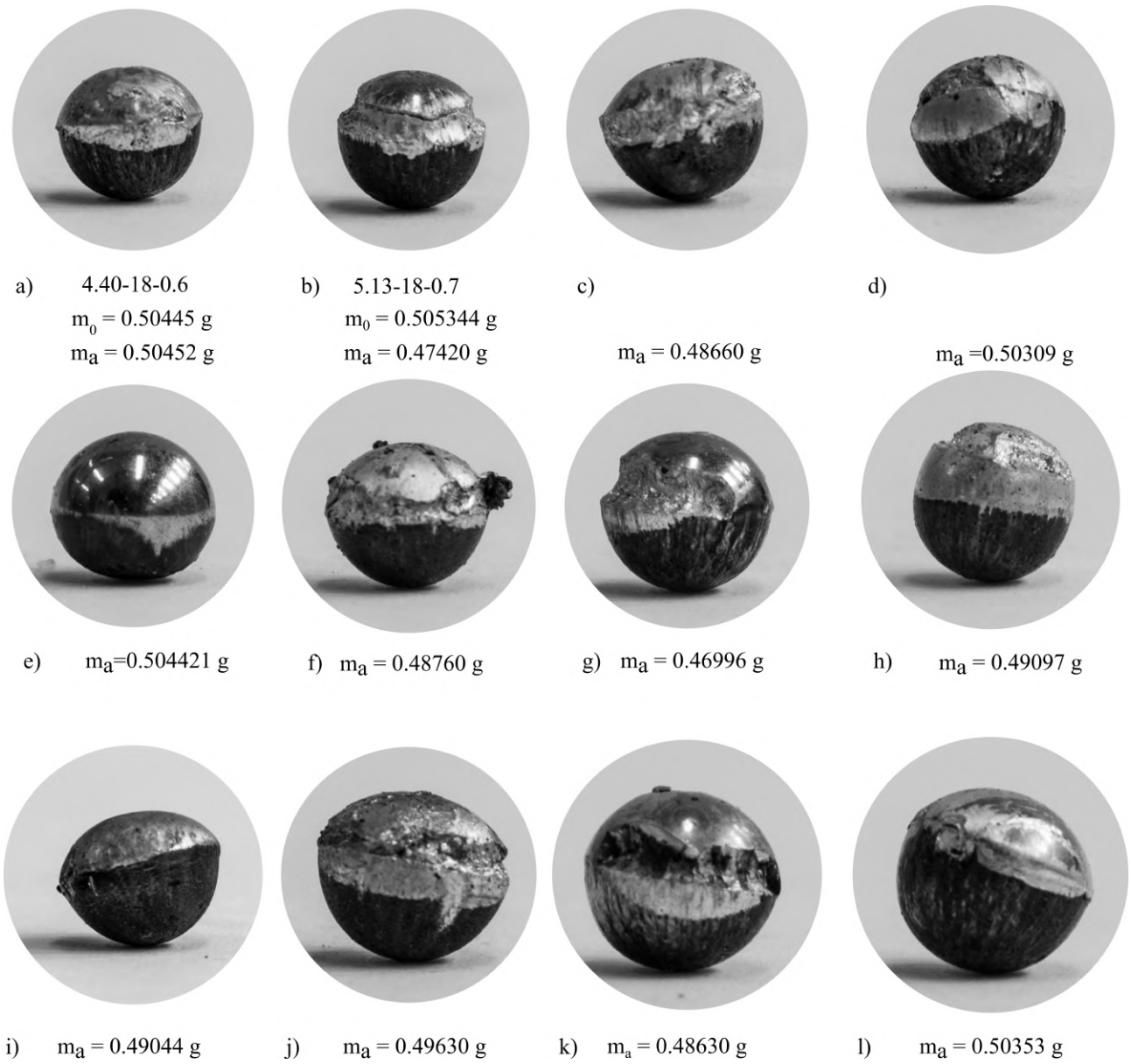

Figure 6.6: A collection of photos showing the blasted ball bearings.

6.1.2 Additional experimental remarks

Some additional observations from the experiments were:

- Ball bearing was not used for experiment 8.07-1.1-18 as it was intended to record the stress signal from the blast event only.
- The data-logging device used to capture the HPB signal of the first five signals appeared to have their built-in signal smoothing software turned on. This resulted in a loss of some EM signals in these experiments.

6.2 Axial impulse results

6.2.1 Impulse from pendulum

A graph of axial impulse versus charge mass is presented in Figure 6.7, grouped by the charge diameter. It was observed that for all charge diameters, impulse increased linearly with the increase in charge mass. The impulse also increased with charge diameter. The graph of impulse versus charge aspect ratio is shown in Figure 6.8 where similar trends are shown. These observation are consistent with results in presented in the Literature Review [11, 15, 49, 50].

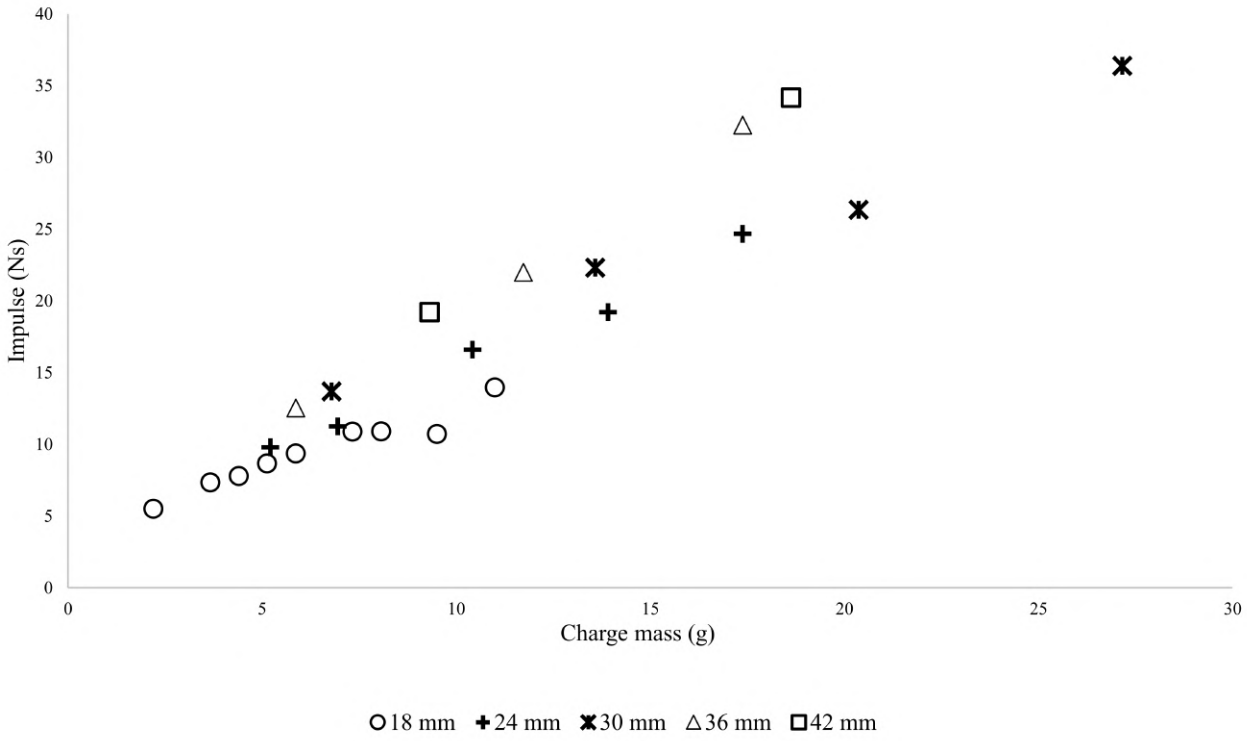

Figure 6.7: Graph showing axial impulse versus charge mass, grouped by charge diameter.

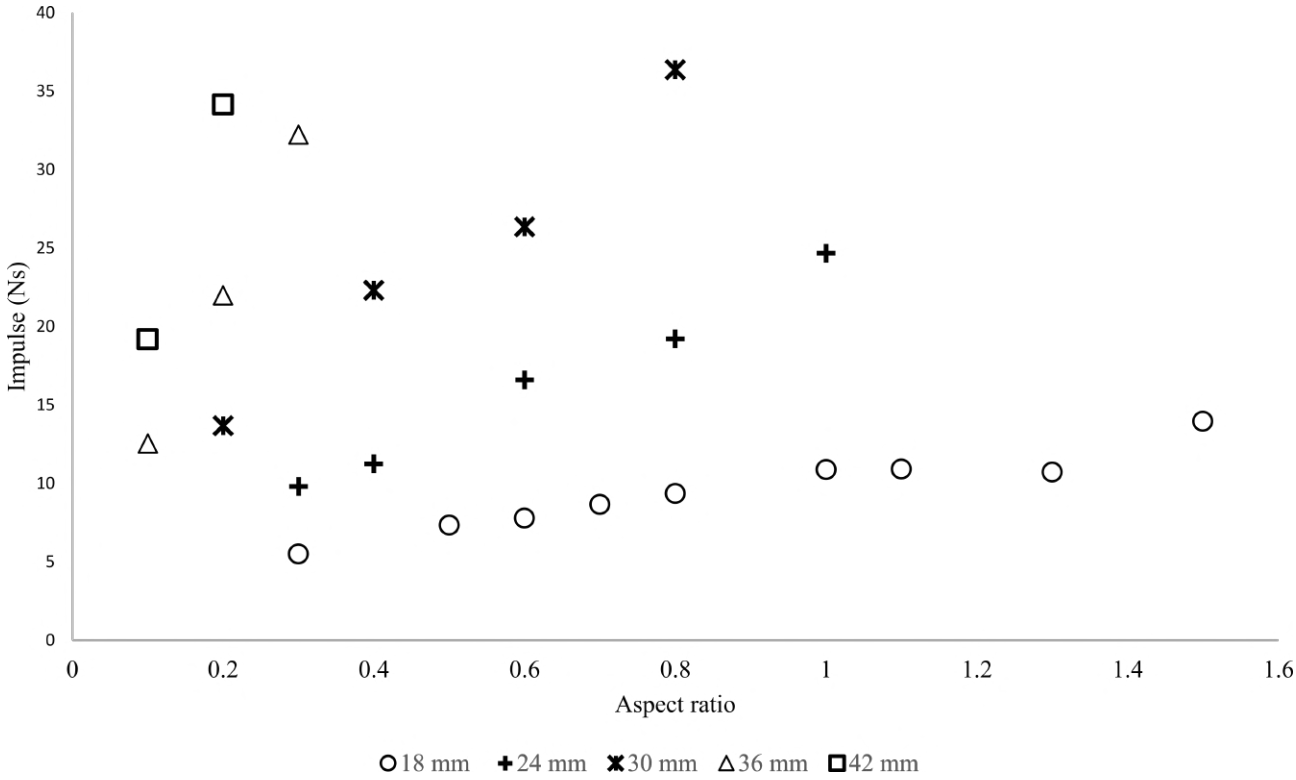

Figure 6.8: Graph showing axial impulse versus charge aspect ratio, grouped by charge diameter.

6.2.2 Impulse from HPB

The axial impulse captured by the HPB is presented in Table 6.2. It was calculated using the method presented in Section 3.5.4. The method removed any voltage peaks from the impact of the ball bearing. Therefore, it assumed that the impulse as a result of gas pressure in the impact duration was negligible.

HPB covered 4% of the total area of the witness plate, but on average, the impulse captured by the bar was 8% of the total impulse. This suggests that the blast pressure experienced at the witness plate is non-uniform which agrees with the observation made by Cloete et al. [27, 28] for this blast tube length.

In general, the HPB impulse increased linearly with the increase in axial impulse as shown in Figure 6.9. The result types ('A','B' and 'P') was an indication of the accuracy of the alignment. Results shown previously on Figure 6.8 and 6.7, which were recorded by the ballistic pendulum, demonstrated the consistency of the impulse results, irrespective of the result type. Unsurprisingly, impulse captured by HPB is more sensitive to the alignment due to the non-uniformly distributed blast load. As shown in Figure 6.9 the linear trend line for result type 'A' and 'B' produced relatively consistent (both are around 9%) but result 'P' yielded smaller impulse (at 6% of pendulum impulse). Therefore, the HPB impulse results for type P were not used in the discussions.

Table 6.2: Table showing the impulse captured by the central Hopkinson bar.

Test ID	Pendulum impulse (Ns)	HPB impulse (Ns)	Bar/pendulum	Result type
2.20-18-0.3	5.5	0.47	8.6%	B
3.67-18-0.5	7.3	0.63	8.6%	A
5.13-18-0.7	7.8	0.71	9.1%	B
5.87-18-0.8	9.4	0.77	8.2%	B
7.33-18-1.0	10.9	0.82	7.5%	B
9.53-18-1.3	10.7	0.91	8.5%	B
11-18-1.5	14	0.80	5.7%	P
5.21-24-0.3	9.8	0.62	6.3%	A
6.95-24-0.4	11.3	0.78	6.9%	B
10.43-24-0.6	16.6	1.36	8.2%	A
13.91-24-0.8	19.2	2.17	11.3%	A
17.38-24-1.0	24.7	1.50	6.1%	P
6.79-30-0.2	13.7	0.69	5.1%	P
13.58-30-0.4	22.3	2.19	9.8%	B
27.16-30-0.8	36.4	3.46	9.5%	A
5.87-36-0.1	12.5	0.65	5.2%	P
11.73-36-0.2	22	2.38	10.8%	B
17.6-36-0.3	32.2	1.60	5.0%	P
9.32-42-0.1	19.2	2.21	11.5%	A
18.63-42-0.2	34.1	2.56	7.5%	A

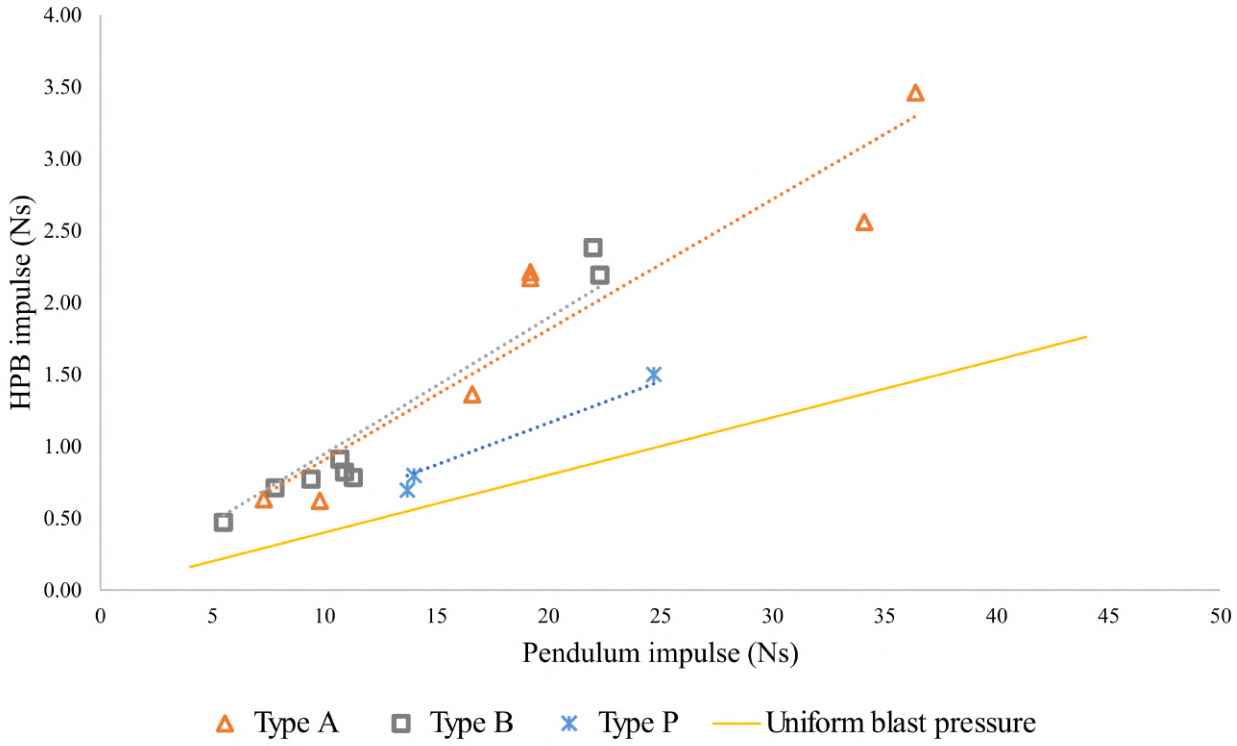

Figure 6.9: Graph showing the impulse captured from the HPB versus the impulse captured from the motion of the instrumented ballistic pendulum.

6.3 Average velocity results

6.3.1 Critical times during detonation

The critical detonation times, t_1, t_2, t_3, t_4, t_5 and the times of impact of the ball bearings for type A and B results are reported in Table 6.3 using methods described in Section 3.5.5. The voltage history for all critical detonation times are shown in Appendix A. Detonation time t_3 was hypothesised to be caused by a burst of electrical energy in the delay circuit which then produced an EM signal. In the method described in Section 3.5.5, the detonation time was taken as the peak voltage in this EM signal as it was easy to identify and to define. Theoretically, the first instance of voltage rise is a more accurate time to use as the detonation time. Therefore, the first rise time of t_{3a} was also reported.

The physical break-wire used in the blast tests were set to pre-record 200 μs before the trigger. Therefore experimentally determined trigger time for all tests was at $200\mu s$. As shown in Figure 6.10, apart from the two outliers, the theoretically determined detonation times, t_3 and $t3a$, are consistently scattered around the experimentally captured detonation time. Figure 6.10 demonstrated three classifications for the detonation time errors: early trigger, consistent with experimental result and late trigger. The theoretically determined detonation time was regarded as consistent with experimental time if $|200 - t_3| < 5$.

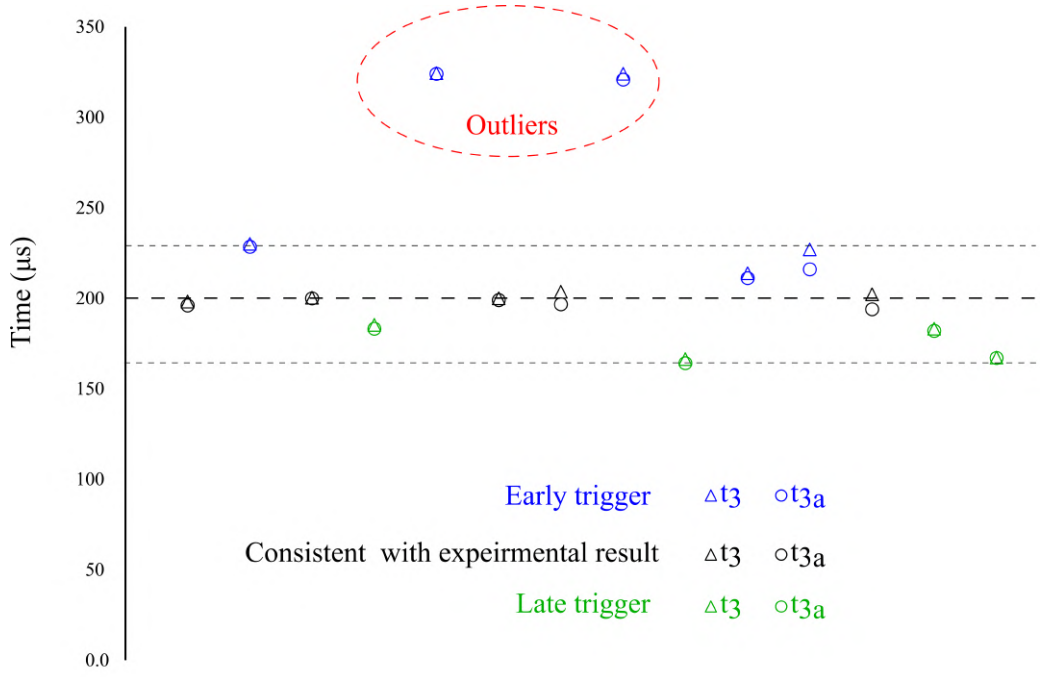

Figure 6.10: Graph showing the theoretically and experimentally determined detonation times.

One possible explanation for the occurrence of an early trigger was due to the presence of strong EM interference. Experiments with early triggers are shown in Figure 6.11 (a-e). The first of which was recorded with a data logging device which smoothed out some EM signals. An EM spike with large magnitude can be found at 200 μs in all other early triggered experiments. These EM spikes are extremely short in duration and high in magnitude. All of which was emitted between t_2 and t_3 which according to the theoretical methods, are EM signals emitted by the resistors in the delay circuit.

Experiment shown in Figure 6.12 were classified as late triggers. Among these experiments, Figure 6.12 (d) did not record any EM spike at 200 μs, thus the trigger was likely to have been caused by the breaking of the foil some time after the detonation. It is impossible for this event to have occurred at denotation since it would have resulted in a negative blast arrival time. The rest of the three late triggered experiments also yielded a negative blast arrival time or extremely unrealistic detonation velocity. Therefore, it can be concluded that the physical triggers did not perform correctly for these experiments. Interestingly, experiment Figure 6.12 (a), (b) and (c) all triggered on an EM spike. This suggests that the EM interference triggered the break-wire before the destruction of the foil.

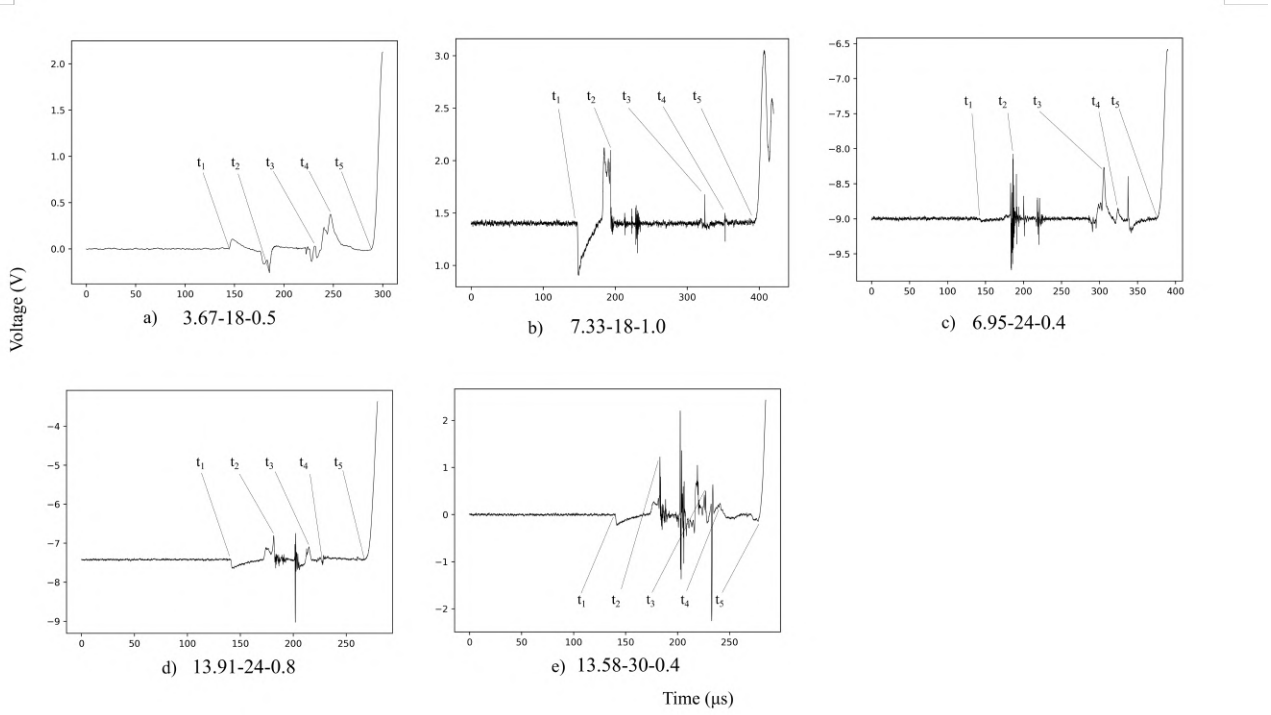

Figure 6.11: Voltage history showing experiments with 'early triggers'.

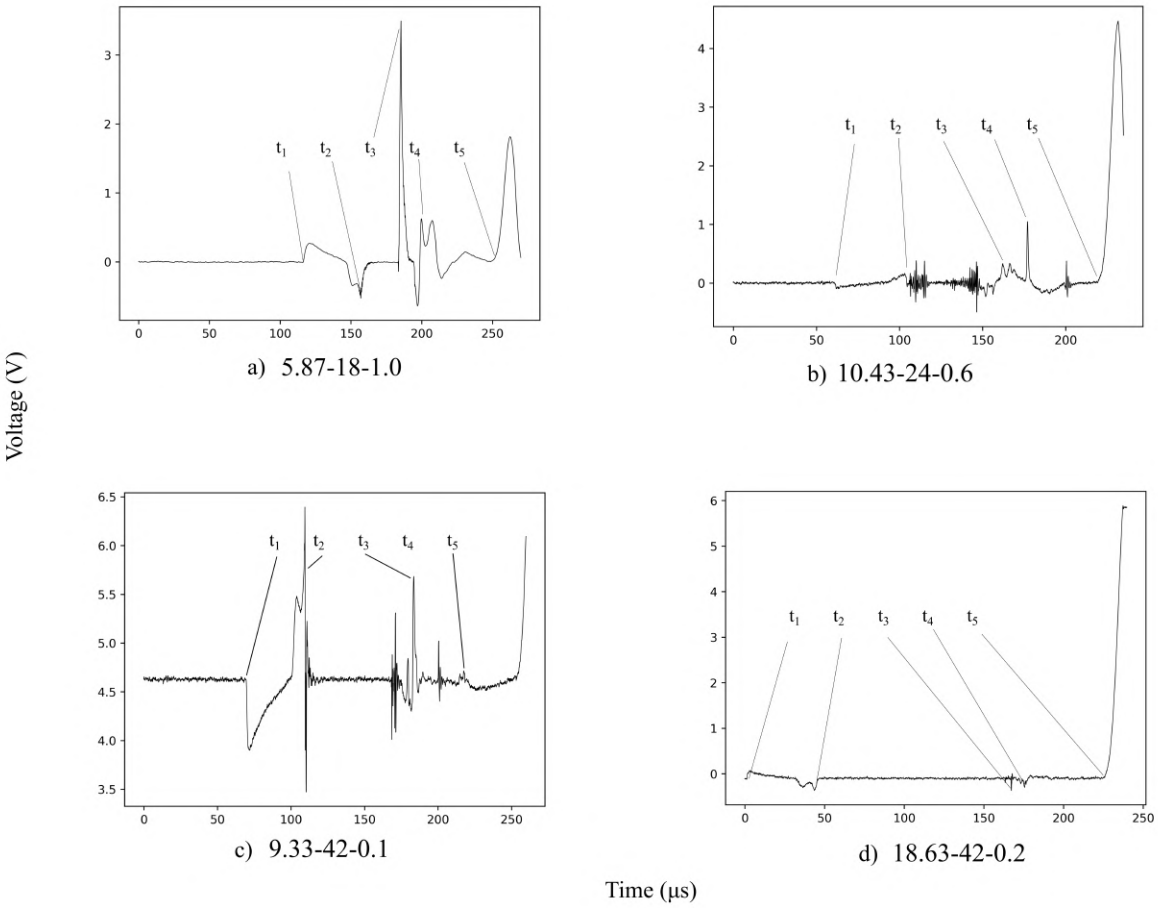

Figure 6.12: Voltage history showing experiments with 'late triggers'.

Table 6.3: Table showing detonation times for result type 'A' and 'B'.

Test ID	t_1 (μs)	t_2 (μs)	t_3 (μs)	t_{3a} (μs)	t_4 (μs)	t_5 (μs)	t_{impact} (μs)
2.20-18-0.3	131.2	172.5	198.2	196.1	207.0	259.4	513.3
3.67-18-0.5	143.2	185.3	230.0	228.5	247.2	288.0	484.0
5.13-18-0.7	143.1	183.5	200.3	200.0	228.7	264.2	449.6
5.87-18-0.8	116.1	156.9	185.2	183.2	207.9	250.0	420.6
7.33-18-1.0	147.6	193.3	324.3	324.0	350.9	394.1	583.2
9.53-18-1.3	125.7	167.5	200.0	199.0	218.0	254.5	402.7
5.21-24-0.3	104.1	147.2	203.5	196.7	215.5	269.1	489.5
6.95-24-0.4	141.3	185.7	305.0	320.9	324.3	376.1	553.9
10.43-24-0.6	60.7	103.4	163.0	160.2	177.0	218.8	373.7
13.91-24-0.8	141.2	181.7	213.8	209.8	226.1	268.2	416.2
13.58-30-0.4	139.7	182.6	227.0	216.0	229.4	277.5	446.7
11.73-36-0.2	127.3	167.9	202.2	193.9	213.6	254.4	478.1
9.32-42-0.1	70.6	109.4	183.2	182.0	214.1	253.1	553.9
18.63-42-0.2	1.0	43.6	167.2	167.0	171.6	225.4	444.4

6.3.2 Interpretation of detonation times

The average ball bearing velocity and other relevant results are presented in Table 6.4. The arrival time of the first blast pressure was calculated as $t_5 - t_3 - c/x_{gauge}$. Where c is the speed of sound in the HPB which was experimentally measured as 5060.8 m/s, and x_{gauge} is the distance of the strain gauge from the blasted loaded face. Note that this distance included the thickness of the inner witness plate and the HPB section. The speed of sound for the bar was also used for the witness plate. Given that the thickness of the plate was only 5.7% of the bar section, the slight difference in c between aluminium and steel was assumed to be negligible.

The time of flight (t_{flight}) for the ball bearing was calculated as:

$$t_{flight} = \frac{t_{impact} - t_3 - c}{x_{gauge}} - \frac{D_c}{L_c} \tag{6.1}$$

Where D_c and L_c are the detonation velocity and the length of the charge. And the distance of flight was $\sqrt{100^2 + deviation^2}$. As shown in Table 6.4, the maximum distance was only 0.7% greater than the designed 100 mm SOD.

'Percentage uncertainty' is a measurement of uncertainty caused by the selection voltage peak time instead of voltage peak initiation time. It was calculated as:

$$Uncertainty = \frac{t_{3a} - t_3}{t_{flight}} \tag{6.2}$$

It can be observed that in comparison to the time of flight which had a mean of time of 210 μs, the slight difference between t_{3a} and t_3 was less significant.

The capacitor discharge time was calculated as t_1 - t_2. As expected, the discharge time was relatively consistent with a standard deviation of 1.8 μs, which was 4% of the mean discharge time.

Table 6.4: Table showing the average velocity of the ball bearing and other relevant information for result types 'A' and 'B'.

Test ID	Blast arrival time (μs)	Time of flight (μs)	Distance of flight (mm)	Velocity (m/s)	Percentage uncertainty %	capacitor Discharge time (μs)
2.20-18-0.3	17.3	270.6	100.5	371.4	-0.8	41.3
3.67-18-0.5	14.1	209.0	100.0	478.6	-0.7	42.1
5.13-18-0.7	20.0	203.9	100.5	492.9	-0.1	40.4
5.87-18-0.8	20.9	189.7	100.4	529.2	-1.1	40.8
7.33-18-1.0	25.9	212.8	100.7	473.2	-0.1	45.7
9.53-18-1.3	10.6	156.0	100.4	643.6	-0.6	41.8
5.21-24-0.3	21.7	241.2	100.1	414.9	-2.8	43.1
6.95-24-0.4	8.2	184.9	100.3	492.1	-1.0	44.4
10.43-24-0.6	8.5	161.7	100.0	606.1	-1.7	42.7
13.91-24-0.8	10.5	155.9	100.2	643.0	-2.6	40.5
13.58-30-0.4	6.6	174.4	100.5	576.4	-6.3	42.9
11.73-36-0.2	8.3	231.2	100.5	434.8	-3.6	40.6
9.32-42-0.1	26.0	326.3	100.2	307.0	-0.4	38.8
18.63-42-0.2	14.3	232.3	100.2	431.5	-0.1	42.6

6.3.3 Average velocity observations

The plot of average velocity versus charge mass is shown in Figure 6.13. The velocity decreased with the increase in charge diameter. The velocity also increased non-linearly at constant charge diameters as shown in ⌀18 mm and ⌀24 mm charges.

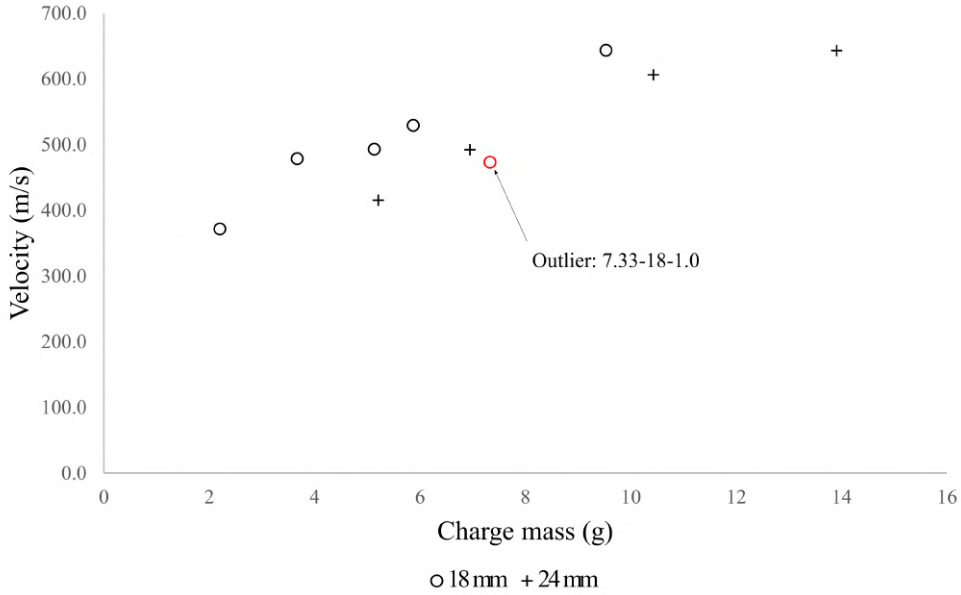

Figure 6.13: Graph of average velocity inferred from HPB data, grouped by charge diameter.

6.4 Impact velocity

6.4.1 Velocity from crater depth correlation

The empirically obtained impact velocity (v) and crated depth(t) relationship was derived in Chapter 3 as:

$$v(t) = -4.833t^2 + 164t + 66.798$$

This equation was used to infer impact velocity using the crater depths measured from the blast experiments. The inferred velocity is presented in Table 6.5 and is visually illustrated in Figure 6.14. Similar to the average velocity results, the impact velocity decreased with the increase in charge diameter for ⌀18 mm and ⌀24 mm charges. However for ⌀30, ⌀36, and ⌀42 mm charges, the impact velocities appeared to have not been affected by the charge diameter. For all charge diameters, a non-linear increase can be observed with the increase in charge mass which is proportional to an increase to charge aspect ratio at constant diameters.

Table 6.5: Table showing the inferred impact velocity of the blast tests using the velocity-crater depth data from the gas gun experiments.

Test ID	Charge diameter (mm)	Inferred impact velocity (m/s)
2.20-0.3-18	18	308
3.67-0.5-18	18	410
4.40-0.6-18	18	392
5.13-0.7-18	18	413
5.87-0.8-18	18	540
7.33-1.0-18	18	578
9.53-1.3-18	18	614
5.21-03-24	24	361
6.953-04-24	24	481
10.43-06-24	24	508
13.91-08-24	24	589
6.79-02-30	30	329
13.58-04-30	30	488
20.37-06-30	30	640
5.87-0.1-36	36	245
11.73-0.2-36	36	394
17.60-0.3-36	36	557
9.32-01-42	42	281
18.63-02-42	42	416

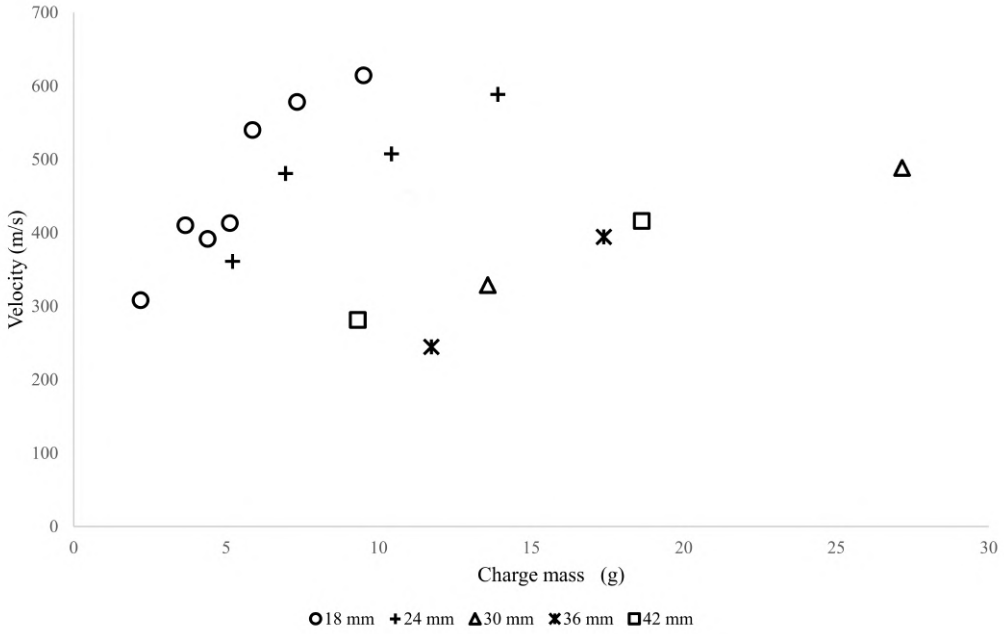

Figure 6.14: Graph showing the impact velocity inferred from crater depth versus charge mass, grouped by charge diameters.

Outliers in the results

The graph of the inferred impact velocity versus charge mass for ⌀18 mm is presented in Figure 6.15. In general, the ⌀18 mm charge results increased with the increase in aspect ratio in a consist, non-linear manner with two exceptions highlighted in red. As shown previously (in Figure 6.4 and Table 6.1), experiment 4.4-18-0.6 produced a crater with a large deviation from the centre, at 22.5 mm. Although the deviation only increased the flight distance of the ball bearing by 2.5 mm, the 13 deg deviation would have experienced a variation in impulse transfer characteristics (type P versus type A and B). Furthermore, the empirically derived velocity and crated depth equation (Equation 3.20) assumed normal (not oblique) impact into its parameters. These two factors account for the lower than expected velocity for the 4.4g detonation. The ball bearing used for experiment 5.13-18-0.7 was found immediately after the blast tests and measured a mass loss of 6.2%. The mass would have resulted in deformation of the ball bearing and further affected the energy transfer.

Expeirment 11-18-1.5 was presented in Table 6.5 was not presented graphically. In this experiment, debris was found at the bottom of the crater which obstructed the measurement of the crater depth. This crater depth experimental data was thus excluded.

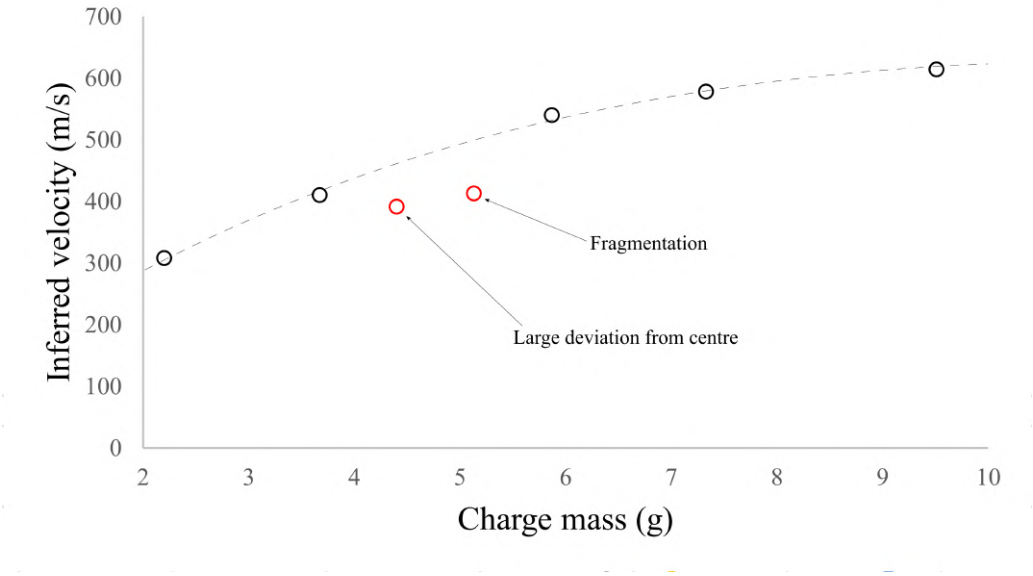

Figure 6.15: Graph showing the inferred impact velocity for ⌀18 mm charges.

6.5 Comparison between average and impact velocity

The comparison between the average and the impact velocity for ⌀18 and 24 charges (where more data points were captured) are shown in Figures 6.16 and 6.17. For both charge diameters, a non-linear curve was fitted over the average velocity, and the crater depth inferred impact velocity data. A similar trend can be observed for the average and impact velocities. The average velocity trend line was of greater magnitude than the impact velocity for both charge diameters with the exception of the 7.33 g detonation. In the 7.33 g experiment, the average velocity was significantly below the trend-line.

In a one dimensional problem as such, the ball bearing velocity profile is dictated by the difference in gas pressure in front and behind the ball bearing. During detonation, the CJ pressure was behind the ball bearing while atmospheric pressure was in front of the ball bearing which caused the ball bearing to accelerate rapidly. Thus a steep velocity increase should be observed. This is then followed by two scenarios: the blast wave can either overtake the ball bearing and reach the witness plate first, and the reflected blast pressure would then reduce the ball bearing velocity before the impact; alternative, the ball bearing accelerated faster than the blast wave at some time after detonation but before reaching the witness plate, causing a continuously increasing velocity history.

The force history from the HPB suggested that the first scenario was more likely to have happened as the overpressure decayed long before the impact event. In the second scenario, the overpressure should have observed after the impact signal. Numerical results are required for more detailed discussions.

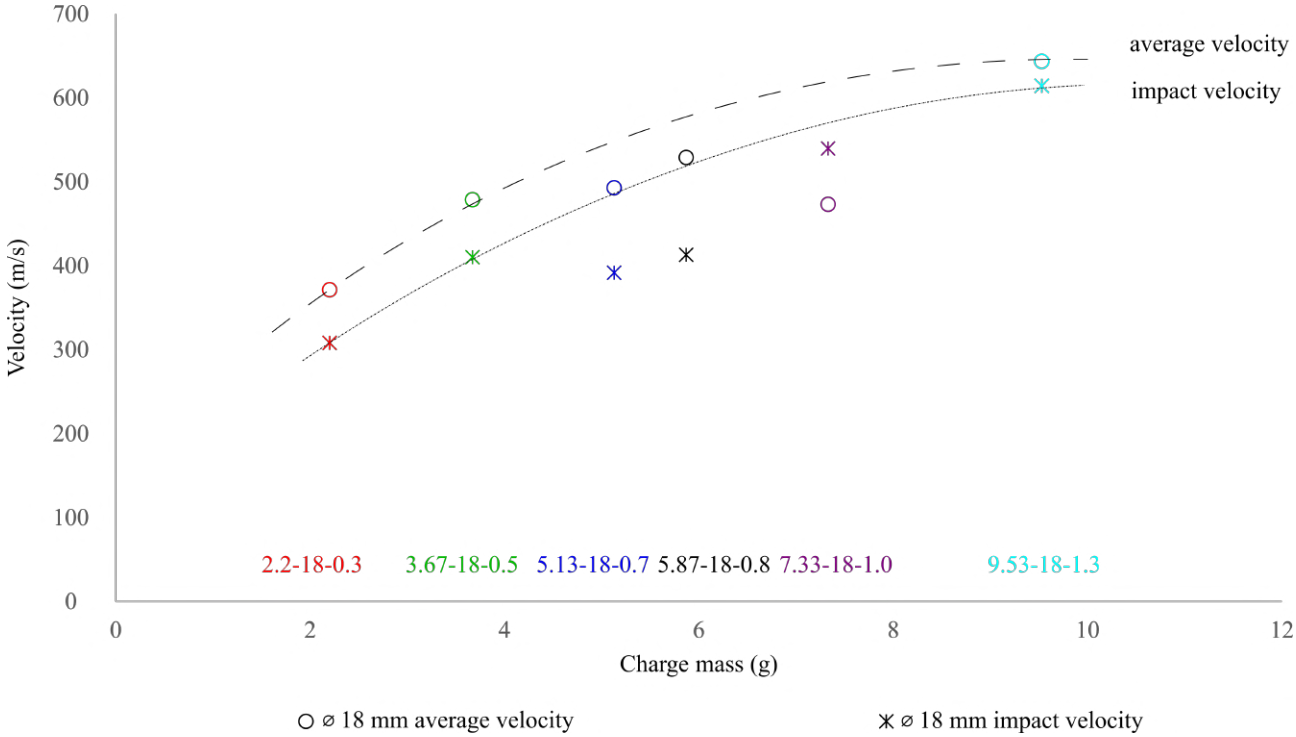

Figure 6.16: Graph showing the comparison between the average and the impact velocity for ⌀18 mm charges.

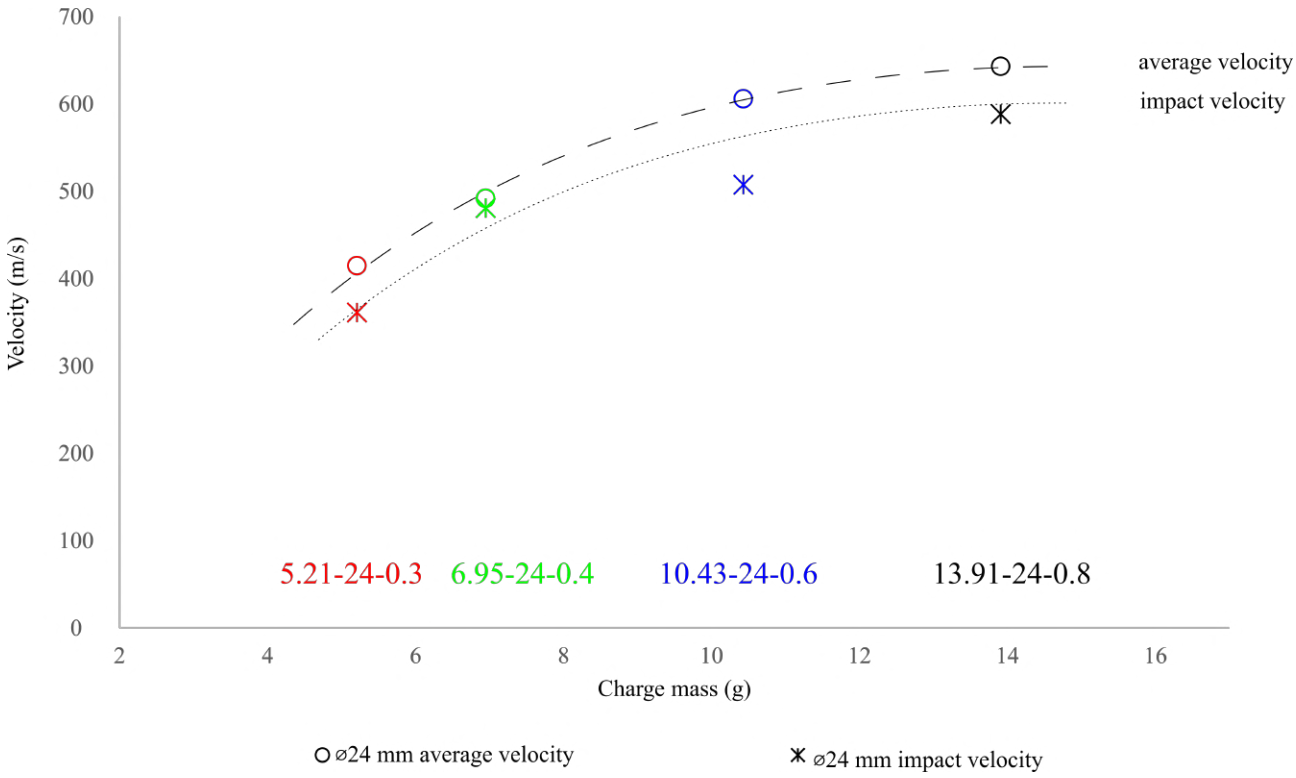

Figure 6.17: Graph showing the comparison between the average and the impact velocity for ø24 mm charges.

6.6 Summary of experimental results

In this chapter, the axial impulse from the pendulum and from the HPB were presented. The pendulum impulse was shown to increase nearly linearly with increase in charge mass at constant diameters. It also increased with the increase in charge diameter. The HPB impulse increased linearly with increasing pendulum impulse. The impulse ratios obtained from the pendulum and HPB suggests that the blast load imparted to the witness plate is non-uniform.

The influence of axial alignment was also presented. It was shown that there was a negligible difference between Type A and Type B results on impulse.

The inferred average and impact velocities were shown in this chapter. The theory used to derive the detonation time was shown to be relatively consistent with the experimental techniques. The difference between them were shown to have limited influence on the average velocities inferred.

The effect of charge geometry on inferred average and impact velocities are consistent. The inferred velocities increased non-linearly with the increase in charge aspect ratio at constant charge diameters. At constant charge mass, the velocities decreased with the increase in charge diameters.

Most of the experimental results produced higher average velocities than impact velocities. This suggested that the ball bearing was slowed down by the reflected blast pressure before impacting the witness plates. However, more insightful observations can be made using the numerical results presented in the next chapter.

Chapter 7

Numerical results and Discussion

This chapter presents the results from the numerical simulations performed using ANSYS Autodyn 18.0. The simulation results are compared with experimental measurements of ball bearing velocity to validate the models. The validated models are then used to further elucidate into the blast behaviour such as the ball bearing velocity profile, the damage mechanism of the ball bearing as well as the blast driving mechanisms.

7.1 Effect of charge geometry on impulse

A total of 48 axisymmetric numerical simulations were performed using ANSYS Autodyn 18.0. The charge properties of the numerical simulations and their corresponding impulse results are presented in Table 7.1.

Table 7.1: Table depicting the charge geometries and their corresponding impulse results from the numerical experiments.

Test ID	Charge mass (g)	Charge diameter (mm)	Aspect Ratio	Pendulum impulse (Ns)	HPB impulse (Ns)
18-0.3-N	2.20	18	0.3	5.56	0.39
18-0.4-N	2.93	18	0.4	6.96	0.48
18-0.5-N	3.67	18	0.5	8.22	0.58
18-0.6-N	4.40	18	0.6	9.33	0.66
18-0.7-N	5.13	18	0.7	9.99	0.71
18-0.8-N	5.87	18	0.8	11.07	0.79
18-0.9-N	6.60	18	0.9	10.55	0.77
18-1-N	7.33	18	1	10.96	0.79
18-1.1-N	8.07	18	1.1	12.59	0.85
18-1.3-N	9.53	18	1.3	13.39	0.90
18-1.5-N	11.00	18	1.5	13.81	0.92
18-2-N	14.67	18	2	14.49	0.94
24-0.3-N	5.21	24	0.3	12.13	0.66
24-0.4-N	6.95	24	0.4	15.22	0.83
24-0.5-N	8.69	24	0.5	17.82	0.97
24-0.6-N	10.43	24	0.6	19.97	1.07
24-0.7-N	12.17	24	0.7	21.57	1.15
24-0.8-N	13.91	24	0.8	22.04	1.20
24-0.9-N	15.64	24	0.9	23.98	1.30
24-1-N	17.38	24	1	24.97	1.35
24-1.1-N	19.12	24	1.1	25.74	1.39
24-1.3-N	22.60	24	1.3	26.79	1.45
24-1.5-N	26.07	24	1.5	27.52	1.51
24-2-N	34.77	24	2	28.55	1.59
30-0.2-N	6.79	30	0.2	16.00	0.83
30-0.3-N	10.19	30	0.3	22.33	1.16
30-0.4-N	13.58	30	0.4	27.00	1.45
30-0.5-N	16.98	30	0.5	31.09	1.69
30-0.6-N	20.37	30	0.6	35.42	1.92
30-0.7-N	23.77	30	0.7	38.31	2.05
30-0.8-N	27.16	30	0.8	39.08	2.11
30-1-N	33.95	30	1	38.63	2.22
30-1.3-N	44.14	30	1.3	45.14	2.66
36-0.2-N	11.73	36	0.2	26.58	1.37
36-0.3-N	17.60	36	0.3	35.56	1.86
36-0.4-N	23.47	36	0.4	41.17	2.24
36-0.5-N	29.33	36	0.5	49.49	2.71
36-0.6-N	35.20	36	0.6	55.59	3.05
36-0.7-N	41.07	36	0.7	60.06	3.35
36-0.8-N	46.93	36	0.8	64.91	3.61
42-0.1-N	9.32	42	0.1	22.19	1.16
42-0.2-N	18.63	42	0.2	39.83	2.01
42-0.3-N	27.95	42	0.3	52.21	2.86
42-0.4-N	37.26	42	0.4	67.17	3.53
42-0.5-N	46.58	42	0.5	74.86	4.06
42-0.6-N	55.90	42	0.6	85.80	4.65
42-0.7-N	65.21	42	0.7	93.21	5.02
42-0.8-N	74.53	42	0.8	98.38	5.31

7.1.1 Total axial impulse

Impulse results

The graph of impulse versus charge mass, grouped by charge diameter, obtained from the simulations is presented in Figure 7.1. Similar to the experimental results, the axial impulse increased with the increase in charge diameter. Unlike the observations made in the experimental results, axial impulse increased non-linearly with the increase in charge mass at constant diameter. This is possibly due to the larger range of aspect ratio (L/D) used in the numerical studies. Generally, axial impulse increased with the increase in charge mass.

The linear impulse-aspect ratio relationship observed experimentally was then only applicable for a limited aspect ratio as shown in Figure 7.2. At a constant charge diameter, the impulse increase non-linearly with the increase aspect ratio. This is particularly more visible at higher charge diameters were experiments were not performed. Charges with similar masses are shown using identical colours in Figure 7.2 to indicate that the increase of impulse with the increase in charge diameter can also be observed when plotted against aspect ratio.

Experimental results from Davids et al.[11] showed that axial impulse resulting from internal blast loading increased linearly with the increase in aspect ratio up to 2.6. As discussed in Section 2.2.3, the charge in David et al.'s work [11] was placed centrally along the length of the tube. The radial pressure emitted from the charge was forced to travel along the inner wall of the blast tube and contributed to the axial motion of the pendulum. In this work, the charges were placed flush with the outside of the blast tube. Therefore, in this arrangement more of the radial blast pressure is expected to escape and not contribute to the axial impulse when compared against work from [11] resulting in a non-linear increase in impulse with the increase in charge aspect ratio.

The effect of charge aspect ratio and diameter on axial impulse therefore agree with work from [15, 49, 50, 51] as discussed in the Literature Review.

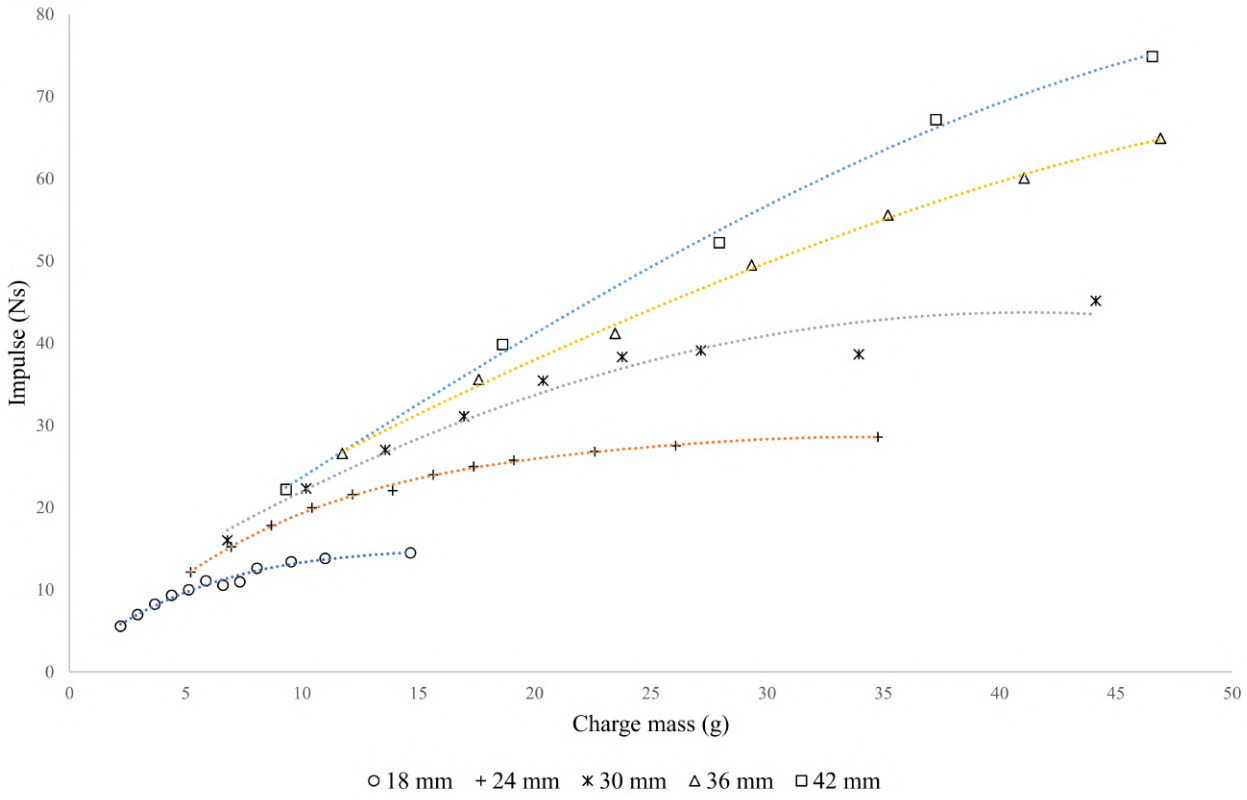

Figure 7.1: Graph of numerical axial impulse results versus charge mass, grouped by charge diameters.

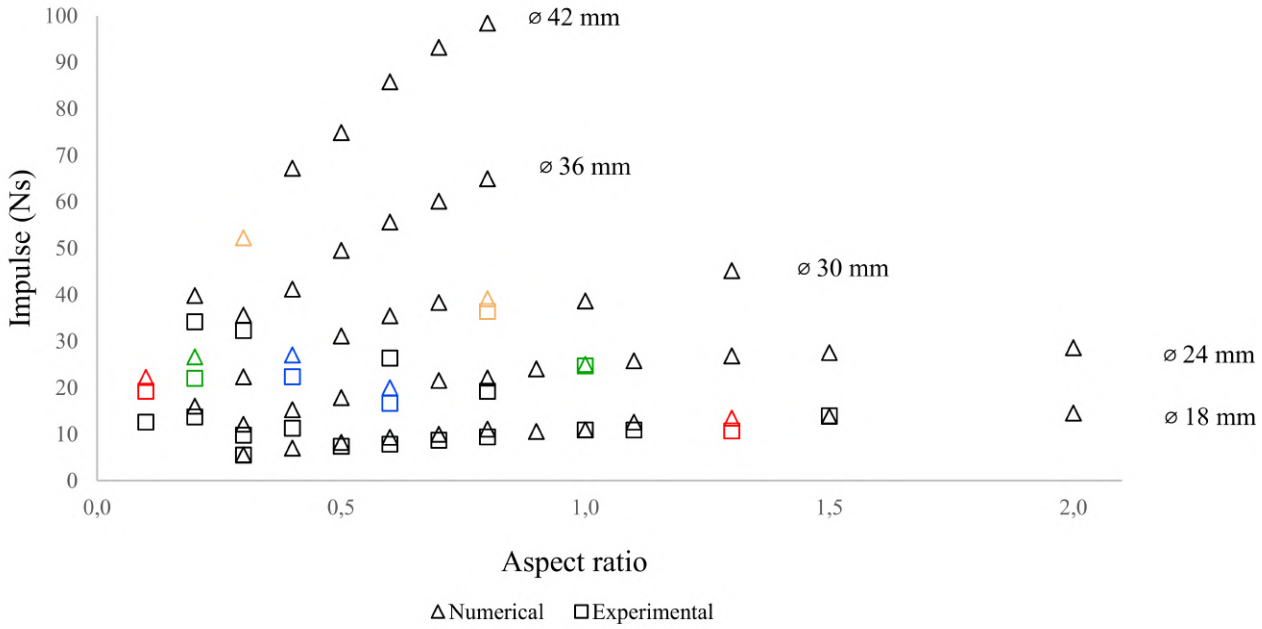

Figure 7.2: Graph showing the axial impulse versus charge aspect ratio where the overlapping region between simulated and experimental results are shown.

7.1.2 Error analysis

The percentage difference ($\%diff$) in impulse between experimental (I_e) and numerical (I_n) results were calculated as:

$$\%diff = \frac{I_n - I_e}{I_e} \tag{7.1}$$

In all but one experiment, the numerical model produced considerably higher impulse. The mean difference was at 15.7% and 95% of the data fit within ± 9.8%. This means although the numerical model yielded higher impulse, the increase was relatively consistent.

The numerically calculated impulse assumed that all the gas pressure at the rear face of the blast tube was converted to axial impulse and that the inner wall of the blast tube was modelled as a reflective boundary. In the experiment, skin friction could reduce the impulse transfer. More importantly, the EOS of PE-4 was not verified experimentally since characterising material parameters for PE-4 was considered beyond the scope of this work.

7.1.3 HPB impulse

The impulse captured by the HPB (I_{e_bar}) was calculated using a similar method as Equation 5.4 over the area of the bar. The graph of HPB impulse versus total axial impulse (I_{e_pen}) for obtained experimentally and numerically is shown in Figure 7.3. A strong linear correlation (correlation coefficient = 0.996) was observed for the numerical results. As expected, experimental results (correlation coefficient = 0.888) were more scattered than the numerical results. Experimental results also recorded considerable higher impulses ratios ($\frac{I_{e_bar}}{I_{e_pen}}$) than what the numerical model suggested. Even when the numerical pendulum impulse(I_{n_pen}) was used as the denominator in both the experimentally and the numerically obtained bar impulses as shown in Figure 7.4, the $\frac{I_{e_bar}}{I_{n_pen}}$ was still greater. So, the physical blast load was likely to be more non-uniformly distributed than what the model suggested.

One possible explanation for the more extreme localised pressure could be due to the presence of Rayleigh-Talyor [94, 95] and Richtmyer-Meshkov [96, 97] instabilities. The instabilities are extremely difficult to capture numerically and are known to be present in physical blast experiments [98]. Furthermore, the instabilities are suggested to be more prominent and caused considerable localisation of pressure and impulse across the target face at the Hopkinson-Cranz scaled distance of Z = 0.37 $m/kg^{1/3}$ [98]. The aspect ratios performed in these experiments overlap with ref [98] with comparable Hopkinson-Cranz scaled distances (0.31 $m/kg^{1/3} < Z < m/kg^{1/3}$) for detonations above 10g.

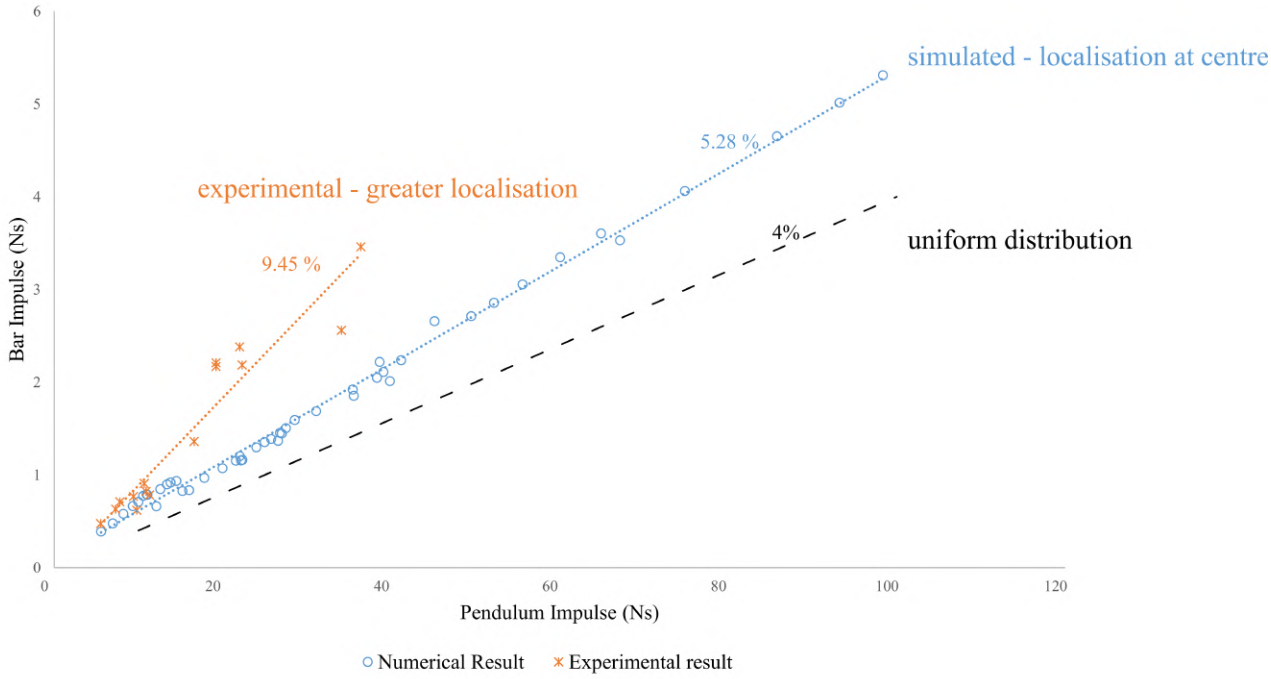

Figure 7.3: Graph showing the experimental (result type A and B) and numerical result of HPB impulse versus axial impulse.

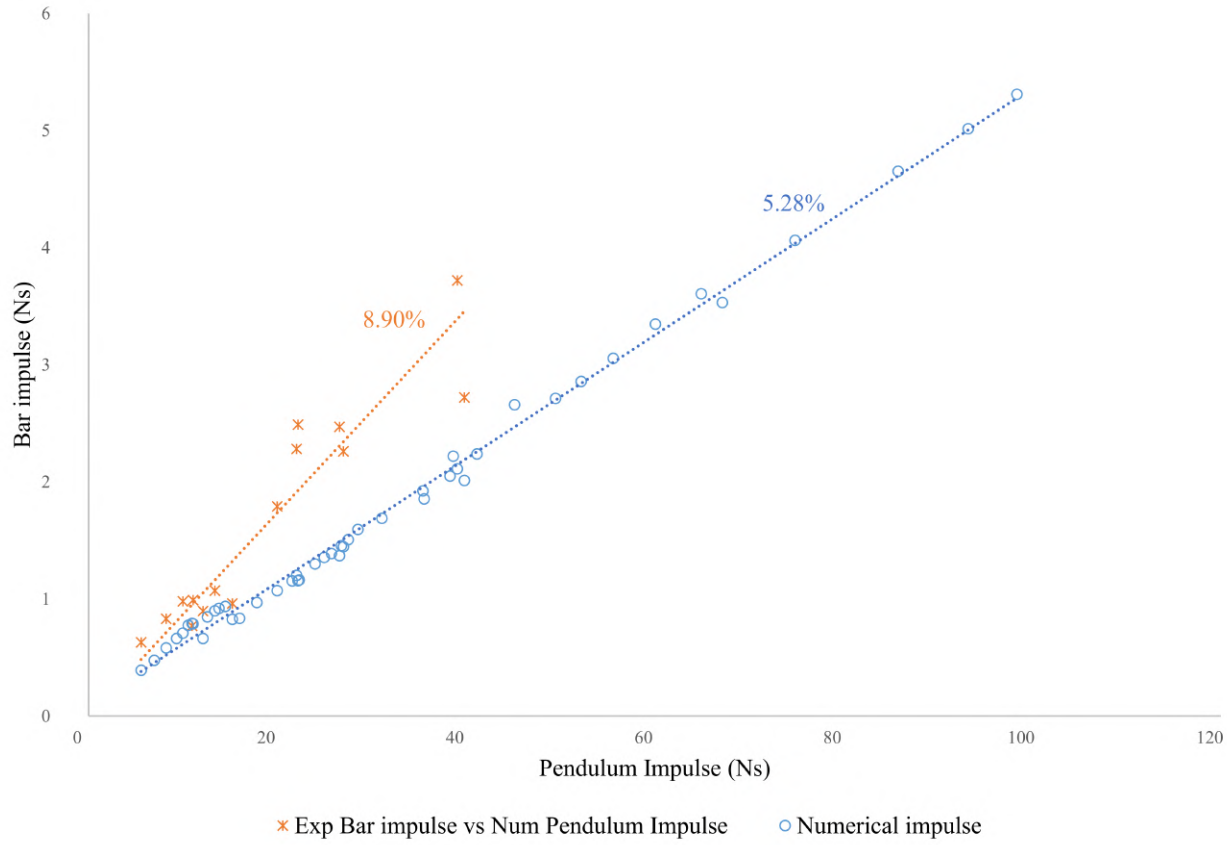

Figure 7.4: Graph showing experimental and numerical HPB impulse versus numerical pendulum impulse.

7.2 Comparison of average ball bearing velocity

The maximum, average and impact velocity of the ball bearing is presented in Table 7.2.

Table 7.2: Table showing the simulated, numerical impact, average and maximum velocities.

Test ID	Charge mass (g)	Maximums Velocity (m/s)	Average Velocity (m/s)	Impact velocity (m/s)	Blast Arrival Time (μs)
18-0.3-N	2.20	328	321	310	21.4
18-0.4-N	2.93	410	394	376	20.6
18-0.5-N	3.67	470	470	432	20.0
18-0.6-N	4.40	515	495	476	19.6
18-0.7-N	5.13	540	520	499	19.4
18-0.8-N	5.87	580	561	537	19.3
18-0.9-N	6.60	604	575	553	19.2
18-1-N	7.33	623	590	561	18.8
18-1.1-N	8.07	638	598	572	18.7
18-1.3-N	9.53	662	625	600	19.2
18-1.5-N	11.00	678	630	606	19.0
18-2-N	14.67	703	656	637	18.8
24-0.3-N	5.21	425	402	384	19.8
24-0.4-N	6.95	515	483	459	19.8
24-0.5-N	8.69	582	540	510	18.5
24-0.6-N	10.43	634	595	554	18.6
24-0.7-N	12.17	676	625	593	18.5
24-0.8-N	13.91	710	655	624	18.4
24-0.9-N	15.64	737	684	646	18.5
24-1-N	17.38	760	699	659	18.6
24-1.1-N	19.12	780	721	680	18.6
24-1.3-N	22.60	812	743	700	18.9
24-1.5-N	26.07	834	748	713	19.6
24-2-N	34.77	868	773	734	20.4
30-0.2-N	6.79	373	351	333	20.3
30-0.3-N	10.19	508	466	435	19.6
30-0.4-N	13.58	606	544	501	18.6
30-0.5-N	16.98	681	606	554	18.4
30-0.6-N	20.37	740	654	593	18.2
30-0.7-N	23.77	788	687	621	18.2
30-0.8-N	27.16	826	720	646	18.3
30-1-N	33.95	887	767	688	18.5
30-1.3-N	44.14	947	805	728	19.2
36-0.2-N	11.73	436	398	373	19.6
36-0.3-N	17.60	581	526	486	18.8
36-0.4-N	23.47	688	610	547	18.4
36-0.5-N	29.33	771	663	587	18.2
36-0.6-N	35.20	837	708	621	18.2
36-0.7-N	41.07	890	741	645	18.3
36-0.8-N	46.93	934	772	661	18.4
42-0.1-N	9.32	261	241	228	21.6
42-0.2-N	18.63	493	444	414	19.1
42-0.3-N	27.95	653	564	511	18.4
42-0.4-N	37.26	764	643	558	18.3
42-0.5-N	46.58	855	687	574	18.3
42-0.6-N	55.90	932	729	587	18.3
42-0.7-N	65.21	985	767	604	18.4
42-0.8-N	74.53	1033	791	619	18.6

7.2.1 Average velocity

The average velocity was obtained from the velocity history as $v_{average} = \frac{0.1}{t_{impact}}$ where t_{impact} is the time of impact.

Detonation time

The comparison between all experimentally and numerically obtained blast arrival times are shown in Figure 7.5 where the blast arrival time is plotted against the charge length. Numerical results indicated that the blast arrival time was the shortest at 14 mm charge length and increased as the charge length deviated away from the 14 mm charge length. Experimental results are much more scattered, but a similar trend was observed. The theoretically derived experimental detonation time using EM signals was proven to be more consistent than trip-wire which was therefore not presented.

Two zones were identified based on the gradient of the numerical results. This is thought to be as a result of the detonation mechanics.

The detonation pressure at different times for a ⌀36 mm charge with a aspect ratio of 2 is shown in Figure 7.6. This depicted how the shape of detonation front can change as it propagated through the charge.

At 0.265 μs after detonation (Figure 7.6 (a)), the detonation front expanded radially and axially as unreacted explosives existed in both directions. If no explosive materials were in front of the reaction zone (in a disk charge), the reaction zone would only propagate radially. This led to a lower percentage of the chemical energy contributing to axial velocity.

At 0.756 μs after detonation (Figure 7.6 (b)), the detonation front covered the full diameter of the charge but the detonation front was still curved. Therefore, the expansion of the detonation front in the radial direction is limited.

Once the detonation front became flat, as shown in Figure 7.6 (c and d), the full volume of explosives across the diameter were utilised in the adiabatic expansion. So, a higher percentage of the explosive materials imparted axial velocity when then charge length was sufficiently long.

In zone 1, shown in Figure 7.5 , the blast arrival time decreased with the increase in charge length with a steeper gradient. In zone 2, the charge length was sufficient for the detonation front to develop fully. This allowed the maximum detonation velocity to be reached by the charge. The blast arrival time was taken as time from the moment of detonation until the first blast wave arrives at the witness plate. Using this method, the distance travelled by the blast waves increased with the increase in charge length. At a constant, maximum detonation velocity, the blast arrival time should increase with the increase in charge length which was observed in zone 2. The gradient was was more gradual than in zone 1.

The mean arrival time using the theoretical method was 16.8μs, while numerical results yielded a mean of 19.0μs. The largest deviation between the two methods was 11.8 μs. This is not significant when divided by the time of flight of the ball bearing which was 174.4 μs for that experiment. i.e 6.7

% of the flight time. The 6.7% deviation was used as the conservative uncertainty estimate.

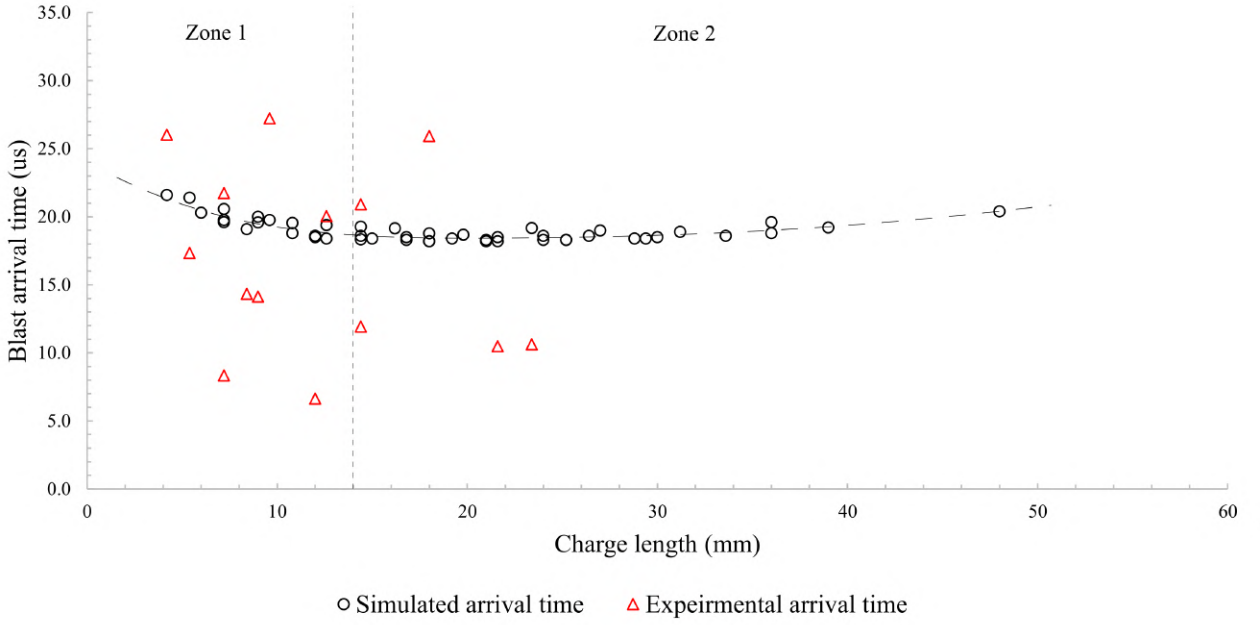

Figure 7.5: Graph of blast arrival time versus charge length, comparing the numerically and experimentally obtained times.

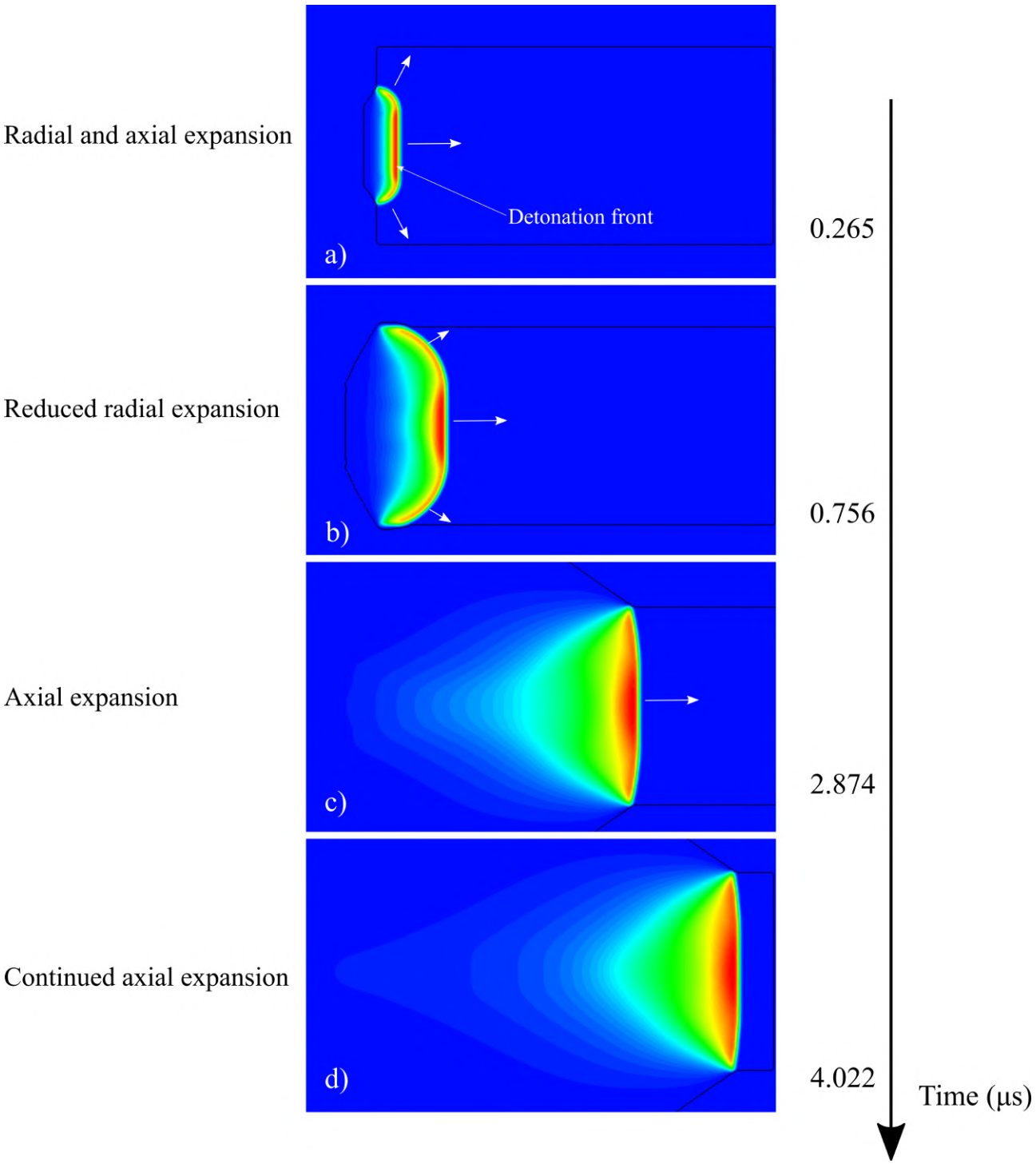

Figure 7.6: Pressure contour development of a 36 mm long charge simulated in Autodyn at: a) 0.265 μs, b) 0.756 μs, c) 2.874 and d) 4.022 μs after detonation.

Comparison of experimental and numerical results

Experimental and numerical results for ⌀18 and ⌀24 mm are presented in Figure 7.7. Charges with masses above 20 g were not shown in this graph. Apart from the two outliers, the experimental and numerical results are within the uncertainty which was a conservative estimate of the uncertainty of the detonation time. In general, numerical and experimental results agreed with each other with a relatively small difference. The mean difference between the numerically obtained average velocity

was 1.8% from the experimentally obtained average velocity. This provides a degree of confidence to the numerical results since the model would have simulated the complex interaction between the blast pressure and ball bearing to achieve this.

The two outliers are experiments 2.2-18-0.3 / 18-0.3-N and 7.33-18-0.3/18-1-N where the difference between numerical experimental results are greater than the error bar. The error for the 2.2g detonation was likely to have caused by the effect of the detonator which was not accounted for in the simulation. At very low charges, the influence of the explosive in the detonator may be more significant as it represents a larger percentage of the net explosive content.

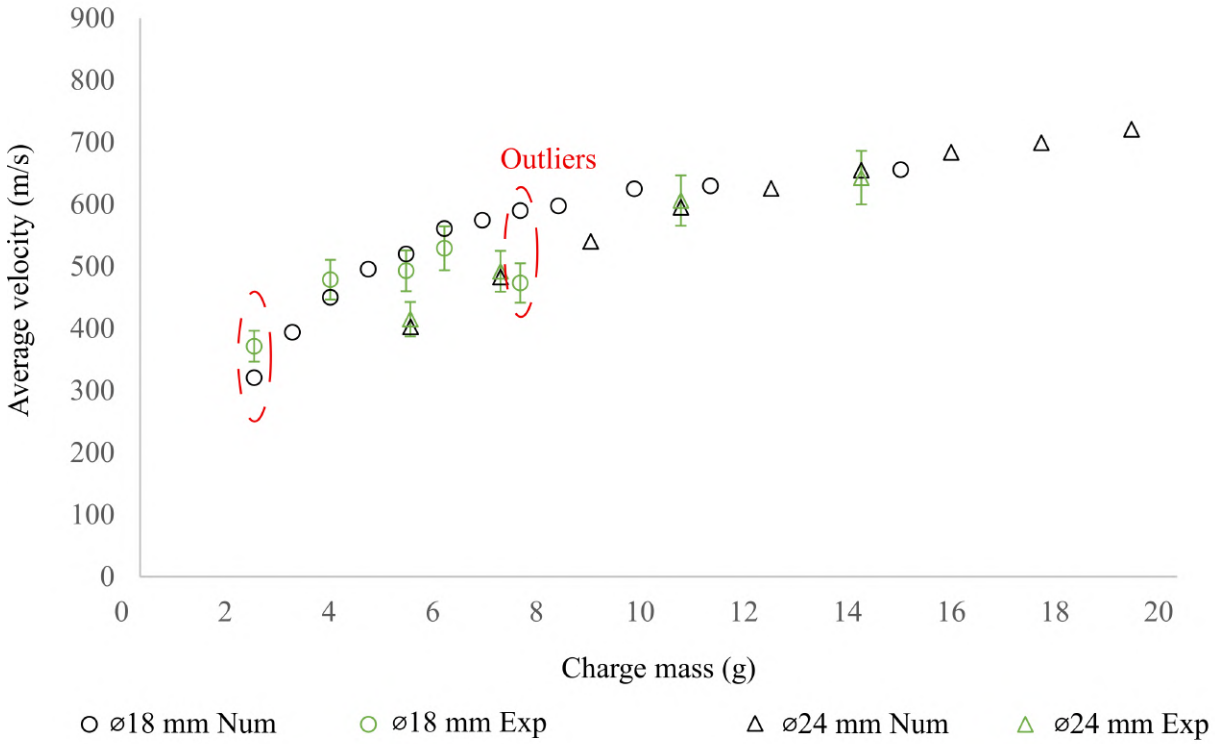

Figure 7.7: Graph showing the comparison between the experimentally and numerically obtained average velocity versus charge mass.

7.3 Comparison of Impact velocity

7.3.1 Bearing geometry

Significant deformation was observed from the blasting of the ball bearings both experimentally and numerically. Figure 7.8 demonstrates a comparison between the experimental and numerical results. The first and last image of Figure 7.8 are resulted from unknown charges. The numerical results were taken just before the bearing had impacted the plate from the two simulations with closest matching shapes to the experimental ball bearings. The two pairs of results at the centre are showing the simulated results for the corresponding experimental results. The red dot on the left side of the numerical results indicates the side of the ball bearing closest to the charge.

The deformation shown in the numerical results was as a result of the blasting only. The experimen-

tal photographs were taken after the complete blast tests, i.e the bearings have undergone blasting and impact. However, as shown in Figure 7.10, the effects of impact as observed from the impact experiments, are negligible when viewed with the naked eye.

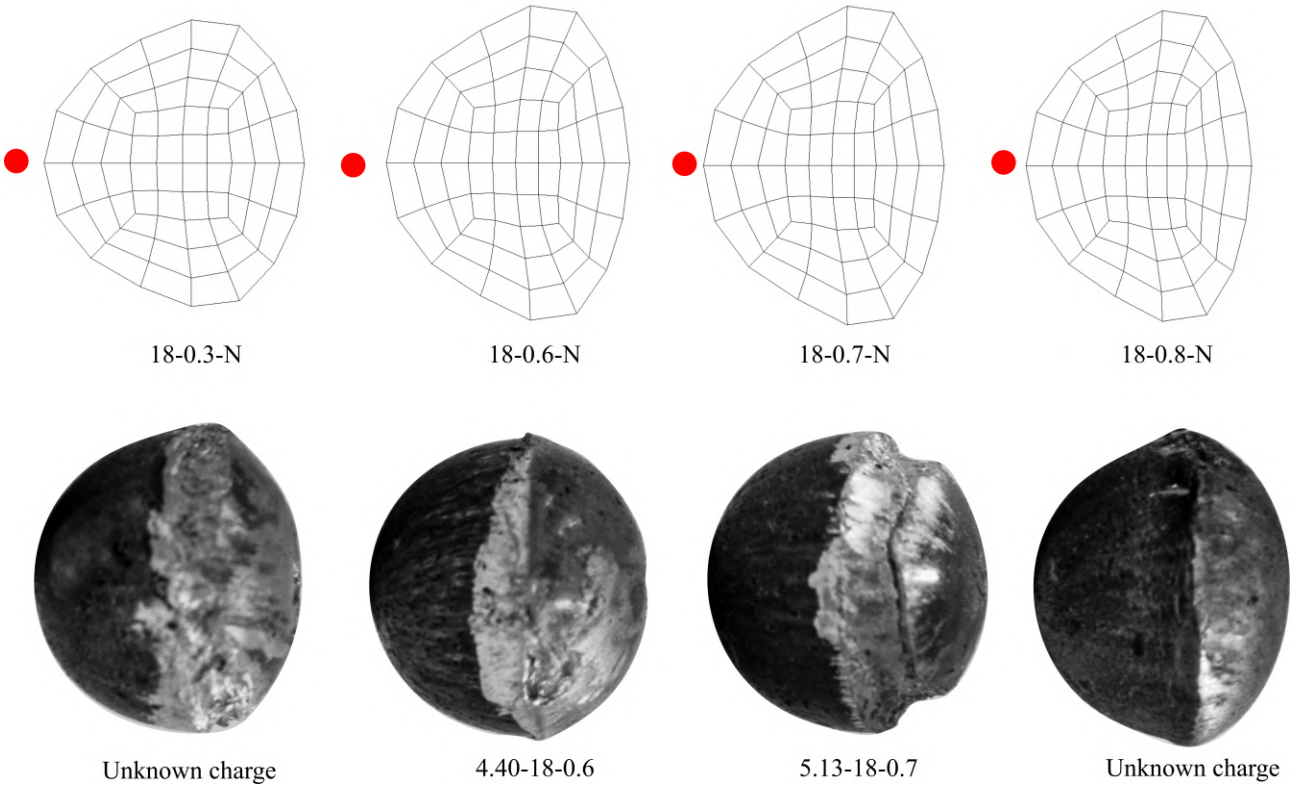

Figure 7.8: Comparison between photographs and the numerical results of the blasted ball bearing.

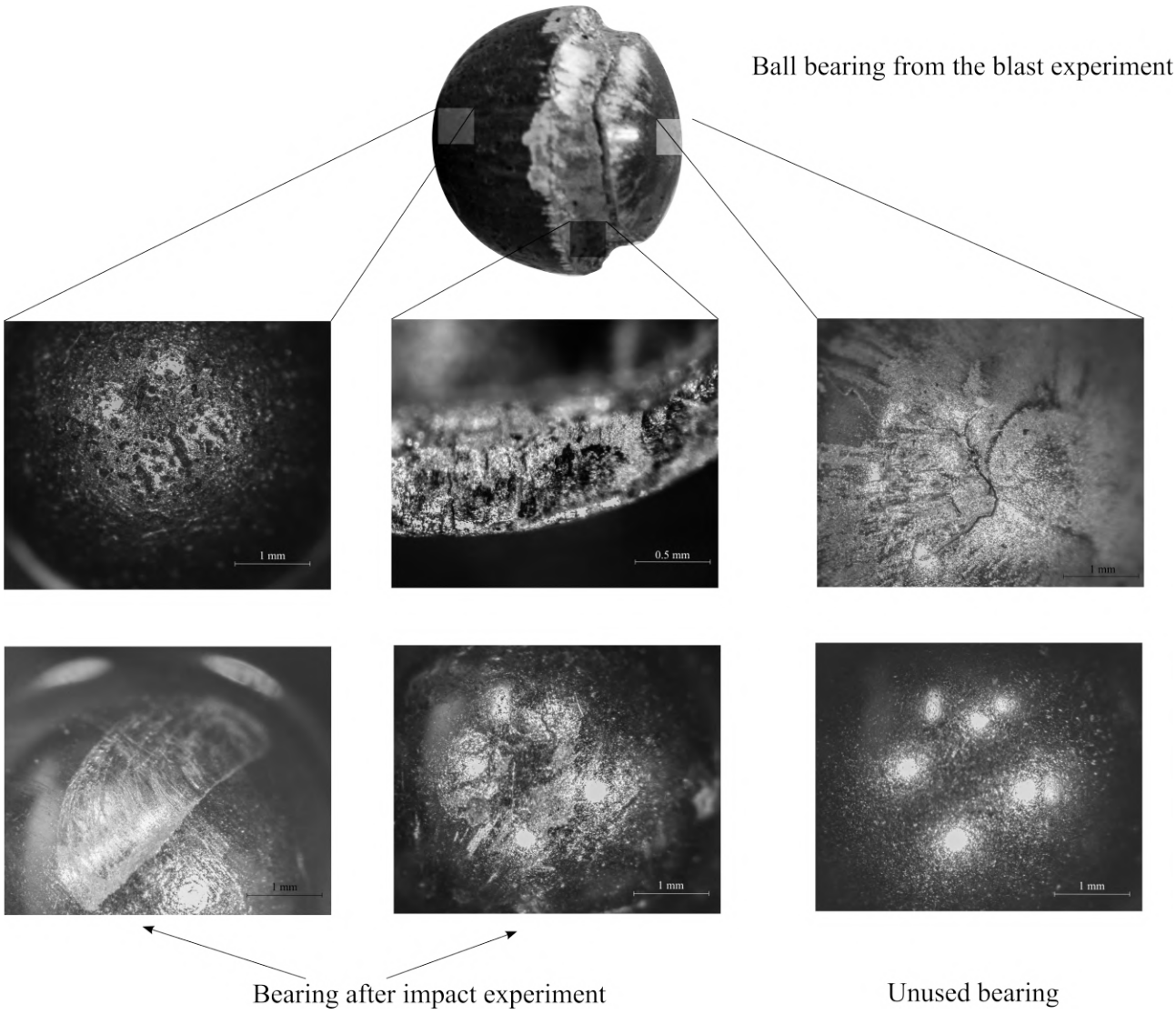

Figure 7.9: Photographs showing the different surfaces observed after blast and impact loading, only impact loading and a unused ball bearing.

At first, the shiny surface of the ball bearing was thought to indicate that this was the blasted side, but further investigation revealed the opposite to be more likely. Firstly, the numerical model also showed two distinct hemispheres, however, the blasted face remained spherical/circular while the opposite face was more deformed/flattened. Secondly, micro-structural investigation conducted by examining the surfaces of the blasted ball bearing using the LEICA MZ 8 stereomicroscope supported the numerical model.

Figure 7.9 shows the comparison of different surfaces observed after the blast experiments, impact experiments and from an unused ball bearing. In the blasted and impacted ball bearing, three distinct surface characteristics were present. These are: pitted surface shown on the spherical side of the blasted ball bearing; rough surface with cleavage shown in the fragmented section of the ball bearing; cracked surface with light lines shown on the right side of the blasted ball bearing; chipped surface that remained shiny also with lines shown on the ball bearings after the impact experiment.

The right hemisphere of the ball bearing from the blast experiment exhibit similar surface characteristics with the ball bearings that have only been impact-loaded. Both of which maintained the

metallic shiny appearance. Lines resembling cracking of the surface and chipping of materials can also be observed.

The central section of the blasted ball was characterised by rough surfaces. This likely resulted from material that had undergone brittle fracture under tensile load. Therefore the loss of material in this section of the ball bearing could be as a result of spalling. The stress wave received from the detonation pressure was of 'compressive' nature. The compressive stress wave then travelled until the 'free end' of the ball bearing and was reflected as a tensile stress wave. The tensile stress caused a brittle fracture of the ball bearing.

The left hemisphere of the blasted ball is characterised by small circular 'pits' scattered densely across the surface, making it dull. This kind of failure was not observed the impact load only specimen. Therefore, it was likely formed from the blast load. The blackened surface was likely to be 'burn marks' as a result of the fireball. Furthermore, the small scatter of craters as a result of the broken ball bearing pieces found on the witness plates could only be possible if the ball bearing and the broken pieces were being accelerated in the same direction. If the fragmented face was the blasted face, then craters should have been found on the inner walls of the blast tube instead of the witness plate. The blast tube was found to be free of craters.

These findings showed that experimental evidence agreed with the numerical results. Both of which, suggested that the spherical hemisphere was the blast loaded side.

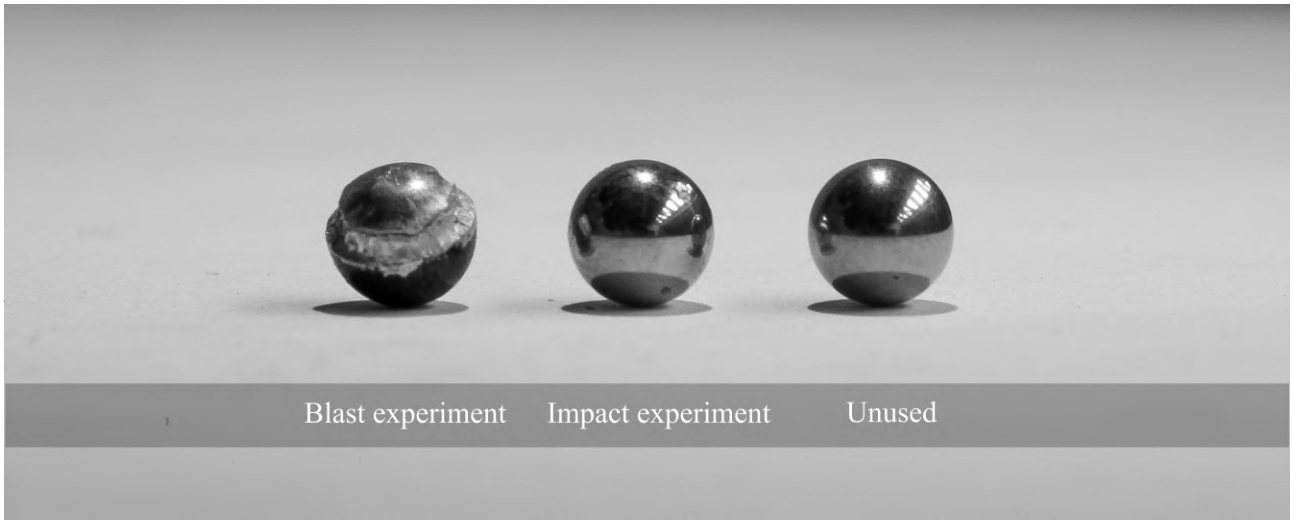

Figure 7.10: Photograph showing the comparison between the ball bearings after the blast, impact experiment and an unused ball bearing.

Additional features observed on the deformed ball bearing

As shown in Figure 7.8, despite the coarse mesh used in the blast experiment simulations, the simulated ball bearing shape still resemble that resulted in the experiments. However, additional features can be observed when a finer mesh was used. As shown in Figure 7.11, where a fine meshed (15 by 30 elements) result is shown. The fragmentation predictions from the numerical model is also presented. Note that as the simulation was in two dimension, therefore the fragmentation shown could be limited to the surface of the ball bearing. Spalling was present on the un-blasted face of the ball bearing in

the simulation and in the photographs. Interestingly, a small caving structure can be noticed at the centre of the experimental and numerical results. Although the features were much more exaggerated in the numerical result, protruding lip-like feature can also be seen across the results which divided the spherical side from the more deformed side.

Since the study of the ball bearing deformation was not the main focus of the work, and the coarse mesh was sufficient for the research questions, the simulations were not repeated for a finer mesh (in general).

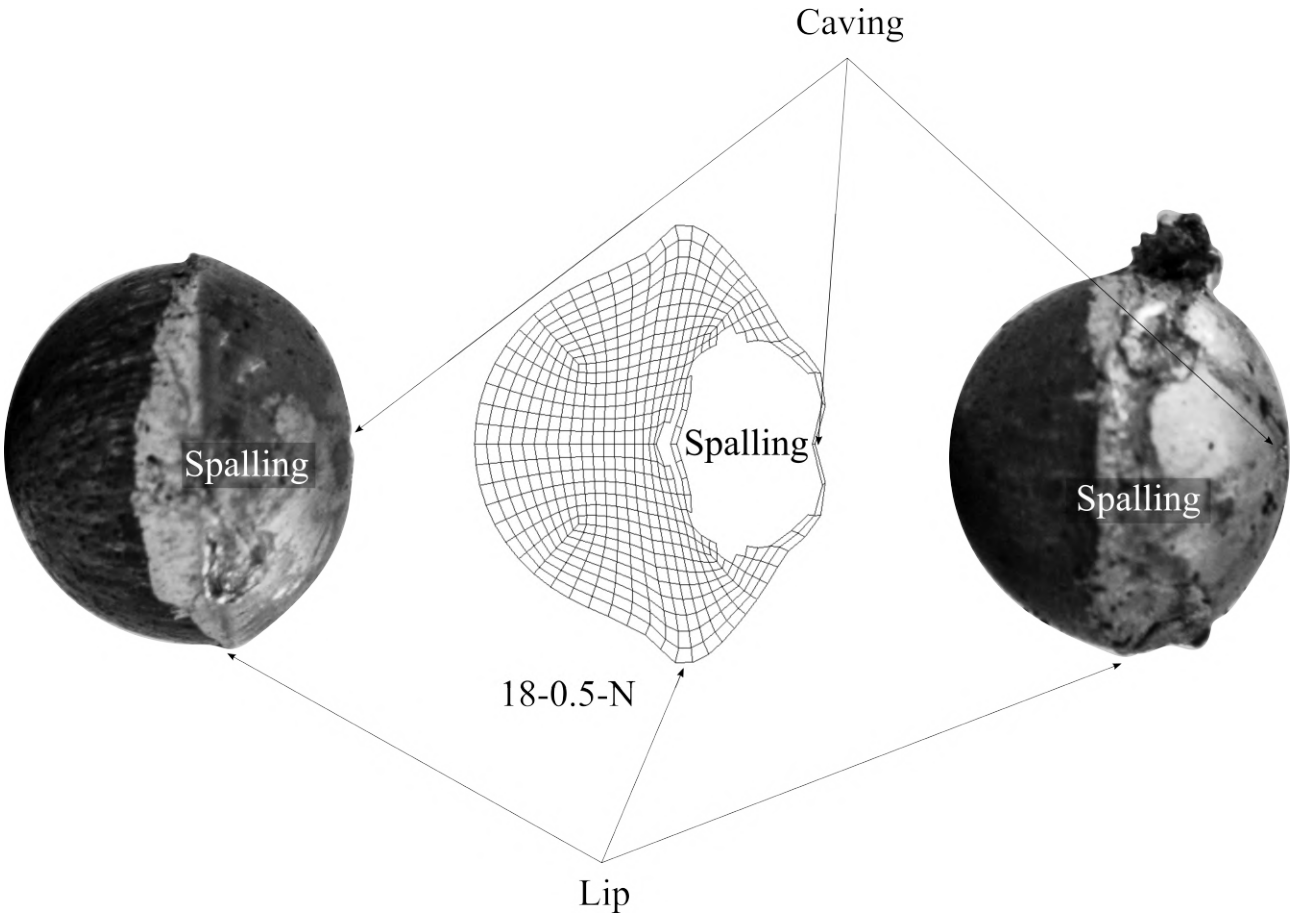

Figure 7.11: Comparison of deformation features of a simulated result from fine mesh and the experimental photographs.

Effect of ball bearing shape on crater depth

It can be observed from the two traceable images in Figure 7.8 that the numerical model grossly overestimated the deformation of ball bearing from blasting. The simulations show a more flattened opposing surface than that observed in the experiment. Previously, as shown in the mesh sensitivity analysis the geometry of the ball bearing has minimum effects on the velocity. However, the results from the impact numerical results showed that the shape of the ball bearing is critical to the crater depth results.

The exaggerated deformation shown numerically was likely due to the inaccurate material model. Characterising a 5 mm ball bearing for blast and impact simulation was out of the scope of this project.

Figure 7.12 illustrates the numerically and experimentally obtained crater depth data for ⌀18 mm. The two results matched relatively closely initially until simulation 18-0.8-N, where the numerical results stopped increasing with the increase in crater depth. It was observed from Figure 7.7 that the ball bearing velocity continued to increase beyond 18-0.8-N. Therefore the asymptotic behaviour seen in crater depth must be influenced by ball bearing shape. As shown in Figure 7.8, the deformation of the ball bearing became more prominent as the charge mass increased. As a result, as the charge mass increased, the ball bearing deformation became greatly exaggerated causing an inaccurate crater depth result.

In comparison, when a spherical ball was used in the impact simulation, the crater depth results are very similar to that of the impact experiments as shown in Figure 7.13. In this set of simulation, the ball bearing was not deformed by the blast load. This shows that when the initial shape factor of the ball bearing was removed, the numerical model yielded fairly consistent results with the experimentally obtained values. The impact mechanics alone was simulated to a reasonable accuracy.

The experimentally obtained crater depth value continued to increase. This was likely to due to two factors. Firstly, from the ball bearings collected after the blast tests, the deformation on the ball bearing was not as severe as that seen numerically. The bottom right ball bearing shown in Figure 7.8 was the most deformed. Secondly, it can be deduced from the deviation from centre value on the witness plate that no experiment conducted was perfectly axisymmetrical. The ball bearings therefore were likely to be rotating during the flight which reduced the probability of having the deformed face impacting the witness plates. Both of these decreased the influence of ball bearing shape on crater depth in the blast experiments.

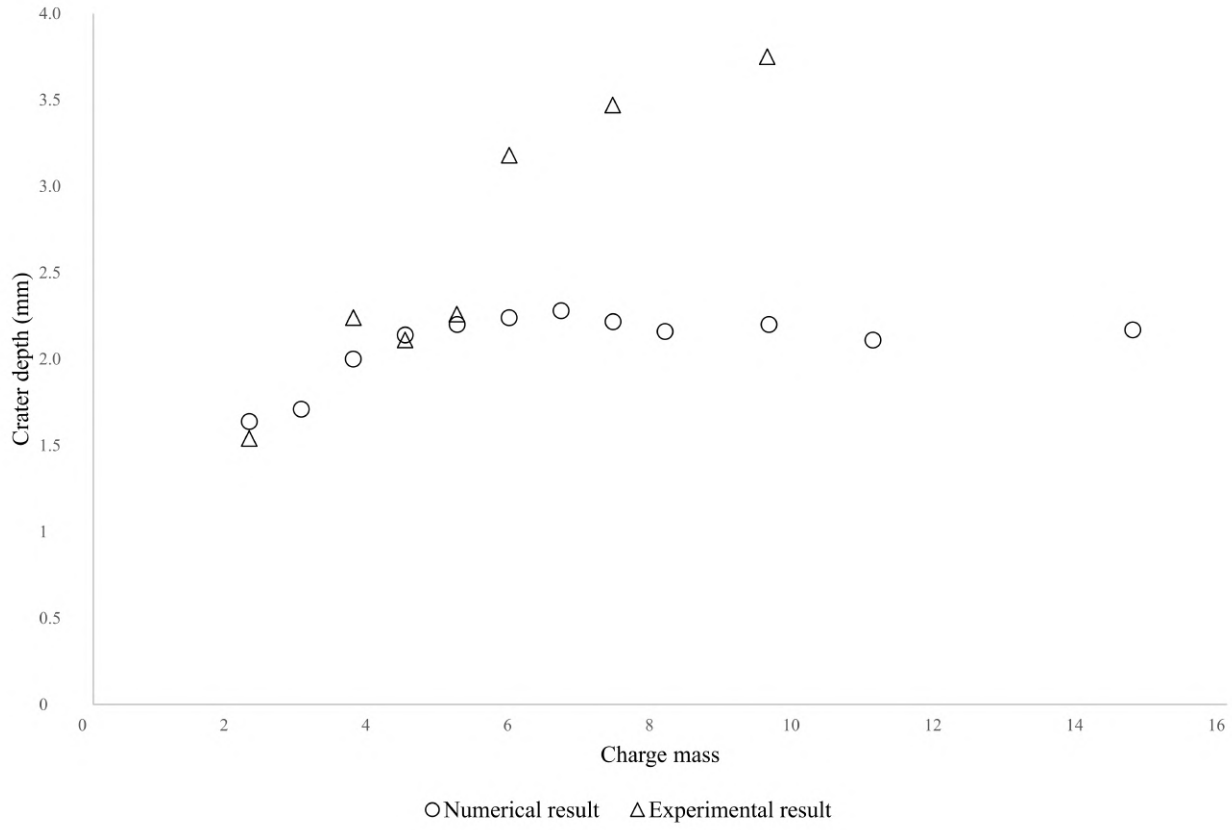

Figure 7.12: Graph showing the numerical and experimental crater depth versus charge mass results for ⌀18 mm detonations.

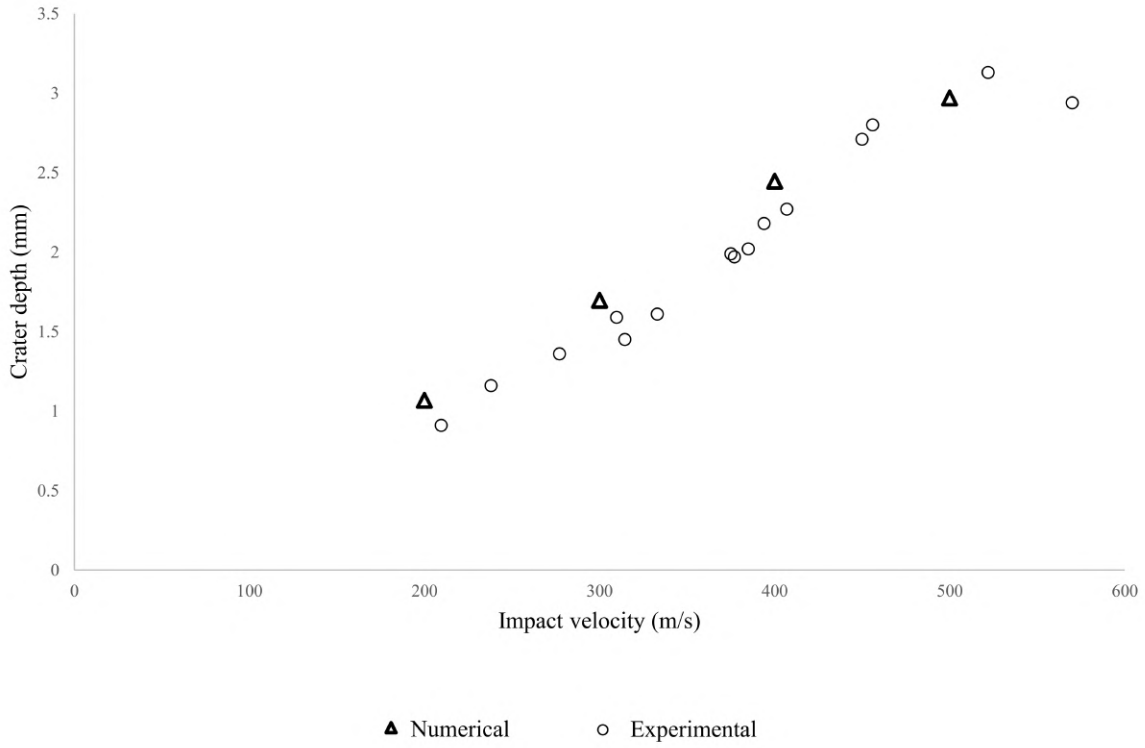

Figure 7.13: Graph showing the impact velocity versus crater depth obtained using the two stage gas gun and from numerical simulation.

7.3.2 Error analysis of the crater depth method

The impact velocity was inferred numerically and experimentally. Velocities inferred using the crater depth method and the numerical simulation produced very similar results. The mean impact velocities inferred experimentally were -1.1% of the numerically velocities.

Intuitively, when all other parameters are constant, less massive projectile should produce a smaller crater. This is supported by the empirical equations presented in Section 2.4.1. Since Equation 3.20 (crater depth-velocity relationship from impact tests) did not include the effect of mass loss and that mass loss was observed in the blasted ball bearings, the crater depth method therefore underestimated the impact velocity.

It is possible to roughly estimate the effect of mass loss using the modified JSC equation (Equation 2.20) which was shown to produce a similar gradient with the results from the impact test. The effect of mass in the JSC equation can be correlated using the density term as:

$$v \propto \sqrt{\frac{1}{\rho}} \tag{7.2}$$

Therefore, a mean mass loss of 2.8% of the ball bearing should roughly be equivalent to a velocity error as:

$$v_{error} \propto (\sqrt{\frac{1}{1}} - \sqrt{\frac{1}{1-0.028}}) = -1.4\% \tag{7.3}$$

So, the crater depth method may have underestimated the velocity by 1.4%. This agreed with the mean difference value. It was also presented in Section 7.3.1 that the effect of plastic deformation on ball bearings from blasting will overestimate the impact velocity and that this effect is very limited. The two factors that affect the velocity estimated using the crater depth method have an error cancelling effect. Therefore, it is unsurprising that the mean difference was smaller in magnitude than that deduced using the mass loss.

7.4 Influence of charge geometry on maximum velocity

The maximum velocity was not determined experimentally. However, a high degree of consistency observed between the experimentally and numerically determined average and the impact velocities provided a sense of validation for the maximum velocity.

The effect of charge diameter on the maximum velocity of the ball bearing can be observed in Figure 7.14. In general, charges with smaller diameters are more effective at driving the ball bearing. At a constant charge diameter, the velocity increase non-linearly until a critical aspect ratio was reached. The critical aspect ratio was suggested as $\sqrt{3/2}$, which is the maximum effective charge aspect ratio reported by [10]. This is demonstrated in Figure 7.15 where a linearly scaled velocity was plotted against a logarithmically scaled charge mass. Ball bearing velocity increased near logarithmically on the left of the critical aspect ratio and increased non-linearly on the log scale on the right of the aspect ratio.

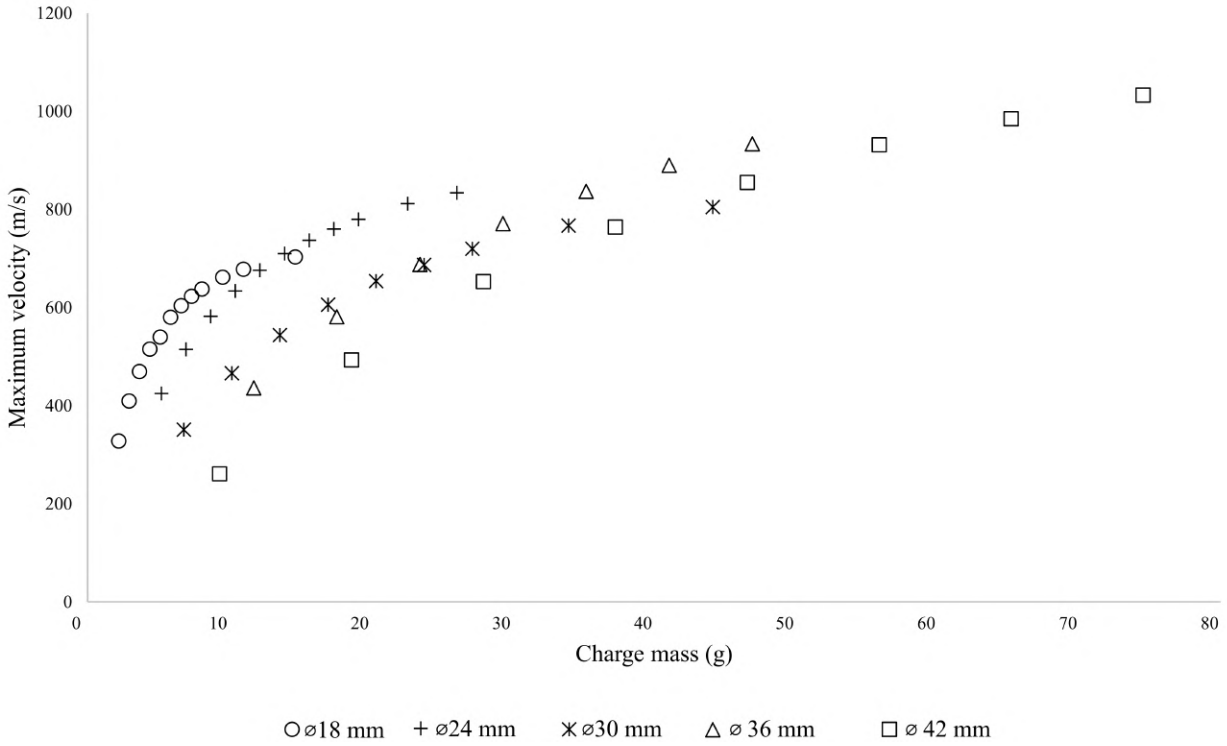

Figure 7.14: Graph of simulated maximum velocity versus charge mass, grouped by charge diameters.

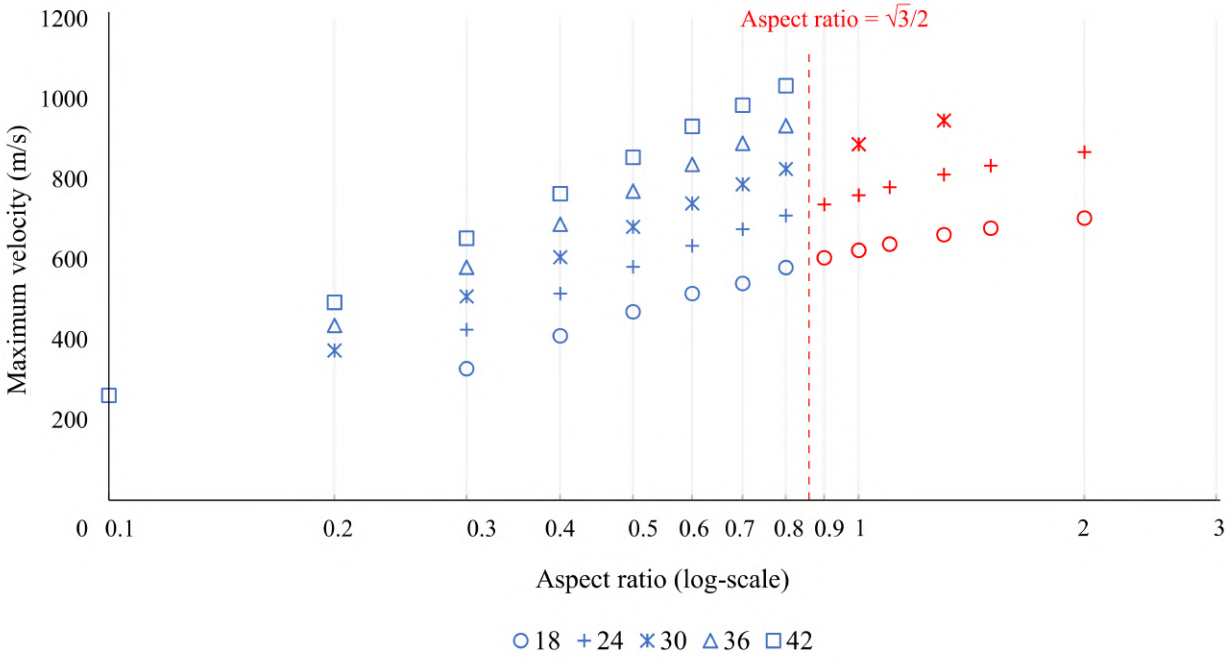

Figure 7.15: Graph of simulated maximum velocity versus charge aspect ratio, grouped by charge diameters shown in log scale.

7.5 Ball bearing velocity profile

A typical ball bearing velocity and acceleration history from experiment 18-1-N is shown in Figure 7.16. The history graphs can be divided into three distinct zones based on the driving mechanisms within each zone. The driving mechanisms are illustrated using the pressure contours and velocity vectors of *air* as well as the velocity and acceleration history from the corresponding numerical models shown in Figure 7.17. The history plots are shown until the time indicated for each sub-figure.

At 2.532 μs after detonation (Figure 7.17 (a)), the detonation had completed. However, the velocity vectors and the magnitude of the pressure of the gaseous product indicated that a significant amount of gas pressure has yet to propagate in the driving direction. The maximum pressure at the shock front was already lower than the C-J pressure of C-4. On the corresponding history graphs, the maximum acceleration had reached a turning point but the ball bearing velocity was still rapidly increasing. The detonation products and the shock front were still behind the ball bearing.

At $t = 5$ μs shown in Figure 7.17 b, the shock front had overtaken the ball bearing. The maximum pressure in the expanding gas was magnitudes lower than in Figure 7.17 (a). The acceleration of the ball bearing decreased sharply to near zero as the velocity had reached its maximum. The ball bearing now maintained its maximum velocity as there was insignificant pressure difference between the front and the back of the ball bearing during its flight through the rarefaction expansion waves.

Noticeable interference initiated at approximately $t = 48.8$ μs, at which time, the reflected initial blast wave began to interact with the ball bearing. The reflected pressure was significantly higher than the gas pressure behind the ball bearing. The pressure differential opposed the motion of the ball bearing, accelerating in the opposite direction. On the history graphics, a small dip in velocity

and acceleration can be observed. Recirculation of the gaseous products can be observed at the end of the blast tube, where the gases on the sides of the blast tube propagated towards the centre of the tube and began to merge.

At $t = 55.5\ \mu s$, the ball bearing velocity had decreased considerably. The recirculated gas products had merged and created additional drag on the ball bearing, but the pressure of gas products was reduced further. Consequently, the deceleration was barely noticeable on the acceleration-time graph.

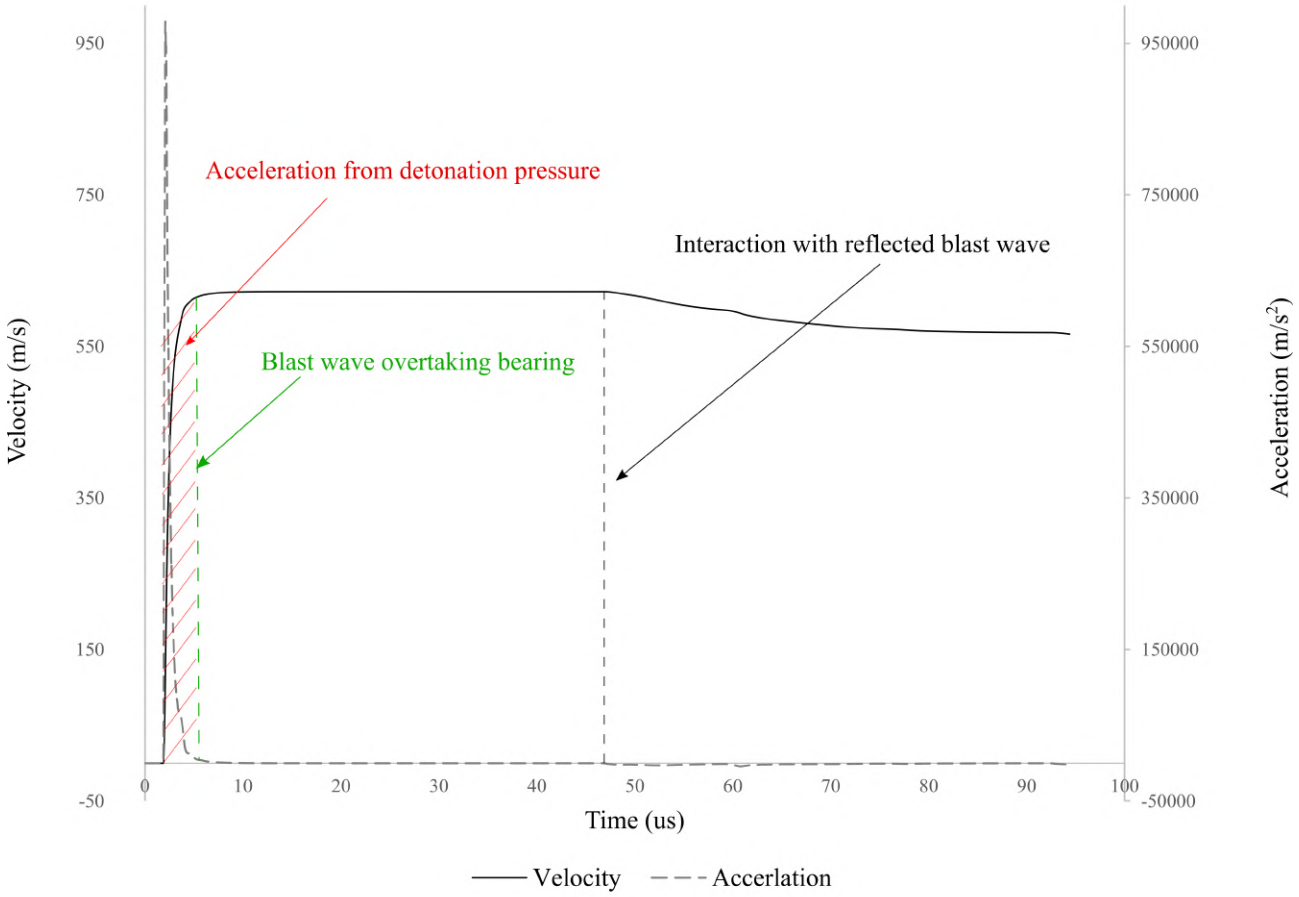

Figure 7.16: Graph showing the simulated acceleration and velocity history for the numerical experiment 18-1-N.

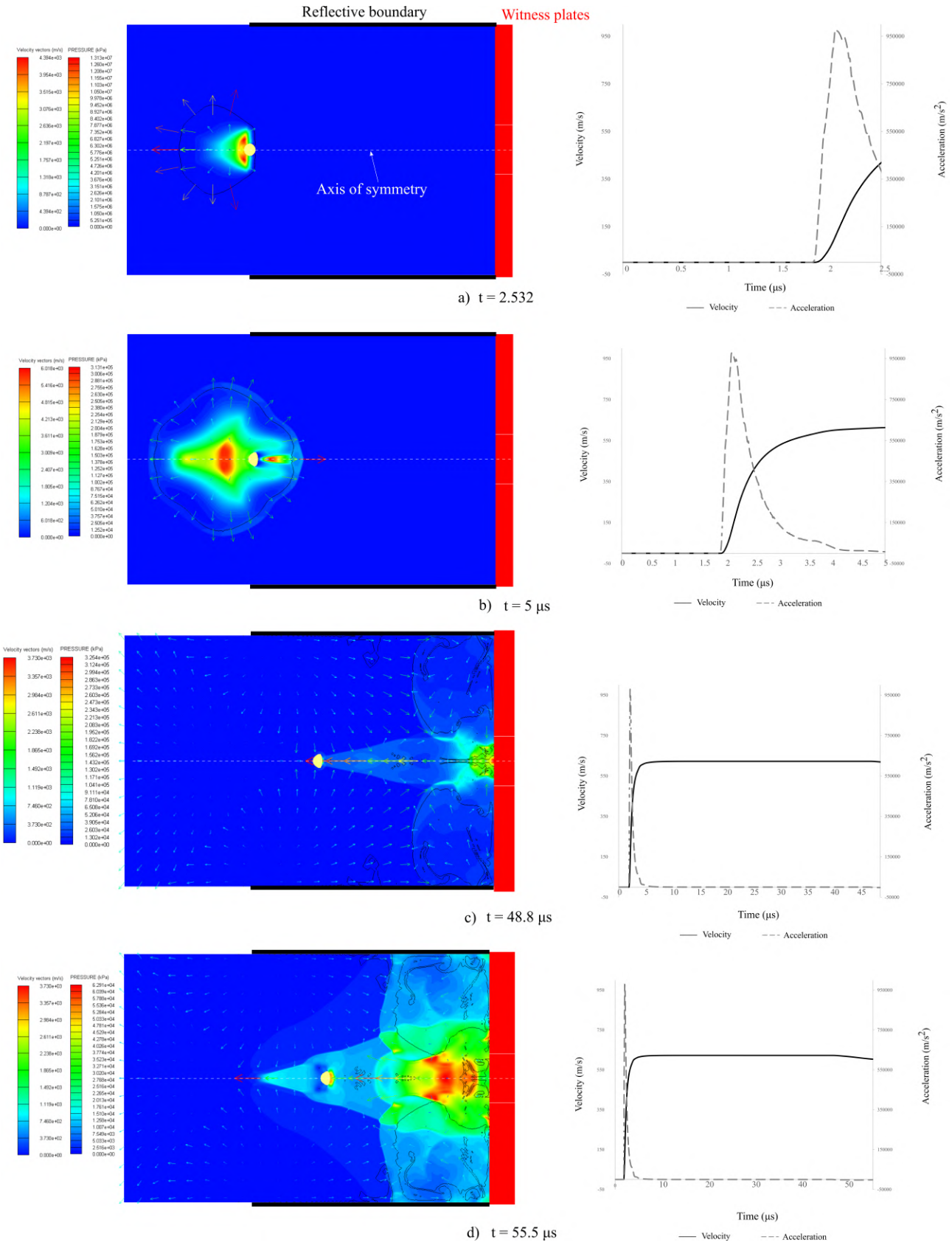

Figure 7.17: Simulated pressure contours, velocity vectors as well as velocity and acceleration history at different times experienced by a typical ball bearing, illustrated using the simulated data from experiment 18-1-N.

7.5.1 Effect of charge geometry on velocity differences

The influence of charge geometry on the velocity profile was investigated by characterising the differences between the maximum and the impact velocity. Figure 7.18 illustrates the velocity difference versus the charge aspect ratio at constant charge diameters. The difference between maximum and impact velocity increased with the increase in charge aspect ratio in all charge diameters. At a constant charge diameter, the increase in aspect ratio resulted in a linear increase in charge mass. Note that the maximum velocity was captured in the simulation before being affected by the reflected pressure. Therefore, the difference in velocity was caused by the influence of the reflected pressure which reduced the impact velocity.

This suggests that at a constant charge diameter the effect of the reflected pressure must be increasing with the increase in aspect ratio. And that at a constant charge aspect ratio, the reflected pressure increased with the increase in charge diameter. This observation agreed with the trends seen in the pendulum and HPB impulse.

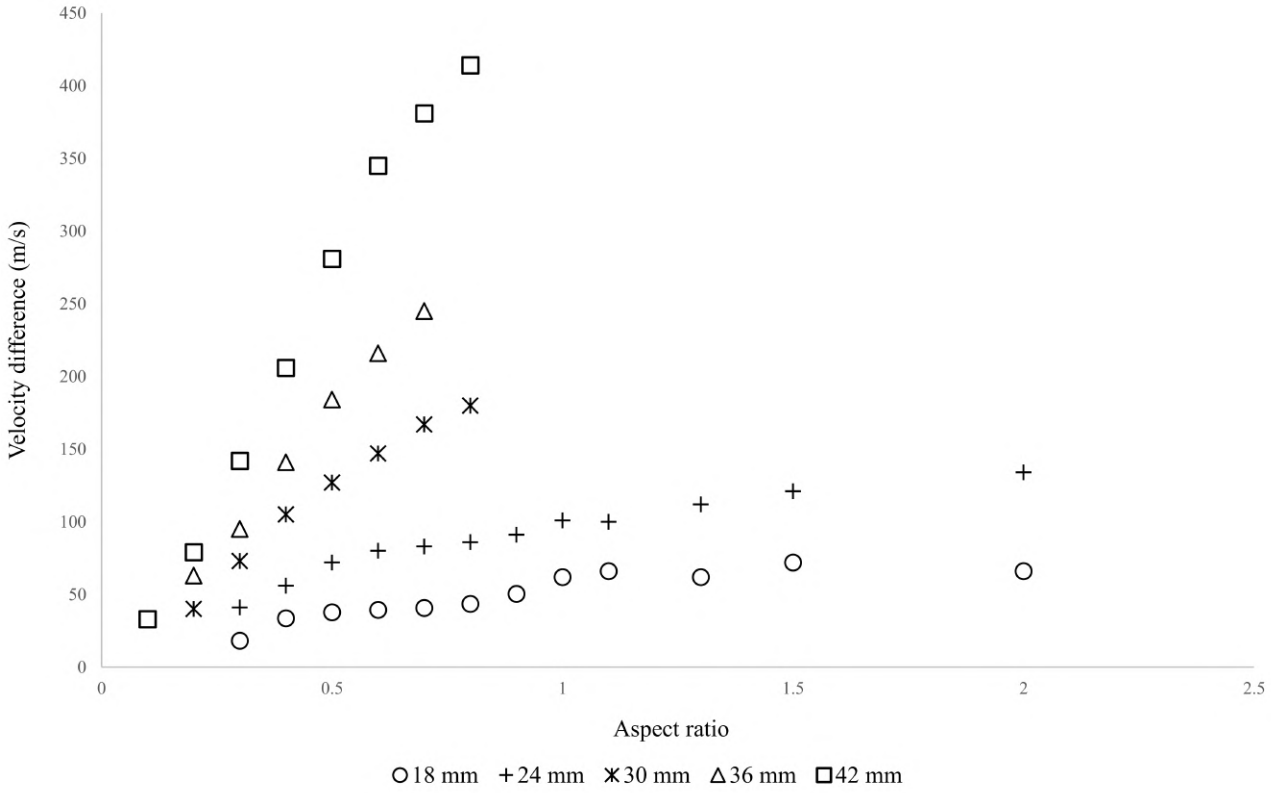

Figure 7.18: Graph of velocity difference versus aspect ratio showing the numerical results, grouped by charge diameters.

7.6 Effect of charge geometry on detonation profile and ball bearing velocity

As shown in Section 7.5, the velocity of the ball bearing, in particular, the maximum velocity was largely dependent on the driving force during and immediately after detonation. Understanding the detonation pressure can provide insightful explanations on the ball bearing velocities observed exper-

imentally and numerically. Therefore, the influence of charge geometry on the detonation pressure profile was investigated numerically.

The pressure contour during detonation at different times were captured for ⌀18 mm charges at $L/D = 0.3$, $L/D = 0.8$, $L/D = 2$; for ⌀24 mm charges at $L/D = 0.3$, $L/D = 2$ and for ⌀42 mm charges at $L/D = 0.3$ and $L/D = 0.8$.

Figure 7.19 illustrates the detonation pressure profile immediately prior to contact with the ball bearing. At a constant aspect ratio, more circular detonation front can be observed with the increase in charge diameter. Since the charge length increased with the increase in charge diameter at constant aspect ratio, the thickness of the region with highly pressurised gas was therefore also increased. At a constant charge diameter, the region of pressurised gas increased in thickness with the increase in charge aspect ratio as a result of the expanding detonation products. At $L/D = 0.8$, the curvature of the tailing pressurised gas mimicked that of the detonation front. At $L/D = 2$, the detonation front was observed to have almost no curvature and that the tailing gas products formed a near triangular geometry.

If one assumed that only the column of pressurised gas with the same diameter as the ball bearing was responsible for propelling the ball bearing forward, as the aspect ratio increased, the column of highly pressurised gas also increased proportionally in thickness. That was until the shape of the profile of the gas started to merge into a triangle, at which point, the volume behind the ball bearing turned from a cylinder to a cone. The velocity of the ball bearing should therefore increase at a constant rate until the gas shape changes to a cone. The critical change was observed at $L/D = 0.8$. This explanation was supported by the experimental and numerical results where the ball bearing velocity increased asymptotically after a critical aspect ratio was reached.

As the charge diameter increased, the highly pressurised gas increased significantly in length, in proportion with the diameter increase, but did not increased significantly in thickness. Therefore, most of the increase in charge mass did not contribute to the column of gases behind the ball bearing. This was also observed in the experimental and numerical results, where the ball bearing velocity increased with the increase in charge diameter when plotted against charge mass.

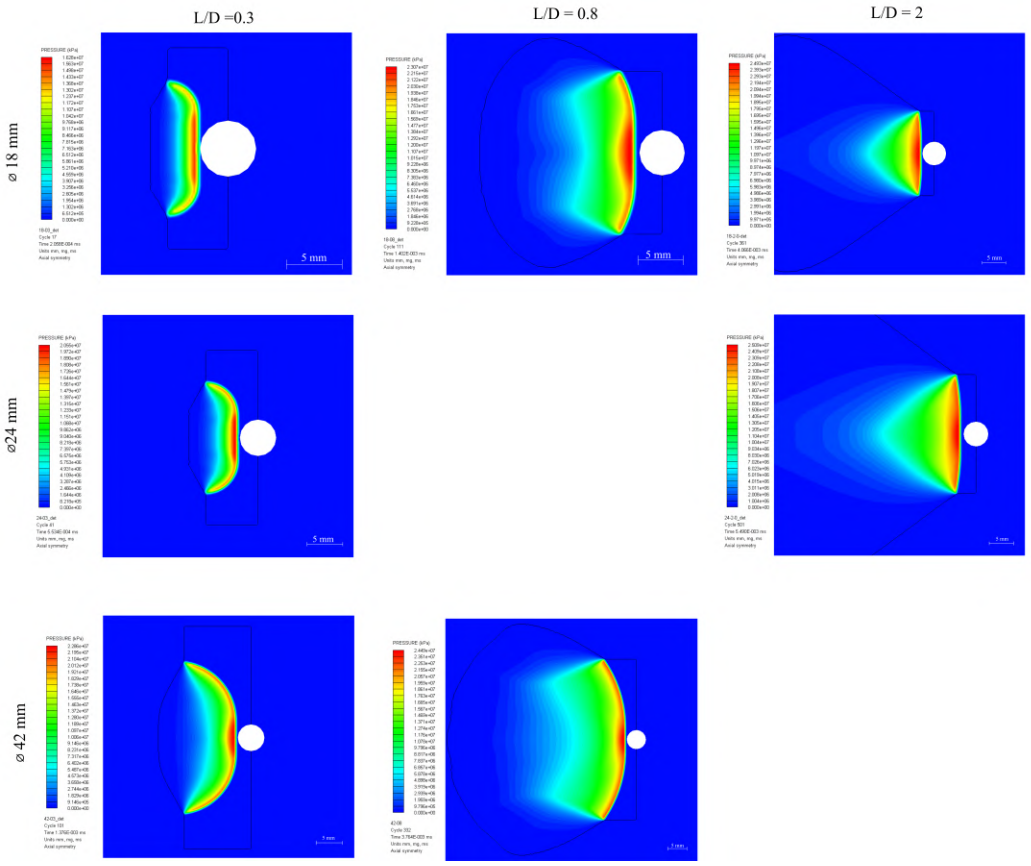

Figure 7.19: A collection of simulated pressure contours of different charges immediately prior contacting the ball bearing.

Chapter 8

Conclusions and future recommendations

8.1 Conclusions

In light of the findings and discussions presented in Chapter 6 and 7, conclusions were drawn based on the objectives listed in Chapter 1.

1) *To investigate the influence of charge aspect ratio on the velocity of the ball bearing in one dimension experimentally.*

- It was observed experimentally that both the average velocity and the impact velocity increased non-linearly with the increase in charge aspect ratio. The increase was observed to be of near logarithmic until a critical aspect ratio was researched. After which, the increase was much more gradual. This critical aspect ratio was suggested around $\sqrt{3}/2$.
- The average and the impact velocity increased in a similar manner and that the average velocity was consistently greater in magnitude than the impact velocity.

2) *To investigate the influence of charge diameter on the velocity of the ball bearing in one dimension experimentally,.*

- Experimental results showed that the effectiveness of accelerating a ball bearing from a cylindrical charge decreases with the increase in charge diameter.

3) *To simulate, using commercially available software, blast propagation and solid-shock interactions by employing the dimensions used in the experimental arrangement.*

A two-dimensional axisymmetrical numerical simulations were conducted in ANSYS Autodyn. The blast propagation, solid-shock interaction and the impact between the ball bearing and the witness plates were simulated.

4) *To validate the model using experimental data.*

- The mean difference in the impact velocity and average velocity determined numerical and experientially was 1.1% and 1.8% respectively. The velocity profile of the ball bearing is therefore consistent between the experimental observation and the numerical observation. This validated the detonation propagation and the solid-shock interaction processes.
- Close agreement between numerical and experimental results could also be observed in the shape of the blast loaded ball bearings, the numerical results are more exaggerated. Less deformation was observed on the blast loaded hemisphere of the ball bearing while spalling was observed in the opposing side.
- Close corrections were also observed in between the experimentally conducted and the numerically simulated gas gun experiments.

Additional observation were made on the impulse results. Similar trends of total axial impulse and HPB impulse were observed numerically and experimentally. The total axial impulse was shown to increase non-linearly with the increase in charge mass and diameter, however (in general) the numerical results were 15.7% higher in the total axial impulse while experimental results were more localised.

8.2 Future Recommendation

1) *Design and implement a better velocity sensor arrangement for the gas gun where the sensor is less likely to be affected by vibrations*

Although satisfactory velocities were achieved from the gas gun using the wax sabot without using the maximum pressure of the gas gun, it could be better utilised if the maximum pressure could be used. At the moment, the sensor is mounted on the barrel which is subjected to vibrations when the ball bearing does not separate from the sabot.

A possible solution is shown in Figure 8.1, where the velocity sensor is mounted independently to the barrel and after the ball bearing as separated from the sabot.

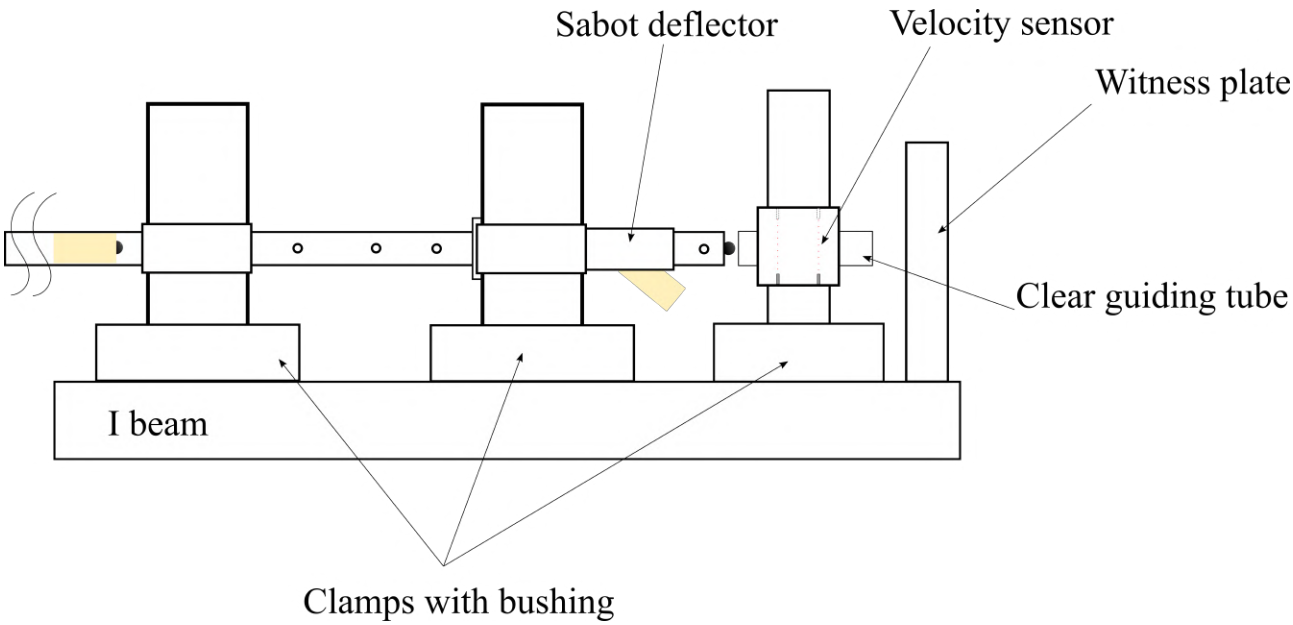

Figure 8.1: Schematic illustrating the recommended velocity sensor arrangement.

2) *Soft capture a detonator to validate the theory used to determine the detonation time.*

The typical composition of a electric detonator was used to derive the detonation time theory in this work. The actual components of the detonators used in the experiments are not known. This could be done by performing a "soft capture" of the detonator by detonating in wax or a viscous liquid.

3) *Investigate the deformation behaviour of the ball bearings.*

Contrary to intuition, the stainless steel ball bearing appeared flattened on the opposite face of detonation in the simulation in the experiments. In this work, the surface of the blasted ball bearings were described and the mechanism to have caused them were suggested. However the actual mechanism which caused the ball bearing to deform in its way was not investigated.

4) *Develop strain rate sensitive material model parameters for the witness plate and ball bearing*

The current model grossly estimated the deformation of the ball bearing under blast loading which resulted inaccurate crater depth results. Better simulation results could be realised by more accurate

material models.

Bibliography

[1] I. Overton, J. Dathan, C. Winter, J. Whittaker, R. Davies, M. Q. Kaaman, and H. Kaaman, "Improvised explosive device (ied) monitor 2017," Action on Armed Violence, Tech. Rep., 2017.

[2] J. A. Zukas, W. Walters, and W. P. Walters, *Explosive effects and applications*. Springer Science & Business Media, 2002.

[3] P. W. Cooper, *Explosives Engineering*, 1st ed. New York: Wiley-VCH, 1996.

[4] F. G. Friedlander, *Propagation of a Pulse in an Inhomogeneous Medium*. New York University, Institute of Mathematical Sciences, 1955.

[5] B. Hopkinson, "British ordnance board minutes," *Rep*, vol. 13565, 1915.

[6] C. Cranz, *Lehrbuch der ballistik*. Ripol Classic, 1925, vol. 1.

[7] C. Knock and N. Davies, "Blast waves from cylindrical charges," *Shock Waves*, vol. 23, no. 4, pp. 337–343, 2013.

[8] C. Knock, N. Davies, and T. Reeves, "Predicting blast waves from the axial direction of a cylindrical charge," *Propellants, Explosives, Pyrotechnics*, vol. 40, no. 2, pp. 169–179, 2015.

[9] K. Ohashi, H. Kleine, and K. Takayama, "Characteristics of blast waves generated by milligram charges," *23rd International Symposium on Shock Waves, Texas*, pp. 1–7, 2001.

[10] J. E. Kennedy, "Explosive output for driving metal," New Mexico, Tech. Rep., 1972.

[11] S. A. Davids, G. S. Langdon, and G. N. Nurick, "The influence of charge geometry on the response of partially confined right circular stainless steel cylinders subjected to blast loading," *International Journal of Impact Engineering*, vol. 108, pp. 252–262, 2017. [Online]. Available: http://dx.doi.org/10.1016/j.ijimpeng.2017.02.015

[12] G. Kinney and J. Graham, K, *Explosive Shocks in Air*, 2nd ed. New York: The Macmillan Company, 1985.

[13] W. Baker, P. Cox, P. Westine, J. Kulez, and R. Strehlow, *Explosion Hazards and Evaluation.*, 1st ed. Elsevier Scienti c Publishing Company, 1983.

[14] NORSOK Standard, "N-004," Tech. Rep., 2004.

[15] G. N. Nurick, S. Mahoi, and G. S. Langdon, "The response of plates subjected to loading arising from the detonation of different shapes of plastic explosive," *International Journal of Impact Engineering*, vol. 89, pp. 102–113, 2016. [Online]. Available: http://dx.doi.org/10.1016/j.ijimpeng.2015.11.012

[16] D. L. Chapman, "Vi. on the rate of explosion in gases," *The London, Edinburgh, and Dublin Philosophical Magazine and Journal of Science*, vol. 47, no. 284, pp. 90–104, 1899.

[17] E. Jouguet, "On the propagation of chemical reactions in gases," *J. de mathematiques Pures et Appliquees*, vol. 1, no. 347-425, p. 2, 1905.

[18] Y. B. Zeldovich, "On the theory of the propagation of detonation in gaseous systems," 1950.

[19] J. Von Neuman, "Theory of detonation waves," Institute for Advanced Study Princeton NJ, Tech. Rep., 1942.

[20] W. Döring, "Über den detonationsvorgang in gasen," *Annalen der Physik*, vol. 435, no. 6-7, pp. 421–436, 1943.

[21] G. Taylor, "The distortion under pressure of a diaphragm which is clamped along its edge and stressed beyond the elastic limit," *Underwater Explosion Research*, vol. 3, pp. 107–121, 1950.

[22] V. Balden and G. Nurick, "Numerical simulation of the post-failure motion of steel plates subjected to blast loading," *International Journal of Impact Engineering*, vol. 32, no. 1-4, pp. 14–34, 2005.

[23] J. Bdzil, "Steady-state two-dimensional detonation," *Journal of Fluid Mechanics*, vol. 108, pp. 195–226, 1981.

[24] J. B. Bdzil and D. S. Stewart, "Time-dependent two-dimensional detonation: the interaction of edge rarefactions with finite-length reaction zones," *Journal of Fluid Mechanics*, vol. 171, pp. 1–26, 1986.

[25] J. B. Bdzil and D. S. Stewart, "Modeling two-dimensional detonations with detonation shock dynamics," *Physics of Fluids A: Fluid Dynamics*, vol. 1, no. 7, pp. 1261–1267, 1989.

[26] J. Lee, E.L.; Hornig, H.C.; Kury, "Adiabatic Expansion of High Explosive," 1968.

[27] T. J. Cloete, G. N. Nurick, and R. N. Palmer, "The deformation and shear failure of peripherally clamped centrally supported blast loaded circular plates," *International Journal of Impact Engineering*, vol. 32, no. 1-4, pp. 92–117, 2006.

[28] T. J. Cloete and G. N. Nurick, "Blast characterization using a ballistic pendulum with a centrally mounted Hopkinson bar," *International Journal of Protective Structures*, vol. 7, no. 3, pp. 367–388, 2016.

[29] S. D. Clarke, S. D. Fay, S. E. Rigby, A. Tyas, J. A. Warren, J. J. Reay, B. J. Fuller, M. T. Gant, and I. D. Elgy, "Blast quantification using hopkinson pressure bars," *Journal of Visualized Experiments*, vol. 2016, no. 113, 2016.

[30] G. N. Nurick and G. Shave, "The deformation and tearing of thin square plates subjected to impulsive loads-An experimental study," *International Journal of Impact Engineering*, vol. 18, no. 1, pp. 99–116, 1995.

[31] C. Geretto, S. C. K. Yuen, and G. N. Nurick, "An experimental study of the effects of degrees of con fi nement on the response of square mild steel plates subjected to blast loading,"

International Journal of Impact Engineering, vol. 79, pp. 32–44, 2015. [Online]. Available: http://dx.doi.org/10.1016/j.ijimpeng.2014.08.002

[32] R. Teeling-Smith and G. N. Nurick, "The deformation and tearing of thin circular plates subjected to impulsive loads," *International Journal of Impact Engineering*, vol. 11, no. 1, pp. Pages 77–91, 1991.

[33] M. Held, "Impulse method for the blast contour of cylindrical high explosive charges," *Propellants, Explosives, Pyrotechnics*, vol. 24, no. 1, pp. 17–26, 1999.

[34] R. J. Curry and G. S. Langdon, "Transient response of steel plates subjected to close proximity explosive detonations in air," *International Journal of Impact Engineering*, vol. 102, pp. 102–116, 2017. [Online]. Available: http://dx.doi.org/10.1016/j.ijimpeng.2016.12.004

[35] S. Rigby, O. Akintaro, B. Fuller, A. Tyas, R. Curry, G. Langdon, and D. Pope, "Predicting the response of plates subjected to near-field explosions using an energy equivalent impulse," *International Journal of Impact Engineering*, vol. 128, pp. 24–36, 2019.

[36] S. Rigby, A. Tyas, R. Curry, and G. Langdon, "Experimental measurement of specific impulse distribution and transient deformation of plates subjected to near-field explosive blasts," *Experimental Mechanics*, vol. 59, no. 2, pp. 163–178, 2019.

[37] W. W. Wood and J. G. Kirkwoob, "Diameter effect in condensed explosives. the relation between velocity and radius of curvature of the detonation wave," *The Journal of Chemical Physics*, vol. 22, no. 11, pp. 1920–1924, 1954.

[38] F. Zhang, *Shock wave science and technology reference library*, 2012, vol. 6.

[39] L. G. Hill, J. B. Bdzil, and T. D. Aslam, "Front curvature rate stick measurements and detonation shock dynamics calibration for pbx 9502 over a wide temperature range," Los Alamos National Lab., NM (United States), Tech. Rep., 1998.

[40] J. B. Bdzil and D. S. Stewart, "Theory of detonation shock dynamics," in *Shock Waves Science and Technology Library, Vol. 6*. Springer, 2012, pp. 373–453.

[41] T. D. Aslam and D. S. Stewart, "Detonation shock dynamics and comparisons with direct numerical simulation," *Combustion Theory and Modelling*, vol. 3, no. 1, pp. 77–101, 1999.

[42] L. Prandtl, "Neue untersuchungen über die strömende bewegung der gase und dämpfe," *Physikalische Zeitschrift*, vol. 8, pp. 23–30, 1907.

[43] T. Meyer, "Über zweidimensionale bewegungsvorgänge in einem gas, das mit überschallgeschwindigkeit strömt. diss. göttingen 1908; vdi-forsch," 1908.

[44] H. Jones and A. Miller, "The detonation of solid explosives: the equilibrium conditions in the detonation wave-front and the adiabatic expansion of the products of detonation," *Proceedings of the Royal Society of London. Series A. Mathematical and Physical Sciences*, vol. 194, no. 1039, pp. 480–507, 1948.

[45] M. L. Wilkins, "The equation of state of pbx 9404 and lx04-01," Lawrence Radiation Laboratory, Tech. Rep., 1964.

[46] E. Grüneisen, "Theorie des festen zustandes einatomiger elemente," *Annalen der Physik*, vol. 344, no. 12, pp. 257–306, 1912.

[47] Esparza and E. D, "Blast measurements and equivalency for spherical charges at small scaled distances," *International Journal of Impact Engineering*, vol. 4, no. 1, pp. 23–40, 1986.

[48] G. Nurick and J. Martin, "Deformation of thin plates subjected to impulsive loads, part ii: experimental studies," *International Journal of Impact Engineering*, vol. 8, p. 17186, 1989.

[49] N. Jacob, S. C. K. Yuen, G. Nurick, D. Bonorchis, S. Desai, and D. Tait, "Scaling aspects of quadrangular plates subjected to localised blast loadsexperiments and predictions," *International Journal of Impact Engineering*, vol. 30, no. 8-9, pp. 1179–1208, 2004.

[50] G. Langdon, S. C. K. Yuen, and G. Nurick, "Experimental and numerical studies on the response of quadrangular stiffened plates. part ii: localised blast loading," *International Journal of Impact Engineering*, vol. 31, no. 1, pp. 85–111, 2005.

[51] S. C. K. Yuen, G. Nurick, G. Langdon, and Y. Iyer, "Deformation of thin plates subjected to impulsive load: Part iii–an update 25 years on," *International Journal of Impact Engineering*, vol. 107, pp. 108–117, 2017.

[52] B. Hopkinson, "X. a method of measuring the pressure produced in the detonation of high, explosives or by the impact of bullets," *Philosophical Transactions of the Royal Society of London. Series A, Containing Papers of a Mathematical or Physical Character*, vol. 213, no. 497-508, pp. 437–456, 1914.

[53] J. Hopkinson, "On the rupture of iron wire by a blow," *Proc. Literary and Philosophical Society of Manchester*, vol. 1, pp. 40–45, 1872.

[54] J. Hopkinson, "Further experiments on the rupture of iron wire," *Proc. Literary and Philosophical Society of Manchester*, vol. 1, pp. 119–121, 1872.

[55] L. Pochhammer, "Über die fortpflanzungsgeschwindigkeiten kleiner schwingungen in einem unbegrenzten isotropen kreiszylinder," *J. reine angew. Math*, vol. 81, p. 324, 1876.

[56] C. Chree, "Longitudinal vibrations of a circular bar," *Quart. J. Pure Appl. Math*, vol. 21, pp. 287–298, 1886.

[57] Q. Zhang, C. Q. Miao, D. C. Lin, and C. H. Bai, "Relation of fragment with air shock wave intensity for explosion in a shell," *International Journal of Impact Engineering*, vol. 28, no. 10, pp. 1129–1141, 2003.

[58] P. K. Choudha, A. Kumaraswamy, and K. D. Dhote, "Parametric study of single confined fragment launch explosive device," *Defence Technology*, vol. 15, no. 2, pp. 179–185, 2018. [Online]. Available: https://doi.org/10.1016/j.dt.2018.08.015

[59] M. A. Wiehahn, G. N. Nurick, and H. C. Bowles, "Some insights into the mechanism of the deformation and tearing of thin plates at high strain rates incorporating temperature dependent material properties," *Structures under Shock and Impact VI*, pp. 35–46, 2000.

[60] D. Felix, I. Colwill, and E. Stipidis, "Real-time calculation of fragment velocity for cylindrical warheads," *Defence Technology*, no. xxxx, pp. 1–8, 2019. [Online]. Available: https://doi.org/10.1016/j.dt.2019.01.007

[61] J. Zhu, Y. Zheng, W. Li, Y. Yang, X. Wang, X. Qiao, and R. Li, "Axial distribution of fragments from the dynamic explosion fragmentation of metal shells," *International Journal of Impact Engineering*, vol. 123, no. October 2018, pp. 140–146, 2019.

[62] J. Kennedy, "Gurney energy of explosives: Estimation of the velocity and impulse imparted to driven metal," Tech. Rep., 1970.

[63] J. E. Kennedy and F. R. Norwood, "New Mexico Institute of Mining and Technology." Tech. Rep., 2000.

[64] I. G. Henry, "The gurney formula and related approximations for high-explosive deployment of fragments," *Hughes Aircraft Company, Culver City, CA, Report No. PUB-189,(AD 813389)*, 1967.

[65] R. W. Gurney, "The initial velocities of fragments from bombs, shell and grenades," Army Ballistic Research Lab Aberdeen Proving Ground Md, Tech. Rep., 1943.

[66] P. C. Souers, J. W. Forbes, L. E. Fried, W. M. Howard, S. Anderson, S. Dawson, P. Vitello, and R. Garza, "Detonation energies from the cylinder test and cheetah v3. 0," *Propellants, Explosives, Pyrotechnics*, vol. 26, no. 4, pp. 180–190, 2001.

[67] J. M. McGlaun, S. L. Thompson, and M. G. Elrick, "CTH: A three-dimensional shock wave physics code," *International Journal of Impact Engineering*, vol. 10, no. 1-4, pp. 351–360, 1990.

[68] S. Mendes and H. Opat, "Tearing and shear failures in explosively loaded clamped beams," *Exp. Mech*, vol. 13, pp. 480–486, 1973.

[69] M. C. Cunningham G.S., Tech. Rep.

[70] K. Hayashida and J. Robinson, "Single Wall Penetration Equations," Structures and Dynamics Laboratory, Science and Engineering Directorate, National Aeronautics and Space Administration, Tech. Rep., 1991.

[71] R. H. Fish and J. L. Summers, "The Effect of Material Properties on Threshold Penetration," National Aeronautics and Space Administration Ames Research Center, Moffett Field, Calif, Tech. Rep., 1965.

[72] K. A. Holsapple and R. M. Schmidt, "On the scaling of crater dimensions - 2. impact processes." *Journal of Geophysical Research*, vol. 87, no. B3, pp. 1849–1870, 1982.

[73] B. Cour-Palais, "Hypervelocity impact investigations and meteoroid shielding experience related to apollo and skylab," Tech. Rep., 1984.

[74] E. Christiansen, "Shield Sizing and Response Equations," Tech. Rep., 1991.

[75] P. Sherkar, J. Shin, A. Whittaker, and A. Aref, "Influence of Charge Shape and Point of Detonation on Blast-Resistant Design," *Journal of Structural Engineering*, vol. 142, no. 2, p. 04015109, 2015.

[76] N. Jacob, "The effect of stand-off distance on the failure of thin plates subjected to blast loads," Master's Dissertation, University of Cape Town, Cape Town, 2005.

[77] S. Davids, "The influence of charge geometry on the response of cylinders to internal air blasting," Master's Dissertation, University of Cape Town, Cape Town, 2016.

[78] G. T. Gray", "Classic split-hopkinson pressure bar testing," in *Mechanical Testing and Evaluation*, D. M. Howard Kuhn, Ed. ASM International, 2000.

[79] F. C. Follansbee P.S., "Wave propagation in the split hopkinson pressure bar," Materials Science and Technology Division, Los Alamos National Laboratory, Tech. Rep., 1983.

[80] C. Shin, T. Ko, S. Lee, M. Cho, J. Yoon, H. Lee, S. Hoblyn, and E. Aw, "Application of multiple-deck-charge blasting with electronic detonator at dtl2 contract 915 in singapore."

[81] G. V. Cloete T., Edwards C., Tech. Rep.

[82] T. R. Koka and A. T. Mathew, "Design of sabot &catcher system ofsingle stage gas gun for bird and hailstone impact test," *Materials Today: Proceedings*, vol. 5, no. 5, pp. 11 827–11 837, 2018.

[83] V. Vemparala, A. T. Mathew, and T. Rao Koka, "Design of single piece sabot for a single stage gas gun," in *Materials Science and Engineering Conference Series*, vol. 263, no. 6, 2017, p. 062059.

[84] Non-Ferrous Metal Works (SA) (Pty) Ltd, "Aluminium 6082," Tech. Rep., 2019.

[85] G. S. Langdon, A. Ozinsky, and S. Chung Kim Yuen, "The response of partially confined right circular stainless steel cylinders to internal air-blast loading," *International Journal of Impact Engineering*, vol. 73, pp. 1–14, 2014. [Online]. Available: http://dx.doi.org/10.1016/j.ijimpeng.2014.05.002

[86] ANSYS Inc., "Ansys autodyn material library (r18)," Tech. Rep., 2018.

[87] C. Kingery, G. Bulmash, and U. A. B. R. Laboratory, *Air Blast Parameters from TNT Spherical Air Burst and Hemispherical Surface Burst*, ser. Technical report ARBRL. Ballistic Research Laboratories, 1984. [Online]. Available: https://books.google.co.za/books?id=lg6cHAAACAAJ

[88] W. J. M. Rankine, "On the thermodynamic theory of waves of finite longitudinal disturbances," *Philosophical Transactions of the Royal Society of London*, vol. 160, pp. 277–288, 1870.

[89] H. Hugoniot, "Mémoire sur la propagation des mouvements dans les corps et spécialement dans les gaz parfaits," *Journal de l'École Polytechnique*, vol. 57, pp. 3–97, 1887.

[90] G. R. Johnson, "A constitutive model and data for materials subjected to large strains, high strain rates, and high temperatures," *Proc. 7th Inf. Sympo. Ballistics*, pp. 541–547, 1983.

[91] P. Yibo, W. Gang, Z. Tianxing, P. Shangfeng, and R. Yiming, "Dynamic mechanical behaviors of 6082-t6 aluminum alloy," *Advances in Mechanical Engineering*, vol. 2013, 2013.

[92] D. Grady, "The spall strength of condensed matter," *Journal of the Mechanics and Physics of Solids*, vol. 36, no. 3, pp. 353–384, 1988.

[93] J. Brnic, S. Krscanski, D. Lanc, M. Brcic, G. Turkalj, M. Canadija, and J. Niu, "Analysis of the mechanical behavior, creep resistance and uniaxial fatigue strength of martensitic steel x46cr13," *Materials*, vol. 10, no. 4, p. 388, 2017.

[94] R. L., "Investigation of the character of the equilibrium of an incompressible heavy fluid of variable density," *Proceeding of the London Mathematics Scociety*, vol. 4, no. 1, pp. 170–177, 1882.

[95] G. I. Taylor, "The instability of liquid surfaces when accelerated in a direction perpendicular to their planes. i," *Proceedings of the Royal Society of London. Series A. Mathematical and Physical Sciences*, vol. 201, no. 1065, pp. 192–196, 1950.

[96] R. D. Richtmyer, "Taylor instability in shock acceleration of compressible fluids," Los Alamos Scientific Lab., N. Mex., Tech. Rep., 1954.

[97] E. Meshkov, "Instability of the interface of two gases accelerated by a shock wave," *Fluid Dynamics*, vol. 4, no. 5, pp. 101–104, 1969.

[98] S. E. Rigby, A. Tyas, R. J. Curry, and G. S. Langdon, "Experimental Measurement of Specific Impulse Distribution and Transient Deformation of Plates Subjected to Near-Field Explosive Blasts," *Experimental Mechanics*, vol. 59, no. 2, pp. 163–178, 2019.

Chapter 9

Appendix A

9.1 Detonation time identification

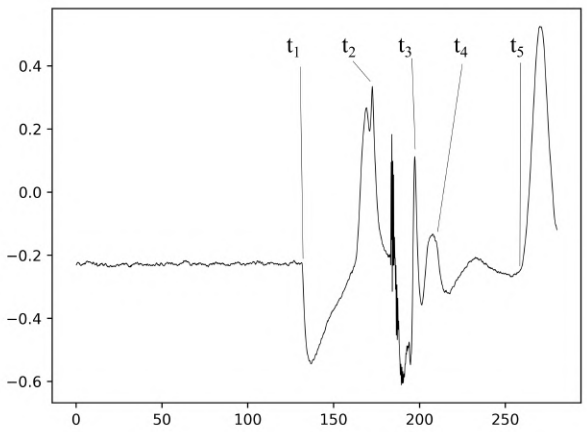

2.20-18-0.3

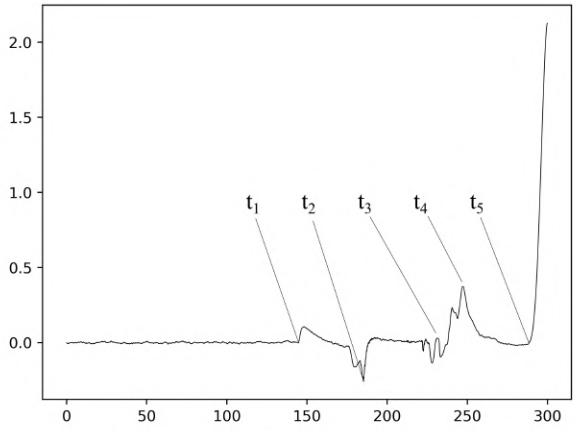

3.67-18-0.5

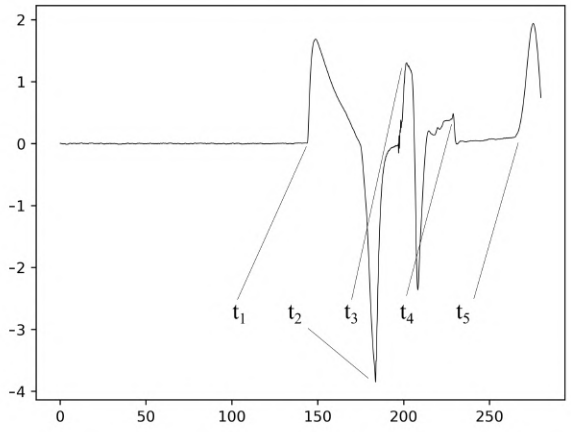

5.13-18-0.7

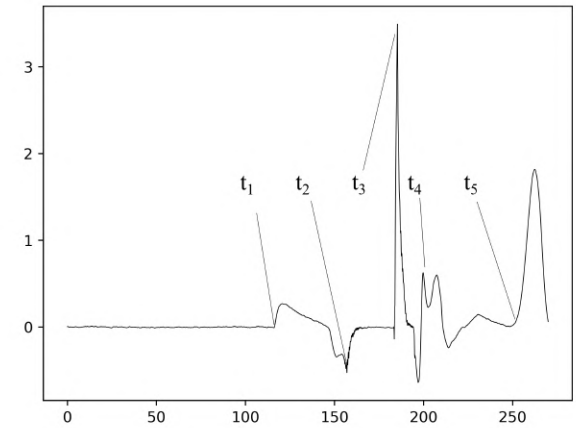

5.87-18-1.0

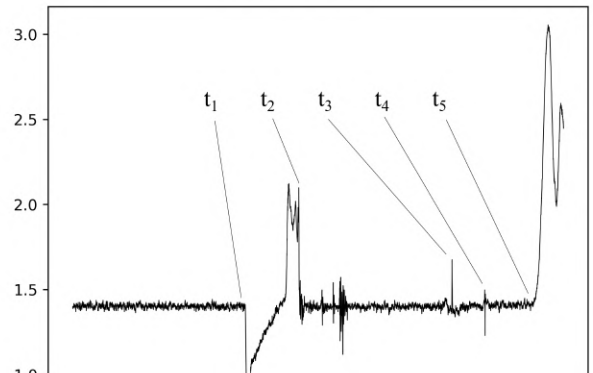

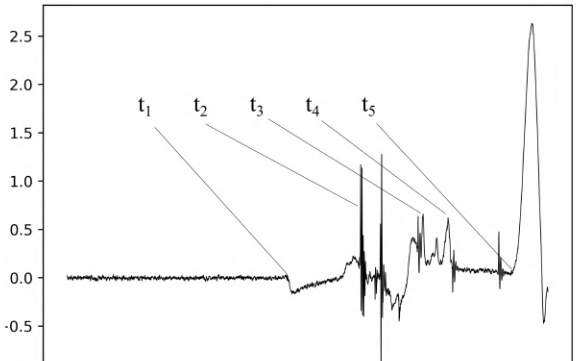

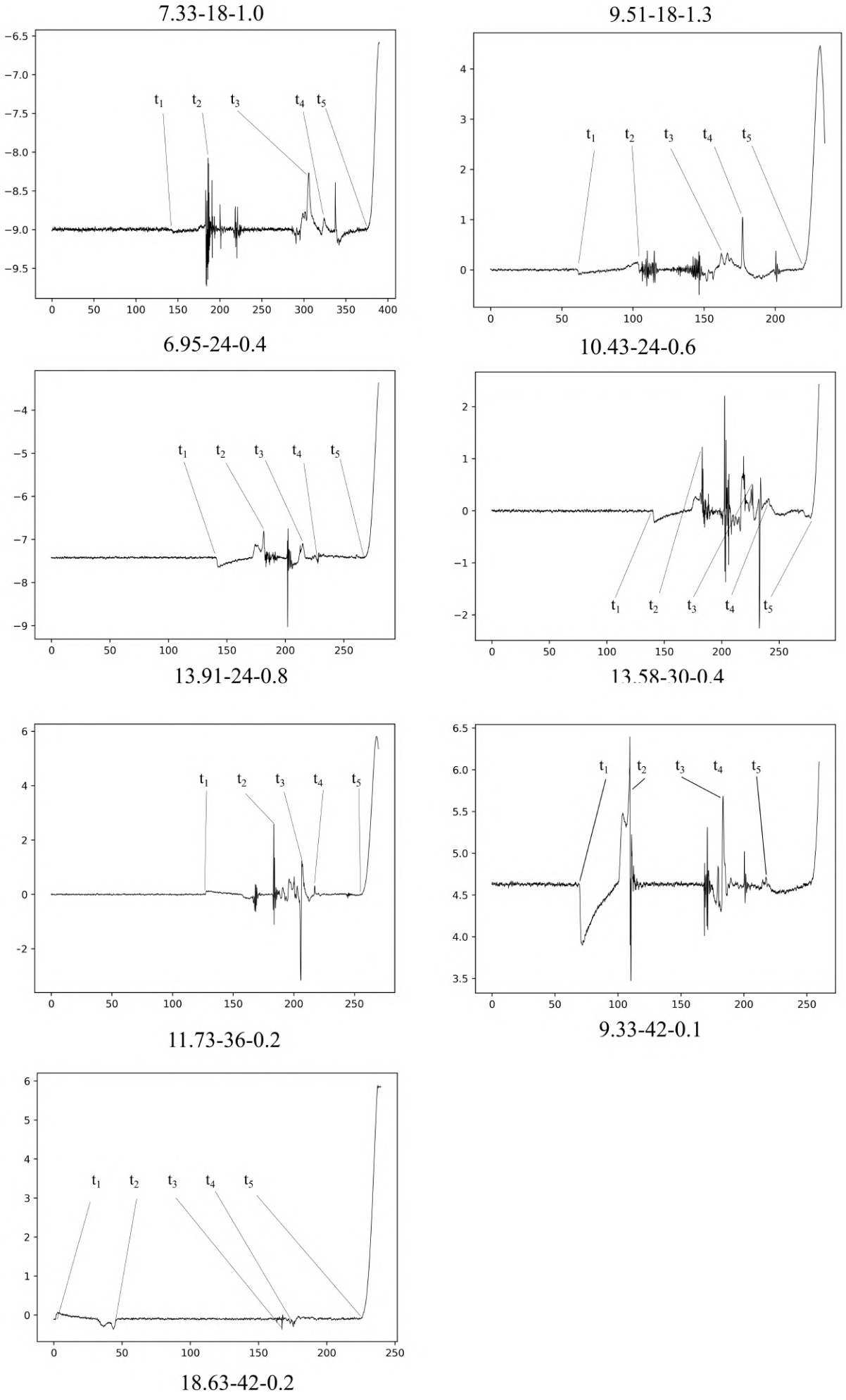

Figure 9.2: A collection of voltage history graphs of the detonation noises captured during experiments, part 2.

Chapter 10

Appendix B

10.1 Technical drawings

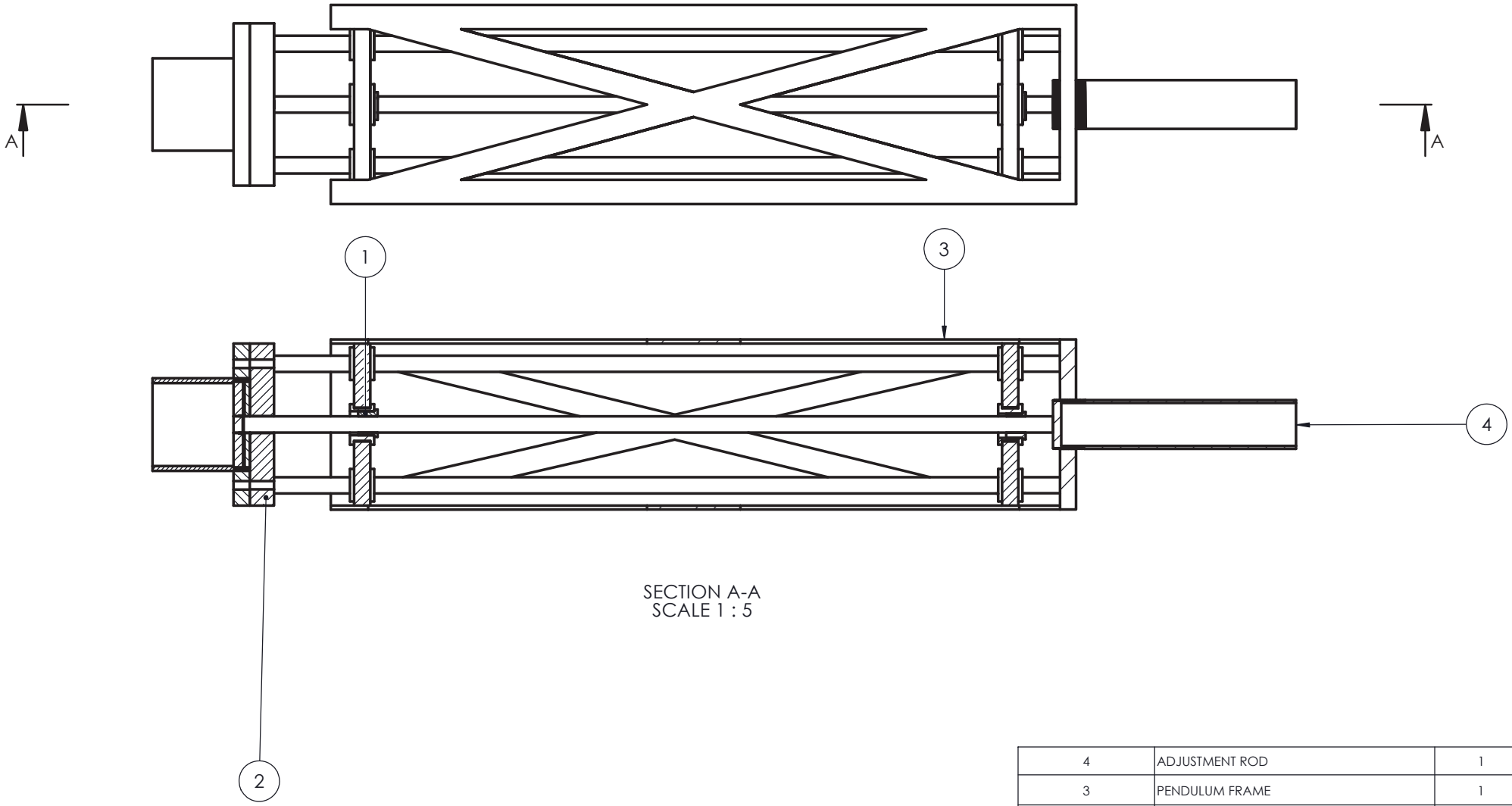

SECTION A-A
SCALE 1 : 5

ITEM NO.	SUB-ASSEMBLY/PART NAME	QTY.
4	ADJUSTMENT ROD	1
3	PENDULUM FRAME	1
2	CLAMP ASSEMBLY	1
1	BUSHING ASSEMBLY	1

Scale: 1:10 on A3	University of Cape Town Department of Mechanical Engineering			
Drawn By: Ruixuan Qi	All un-toleranced dimensions to adhere to ISO 2768-m	Title: Blast Tube on Pendululm Assembly		
Checked :	Assembly drawing	Drawing Number : BTPA	Rev. : A	Sheet : 2 of 2

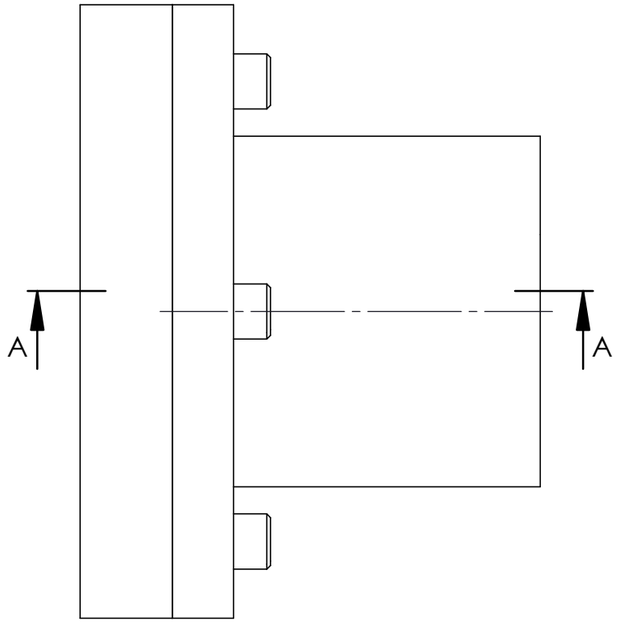

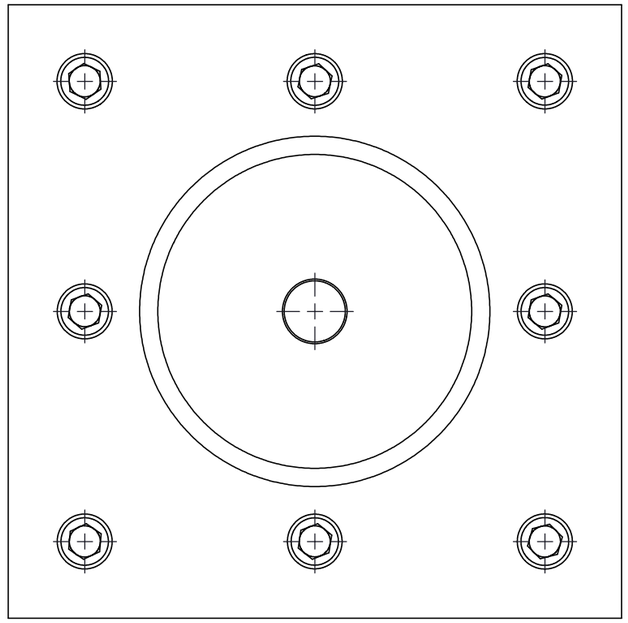

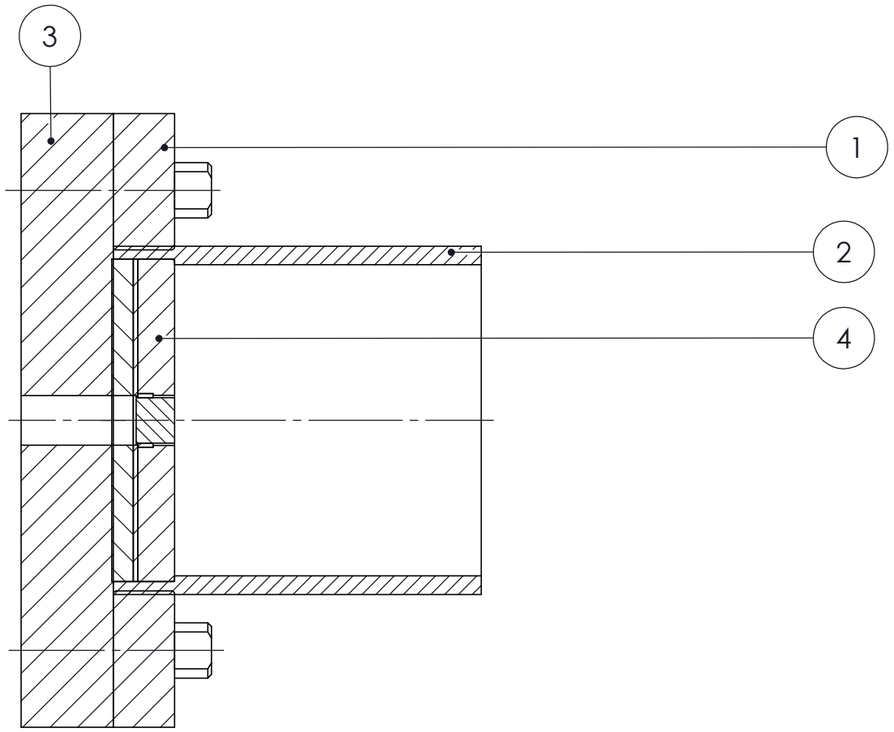

SECTION A-A
SCALE 1 : 2

ITEM NO.	PART/SUB-ASSEMBLY NAME	MATERIAL	QTY.
4	WITNESS PLATE ASSEMBLY	N/A	1
3	BACK CLAMP	MILD STEEL	1
2	STEELTUBE	MILD STEEL	1
1	FRONT CLAMP	MILD STEEL	1

Scale: 1:5 on A3	University of Cape Town Department of Mechanical Engineering			
Drawn By: Ruixuan Qi	All un-toleranced dimensions to adhere to ISO 2768-m	Title: Clamp assembly		
Checked :	Assembly drawing	Drawing Number : BTPA-CA	Rev. : A	Sheet : 1 of 1

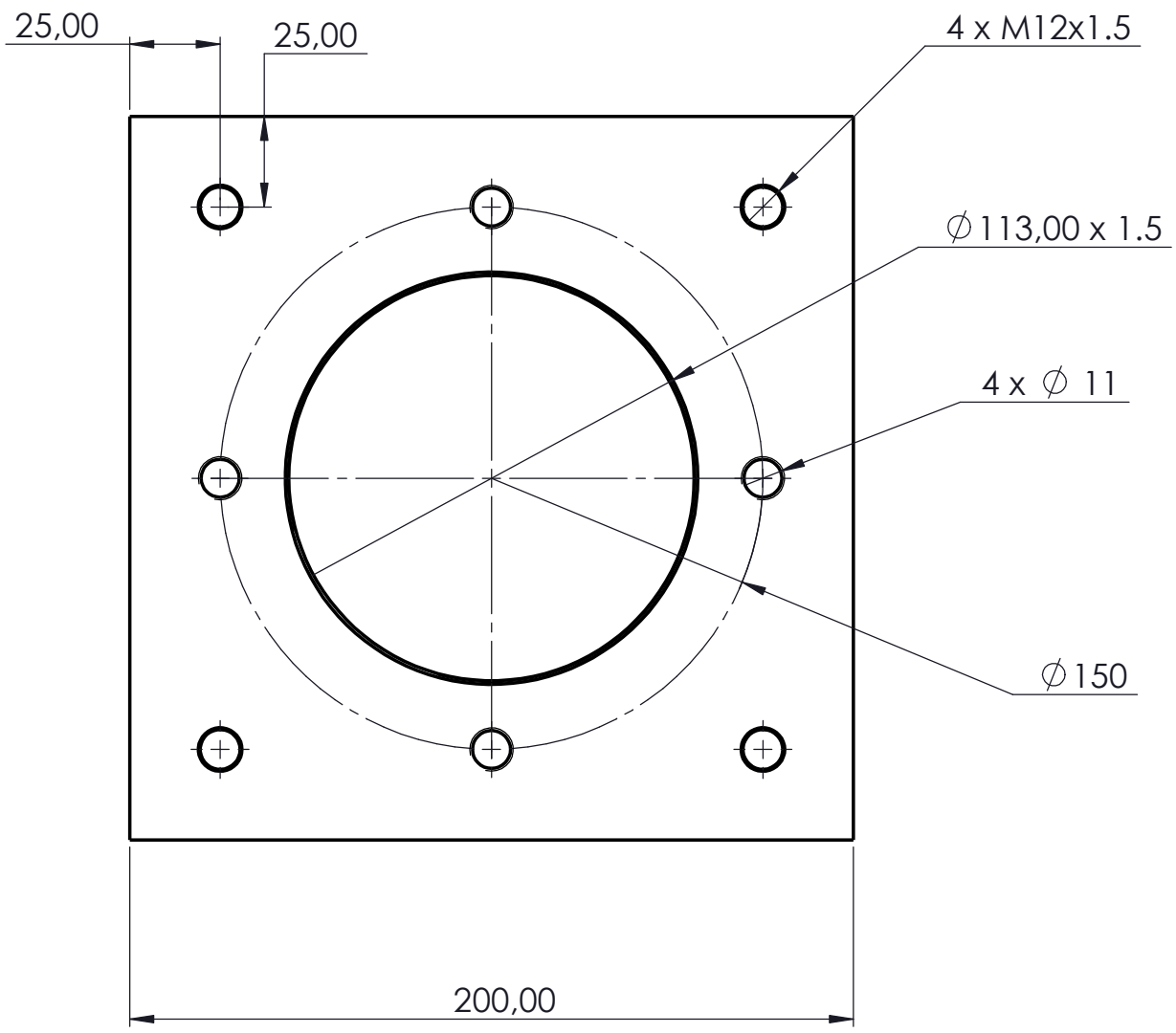

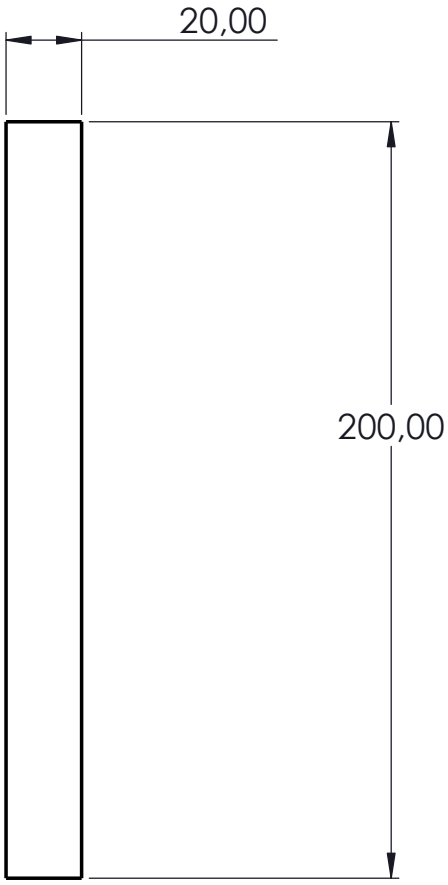

Scale: 1:2 on A4	University of Cape Town Department of Mechanical Engineering			
Drawn By: RUIXUAN QI	All un-toleranced dimensions to adhere to ISO 2768-m	Title: FRONT CLAMP		
Checked : Prof G Langdon	Material : MILD STEEL	Drawing Number : BTPA-CA-1	Rev. : A	Sheet : 1 of 1

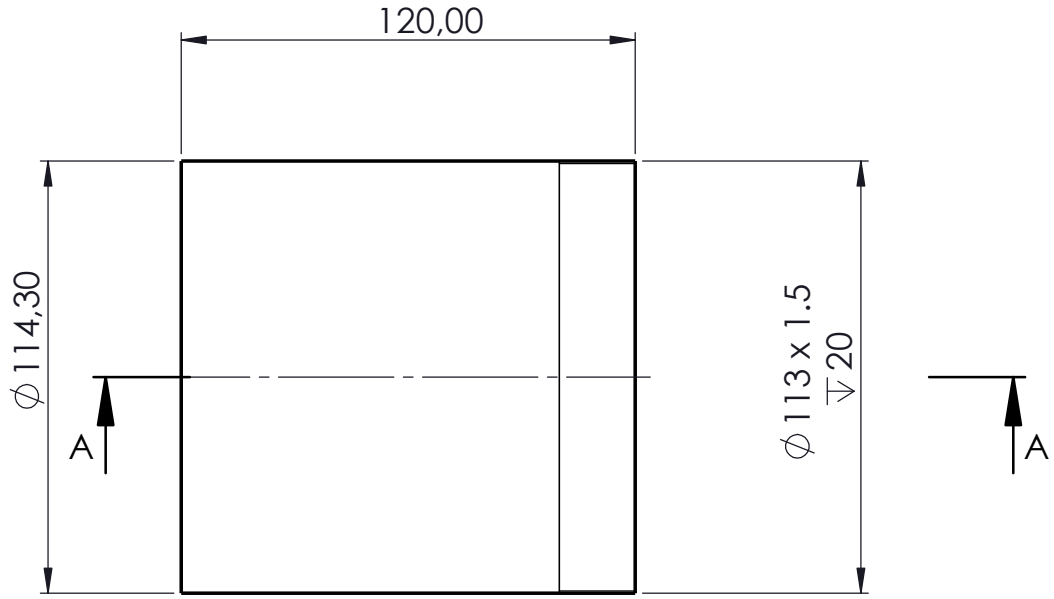

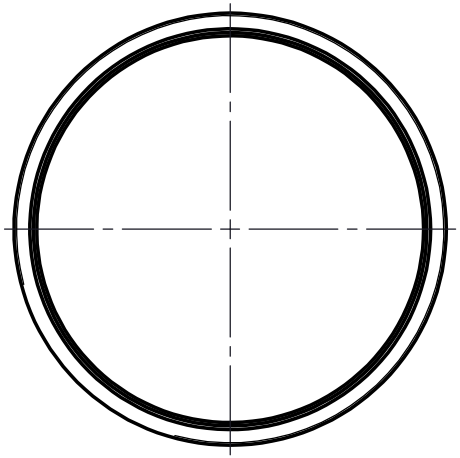

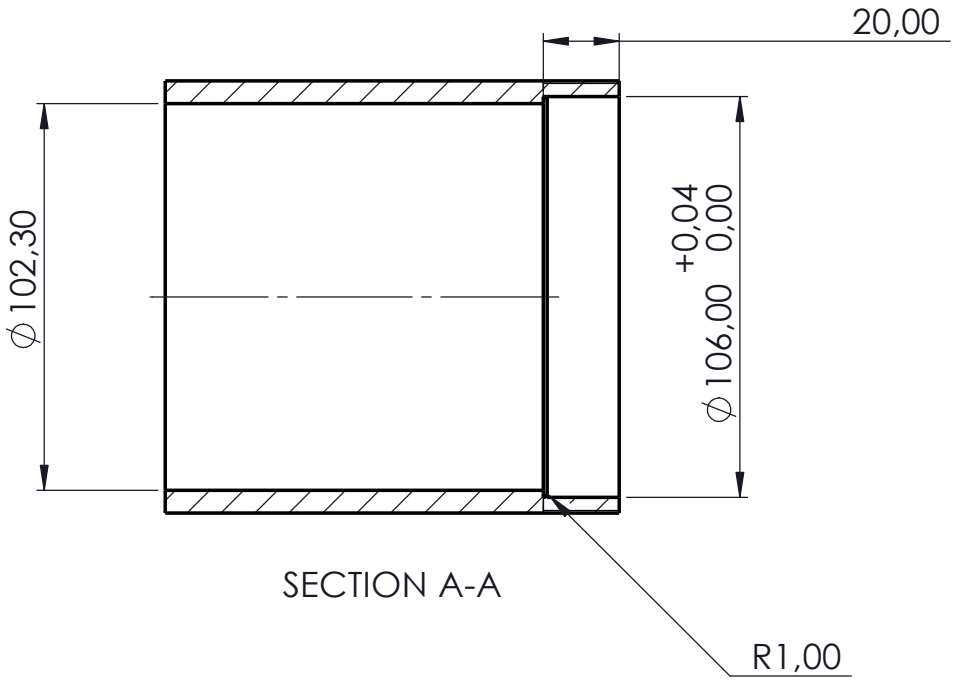

SECTION A-A

Scale: 1:2 on A4	University of Cape Town Department of Mechanical Engineering			
Drawn By: RUIXUAN QI	All un-toleranced dimensions to adhere to ISO 2768-m	Title: BLAST TUBE		
Checked : Prof. G Langdon	Material : MILD STEEL	Drawing Number : BTCA-CA-2	Rev. : A	Sheet : 1 of 1

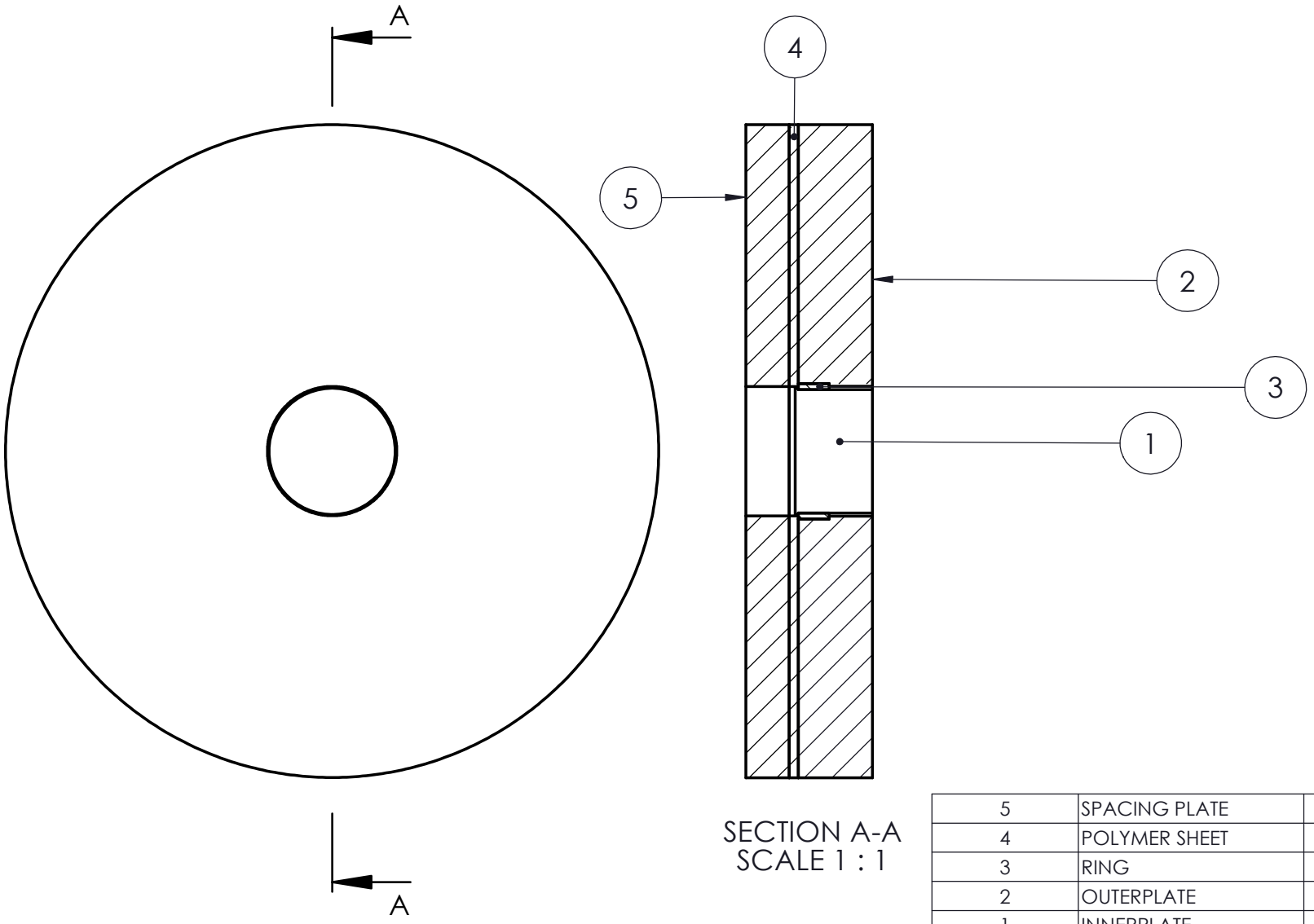

SECTION A-A
SCALE 1 : 1

ITEM NO.	PART NAME	MATERIAL	QTY.
5	SPACING PLATE	MILD STEEL	1
4	POLYMER SHEET	RUBBER	1
3	RING	STEEL	24
2	OUTERPLATE	AL 6082- T6	10
1	INNERPLATE	AL 6082-T6	24

Scale: 1:2 on A4	University of Cape Town Department of Mechanical Engineering			
Drawn By: Ruixuan Qi	All un-toleranced dimensions to adhere to ISO 2768-m	Title: Witness plate assembly		
Checked : Prof G Langdon	Assembly Drawing	Drawing Number : BTPA-CA-WP	Rev. : A	Sheet : 1 of 1

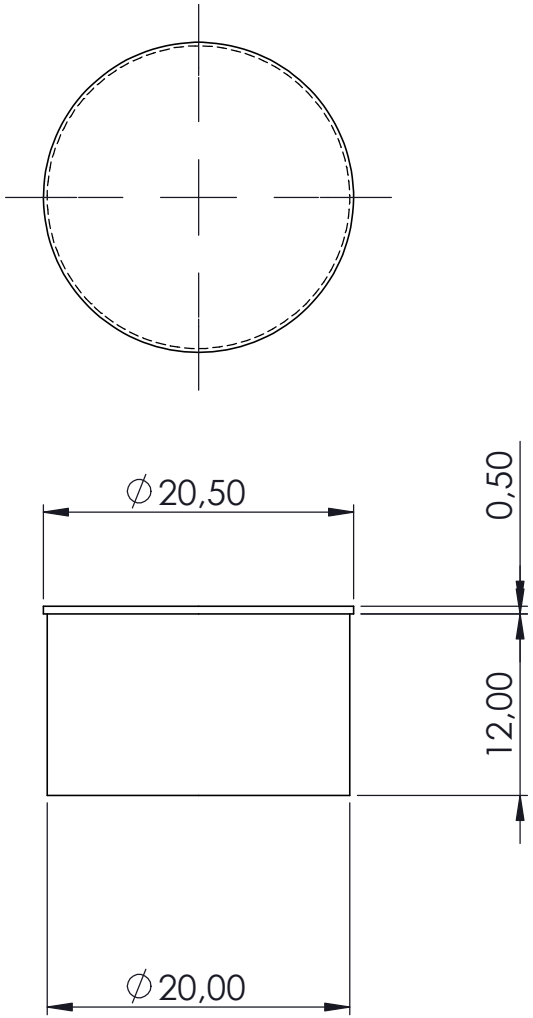

Scale: 2:1 on A4	University of Cape Town Department of Mechanical Engineering			
Drawn By: Ruixuan Qi	All un-toleranced dimensions to adhere to ISO 2768-m	Title: Inner witness plate		
Checked :	Material : AL 6082-T6	Drawing Number : BTPA-CA-WP-1	Rev. : A	Sheet : 1 of 1

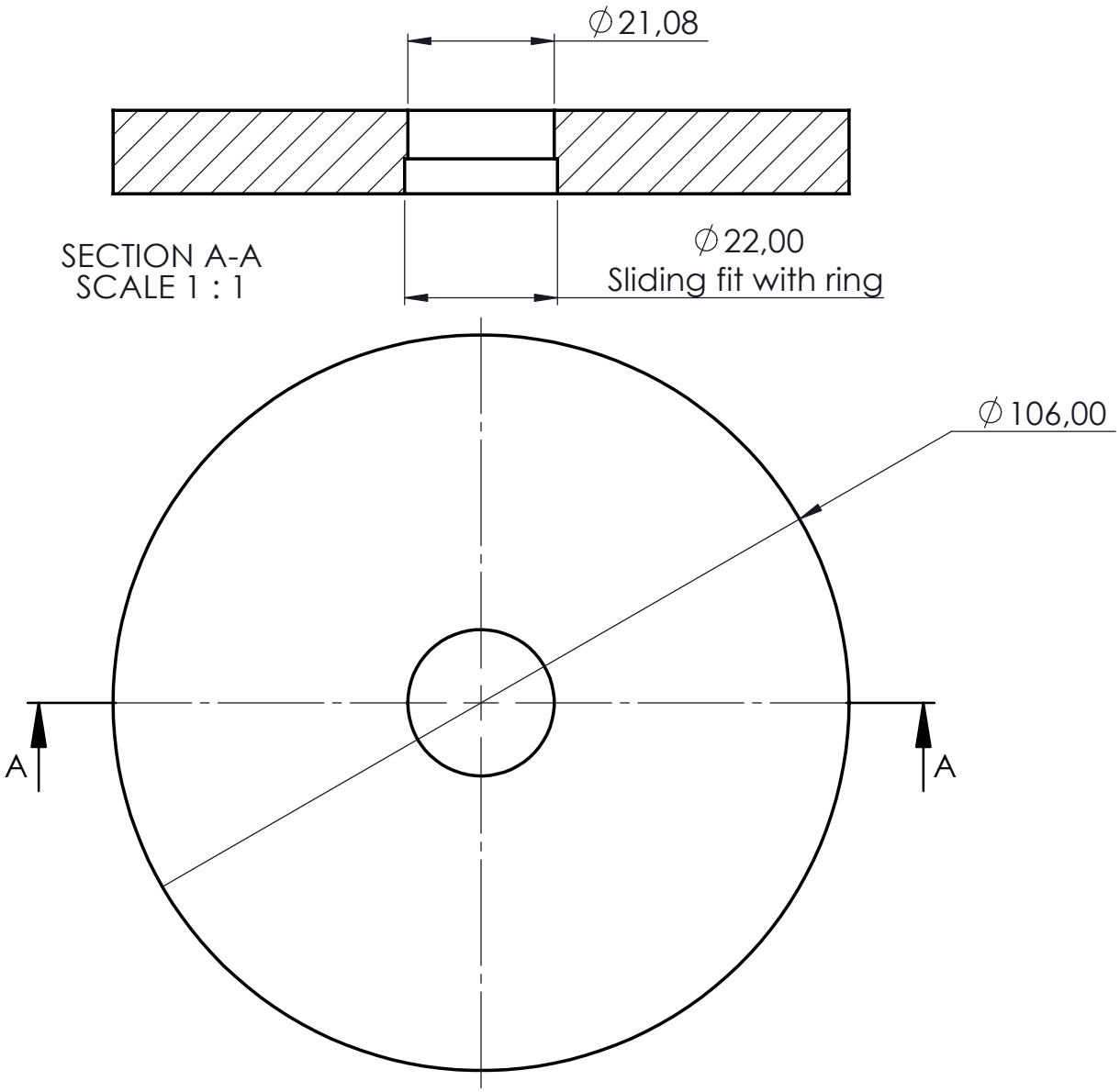

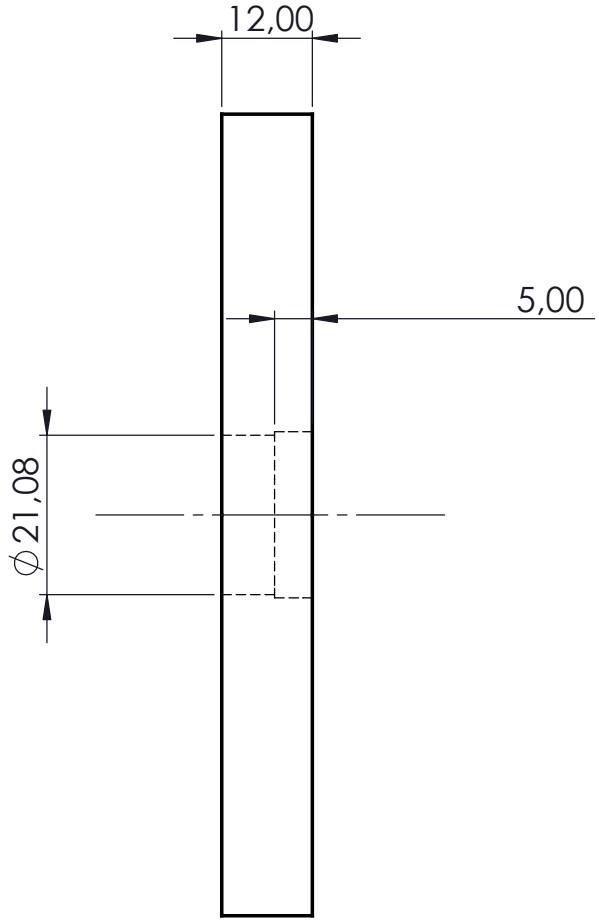

Scale: 1:2 on A4	University of Cape Town Department of Mechanical Engineering			
Drawn By: Ruixuan Qi	All un-toleranced dimensions to adhere to ISO 2768-m	Title: Outer witness plate		
Checked : Prof G Langdon	Material : Al 6082-T6	Drawing Number : BTPA-CA-WP-2	Rev. : A	Sheet : 1 of 1

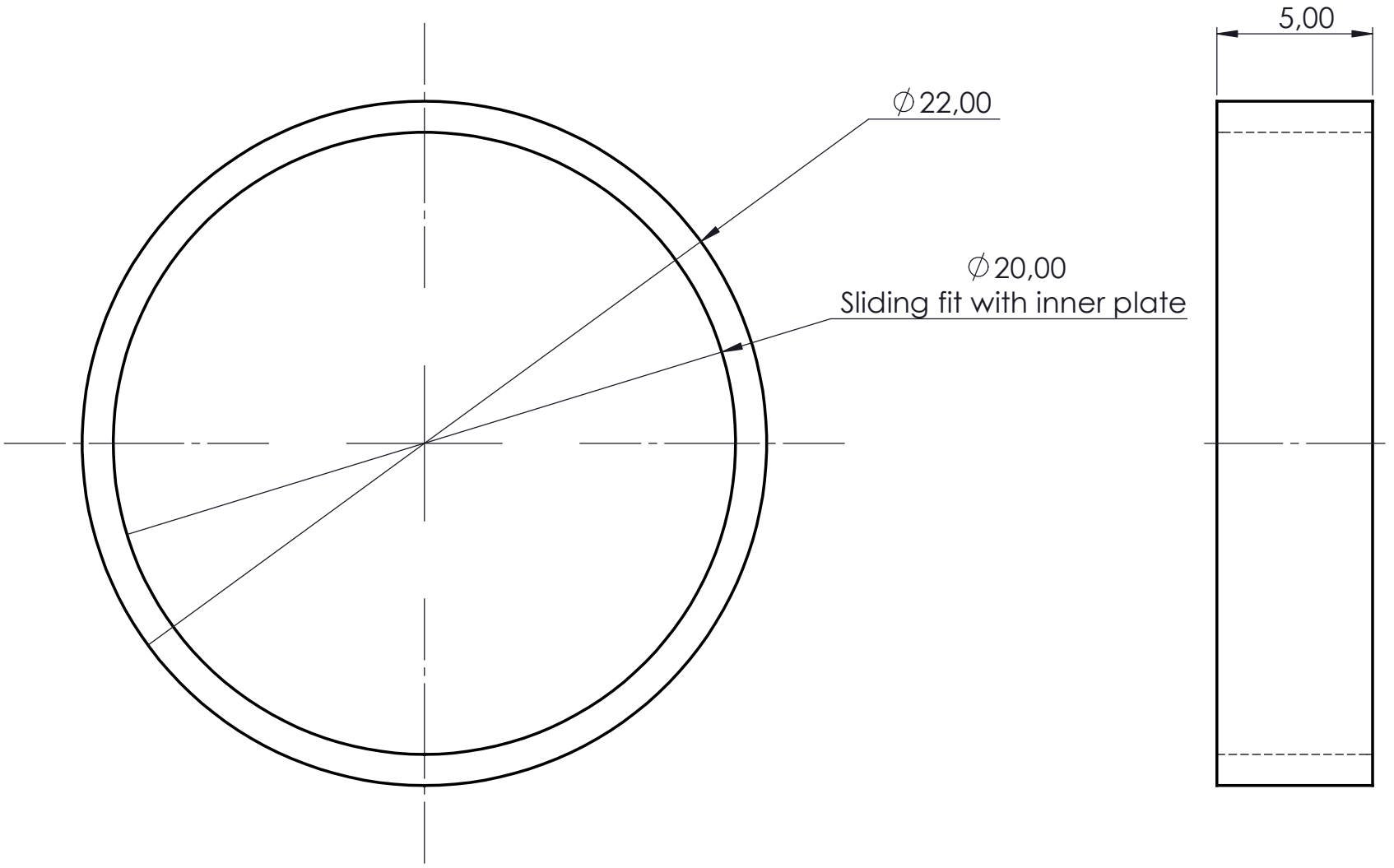

Scale: 5:1 on A4	University of Cape Town Department of Mechanical Engineering			
Drawn By: Ruixuan Qi	All un-toleranced dimensions to adhere to ISO 2768-m	Title: Ring		
Checked : Prof G Langdon	Material : Steel	Drawing Number : BTPA-CA-WP-03	Rev. : A	Sheet : 1 of 1

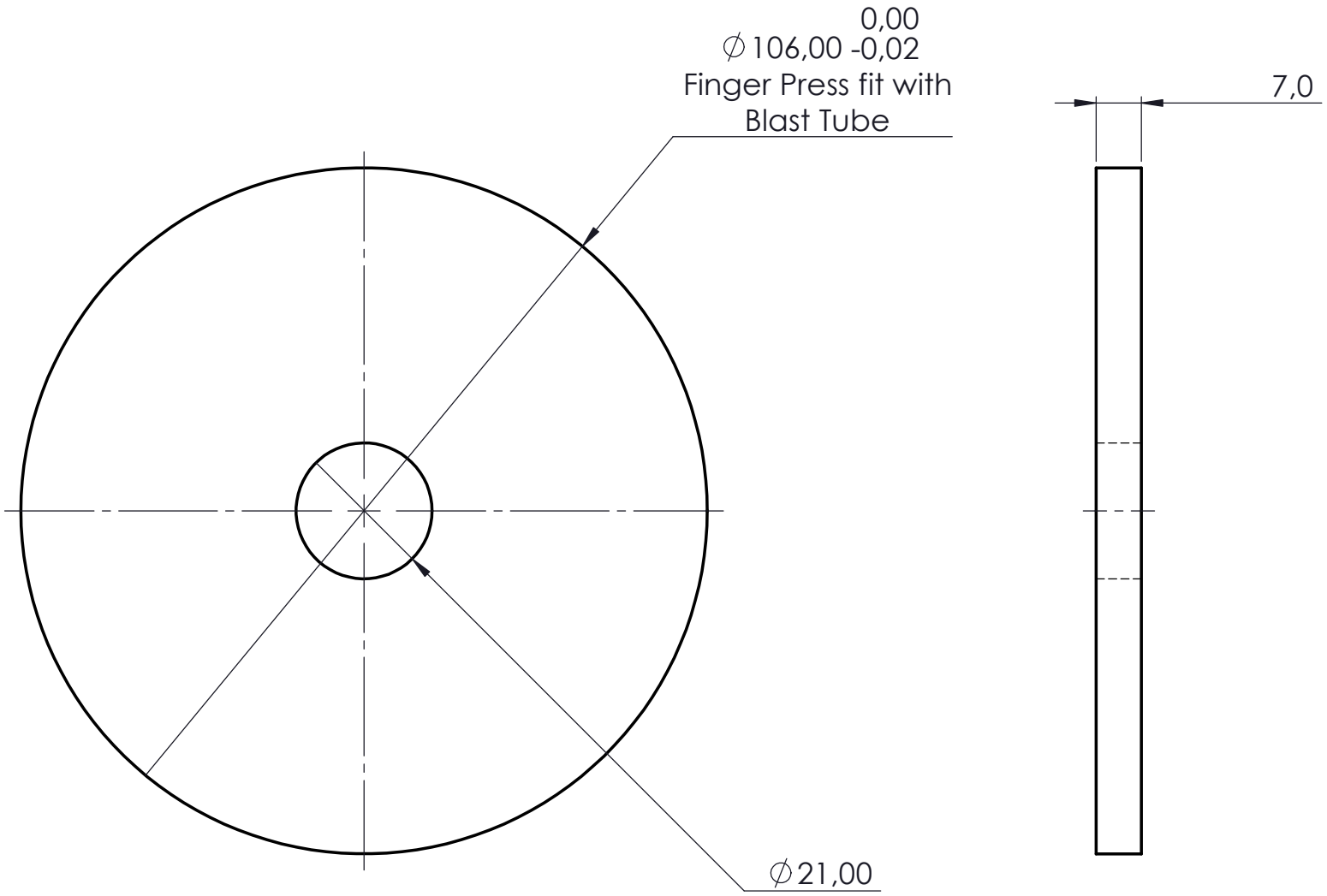

	Scale: 1:1 on A4	University of Cape Town Department of Mechanical Engineering		
Drawn By: Ruixuan Qi	All un-toleranced dimensions to adhere to ISO 2768-m	Title: Spacing Plate		
Checked : Prof G Langdon	Material : Mild Steel	Drawing Number : BTPA-CA-WP-5	Rev. : E-04	Sheet : 1 of 1

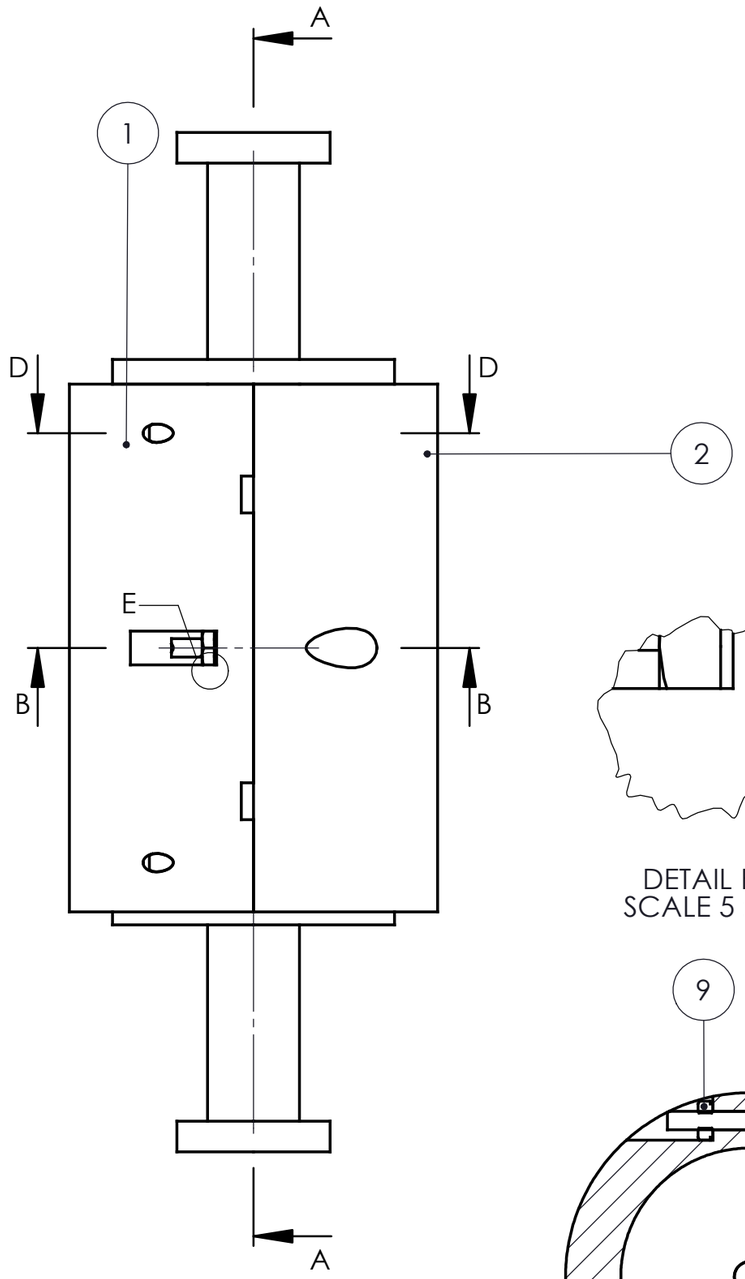

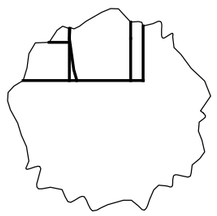

DETAIL E
SCALE 5 : 1

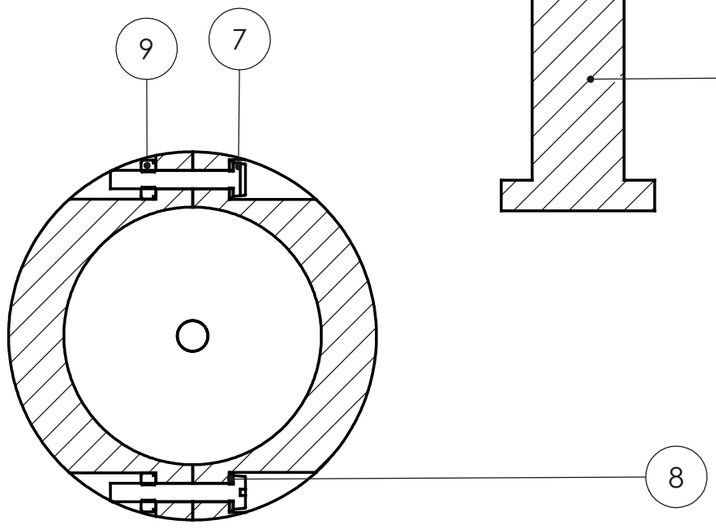

SECTION B-B
SCALE 1 : 1

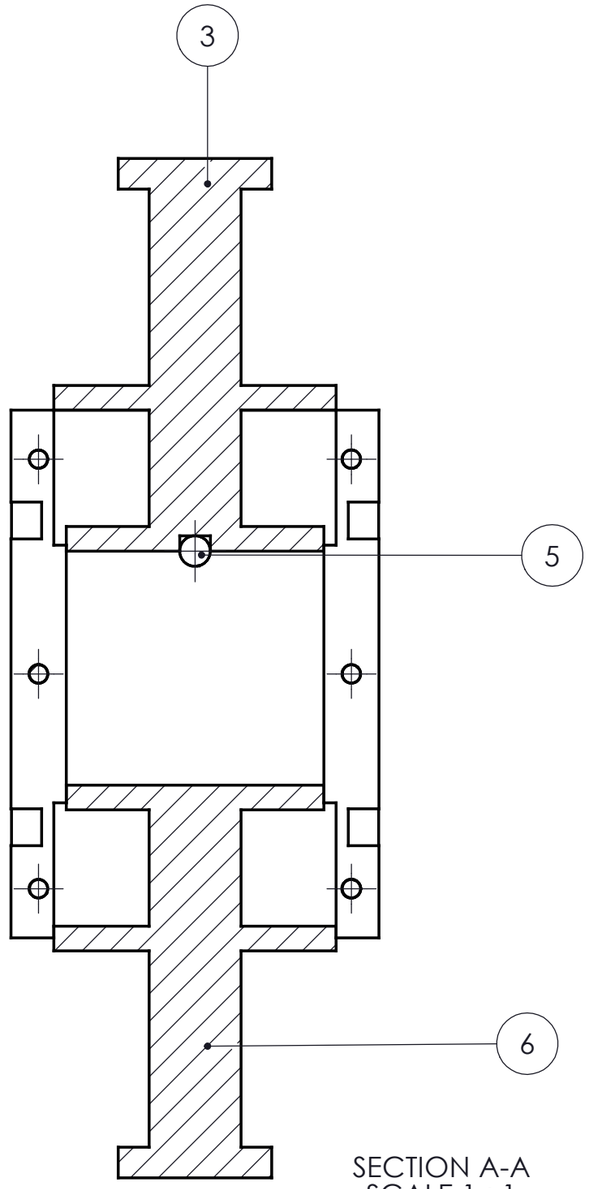

SECTION A-A
SCALE 1 : 1

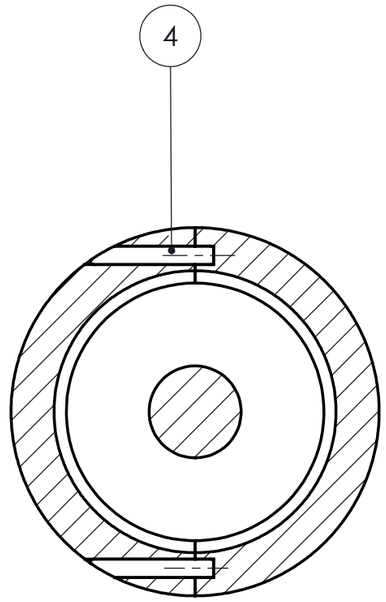

SECTION D-D
SCALE 1 : 1

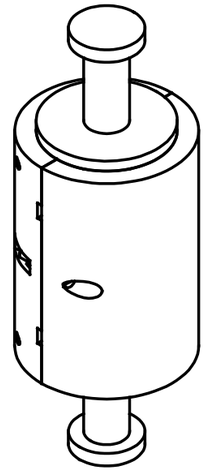

ITEM NO.	PART NUMBER	MATERIAL	QTY.
9	DIN 934 HEX NUT M3 WASHER FACE	BRASS	2
8	DIN 433 SMALL OD FLAT WASHER	BRASS	2
7	DIN84 SLOTTED CHEESE HEAD - M3 X 20	BRASS	2
6	PRESS BOTTOM	TEFLON	1
5	5mm BEARING BALL	STAINLESS 420	1
4	DOWEL PIN M3 X 8	BRASS	4
3	PRESS	TEFLON	1
2	SPLIT MOULD PART 2	TEFLON	1
1	SPLIT MOULD PART 1	TEFLON	1

Scale: 1:2 on A3

University of Cape Town
Department of Mechanical Engineering

Drawn By: Ruixuan Qi

All un-toleranced dimensions to adhere to ISO 2768-m

Title: 42 mm Split Mould

Checked : Prof S Chung

Assembly drawing

Drawing Number : 01

Rev. : A

Sheet : 1 of 1

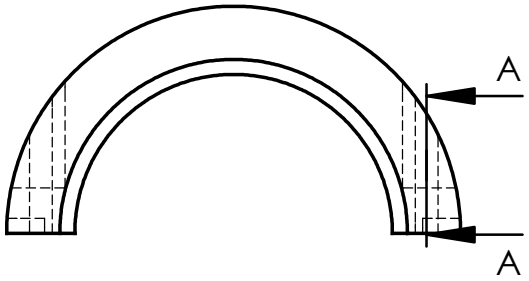

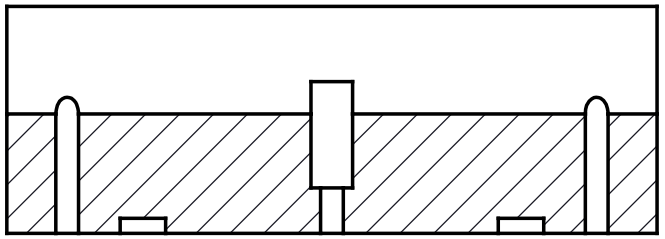

SECTION A-A

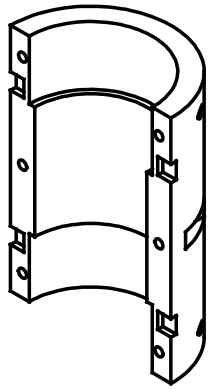

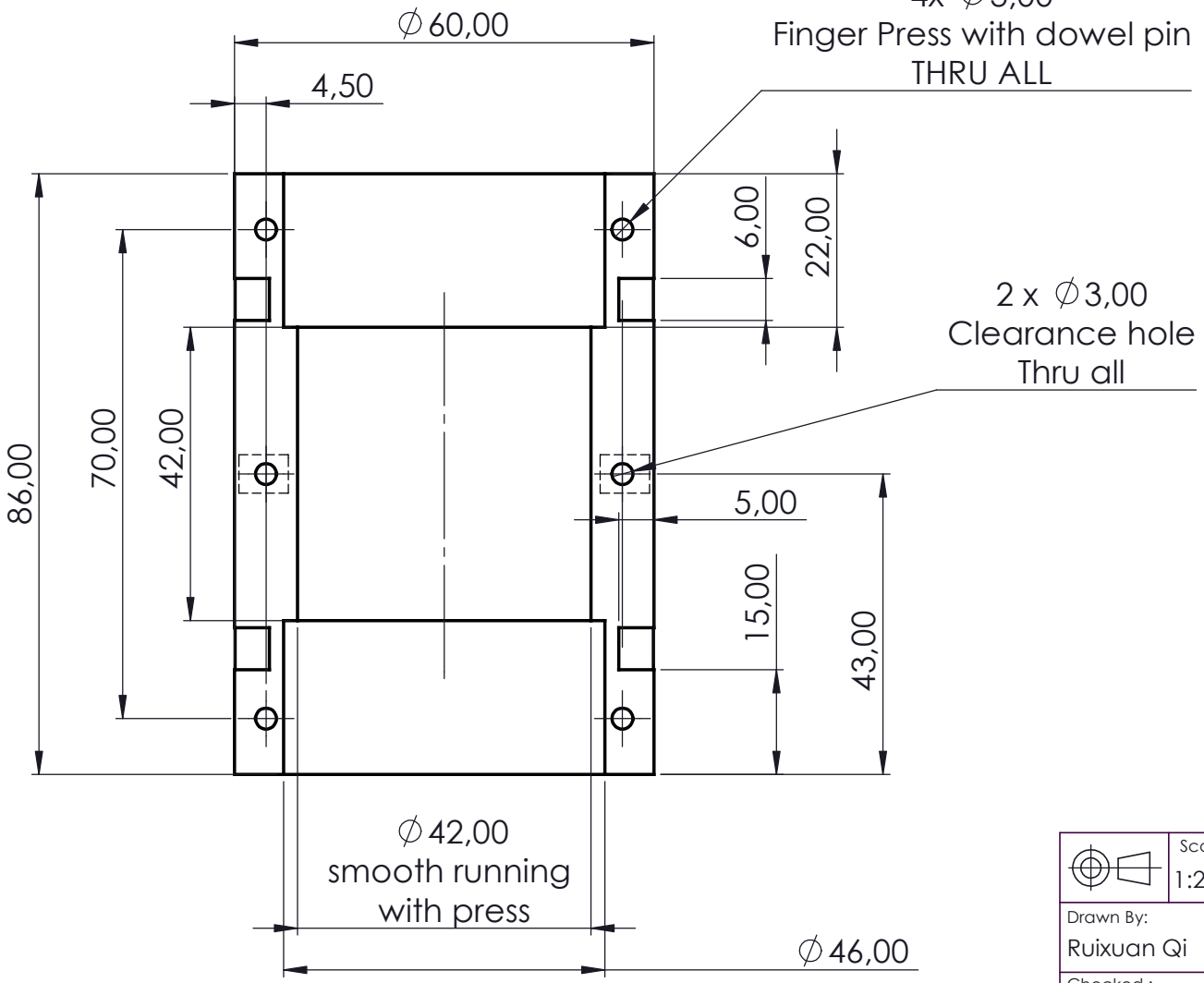

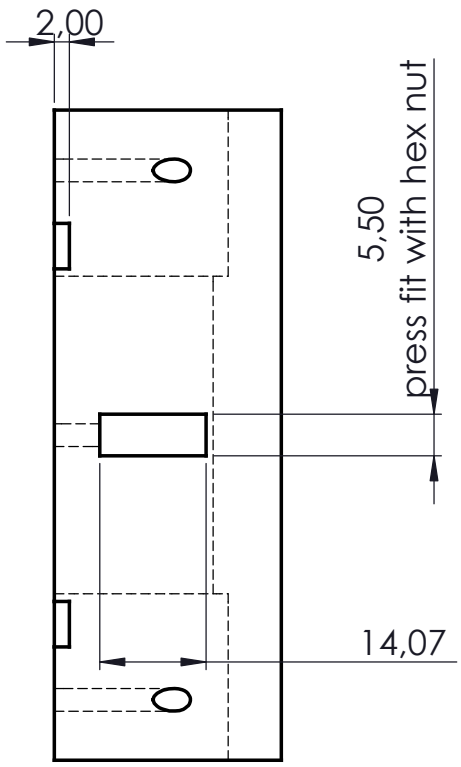

Scale: 1:2 on A4	University of Cape Town Department of Mechanical Engineering			
Drawn By: Ruixuan Qi	All un-toleranced dimensions to adhere to ISO 2768-m	Title: Split Mould Part 1		
Checked : Prof S Chung	Material : Teflon	Drawing Number : 1-1	Rev. : A	Sheet : 1 of 1

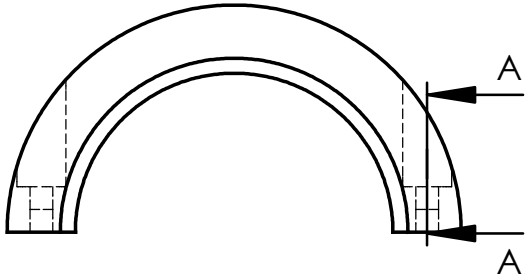

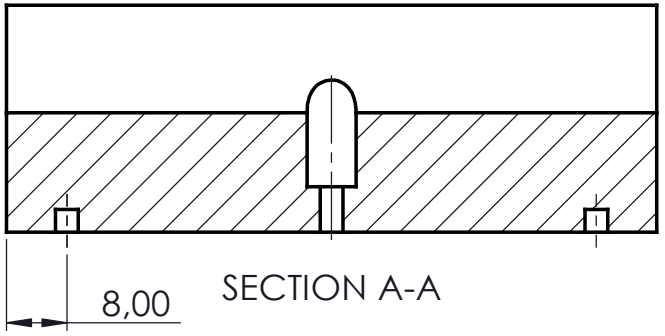

SECTION A-A

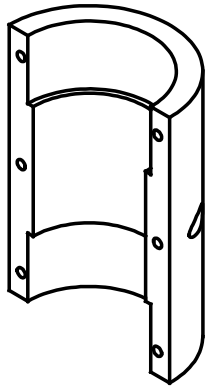

4 X ⌀3,00
↧4

4,50

finger press with dowel pin

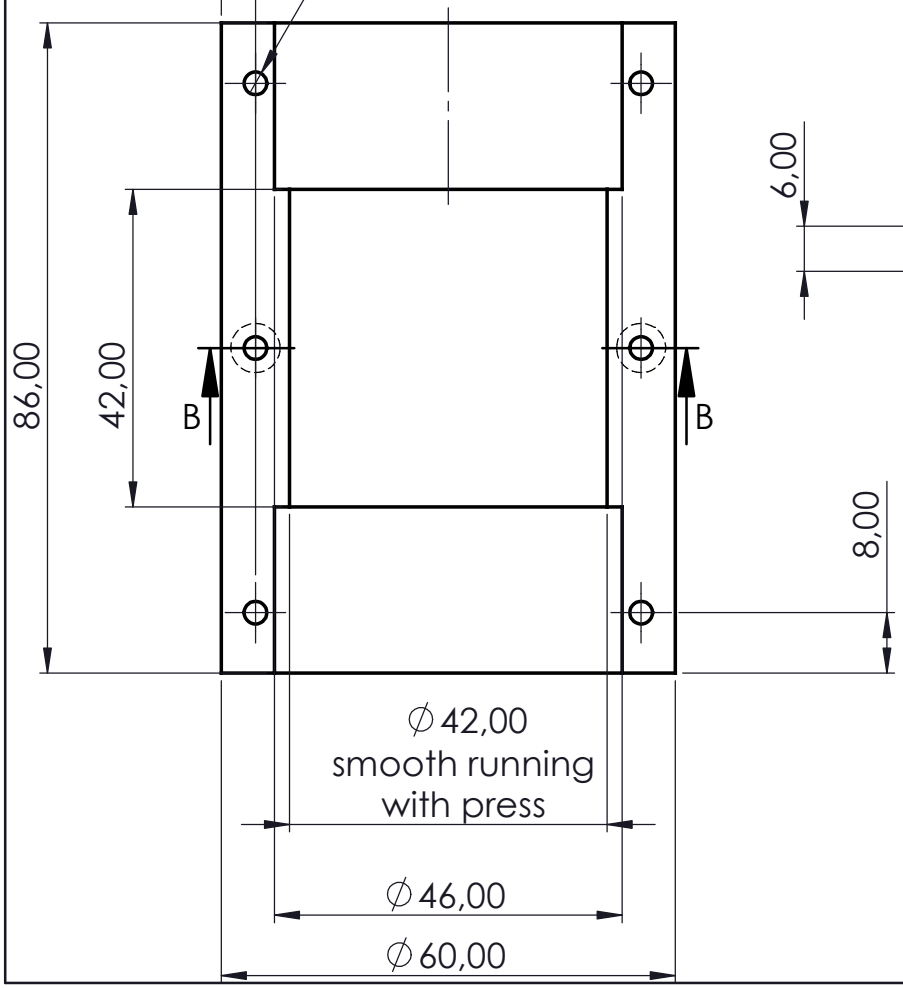

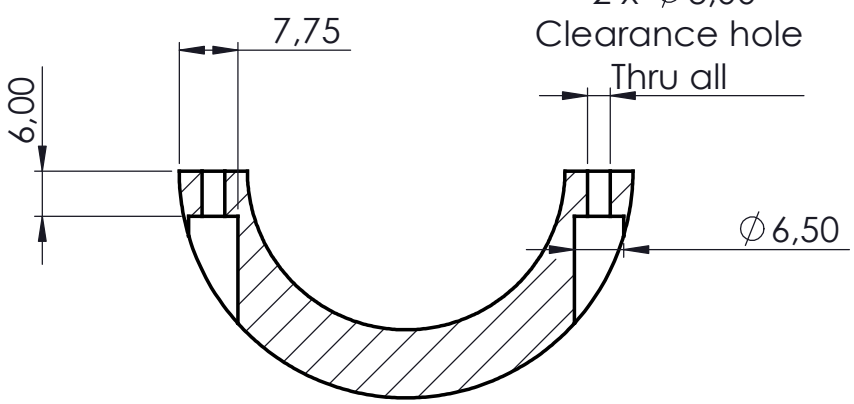

SECTION B-B

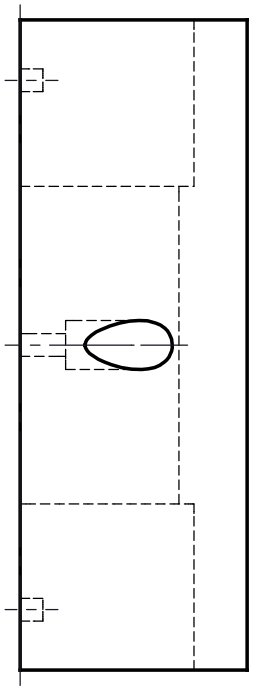

Scale: 1:1 on A4	University of Cape Town Department of Mechanical Engineering			
Drawn By: Ruixuan Qi	All un-toleranced dimensions to adhere to ISO 2768-m	Title: Split mould part 2		
Checked : Prof S Chung	Material : Teflon	Drawing Number : 1-02	Rev. : A	Sheet : 1 of 1

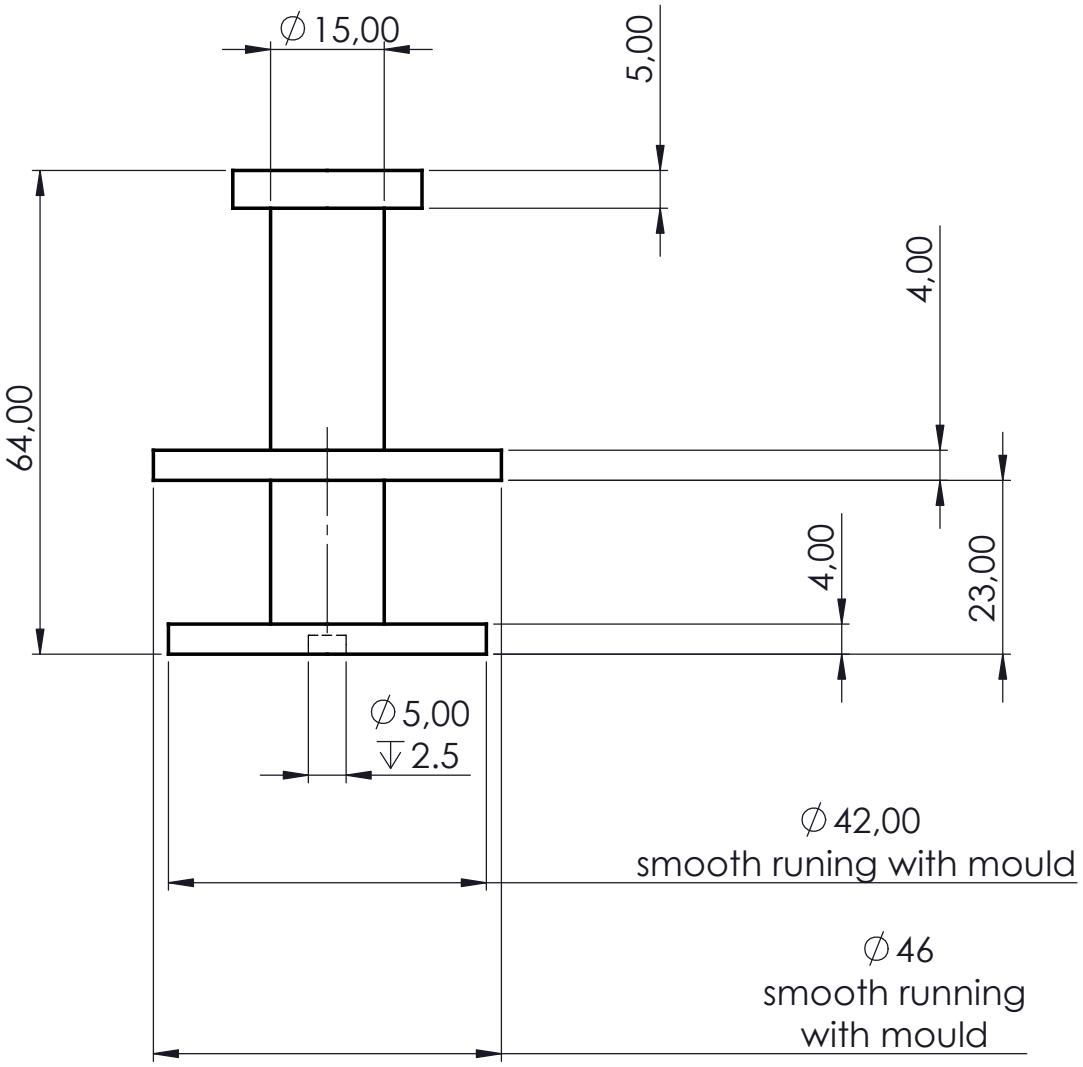

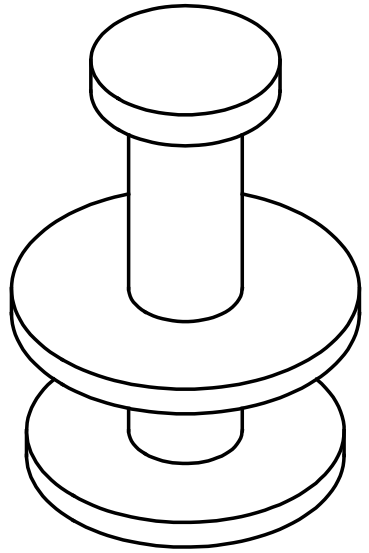

Scale: 1:1 on A4	University of Cape Town Department of Mechanical Engineering			
Drawn By: Ruixuan Qi	All un-toleranced dimensions to adhere to ISO 2768-m	Title: Top Press		
Checked : Prof S Chung	Material : Teflon	Drawing Number : 1-03	Rev. : A	Sheet : 1 of 1

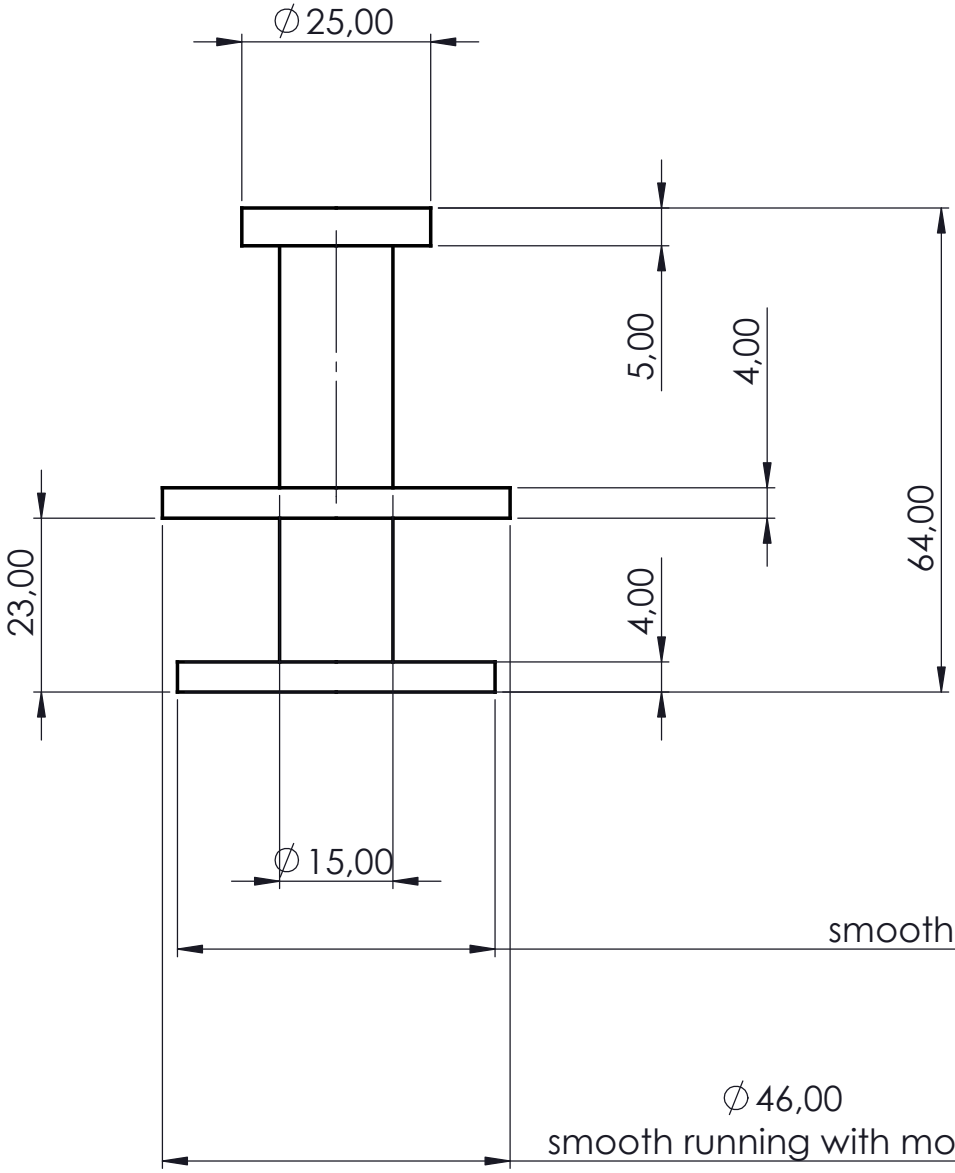

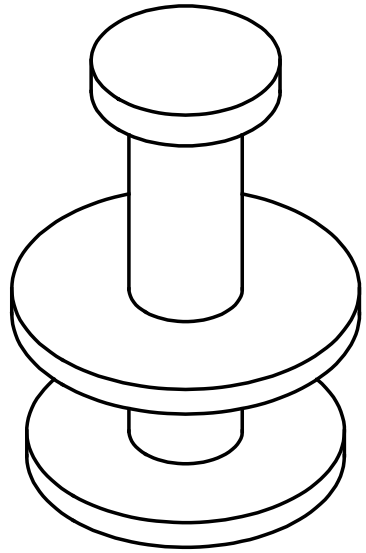

Scale: 1:1 on A4	University of Cape Town Department of Mechanical Engineering			
Drawn By: Ruixuan Qi	All un-toleranced dimensions to adhere to ISO 2768-m	Title: Bottom Press		
Checked : Prof S Chung	Material : Teflon	Drawing Number : 01-6	Rev. : A	Sheet : 1 of 1